GaN/AlGaN heterostructures for infrared optoelectronics : polar vs nonpolar orientations

Caroline Botum Lim

Communauté
UNIVERSITÉ Grenoble Alpes

THÈSE

Pour obtenir le grade de

DOCTEUR DE LA COMMUNAUTÉ UNIVERSITÉ GRENOBLE ALPES

Spécialité : **Physique**

Arrêté ministériel : 25 mai 2016

Présentée par

Caroline Botum LIM

Thèse dirigée par **Dr. Eva MONROY**, **CEA Grenoble**
préparée au sein du **Laboratoire Nanophysique et Semi-Conducteurs (CEA / INAC / PHELIQS)**
dans **l'École Doctorale de Physique, Université Grenoble Alpes**

Hétérostructures de GaN/Al(Ga)N pour l'optoélectronique infrarouge : orientations polaires et non-polaires

Thèse soutenue publiquement le **26 juin 2017**
devant le jury composé de :

Prof. Henning RIECHERT
Paul-Drude-Institut für Festkörperelektronik, Berlin, Rapporteur
Prof. Eric TOURNIÉ
Institut d'Électronique et des Systèmes, Université de Montpellier, Rapporteur
Dr. Catherine BOUGEROL
Institut Néel, CNRS et Université Grenoble-Alpes, Présidente
Dr. Jean-Michel CHAUVEAU
CNRS, CRHEA, Membre
Dr. Lorenzo RIGUTTI
Université de Rouen, Membre
Dr. Eva MONROY
Institut Nanosciences et Cryogénie, CEA Grenoble, Membre

Acknowledgements

Where there's a will, there's a way.

Voici pour moi, peut-être, la partie de ce manuscrit la plus difficile, mais la plus plaisante, à écrire. Non pas à cause de son contenu scientifique édifiant (!), mais parce qu'elle me tient beaucoup à cœur. Car comment commencer à remercier tous ceux qui m'ont accompagnée au long de ces trois ans ?

Ne parvenant pas à choisir entre Français et Anglais, j'ai décidé d'adapter la langue de mes remerciements aux personnes auxquelles ils sont adressés, pour que je puisse à la fois exprimer au mieux mon sentiment et être comprise.

Je tiens d'abord à remercier ma directrice de thèse Dr. Eva Monroy. Merci pour cette rencontre que nous n'avions pas prévue, merci de m'avoir proposé ce si *joli* sujet, et avec un enthousiasme tel que poursuivre en thèse était immédiatement devenu une évidence pour moi. Merci ensuite pour ces trois années passées à me guider et à m'encourager avec un sourire permanent, à prendre le temps de m'aider dans mes manips alors qu'une to-do list bien trop longue t'attendait encore dans ton bureau. Merci de m'avoir envoyée aux quatre coins du monde (la thèse m'aura aussi appris à plier bagage efficacement). Merci d'être aussi passionnée, enthousiaste, patiente, investie… merci pour cette chance d'avoir eu une thèse dont je peux dire qu'elle était *fun*, car ce quotidien va me manquer ! Merci d'avoir été autant un modèle scientifique qu'une amie. Tu es une source d'inspiration, et j'espère que nos chemins se recroiseront souvent. Merci Eva.

Je tiens également à remercier Henri Mariette (Directeur du groupe NPSC lorsque j'ai commencé ma thèse), Régis André et Bruno Gayral (actuels Directeurs du groupe NPSC), ainsi que Jean-Michel Gérard (Directeur de PHELIQS), pour m'avoir accueillie dans ce groupe et m'avoir donné l'opportunité de m'épanouir en tant que jeune chercheuse dans ce projet. Je voudrais de plus remercier Carmelo Castagna, Céline Conche et Sarah Mauduit, pour leur aide précieuse à chacune des nombreuses étapes administratives rencontrées pendant ces trois années.

I would also like to thank all the members of the jury, the "rapporteurs" Prof. Henning Riechert and Prof. Eric Tournié, and the "examinateurs" Dr. Catherine Bougerol, Dr. Jean-Michel Chauveau, and Dr. Lorenzo Rigutti, for their time and comprehensive feedback on my work, and for coming all the way to Grenoble. Thank you also for the nice discussions, questions, and comments during my defense, which I enjoyed a lot. Also I would like to thank Joël Bleuse and Régis André for their help in preparing my defense in the best way possible.

I would like to thank the group in Giessen: Jörg Schörmann, Pascal Hille and Martin Heickhoff for the nice collaborations.

Je souhaite remercier aussi tous mes collègues du CEA, sans qui ce travail n'aurait pas été possible. Merci à Yoann Curé, Yann Genuist, Didier Boilot et Jean Dussaud pour toute l'aide technique et pratique apportée au quotidien (que ce soit ouvrir la MBE, nous sauver pendant une panne de climatisation, ou autre !). Merci également à Edith Bellet-Amalric et Stéphanie Pouget pour leur aide précieuse avec le diffractomètre à rayons x, merci à Catherine Bougerol pour ses belles images de microscopie et son expertise, merci à Lucien Notin pour son aide avec l'AFM (et la Bricothèque !).

J’adresse également un énorme merci à (Dr.) Mark Beeler et (soon-to-be Dr.) Akhil Ajay, pour votre bonne humeur à toute épreuve ainsi que votre aide (et votre soutien) autant scientifique que moral. Ça a été un plaisir de vous côtoyer au quotidien et de travailler avec vous, et je vous souhaite le meilleur pour le futur. Je remercie aussi tous les autres membres de l’équipe, David Browne, Luca Redaelli, Jonas Lähnemann, Sirona Valdueza-Felip mais aussi Amine El Kacimi, Martin Vallo, Matthias Belloeil, Anna Mukhtarova et Agnès Messanvi. Merci de même à Thibault Crémel, Zhihua Fang, Tobias Sattler, Tomasz Jakubczyk et Alberto Artioli, mais aussi Madalina Siladie, Marion Gruart, Maria, Romain et Akansha, de contribuer à ce que cette joyeuse et dynamique atmosphère règne dans ce groupe.

Mes remerciements vont aussi naturellement à mes amis qui, au quotidien à Grenoble, ou quand ils le pouvaient depuis Paris (ou Avignon !), m’ont soutenue et redonné courage chaque fois que j’en avais besoin. Merci à mes copines de toujours, Noémie et Sarah : grâce à vous ça va toujours mieux, même quand il ne fait pas beau, merci d’être vous, merci d’être là. Merci à Nico, Adrien, Lynda et Cédric pour les soirées, les séances à broyer du *gris*, les thés du dimanche et les raclettes. Merci aussi à Mathieu-Noah, Merwan, Vuddhi, et tous ceux que j’oublie, qui étaient avec moi pendant ces trois ans depuis Paris.

Merci à ma Famille, sans qui je ne serais pas là aujourd’hui. En particulier, merci d’abord à mes parents, pour qui ces lignes seront bien trop courtes pour exprimer toute ma reconnaissance. Merci de m’avoir toujours soutenue malgré les sacrifices, et d’avoir cru en moi quand moi-même je n’y croyais plus. Merci de m’avoir guidée à devenir qui je suis aujourd’hui, et surtout, merci d’être fiers de moi pour avoir fait de mon mieux. Merci à mes grands-parents, merci Yeay et Ta, Tonton Chet et Tata Anne, d’être toujours là pour moi et fiers de moi. Votre regard et votre soutient me sont des plus précieux. Merci à mes cousins, que ce soit ceux qui m’ont suivie jusqu’au bout du monde, ou encore ceux qui ont eu le plaisir de passer le Bac (ou supporter lesdits candidats) alors que j’écrivais ces lignes, merci à vous, Charlotte, Moni, Valentin, Léo, Ed, et Rattana.

Enfin, je remercie mon Mathieu, sans qui mener cette thèse n’aurait littéralement pas été possible. Merci d’être à la fois pour moi un amoureux, un partenaire, un ami, un chef de cuisine, un pilote, un coach, un musicien, ou encore un chercheur passionné. Merci pour ton soutien, merci de croire en moi, et merci de prendre soin de nous au quotidien.

A few words in French

Ce manuscrit étant complètement écrit en anglais, ces quelques pages résument en français les problématiques et les expériences menées ainsi que leurs résultats.

Contexte et motivations

Ce mémoire de thèse est consacré à l'étude de nanostructures semi-conductrices à base de GaN, telles que les multi-puits quantiques 2D et les multi-puits quantiques insérés dans des nanofils. L'intérêt de ces nanostructures réside dans leurs propriétés optoélectroniques: grâce à l'interaction lumière-matière, l'excitation de ces multi-puits quantiques et donc des électrons confinés de la structure par une onde électromagnétique ou par un courant électrique, par exemple, rend possible l'émission ou l'absorption de lumière par la structure, ce qui correspond à des transitions d'énergie d'électrons (transfert d'énergie de la radiation vers un électron ou émission de lumière par un électron qui se désexcite). Ces transitions peuvent avoir lieu entre des états d'énergie de la bande de conduction et de la bande de valence du semi-conducteur (transition interbande) ou entre des états d'énergie de la même bande (transition intersousbande). En particulier, nous nous intéressons au possible développement de composants optoélectroniques intersousbandes à base de nitrures opérant dans la fenêtre spectrale infrarouge (c'est-à-dire fonctionnant à des longueurs d'onde comprises entre le visible – 800 nm – et le mm). Pour ce faire, la conception des nanostructures est primordiale : leur composition et leurs dimensions sont les paramètres à définir pour ajuster les longueurs d'onde d'absorption ou d'émission. Nous avons utilisé le logiciel Nextnano^3 pour résoudre les équations de Schrödinger-Poisson avec la méthode k.p à 8 bandes, et ainsi simuler les propriétés optoélectroniques des nanostructures selon ces paramètres. L'étape suivante a consisté à fabriquer les nanostructures par épitaxie par jets moléculaires assistée par plasma, et enfin nous avons réalisé les caractérisations structurales et optiques des échantillons.

Le manuscrit commence par une introduction générale du contexte de l'étude et de ses objectifs. On présente un bref historique du développement des technologies optoélectroniques dans la gamme infrarouge et on décrit les raisons motivant l'exploration des matériaux III-nitrures GaN et AlN pour ces applications. En particulier, on peut retenir que la première application des rayonnements infrarouges fut consacrée à l'imagerie thermique dans un contexte militaire. De nos jours, les technologies d'émission et de détection infrarouges sont présentes dans de nombreux domaines d'applications différents : la fenêtre 1.3-1.55 µm est dédiée aux télécommunications par fibre optique, les fenêtre 3-5 µm et 8-14 µm sont exploitées pour l'imagerie thermique, et la fenêtre THz (longueur d'onde supérieure à 10 µm) est utilisées pour un large panel d'applications allant des technologies de l'information et de la communication au contrôles de sécurité, en passant par l'imagerie médicale et le contrôle qualité.

Les technologies intersousbandes sont basées sur les transitions optiques entre des états d'énergie électroniques confinés dans la bande de conduction dans le cas de nanostructures III-nitrures. Ces technologies ont d'abord été développées avec des matériaux III-arséniures et III-phosphures et ont donné lieu à la réalisation de détecteurs et lasers opérant dans le moyen et le lointain infrarouge. Cependant, les propriétés de ces matériaux compliquent le développement de ces composants dans les fenêtres proche infrarouge (décalage de bande de conduction insuffisante) et THz. En particulier, la bande 5-10 THz est intrinsèquement interdite aux arséniures. Les III-nitrures

doivent permettre d'étendre la gamme spectrale de fonctionnement vers le proche-infrarouge et vers le lointain infrarouge et les THz, et ce à température ambiante.

De nos jours, les III-nitrures sont des matériaux privilégiés pour les composants optoélectroniques, et ils ont permis en particulier le développement des LED rouge-vert-bleu et UV, dont les applications sont très nombreuses : éclairage, stockage de l'information, purification de l'eau, etc. Ils sont également utilisés pour la détection UV et pour l'électronique de haute-puissance. Pour leur application dans le domaine de l'optoélectronique intersousbande, le large désaccord de maille dans le système GaN/AlN et la présence de champs de polarisation intenses complique le développement de composants. Dans ce travail de thèse, on cherche à exploiter la production récente de substrats massifs de très bonne qualité cristalline de GaN non-polaire (plan *a* et plan *m*) pour réaliser des structures GaN/AlGaN intersousbandes infrarouges et THz non-soumises à un champ de polarisation interne.

Deux problématiques sont soulevées et sont étudiées dans les deux chapitres de résultats. L'observation d'absorption intersousbande nécessite de doper les structures, ce qu'il est possible de faire avec du Si ou avec du Ge. C'est pourquoi le chapitre 3 est d'abord consacré à l'étude du Ge en tant que dopant alternatif au Si (généralement utilisé). Le chapitre 4 en vient au cœur du sujet et traite de la possibilité d'utiliser du GaN non-polaire pour développer des structures GaN/AlGaN présentant de l'absorption intersousbande dans les fenêtres proche, moyen et lointain infrarouge (en particulier THz).

Chapitre 1. Introduction

Le premier chapitre introduit les connaissances de physique des semi-conducteurs nécessaires à la bonne compréhension du reste du manuscrit. On s'intéresse d'abord aux propriétés physiques des semi-conducteurs III-nitrures massifs GaN et AlN dont il est question dans le reste de cette thèse. On commence par détailler la structure cristalline wurtzite dont découlent les propriétés électroniques et optiques de ces matériaux. La résolution de l'équation de Schrödinger permet de démontrer la structure de bande des états d'énergie électroniques de ces matériaux, et de définir les bandes d'énergies autorisées et interdites, comme schématisé dans l'Illustration 1. Connaître ces diagrammes de bandes est primordial pour pouvoir exploiter correctement les possibles transitions énergétiques dans un couplage lumière-matière. Le champ de polarisation spontanée résultant de la faible symétrie des cristaux wurtzite est également décrit car il peut modifier le diagramme de bandes, ainsi que les propriétés optiques du GaN. On introduit en particulier la notion de phonon optique, qui correspond à un mode de vibration du réseau cristallin qui peut entrer en résonance avec des radiations infrarouges.

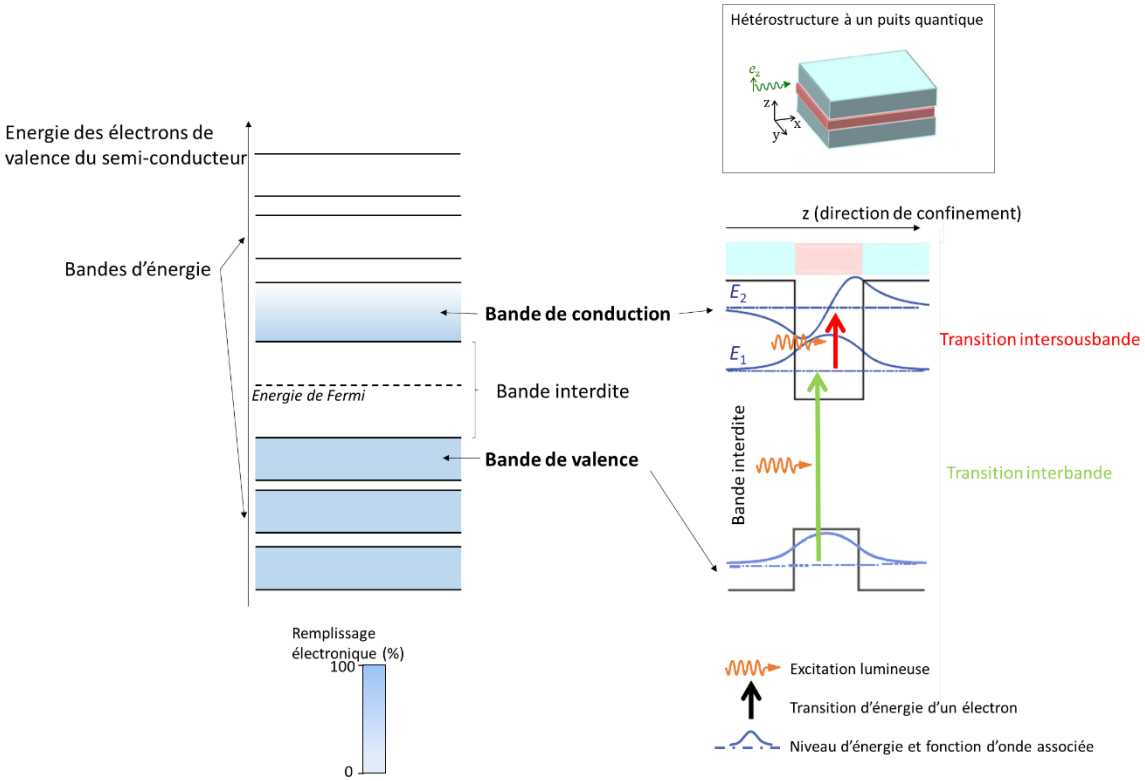

Illustration 1 Structure électronique à T ≠ 0 K et transitions d'énergie électroniques d'une hétérostructure de type n à un puits quantique de type I.

Pour réaliser des multi-puits quantiques, on réalise des hétérostructures en empilant plusieurs couches de matériaux semi-conducteurs différents, de façon à obtenir un confinement quantique des électrons de la structure, comme schématisé dans l'Illustration 1. La deuxième partie du chapitre est donc consacrée aux propriétés structurales, électroniques et optiques d'hétérostructures III-nitrures. L'empilement de semi-conducteurs de paramètres de maille différents conduit à l'établissement d'un état de contrainte dans la structure, qui est compensé par ondulation de la surface ou par formation de défauts cristallins. On présente ainsi la zoologie des défauts généralement observés dans les matériaux GaN/AlGaN, et on souligne en particulier la présence des fautes d'empilements. Ces défauts peuvent être très dommageables pour les performances optoélectroniques des composants. La différence de paramètre de maille dans l'hétérostructure engendre également la génération d'un champ piézoélectrique en réponse à la contrainte mécanique exercée dans la structure, qui s'ajoute au champ de polarisation spontanée interne à chaque matériau massif. L'effet du champ électrique interne sur les bandes d'énergie est ensuite pris en compte, ce qui nous amène à décrire le Quantum Confined Stark Effect (QCSE).

Dans la troisième partie du chapitre, on s'intéresse aux transitions intersousbandes. On établit la structure de bande des multi-puits quantiques, nécessaire à la conception des architectures. On résout ensuite l'équation de Schrödinger pour les états d'énergie électroniques dans la bande de conduction, et on en déduit les règles de sélection qui gouvernent ces transitions intersousbandes: seules les radiations polarisées transverse magnétique (TM) peuvent se coupler a ces transitions optiques. Ainsi seules les radiations polarisées TM peuvent être absorbées par transition intersousbande. Les mécanismes de relaxation d'électrons excités dans l'hétérostructure sont ensuite décrits, et les effets à corps multiples à prendre en compte suite au dopage des structures sont étudiés. On termine cette section par un état de l'art des structures intersousbandes GaN/AlGaN d'orientations cristallographiques polaire, semi-polaire et non-polaire. On peut retenir que les structures polaires

sont les systèmes privilégiés par la communauté scientifique en partie pour la moindre dégradation structurale conséquente à l'hétéroépitaxie comparé aux autres orientations. Pour répondre à la problématique du QCSE, la mise au point de structures complexes permettant de compenser en partie le champ électrique et d'obtenir des puits globalement carrés a permis de démontrer des transitions intersousbandes THz dans des systèmes GaN/AlGaN polaires. En termes de composants, des switches tout-optiques multi-Tbit/s ont été démontrés à 1.5 µm, ainsi que des modulateurs électro-optiques, mais également des photodétecteurs dans le proche et le lointain infrarouge. Avec la démonstration du concept de mise en cascade, des photodétecteurs à cascade quantiques ont été développés dans la fenêtre 1.5-2 µm et ont ouvert la voie pour le développement de lasers à cascade quantiques. Pour ce qui est des systèmes semi-polaires, des transitions intersousbandes ont pu être démontrées seulement dans la fenêtre proche-infrarouge et ce très récemment. Finalement, des photodétecteurs QWIP plan *m* dans le moyen infrarouge ont été développés et des hétérostructures plan *m* présentant de l'absorption intersousbande THz ont été démontrées en 2014.

Chapitre 2. Méthodes

Le chapitre 2 est consacré à la description des techniques utilisées. Concernant la conception des structures, on utilise le logiciel Nextnano[3] qui permet de simuler l'état de contrainte, les diagrammes de bandes et les niveaux électroniques des systèmes selon leurs dimensions et compositions. La présence des champs de polarisation est prise en compte et les paramètres des matériaux sont détaillés.

Ensuite, on se concentre sur la technique de croissance: l'épitaxie par jets moléculaires assistée par plasma. On commence par lister et décrire les différents substrats utilisés dans ce travail de thèse, puis on décrit l'équipement d'épitaxie et son fonctionnement. On donne également un bref état de l'art de la croissance de GaN, AlN et AlGaN d'orientations polaire, semi-polaire et non-polaire.

Les techniques de caractérisation structurales et optiques que j'ai utilisées sont ensuite détaillées :

- Microscopie à force atomique, pour étudier la morphologie de la surface des échantillons
- Diffraction à rayons x, pour étudier la structure globale des systèmes (épaisseurs des puits et barrières, état de contrainte, mosaicité et qualité structurale)
- Photoluminescence, pour étudier les propriétés interbandes des structures
- Spectroscopie infrarouge à transformée de Fourier, pour étudier les propriétés intersousbandes
- Effet Hall, pour déterminer les concentrations de porteurs résultant du dopage des structures
- Microscopie électronique à balayage, pour étudier la morphologie de surface des échantillons à plus grande échelle qu'en microscopie à force atomique

Et on décrit également les caractérisations utilisées pour l'étude des échantillons mais que je n'ai pas réalisées moi-même:

- Microscopie électronique à transmission, pour étudier localement la structure des échantillons (épaisseurs, composition, défauts cristallins)
- Cathodoluminescence, pour étudier l'homogénéité de la qualité de la structure

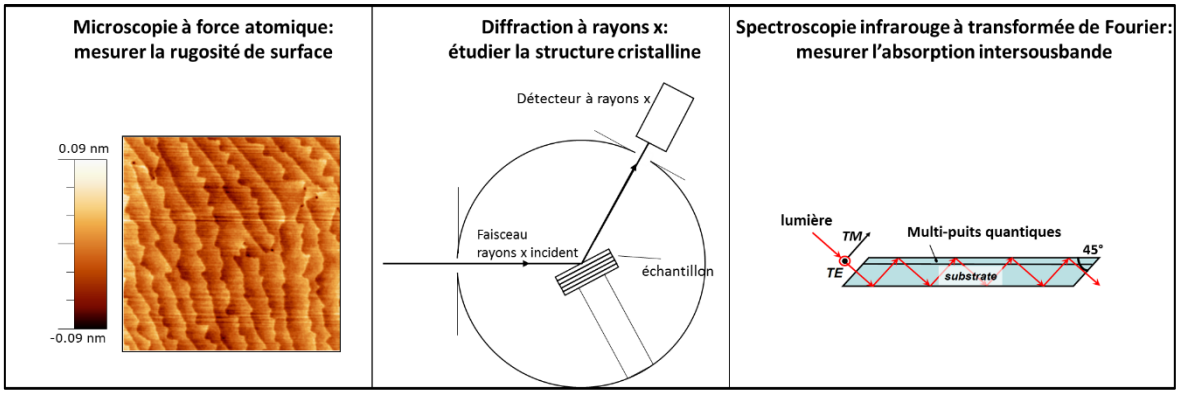

Illustration 2 Exemples de techniques utilisées.

Chapitre 3. Dopages Germanium et Silicium

Le chapitre 3 est consacré à l'étude de l'effet du dopage Germanium sur les propriétés optiques et structurales de structures polaires à multi-puits quantiques GaN/AlGaN présentant des transitions intersousbandes dans les fenêtres infrarouge à ondes courtes, moyen et lointain infrarouges. Le principe du dopage est représenté par l'Illustration 3. On commence par expliquer les problématiques liées au dopage Silicium généralement utilisé et on détaille les avantages de l'alternative Germanium. Pour illustrer le potentiel du dopage Germanium, on étudie son effet sur les propriétés optiques de nanofils de GaN/AlN. Ensuite on compare les performances optiques et structurales de multi-puits quantiques polaires de GaN/AlGaN dopés avec du Silicium et avec du Germanium dans le proche et le moyen infrarouge.

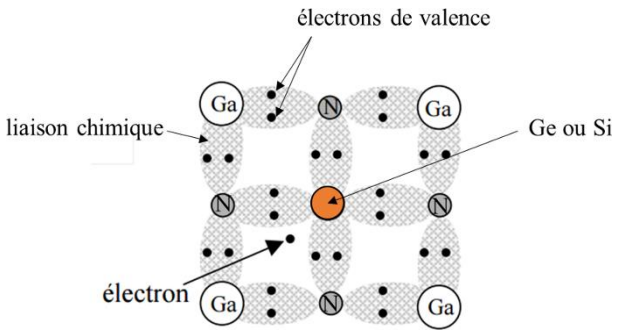

Illustration 3 Dopage du GaN: des atomes de Ga du réseau cristallin sont remplacés par des atomes de Germanium ou de Silicium, dont l'excès d'électrons de valence contribue à peupler les niveaux d'énergie électroniques.

Le Silicium est le dopant de type *n* de référence pour le GaN wurtzite, malgré qu'il contribue à la formation de dislocations et engendre une augmentation de la contrainte dans la structure, éventuellement conduisant à la formation de fissures. Le dopage Silicium de nanofils dégrade aussi leur rapport d'aspect et leur morphologie. C'est pour toutes ces raisons et pour les propriétés intrinsèques du Germanium que la possibilité de remplacer le Silicium par du Germanium est considérée: en particulier, le Germanium a un rayon ionique plus proche de celui du Gallium ce qui doit permettre de réduire les distorsions du réseau cristallin.

D'abord, on étudie les potentielles conséquences du dopage Germanium sur le processus de croissance du GaN, via la caractérisation de la désorption du Ga sur la surface de GaN. On démontre que la présence du flux de Germanium ne perturbe pas la cinétique de croissance, même pour les flux

les plus élevés. Le dopage de couches minces de GaN dopées avec du Germanium ne dégrade pas la morphologie de surface des couches et l'effet du dopage sur les propriétés interbandes du GaN est en accord avec la théorie. On conclut que le Germanium est une alternative possible au Silicium.

Concernant les nanofils de GaN/AlN dopés Germanium, on démontre que le Germanium diffuse de façon homogène dans les couches contrairement au Silicium ce qui permet de conserver la géométrie des nanofils et d'obtenir un dopage plus efficace, mais aussi que le dopage Germanium a un effet d'écrantage très puissant sur le champ électrique interne, ce qui permet de contrôler les temps de vie des porteurs dans les structures (primordial pour le développement de composants optoélectroniques).

En étudiant les multi-puits quantiques 2D de GaN/AlGaN polaires, on montre que les structures à grand désaccord de maille GaN/AlN dopées Germanium ont une meilleure mosaicité que celles dopées Silicium, tandis qu'aucune différence n'est notée pour les structures GaN/AlGaN où le désaccord de maille est réduit. Les propriétés interbandes des systèmes GaN/AlN ne semblent pas être affectées par la nature du dopant. Au contraire, l'absorption intersousbande est spectralement élargie à mesure que la concentration de dopants est augmentée dans le cas du dopage Silicium. Le décalage en énergie du pic d'absorption est similaire pour les deux dopants. Pour les systèmes GaN/AlGaN, le pic est décalé et est élargi, mais avec un plus fort effet dans le cas du dopage Silicium. En conclusion, le Germanium semble être une alternative prometteuse au Silicium pour doper des structures GaN/AlGaN à grand désaccord de maille.

Chapitre 4. L'orientation non-polaire

La plupart des études sur le GaN se sont concentrées sur le GaN d'orientation polaire, dans lequel la présence d'un champ électrique rend les puits de potentiel asymétriques (triangulaires) et augmente le confinement des électrons dans les puits et finit par saturer la distance entre les niveaux d'énergie électroniques, empêchant ainsi l'extension des transitions intersousbandes dans les systèmes polaires GaN/AlGaN aux petites énergies de la fenêtre lointain infrarouge. L'utilisation de puits quantiques GaN/AlN épitaxiés selon les orientations non-polaires comme le plan *m* {1-100} et le plan *a* {11-20} est une alternative pour obtenir des hétérostructures sans champ électrique interne et ainsi, des puits de potentiel carrés. L'Illustration 4 montre la structure cristalline du GaN wurtzite étudié et les différents plans cristallographiques en jeu. Avant le début de ma thèse, l'hétéroépitaxie de multi-puits quantiques de GaN/AlN plan *a* sur des substrats de saphir plan *r* avait permis de démontrer de l'absorption intersousbande à 2.1 µm, mais les nombreux défauts cristallins résultant de la croissance sur des substrats en large désaccord de maille avec le GaN non-polaire rendait très difficile d'obtenir plus de résultats. Quelques mois avant le début de ma thèse, il fut possible de se procurer des substrats massifs de GaN non-polaire plan *a* et plan *m* de grande qualité cristalline, ce qui a stimulé la recherche dans ce domaine et conduit à de rapides progrès quant à l'épitaxie des structures et le développement de technologies intersousbandes à base de GaN non-polaire, telles qu'un détecteur QWIP plan *m* par exemple. Aux vues des résultats prometteurs obtenus après homoépitaxie de GaN non-polaire, nous avons décidé au début de ma thèse d'évaluer le potentiel des multi-puits quantiques 2D de GaN/AlGaN non-polaires pour l'optoélectronique infrarouge.

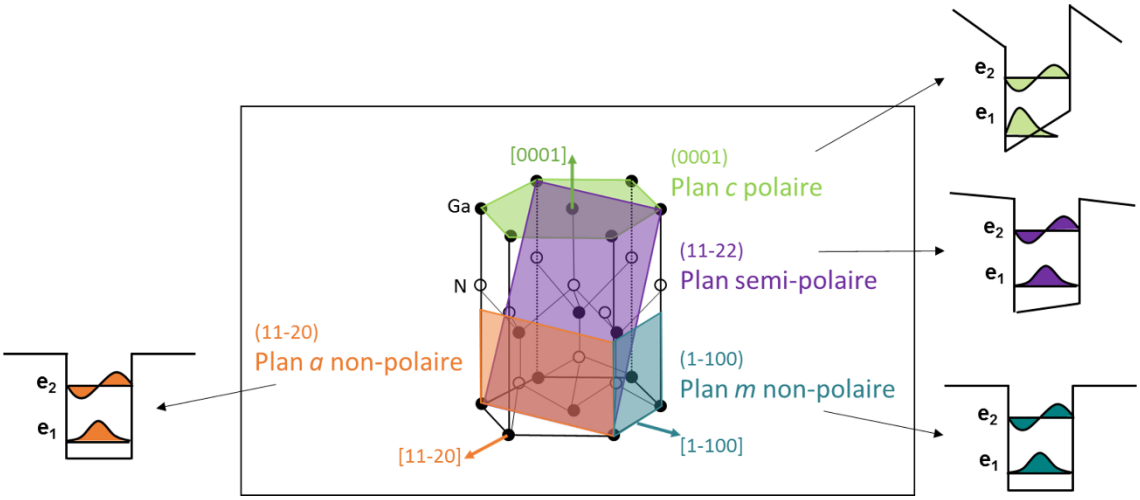

Illustration 4 Structure cristalline du GaN wurtzite et diagrammes de bande d'un puits quantique dans chaque orientation cristalline représentée.

On commence par étudier les conditions de croissance du GaN non-polaire. On sait d'après la littérature que la croissance du GaN polaire donne lieu au dépôt d'une couche lisse de GaN dans les conditions de croissance permettant la formation d'une bicouche de Gallium au-dessus de la surface de croissance. En étudiant la désorption du Gallium sur la surface de croissance du GaN, on démontre que de telles conditions existent également pour la croissance du GaN plan *m*, et qu'elles sont compatibles avec les conditions de croissance optimales du GaN polaire: à la même température de substrats polaire et non-polaire plan *m*, il existe une valeur de flux de Gallium pour laquelle une bicouche de Gallium se forme au-dessus de la surface de croissance pour les deux orientations cristallines. On vérifie également que la rugosité du GaN plan *m* est similaire à celle du GaN polaire. En revanche, il a été impossible d'obtenir une surface aussi peu rugueuse pour du GaN non-polaire plan *a* dans les mêmes conditions de croissance. On peut ensuite se concentrer sur l'étude de multi-puits quantiques de GaN/AlGaN.

On commence par étudier des hétérostructures de GaN/AlN épitaxiés simultanément sur des substrats de GaN polaire et non-polaires massifs plan *a* et plan *m*. En faisant varier la largeur des puits quantiques de GaN, la longueur d'onde d'absorption intersousbande est ajustée. Comparés aux échantillons non-polaires plan *a*, les structures plan *m* ont montré de meilleurs résultats en termes de mosaicité, rugosité de surface, largeur de raie et intensité de photoluminescence, et absorption intersousbande. De plus, les multi-puits quantiques GaN/AlN plan *m* ont montré de l'absorption intersousbande dans la gamme 1.5-2.9 µm, couvrant ainsi la fenêtre infrarouge ondes courtes, et avec des performances comparables aux structures polaires de référence. Cependant, la qualité structurale des puits non-polaires restait trop faible pour envisager de développer des composants optoélectroniques.

On a donc ensuite étendu l'étude à la gamme spectrale moyen infrarouge en se concentrant sur des structures non-polaires GaN/AlGaN seulement plan *m*. En faisant varier la largeur des puits et la composition de l'alliage AlGaN, on peut ajuster la longueur d'onde d'absorption intersousbande. En remplaçant les barrières d'AlN par des barrières d'AlGaN, on réduit la teneur en Aluminium moyenne de l'hétérostructure et ainsi on réduit le désaccord de maille. On obtient une densité de fissures moindre que pour les structures GaN/AlN. Cependant, des fautes d'empilement sont toujours observées, ainsi que des amas d'AlN dans les barrières d'AlGaN. Les fortes densités de défauts sont encore trop élevées pour pouvoir concurrencer les structures polaires dans cette gamme spectrale. On

démontre néanmoins de l'absorption intersousbande dans des multi-puits quantiques de GaN/AlGaN plan *m* dans la fenêtre moyen infrarouge 4.0-5.8 µm.

Ensuite, on a étudié la possibilité de développer ces multi-puits quantiques dans la fenêtre lointain infrarouge. Dans cette gamme spectrale, des teneurs en Aluminium bien plus faibles sont nécessaires, ce qui contribue à réduire encore le désaccord de maille. On a donc épitaxié des structures GaN/AlGaN avec moins de 10% d'Aluminium dans les barrières. Les nanostructures présentent des couches régulières et sans rugosité dans les deux directions du plan de croissance, et une très bonne qualité cristalline. Aucun défaut de structure ne fut observé et des fissures se sont formées seulement pour des échantillons d'épaisseur supérieure à 1.2 µm. Des inhomogénéités d'alliage ont tout de même été observées dans la direction de croissance. Concernant les performances optiques, les structures ont montré de l'absorption intersousbande à température cryogénique dans la fenêtre 1.5-9 THz. Ce résultat prouve la possibilité de couvrir une bonne partie de la bande interdite aux arséniures entre 7 et 10 THz grâce au GaN.

Les absorptions intersousbandes démontrées dans le lointain infrarouge étaient cependant très larges spectralement en raison d'une trop forte densité de dopage Silicium, ce qu'on a démontré en faisant varier la concentration de Silicium dans des structures identiques. On montre qu'augmenter le niveau de dopage conduit à un pic d'absorption intersousbande décalé vers les hautes énergies et de plus grande magnitude et largeur de raie. On observe également une saturation de l'absorption intersousbande à partir de 1×10^{12} cm^{-2} de densité de dopage, densité à partir de laquelle le niveau électronique excité commence également à être peuplé.

Ces résultats nous ont conduits à considérer l'alternative du dopage Germanium pour obtenir de forts niveaux de dopage sans saturer la transition intersousbande THz. On obtient des multi-puits quantiques dopés Germanium avec une structure comparable aux puits dopés Silicium en termes de rugosité et de qualité cristalline. Aucun défaut de structure ne fut observé. En ce qui concerne les performances optiques, pour des densités de dopage Germanium et Silicium équivalentes, les structures dopées Germanium ont montré des pics d'absorption intersousbande avec un élargissement spectral légèrement inférieur.

Chapitre 5. Conclusions et perspectives

L'objectif de ce travail de thèse était d'explorer des alternatives aux multi-puits quantiques GaN/AlGaN plan *c* généralement dopés avec du Silicium, pour obtenir de meilleures performances en terme d'absorption intersousbande dans la gamme infrarouge. D'une part, on a discuté de la possibilité d'utiliser le Germanium comme dopant. D'autre part, on a étudié les performances optiques et structurales de multi-puits quantiques GaN/AlGaN d'orientations non-polaires (1-100) et (11-20) (plans *m* et *a*) de façon à obtenir des profils de potentiels symétriques et à observer de l'absorption intersousbande dans la région infrarouge et en particulier dans la fenêtre THz.

De nos résultats, on peut conclure que le Germanium est effectivement une alternative envisageable au Silicium pour le dopage de type *n* du GaN, mais qu'ils sont aujourd'hui insuffisants pour pouvoir déterminer lequel des deux dopants serait le plus favorable. En particulier, pour les densités de dopage les plus fortes, le dopage Germanium permet de réduire la largeur de raie de l'absorption intersousbande, comparé au dopage Silicium.

Pour ce qui est de l'étude du GaN non-polaire, on a démontré que les structures non-polaires GaN/AlN plan *m* présentaient de meilleures performances structurales et optiques que les structures plan *a*. On a cependant montré que les structures plan *m* ne peuvent pas rivaliser avec les structures

polaires dans les gammes infrarouge ondes courtes et infrarouge moyen, dû à de trop grande densités de défauts structuraux résultant du grand et anisotrope désaccord de maille. Pour pouvoir développer des composants non-polaires dans cette gamme, il serait nécessaire d'étudier plus en détail et d'améliorer l'homogénéité d'alliage d'AlGaN en fonction des conditions de croissance dans ces structures. Néanmoins, les hétérostructures GaN/AlGaN plan *m* présentant de l'absorption intersousbande dans le lointain infrarouge ont montré de grandes qualités structurales et de très bonnes performances optiques, ce qui nous a permis d'observer de l'absorption intersousbande THz en accord avec les prédictions théoriques et ce, en utilisant des structures très simples. En exploitant notre étude sur l'effet du dopage sur l'absorption intersousbande dans ces structures, on peut envisager de fabriquer des composants tels que des photodétecteurs ou des lasers à cascade quantique, en s'inspirant des structures déjà développées pour les systèmes GaAs. Dans cette optique, on propose de réaliser d'abord des expériences d'électroluminescence et d'étudier les possibles propriétés d'effet tunnel résonnant de ces structures THz. Ces résultats sur le GaN non-polaire peuvent être utile pour le développement et l'amélioration des LEDs UV et vertes, dont les structures polaires subissent également l'effet du champ électrique interne. Cependant, la possibilité du développement et de la commercialisation à grande échelle de composants non-polaires dépend encore de la baisse du coût encore élevé des substrats massifs de GaN non-polaire et sur l'augmentation de la taille de ces substrats.

Glossary

Abbreviations

AFM	atomic force microscopy
AlGaN	aluminium gallium nitride
AlN	aluminium nitride
B-E	basal extrinsic stacking fault
BGR	bandgap renormalization
B-I_1	basal intrinsic stacking fault
B-I_2	basal intrinsic stacking fault
BME	Burstein–Moss effect
BS	beam splitter
BSF	basal stacking fault
CB	conduction band
CCD	charge-coupled device
CL	cathodoluminescence
cps	counts per second
EDX	energy-dispersive x-ray spectroscopy
FIB	focus ion beam
FIR	far-infared
FTIR	Fourier transform infrared spectroscopy
FvdM	Franck van der Merwe
FWHM	full width at half maximum
GaN	gallium nitride
GaN:x	GaN doped with x
Ge	germanium
HAADF-STEM	high angle annular dark field scanning transmission electron microscopy
HEMT	high electron mobility transistor
HR-TEM	high resolution transmission electron microscopy
HR-XRD	high resolution x-ray diffraction
HVPE	hydride vapor phase epitaxy
IR	infrared
ISB	intersubband
LO	longitudinal-optical
MBE	molecular beam epitaxy
MD	misfit dislocation
MIR	mid-infrared
ML	monolayer
MOCVD	metalorganic chemical vapor deposition
MOVPE	metalorganic vapor phase epitaxy
MQW	multi-quantum well
n.i.d.	non-intentionally doped
N_D	*n*-type dopant concentration
NIR	near-infrared
NWs	nanowires
PL	photoluminescence
PSF	prismatic stacking fault
QCL	quantum cascade laser
QD	quantum dot
QW	quantum well
QWIP	quantum well infrared photodetector
RHEED	reflection high-energy electron diffraction
RMS	root mean square
s.i.	semi-insulating

SEM	scanning electron microscopy
SF	stacking fault
Si	silicon
SK	Stranski-Krastanov
SS	stacking sequence
SWIR	short-wavelength infrared
TD	threading dislocation
TE	transverse-electric
TO	transverse-optical
TM	transverse-magnetic
ToF-SIMS	time-of-flight secondary ion mass spectroscopy
TRPL	time-resolved PL
VB	valence band

Physics values and parameters

$\langle 0 \rangle$	excited state
$\langle 1 \rangle$	emitting state
1/e decay time	
2θ	angle of detector rotation
A	potential vector
A	normalized absorbance
a	lattice parameter
a	base hexagone side along the [11-20] axis
a_1	lattice vector
A_1	Luttinger parameter
a_2	lattice vector
A_2	Luttinger parameter
a_3	lattice vector
A_3	Luttinger parameter
A_4	Luttinger parameter
A_5	Luttinger parameter
A_6	Luttinger parameter
A_7	Luttinger parameter
a_{c1}	deformation potential
a_{c2}	deformation potential
a_{GaN}	lattice parameter a of GaN
A_{osc}	RMS oscillation amplitude
b	Burger vector
b	bowing parameter
B_d	detection bandwidth
BS	beam-splitter
χ	angle of sample rotation
c	Ga coverage
c	height of the GaN hexagonal prism
c	speed of light in free space
c_{GaN}	lattice parameter c of GaN
C_{ij}	elastic constant
D	detector
d	interplane spacing
D_i	deformation potential
d_u	interplanar distance
e	elementary charge
E	energy
$E^{\parallel}{}_P$	Luttinger parameter
$E^{\perp}{}_P$	Luttinger parameter
e_{13}	piezoelectric constant
E_{21}	ISB transition energy

e_{33}	piezoelectric constant
E_a	activation energy
E_a	activation energy of the nonradiative process in state $\langle 0 \rangle$
E_b	activation energy
E_{dir}	direct Coulomb interaction
E_{exch}	exchange interaction
E_g	bandgap energy
E_{Ge}	thermal evaporation energy of Ge
E_{Loc}	localization energy
E_{PL}	PL energy
E_{Si}	thermal evaporation energy of Si
F	electric field
F	force
f	envelope function
H	Hamiltonian
$\hbar$	reduced Planck constant
H_{int}	interaction Hamiltonian
I	intensity of the measured data
I_0	peak intensity
φ	angle of sample rotation
k	wavevector
k_B	Boltzmann constant
kT	thermal energy
L	distance between surface normal and screen in RHEED measurement
m	mass
M	mirror
m_{eff}	electron effective mass in GaN
n	refractive index
n_0	optically excited population of the level
n_1	population of the exciton emitting state
n_{3D}	3D free carrier concentration
n_s	2D doping density = 2D density of charge
p	measured lattice parameter along this axis p
p	momentum operator
P_{MQW}	MQWs period
P_{PZ}	piezoelectric polarization
p_r	theoretical value of assuming that the structure is relaxed
P_{SP}	spontaneous polarization
Q	the quality factor of the resonance
q(0001)	projection of the reciprocal space vector along [0001]
r	space vector
S	source
T	sample temperature during the measurement
t	distance between two RHEED streaks
T_{Ge}	Ge cell temperature
TM_{MQW}	TM-polarized transmission of the MQWs
TM_{sub}	TM-polarized transmission of the substrate
T_s	growth temperature, i.e. substrate temperature
u	anion-cation bond length in the [0001] direction
U	crystal potential
U_{xc}	exchange-correlation potential
u_v	Bloch function
ω	angle of sample rotation
ω_0	resonant frequency
ω_i	incidence angle of x-ray and the sample
ω_{LO}	LO phonon frequency
ω_{TO}	TO phonon frequency
x, y, z	space directions
α	depolarization shift
α_1	constant

α_2	constant
α_3	constant
α_V	Varshni coefficient
β	exciton shift
β_1	constant
β_D	Debye coefficient
Γ	symmetry point of the reciprocal space for k = 0
Δ	roughness parameter
$\Delta E/E$	normalized broadening
ΔE_{dep}	shift of the ISB energy induced by depolarization
ΔP	electric displacement vector
$\delta\omega_p$	tilt angles towards the in-plane direction p
$\Delta\Theta$	divergence
ϵ_0	electric permittivity
ε_p	strain along the axis p
ϵ_R	dielectric constant in GaN
ε_{xx}	strain component along the <11−20> direction
ε_{xz}	shear strain components
ε_{yz}	shear strain components
ε_{zz}	strain component along the <0001> direction
θ	coverage rate on growing surface
$\theta_{\pm n}$	±m-order MQW satellite
λ	correlation length
λ_0	electron wavelength
λ_{PL}	excitation wavelength for the PL measurement
λ_{TRPL}	excitation wavelength for the TRPL measurement
λ_{XRD}	x-ray wavelength
τ_{NR}	characteristic time associated to the nonradiative processes
τ_{R0}	characteristic time associated to the relaxation to the exciton emitting state
τ_{R1}	characteristic time of the population of the exciton emitting state
Φ	GaN growth rate
Φ_c	carrier generation rate
ϕ_j	electron wavefunction for the j^{th} subband

Table of contents

Context and motivation

This is a Haiku 俳句
On my PhD Thesis
Here starts my Thesis

III-nitride semiconductors are key materials for the development of optoelectronic and electronic devices. Thanks to their direct wide bandgap and doping capabilities, they are the basic material which allowed the fabrication of blue/green light-emitting diodes (LEDs), which have led to the implementation of full-color displays or white LED bulbs. As a prospect, they constitute the only solid-state alternative to mercury lamps as an ultraviolet (UV) source [1]. GaN-based LEDs have already found a number of applications, including not only indoor and outdoor lighting, but also blue laser diodes for data storage (Blu-ray players), car lights, traffic and emergency vehicle signals, etc. III-nitrides are also currently used in high-power electronics for their mechanical and thermal robustness, high electrical breakdown fields, and high electron mobility [2]. In the context of environment protection and green energy production, III-nitrides have also raised interest for the development of piezo-generators [3] and solar cells, due to the possibility of making InGaN alloys optically active over the full spectrum of sunlight [4]. Last but not least, III-nitrides have also become interesting for infrared (IR) optoelectronics using intersubband (ISB), which is the purpose of this thesis. Examples of potential applications of a nitride IR technology are presented in Figure 1.

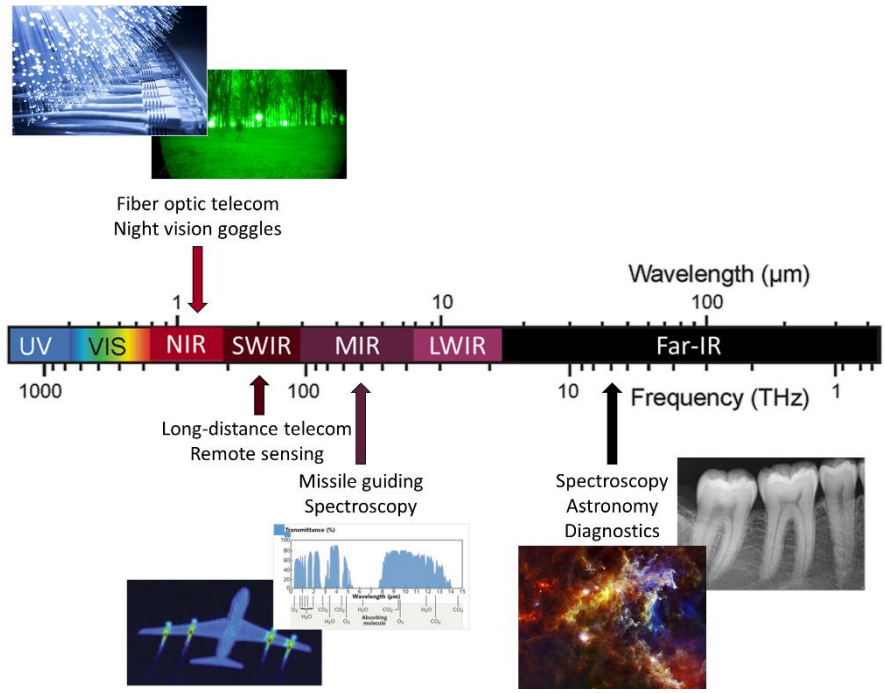

Figure 1 Examples of possible applications of GaN-based optoelectronics devices in the infrared range. [5–8]

A brief history of infrared optoelectronics

The IR spectral region covers the electromagnetic radiation with submillimeter wavelength longer than the visible (*i.e.* beyond the red), and the most appropriate classification of IR regions for our work is detailed in Table 1. The history of IR detectors was reviewed by Rogalski *et al.* [9]. The IR radiation was discovered by Hershel in 1800. He developed the first thermal IR detector, where a blackened bulb was used to absorb the radiation, which warmed up a liquid, whose temperature was measured by a glass thermometer. With the discovery of the thermoelectric effects by Seebeck 20 years later [10], the basic thermometer-based IR detector could be improved in terms of sensitivity and distance range of detection.

Table 1 Classification of the IR spectral range **[11]**.

Classification	Wavelength (µm)
Near-IR	0.75 – 1.4
Short-wavelength IR	1.4 – 3
Mid-wavelength IR	3 – 8
Long-wavelength IR	8 – 15
Far-IR	15 – 1000

The discovery of the first photoconductive effect in 1873 by Smith [12] stimulated great effort from the scientific community towards the development of new IR detectors based on photon detection, with the possibility for higher sensitivity, and with an interest for the study of the atmosphere composition, blackbody radiation, etc. These so-called "photodetectors" are based on the interaction between the incident radiation and the semiconductor material composing the device. The photodetector operation spectral range thus depends on the semiconductor properties, and narrow bandgap materials like InSb, PbTe and PbS were initially used for IR operation. Image converters as well as IR spectroscopy techniques were developed during the interwar years for military applications (especially night vision). In 1957, Lawson, Nelson and Young revealed the IR detection properties of the HgCdTe alloy, which was thus followed by the introduction of the II−VI ($Hg_{1-x}Cd_xTe$) ternary alloys, as well as the III−V ($InAs_{1-x}Sb_x$) and IV−VI ($Pb_{1-x}Sn_xTe$) alloys, to offer a broader possibility of wavelength tuning, as illustrated by the different bandgaps represented in Figure 2 [9].

Today, the low cost and room-temperature operation of thermal detectors have led to their popularization, in spite of their lower sensitivity and slower response compared to photodetectors. In terms of photodetectors, HgCdTe devices are still today amongst the most widely used. If thermal imaging for military purpose were the first applications of IR radiations (with the night vision sensors, tank sight systems, heat seeking missiles, etc.), IR technologies are nowadays widely used in a number of different fields. Especially, the 1.3-1.55 µm window is dedicated to optic fiber telecommunication [13], the 3-5 and 8-14 µm window are applied to thermal imaging and the longer wavelength IR range is even used for space applications [14]. Finally the longest wavelength IR window (> 30 µm), which is also called the THz or T-rays region, has a variety of applications such as security and medical screening, quality control, environment monitoring, etc.

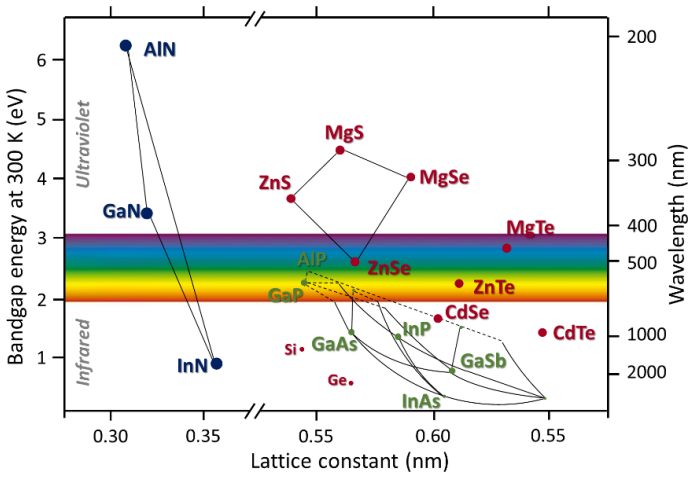

Figure 2 Schematic of the bandgap energy dependence on the material lattice constant. (Modified from **[15]**)

ISB transitions are optical transitions between quantum-confined electronic states within quantum wells (QWs) or quantum dots (QDs). In 1985, West and Eglash performed the first measurement of ISB absorption in GaAs quantum wells [16]. This result led to the fabrication of the first quantum well infrared photodetector (QWIP) [17,18]. Compared to HgCdTe photodetectors, QWIPs offer lower dark currents, higher detectivities and better resolution. Infrared ISB technologies were thus first developed based on the already mature III-As and III-P materials, as illustrated by Figure 3. These ISB devices include detectors and lasers based on GaInAsN/AlAs [19], GaAs/AlGaAs [20,21] and GaInAs/AlAsSb [22,23], which can be tuned from the mid- to the far-IR region (MIR, FIR). However, the small conduction band offset intrinsic to the III-As and III-P materials complicated the extension of these technologies to the near-IR (NIR). Furthermore, the spectral window from 30 to 40 µm (5 to 10 THz) corresponds to the Reststrahlen band of arsenides, which have made it impossible to cover this range with such materials [24]. Finally, the small energy of longitudinal optical phonon of arsenides has hampered the development of room-temperature THz devices.

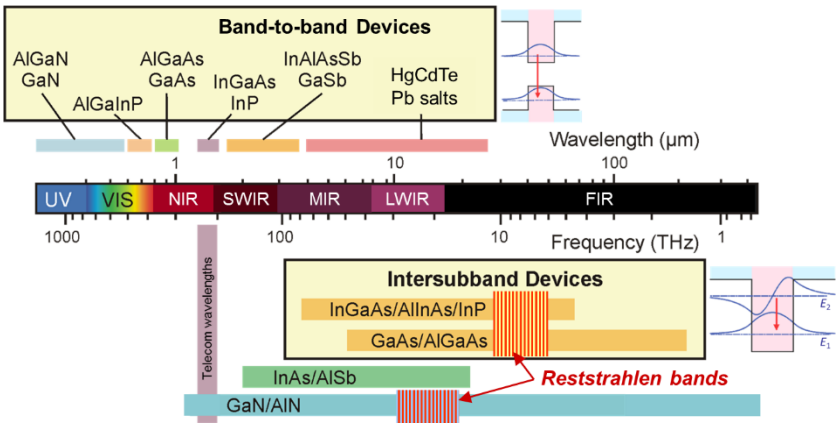

Figure 3 Spectral coverage by band-to-band and ISB devices based on different material systems.

Motivation and targets

Overcoming these challenges and extending the ISB technology to the NIR and THz windows require a major technology revolution, through the introduction of a new material system. III-nitrides, with their large conduction band offsets (about 1.8 eV for GaN/AlN) [25,26] and sub-picosecond ISB relaxation times are appealing materials for ultrafast photonic devices in NIR telecommunication networks. Furthermore, the high energy of their longitudinal-optical phonons (92 meV for GaN) [27,28] opens prospects for high-temperature ISB devices operating in the THz spectral range and especially covering the 5–10 THz band, inaccessible to As-based technologies.

However, the GaN technology has several drawbacks associated to the structural defects resulting from heteroepitaxy and high lattice mismatched structures, which result in the degradation of the optical and electrical properties of the device. Furthermore, the influence of the polarization fields present in these materials is an additional complicating parameter to be taken into account for the design and development of optoelectronics devices. If complex design and engineering is a possible approach to overcome this issue, the introduction of nonpolar crystallographic orientations of GaN is an alternative approach to obtain structures without internal electric field, which we explore in this thesis. The recent availability of affordable high-quality free-standing GaN substrates has led to rapid progress of the field.

With this idea in mind, the work described in this thesis has aimed at improving the performance and understanding of the material issues involved in the extension of the GaN/AlGaN ISB technology to the THz range. On the one hand, we have focused on the issue raised by the polarization electric field presence in the widely used polar GaN, and assess the possibility of developing nonpolar GaN/AlGaN ISB infrared devices. On the other hand, we have addressed the problem of *n*-type doping of quantum wells, which is required to observe ISB absorption. With this purpose, we have assessed the possibility of using Ge as an alternative dopant to the conventional Si.

During my PhD research, I engineered the conduction band profiles to target certain operating wavelengths from the short-wavelength to the FIR by simulating the structures using the commercial Nextnano^3 software [29]. I was then in charge of the growth of these structures by plasma-assisted molecular beam epitaxy. For the study of nonpolar GaN, the SWIR planar structures were grown by former PhD student Mark Beeler, and I grew the MIR and FIR structures. The polar structures related to the study of Ge-doping were grown either by me or by PhD student Akhil Ajay. The nanowire (NW) heterostructures were grown by the group of Prof. Martin Eickhoff at the Justus Liebig University of Giessen, Germany. I performed the optical characterization of the NW heterostructures by photoluminescence and measured photoluminescence and Fourier transform infrared spectroscopy on the planar samples in collaboration with Mark Beeler and Akhil Ajay. Time-resolved photoluminescence measurements were carried out by Mark Beeler under the supervision of Joël Bleuse. Structural characterization by transmission electron microscopy was performed by Catherine Bougerol and her PhD students for the planar structures and by the group of Prof. Jordi Arbiol at the Institut Català de Nanociència I Nanotecnologia of Barcelona, Spain, for the NW heterostructures. I performed the x-ray diffraction measurements of planar structures in collaboration with Dr. Edith Bellet-Amalric, Mark Beeler, and David Browne. I measured atomic force microscopy images in collaboration with Akhil Ajay.

Organization of the manuscript

After these few preview pages, Chapter 1 starts with a general introduction to III-nitride semiconductors and ISB transitions. We first describe the crystalline structure of GaN and AlGaN materials as well as their electronic, mechanical and optical properties. Then, we introduce the basic knowledge and equations related to the physics of ISB transitions. We highlight the selection rules that govern these transitions, as well as the scattering processes and many-body effects that need to be considered. Finally, a brief review of the state-of-the-art on ISB transitions in III-nitrides with polar, semipolar and nonpolar crystallographic orientations is provided.

Chapter 2 describes the simulation tool and experimental techniques used in this work. We give a general introduction on molecular-beam epitaxy, through the presentation of the different substrates we used, the growth process and the in-situ monitoring technique, as well as reviewing the state-of-the-art growth of polar, semipolar and nonpolar GaN and AlGaN. The structural, optical and electrical characterization techniques are then described.

The results of this thesis are then divided into two chapters, each of them addressing one of the above-described targets of this work. Chapter 3 first explores the possibility to use Ge as an alternative dopant to Si. The effects of Ge introduction on the GaN growth kinetics, layer structure and optical and electrical properties are characterized. As an example of the relevance of Ge-doping, the giant screening effect of Ge-doping on the electric field in GaN/AlN NWs is assessed. Then, the study focuses on the use of Ge-doping for planar GaN/AlGaN heterostructures with ISB transitions in the short-wavelength infrared (SWIR) and MIR ranges, and compares the structural and optical performance of the obtained structures with reference Si-doped samples. As a result, we conclude that both Si and Ge are valid approaches to obtain ISB absorption in the SWIR and MIR. However, the use of Ge comes with a certain improvement of structural quality and ISB performance of high lattice mismatched GaN/AlGaN multi-quantum wells (MQWs) when compared to using Si.

Then, Chapter 4 explores the possibility to use nonpolar crystallographic orientations of GaN. We start by comparing GaN/AlN heterostructures grown in the polar *c* orientation of GaN to similar structures grown in the two nonpolar orientations *a* and *m*. In terms of structural and optical characteristics, the *m* orientation of GaN appear as the best nonpolar choice which is the reason why the rest of the nonpolar study is then carried out using this orientation. The applicability of *m*-GaN for MIR and FIR GaN/AlGaN MQWs is then explored. In particular we demonstrate that *m*-GaN/AlGaN MQWs can cover the 5-10 THz range, inaccessible to As-based technologies.

To end this manuscript, Chapter 5 summarizes the accomplished work and main achievements, and considers its relevance and impact for future developments.

We wish you a pleasant reading.

Chapter 1.
Introduction

Pretty quantum wells
Big or small this is your call
But please shoot photons !

In this chapter, we introduce the basic knowledge on III-nitride semiconductors necessary to understand, design and realize intersubband devices based on these materials. First, we describe the structural, electronic and optical characteristics of bulk GaN, AlN and AlGaN. Then, we consider the properties resulting from the staking of these materials in heterostructures. The issues related to the presence of internal spontaneous and piezoelectric polarization fields in the material are discussed. Finally, we focus on the theory of intersubband transitions and report on the latest developments of GaN-based infrared intersubband technologies.

As explained in the previous pages, this PhD work aims at improving the performance and understanding of the material issues involved in the extension of the GaN/AlGaN intersubband technology to the THz range. This requires mastering the basic knowledge on III-nitride semiconductors and heterostructures, as well as the fundamental principles of intersubband transitions. The chapter is divided into 3 sections. First, we start by describing the crystalline structure of bulk III-nitrides and explain the general electronic and optical properties resulting from this structure. This includes the description of their energy band structure and bandgap, as well as the presence of a spontaneous polarization field across the crystal. The second section considers the properties resulting from the stacking of different nitride materials in a heterostructure. We detail the properties at the heterointerfaces as well as those of the whole stack. Finally, the third section focuses on the physics of intersubband transitions. We first demonstrate that the quantum confinement of the electrons in the heterostructures results in discrete energy states, which can be used to obtain optical emission or absorption of light at a certain energy. Especially, intersubband transitions are electronic transitions which correspond to photon energies in the infrared range. The main equations governing intersubband transitions are described, as well as the possible scattering processes and the many-body effects that must be taken into account. The chapter ends on a brief review of the state-of-the-art of intersubband transitions in III-nitride GaN/AlGaN heterostructures.

1.1 Introduction to III-nitride semiconductors

The periodic table of elements is shown in Figure 4. In red, we highlighted the chemical elements of interest for this work: Ga, Al (column III) and N (column V) are the chemical elements composing the semiconductor materials under study in this manuscript. Ge and Si (column IV) are the semiconductor materials that can be used to n-dope GaN (studied in sections 3.1, 4.6 and 4.7). In this section, the unique structural, electrical and optical properties of GaN, AlN and AlGaN are discussed in view of developing intersubband (ISB) devices operating in the infrared range.

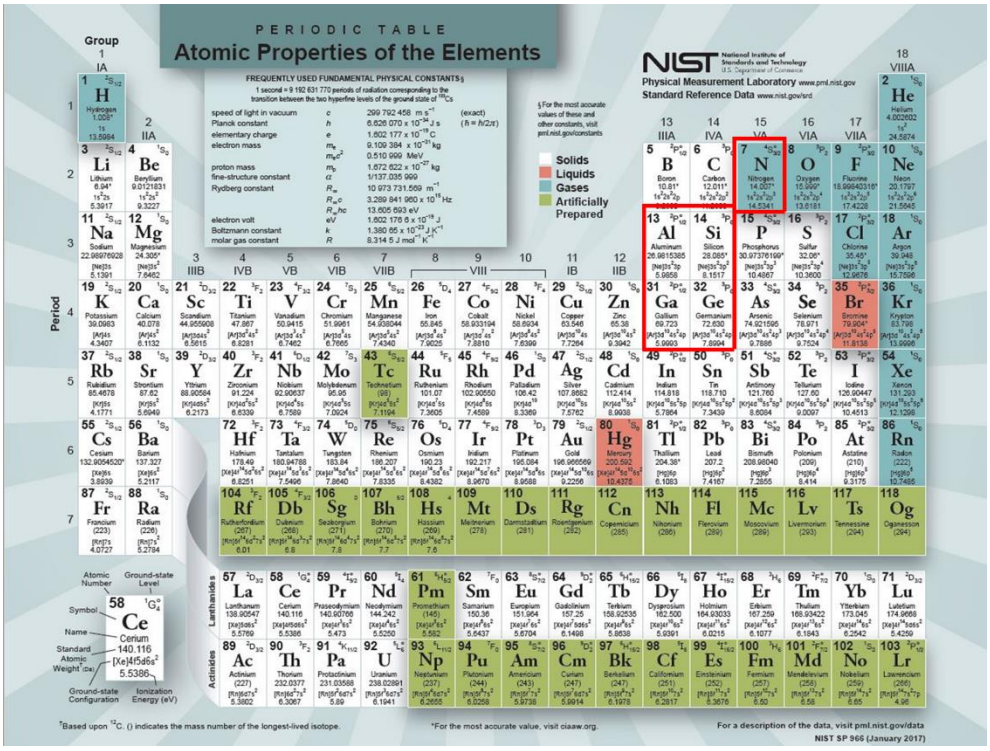

Figure 4 Periodic table of elements. The red borders indicate the materials of interest in this work. (modified from **[30]**).

1.1.1. Crystalline structure

GaN, AlN and AlGaN can exist in two crystallographic arrangements, namely wurtzite (α-phase, hexagonal symmetry) and zinc-blende (β-phase, cubic symmetry), illustrated in Figure 5. The wurtzite phase being more thermodynamically stable than the zinc-blende phase, this is the preferred and addressed material in this work. Using Group Theory, wurtzite GaN belongs to the C_6v (in Schoenflies notation) or P_6mm (in the Hermann-Mauguin notation) point symmetry, which is a subgroup of the full hexagonal symmetry (labelled D_6h in Schoenflies notations or P_6/mmm in the Hermann-Mauguin one). These theoretical and geometrical considerations result in the isolation of geometrical patterns and 3D translational invariances, leading to the notion of 3D periodic crystalline lattice, which is today the principle on which the determination of the crystallographic structure of materials is based [31]. The study of crystals physics properties is essentially made by diffraction of an x-ray beam. The beam-atom interaction results in the Fourier transform of the crystalline network, and we obtain an image of what is called the reciprocal space.

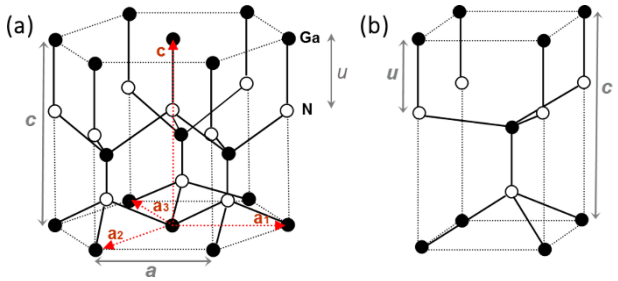

Figure 5 (a) Wurtzite and (b) zinc-blende crystallographic structures of GaN.

The planes and directions in hexagonal structures are conventionally described with four Miller-Bravais indices *hkil* associated to the lattice vectors a_1, a_2, a_3 and *c*, represented in Figure 5. The base vectors a_1, a_2, a_3 are separated by an angle of 120° and their sum is null, leading to $i = -(h + k)$. Wurtzite GaN consists of two hexagonal sublattices, each composed of Ga and N atoms, respectively, and which are merged and shifted by u = 3/8c along the [0001] direction, u being the anion-cation bond length along the <0001> axis and *c* being the height of the hexagonal prism. In the ideal wurtzite structure, $c = \sqrt{2/3}\, a$, where *a* is the base hexagon side along the [11-20] axis. The anion-cation bond length dependence on the cation nature and ionic radius results in practice in deviation from this ideal structure [32]. The lattice parameters of bulk GaN and AlN at room temperature are presented in Table 2. Regarding the $Al_xGa_{1-x}N$ alloys, the lattice parameter vary linearly with the composition, as described by the Vegard's law [33]:

$$\mathrm{a(Al_xGa_{1-x}N)} = \mathrm{x.\,a(AlN)} + (1 - \mathrm{x}).\,\mathrm{a(GaN)} \qquad (1)$$

Table 2 Lattice parameters of bulk wurtzite GaN and AlN at room temperature.

Lattice parameter	GaN	AlN	Ref.
a (Å)	3.189	3.112	[34]
c (Å)	5.185	4.982	[34]
u (Å)	0.377	0.382	[35]

We must keep in mind that in hexagonal structures, equivalent crystallographic planes can be identified by permutation of the three basal Bravais indices *h k i*. The planes orthogonal to the <0001> axis are called *c*-planes, defined by the {0001} plane family. The <0001> axis is thus called the *c* axis. The {11-20} and {1-100} plane families, parallel to the <0001> *c* axis, are called *a*- and *m*-planes, respectively. The <11-20> and <1-100> directions are called the *a* and *m* axis, respectively. It is important to notice that, in general, the directions defined in the hexagonal structures are not orthogonal to the corresponding planes. Figure 6 shows the *c*, *a* and *m* planes and corresponding axis of the hexagonal structure.

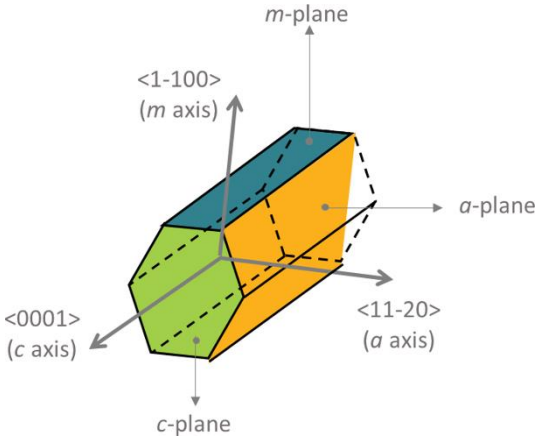

Figure 6 Hexagonal unit cell showing the *c*-, *a*- and *m*-planes and corresponding axis.

The wurtzite structure is asymmetric in the [0001] and [000-1] directions. When the vector of the metal-nitrogen bond $\vec{u}$ points towards the nitrogen atom (*i.e.* $\vec{u}$ along [0001]), the material is called metal-polar. In the case of a nitrogen-polar material, the metal-nitrogen bond vector $\vec{u}$ points towards the metal atom (*i.e.* $\vec{u}$ along [000-1]). This is illustrated by Figure 7. The material polarity

can be controlled by choosing the substrate and growth conditions [36,37], and it affects the surface properties in terms of chemical behavior morphology and thermal stability [38–40]. Ga-polar GaN is usually preferred because it favors 2D growth: it is more chemically stable and it is easier to control its surface morphology during growth. In this work, we only consider Ga-polar structures. Figure 8 represents the stacking sequence of the *c* plane of wurtzite GaN, which is ABAB…

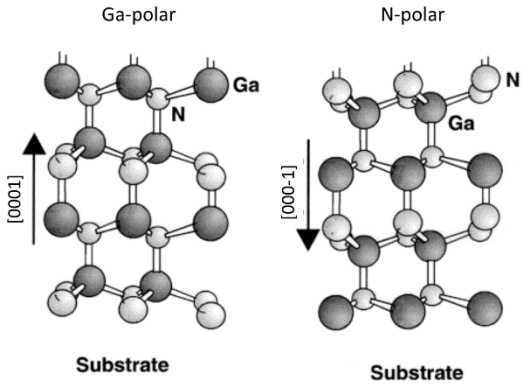

Figure 7 Crystalline structure of Ga- and N-polar wurtzite GaN. (Modified from **[2]**)

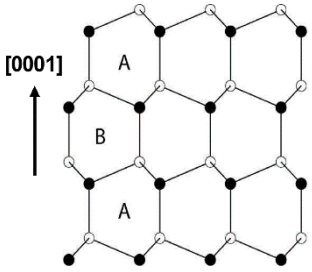

Figure 8 Stacking sequence of the (0001) *c* plane of wurtzite GaN.

1.1.2. Band structure in the k·p approximation

Now that we have established the elements of crystallography describing the III-nitrides, we can focus on their resulting electronic properties. The allowed electronic states are described by energy bands, which we introduce in this section. In solid-state physics, the valence band and conduction band are the bands closest to the Fermi level (energy level of an electron such that at thermodynamic equilibrium, this energy level would have a 50% probability of being occupied at any given time), and thus determine the electrical conductivity of the solid. In semiconductors, the two bands are separated by a bandgap, where no electron state can exist due to quantization of energy. For intrinsic semiconductors at 0 K, the last fully-occupied band is the valence band, and the first non-occupied band is the conduction band. This band structure is schematically illustrated by Figure 9.

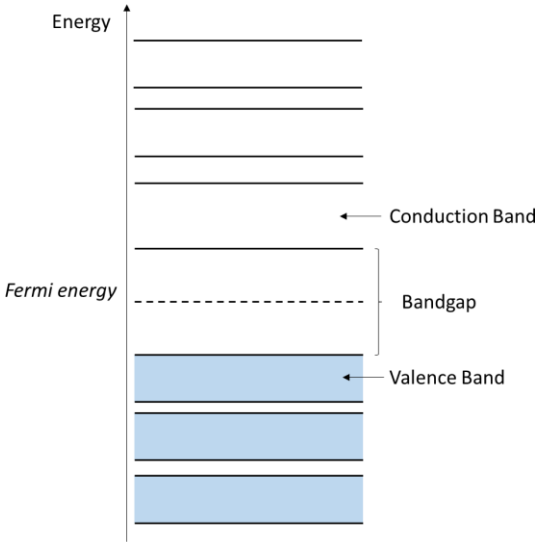

Figure 9 Schematic illustration of the energy bandgap around the Fermi energy and of the allowed energy bands at T = 0 K. In blue we represent the presence of electrons.

The electrons of the atoms constituting the semiconductor crystal mainly undergo the Coulomb potential of the atoms nuclei, and the ideally periodical arrangement of these atoms in the crystal leads to a periodicity of the potential energy, which is seen by the electrons along each of the three space dimensions, as illustrated in Figure 10.

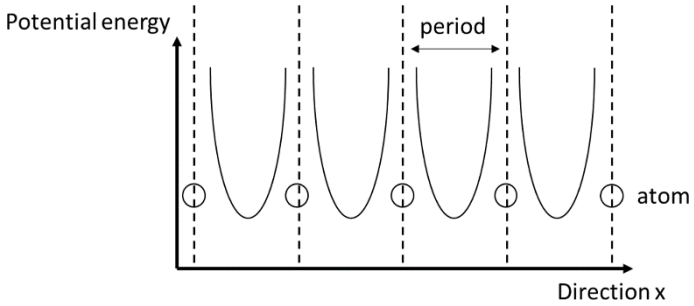

Figure 10 Simplified schematic of the crystallographic arrangement along the *x* direction, with the periodic potential energy (considering the simplest approach of a free electron).

In a single atom, the wave-like behavior of an electron is mathematically described by the model of the atomic orbitals. In this model, the probability of presence of an electron in certain space regions around the atomic nucleus, and thus the energy state of the electron, is described by the electron wavefunction. In a crystal, the formation of atomic bonds can be described by the overlapping of valence atomic orbitals. The issue is to determine the possible energy states and wavefunctions of the involved valence electrons. In the crystal, the great number and spatial proximity of the atoms bring together the discrete energy states of the electrons into continuous energy bands. The determination of these energy bands is done by solving the Schrödinger equation for a crystal, which fully describes the behavior of the electrons when using an appropriate Hamiltonian:

$$\left(\frac{\mathrm{p}^2}{2\mathrm{m}} + \mathrm{U}(\vec{\mathrm{r}}) + \frac{\hbar^2}{4\mathrm{m}^2\mathrm{c}^2}\left(\vec{\sigma} \times \frac{\partial \mathrm{U}}{\partial \vec{\mathrm{r}}}\right) \cdot \vec{\mathrm{p}}\right) \phi(\vec{\mathrm{r}}) = \mathrm{E}\phi(\vec{\mathrm{r}}) \qquad (2)$$

also expressed as $\mathrm{H}\phi = \mathrm{E}\phi$, where *H* is the Hamiltonian of the system, and where *m* is the electron mass, *c* is the speed of light in free-space, $\vec{r}$ is the space vector, *U* is the energy potential from the atoms in the crystal (crystal potential), *E* is the energy of the valence orbital, $\vec{p}$ is the momentum

operator defined by $\vec{\mathrm{p}} = -\mathrm{i}\hbar\frac{\partial}{\partial\vec{\mathrm{r}}}$, ϕ is the electron wavefunction, and $\vec{\sigma}$ accounts for the spin-orbit coupling of the electron (which refers here to the interaction of the electron's spin and the magnetic field resulting from its motion). The direct resolution of the equation is very complex, this is why we first propose a simple resolution of this equation, which demonstrates the band structure of semiconductor crystals electronic states. Then, we describe the general resolution of the Schrödinger equation based on the (complex) k·p theory.

Simplified resolution

For simplification, we neglect the spin-orbit coupling and consider the resolution in one space dimension *x*:

$$-\frac{\hbar^2}{2\mathrm{m}}\frac{\partial^2\phi}{\partial\mathrm{x}^2} + \mathrm{U(x)}\phi(\mathrm{x}) = \mathrm{E}\phi(\mathrm{x}) \tag{3}$$

The most accurate simple approach is to use the quasi-free electron model considering a 1D periodicity. Since the atom arrangement in the crystal is considered periodic, the atomic potential is assumed to be periodic. With *a* being the period of the lattice, this results in:

$$\mathrm{U(x+a)} = \mathrm{U(x)} \tag{4}$$

and the periodic atomic potential can be expressed as a Fourier series decomposition:

$$\mathrm{U(x)} = \sum_{\mathrm{G}} \mathrm{U_G exp(-iGx)} \tag{5}$$

where $\mathrm{G} = \frac{2\mathrm{l}\pi}{\mathrm{a}}$ and *l* is an integer.

According to the Bloch Theorem, any wavefunction ϕ subject to a periodic potential has the same periodicity:

$$\phi(\mathrm{x+a}) = \phi(\mathrm{x}) \tag{6}$$

and the wavefunctions can thus be decomposed as a Fourier series too:

$$\phi(\mathrm{x}) = \sum_{\mathrm{K}} \mathrm{C_K exp(iKx)} \tag{7}$$

where $\mathrm{K} = \frac{2\mathrm{n}\pi}{\mathrm{L}}$ and $\mathrm{L} = \mathrm{Na}$ is the crystal dimension, *n* is an integer.

The wavefunctions $\phi(x)$ are solutions of the Schrödinger equation. By substituting equations (5) and (7) in the Schrödinger equation (3), we obtain:

$$\frac{\hbar^2}{2\mathrm{m}}\sum_{\mathrm{K}} \mathrm{K^2 C_K \exp(iKx)} + \sum_{\mathrm{G}}\sum_{\mathrm{K}} \mathrm{U_G C_K \exp(i(K-G)x)} = \mathrm{E}\sum_{\mathrm{K}} \mathrm{C_K \exp(iKx)} \tag{8}$$

$$\sum_{\mathrm{K}} \exp(\mathrm{iKx})\left(\left[\frac{\hbar^2}{2\mathrm{m}}\mathrm{K^2} - E\mathrm{C_K}\right] + \sum_{\mathrm{G}} \mathrm{U_G C_K \exp(-iGx)}\right) = 0 \tag{9}$$

The $(exp(iKx))$ constitute a base of the vectorial space, which leads to all the terms of the sum on *K* being equal to 0: $\left(\frac{\hbar^2}{2\mathrm{m}}\mathrm{K^2} - \mathrm{E}\right)\mathrm{C_K} + \sum_{\mathrm{G}} \mathrm{U_G C_{K-G}} = 0$. Defining $\lambda_{\mathrm{K}} = \frac{\hbar^2}{2\mathrm{m}}\mathrm{K^2}$, we obtain:

$$\begin{cases} (\lambda_{\mathrm{K}} - \mathrm{E})\mathrm{C_K} + \sum_{\mathrm{G}} \mathrm{U_G C_{K-G}} = 0 \\ \phi(\mathrm{x}) = \sum_{\mathrm{G}} \mathrm{C_{K-G}} \exp(\mathrm{i(K-G)x}) \end{cases} \tag{10}$$

Each value of *G* corresponds to a wavefunction which depends on *K*. This wavefunction is referred to as $\phi_K(x)$ and is defined as: $\phi_{\mathrm{K}}(\mathrm{x}) = \mathrm{C_{K-G}} \exp(-\mathrm{iGx}) \exp(\mathrm{iKx})$, where $exp(-iGx)$ is a

periodic function of the crystal lattice *a* which is accounting for the periodic potential, and $exp(iKx)$ is a periodic function of the crystal dimension *L* that describes the wavefunction of a free electron (solution of the Schrödinger equation without taking into account the periodic potential, *i.e.* for $U = 0$).

All we need to do then is to calculate the C_{K-G} and the energies. *K* and *G* go from $-\infty$ to $+\infty$, which results in an infinity of equations to solve. We thus apply the following (strong) simplifications:

- We neglect the overlap between the potentials of two adjacent atoms, and consider only the interaction between the nearest neighbors. Thus only the fundamental terms (first two terms) of the Fourier series development of *U(x)* (equation (5)) are significant, and the harmonics are neglected. This gives $\mathrm{U(x)} = 2\mathrm{U_1}\cos(\mathrm{G_1 x})$, which is represented schematically in Figure 11.
- The potential is weak and considered as a perturbation, meaning that U_1 is weak compared to the free electron energy corresponding to the wavefunction.

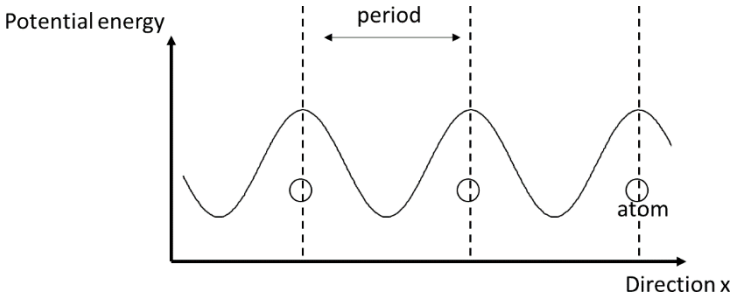

Figure 11 Schematic of the potential energy in the crystal along one space dimension and considering the quasi-free electron model.

Taking 0 and G_1 as the two values for *G*, the wavefunction described by equation (10) can thus be expressed as:

$$\phi(\mathrm{x}) = \mathrm{C_K}\exp(\mathrm{iKx}) + \mathrm{C_{K-G_1}}\exp(\mathrm{i(K-G_1)x}) \qquad (11)$$

Since the periodic potential $U(x)$ is real, we have $\mathrm{U_{G_1}} = \mathrm{U_{-G_1}} = \mathrm{U_1}$. Since *K* varies from $-\infty$ to $+\infty$ in the Fourier series development of the wavefunction (equation (7)), changing *K* in *–K* does not affect the shape of the wavefunction nor the energy value. We obtain for equation (10):

$$\begin{cases} (\lambda_\mathrm{K} - \mathrm{E})\mathrm{C_K} + \mathrm{U_1 C_{K-G_1}} = 0 \\ (\lambda_\mathrm{K-G_1} - \mathrm{E})\mathrm{C_{K-G_1}} + \mathrm{U_1 C_K} = 0 \end{cases} \text{ with } \begin{cases} \lambda_\mathrm{K} = \dfrac{\hbar^2}{2\mathrm{m}}\mathrm{K}^2 \\ \lambda_\mathrm{K-G_1} = \dfrac{\hbar^2}{2\mathrm{m}}(\mathrm{K}-\mathrm{G_1})^2 \end{cases} \qquad (12)$$

A non-zero solution can exist for this system of equations if and only if its determinant is null:

$$(\lambda_\mathrm{K} - \mathrm{E})(\lambda_\mathrm{K-G_1} - \mathrm{E}) - \mathrm{U_1}^2 = 0 \qquad (13)$$

i.e.:

$$\mathrm{E}^2 - (\lambda_\mathrm{K} + \lambda_\mathrm{K-G_1})\mathrm{E} + \lambda_\mathrm{K}\lambda_\mathrm{K-G_1} - \mathrm{U_1^2} = 0 \qquad (14)$$

whose solutions are:

$$E_{\pm} = \frac{1}{2}\frac{\hbar^2}{2m}\cdot \left(K^2 + (K-G_1)^2 \pm \sqrt{(K^2+(K-G_1)^2)^2 + 4\left(\frac{2mU_1}{\hbar^2}\right)^2 K^2(K-G_1)^2}\right) \quad (15)$$

This demonstrates the existence of a forbidden band of energies, illustrated by Figure 12. Also, this shows that the energy bands present a parabolic dispersion in $k = 0$, which is characteristic of semiconductor materials.

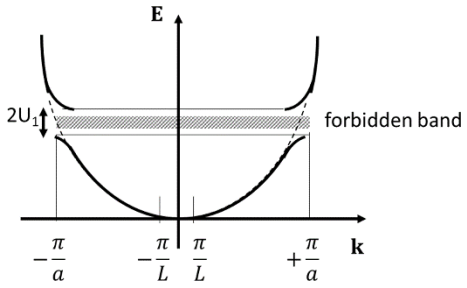

Figure 12 Energy diagram of an electron in a crystal of length *L* with periodic potential of period *a*.

From this simple 1D resolution, we demonstrated the existence of allowed and forbidden energy bands in a direction of the semiconductor crystal, which is seen in real semiconductors in the 3 space directions. Especially, this results in the definition of the valence and conduction bands as the last fully-occupied and first non-fully-occupied bands of energy states (subbands), respectively. The bandgap is the forbidden band energy between the conduction and valence bands.

Besides, this resolution also introduces the concept of effective mass. The free electron model is an ideal general description of the semiconductor band energy structures, which defines the energy of a free electron as $E = \frac{\hbar^2 k^2}{2m}$. The mass m is thus related to the curvature of the subband energy and is homogeneous to $\frac{\hbar^2}{\partial^2 E/\partial k^2}$. By defining the effective mass $m^* = \frac{\hbar^2}{\partial^2 E/\partial k^2}$ (in the case of isotropic subbands, otherwise we define a tensor $m^* = \frac{\hbar^2}{\partial^2 E/\partial k_i\,\partial k_j}$), we account for the effect of the lattice potential on the movement of the electron in the crystal compared to its movement in free space. In other terms, the energy of a carrier in the crystal is considered equivalent to the energy of a free carrier of mass m^*.

In this simplified resolution, we considered a potential in the crystal that is influenced only by the first neighboring atoms, which is a very strong hypothesis. Also, in practice the lattice parameter and periodicity of the crystal vary versus the different space directions, which results in the potential energy dependence on the crystallographic direction.

General resolution

The general resolution avoids making these simplifications and is much more complex [41]. Coming back to the 3D Schrödinger equation, we consider the solution wavefunctions expressed as Bloch functions (as shown earlier in this section):

$$\phi_{n\vec{k}}(\vec{r}) = \exp\left(i\vec{k}\vec{r}\right) u_{n\vec{k}}(\vec{r}) \quad (16)$$

and by substituting them into the Schrödinger equation we obtain:

$$\begin{aligned}\vec{p}.\left(\exp\left(i\vec{k}\vec{r}\right)u_{n\vec{k}}(\vec{r})\right) &= -i\hbar\frac{\partial}{\partial\vec{r}}\left(\exp\left(i\vec{k}\vec{r}\right)u_{n\vec{k}}(\vec{r})\right)\\ &= \exp\left(i\vec{k}\vec{r}\right)(\vec{p}+\hbar\vec{k})u_{n\vec{k}}(\vec{r})\end{aligned} \tag{17}$$

and the Schrödinger equation thus becomes:

$$\left(\frac{p^2}{2m}+\frac{\hbar}{m}\vec{k}.\vec{p}+\frac{\hbar^2k^2}{2m}+U(\vec{r})\right)u_{n\vec{k}}(\vec{r}) = E_{n\vec{k}}u_{n\vec{k}}(\vec{r}) \tag{18}$$

The Hamiltonian $H = H_0 + W\left(\vec{k}\right)$ can be splitted into a *k*-independent part:

$$H_0 = \frac{p^2}{2m}+U(\vec{r}) \tag{19}$$

and a *k*-dependent part:

$$W\left(\vec{k}\right) = \frac{\hbar^2k^2}{2m}+\frac{\hbar}{m}\vec{k}.\vec{p} \tag{20}$$

and the solutions of the equation:

$$H_0u_{n0}(\vec{r}) = E_{n_0}u_{n0}(\vec{r}) \tag{21}$$

are the energies of the band structure at the Γ point $k = 0$.

Applying the effective mass approximation, we consider that the energy subbands each have an effective mass given by their mass at the Γ point ($k = 0$). The key then lies in the $k \cdot p$ approximation, which fundamental idea is to use the exact solutions of the Schrödinger equation at $k = 0$, $u_{n0}(\vec{r})$, which are determined by experiment (using cyclotron resonance for example), as a basis for the expansion of the wavefunctions and energies at finite values of *k*. In other words, the $k \cdot p$ approximation considers the energy dispersion around the Γ point and neglects the interaction between the conduction band and the valence band. This approximation is quite accurate in the case of wavefunctions in the conduction band of wide bandgap semiconductors. It is not valid in the case of the valence band which structure is very complicated, nor in the case of small bandgap semiconductors where the interaction between the valence band and the conduction band cannot be neglected. Since the $u_{n0}(\vec{r})$ are exact solutions of the Schrödinger equation, the accuracy of the obtained solutions are only limited by the expansion degree.

In the simplest cases, limiting ourselves to the conduction band, the second-order expansion gives:

$$E_{c(k)} = E_{c(0)}+\frac{\hbar^2k^2}{2m_0}+\frac{\hbar^2k^2}{m_0}\sum_{m\neq c}\frac{\left|\langle u_{c,0}|p|u_{m,0}\rangle\right|^2}{E_c-E_m} \tag{22}$$

where $\langle l|m|n\rangle = \int_{\text{unit cell}} u_l^* n u_m d^3r$.

In the lowest order approximation, all bands except for the valence band may be neglected, resulting in:

$$E_{c(k)} = E_G+\frac{\hbar^2k^2}{2m_0}+\frac{\hbar^2k^2}{m_0}\frac{\left|\langle u_{c,0}|p|u_{v,0}\rangle\right|^2}{E_G} \tag{23}$$

where E_G is the bandgap energy, and the zero energy is taken at the top of the valence band. Defining the Kane energy as $E_P = \frac{2}{m_0}\left|\langle u_{c,0}|p|u_{v,0}\rangle\right|^2$, the dispersion of the conduction band can be written as:

$$E_{c(k)} = E_c+\frac{\hbar^2k^2}{2m_0}\left(1+\frac{E_P}{E_G}\right) \tag{24}$$

The Kane energy is much larger than the energy bandgap and is rather constant across III-V semiconductors.

To determine the dispersion of the valence band, the full k · p envelope function model must be solved, that is a set of 8 differential equations.

The band structures of wurtzite GaN and AlN

The resulting complex band structures of wurtzite GaN and AlN were studied by several groups using different methods like ab initio linearized plane wave method [42], time-resolved photoluminescence measurements and theoretical calculations based on the local density approximation [43,44], or muffin tin potential [45]. The band structures of GaN and AlN are calculated with an empirical pseudopotential method [46] and are represented in Figure 13, taking into account the spin-orbit coupling of the electrons. The valence band is the Γ_5 band and the first conduction band is the Γ_1 band. The valence and conduction bands are separated by an energy gap and are of opposite curvature, and they show a direct bandgap with the conduction and valence band minima located at $k = 0$ (Γ point) in the reciprocal space. The lateral valleys for GaN and AlN are energetically far from the band minima. This is crucial for intersubband optoelectronics, to prevent inter-valley electron scattering [47].

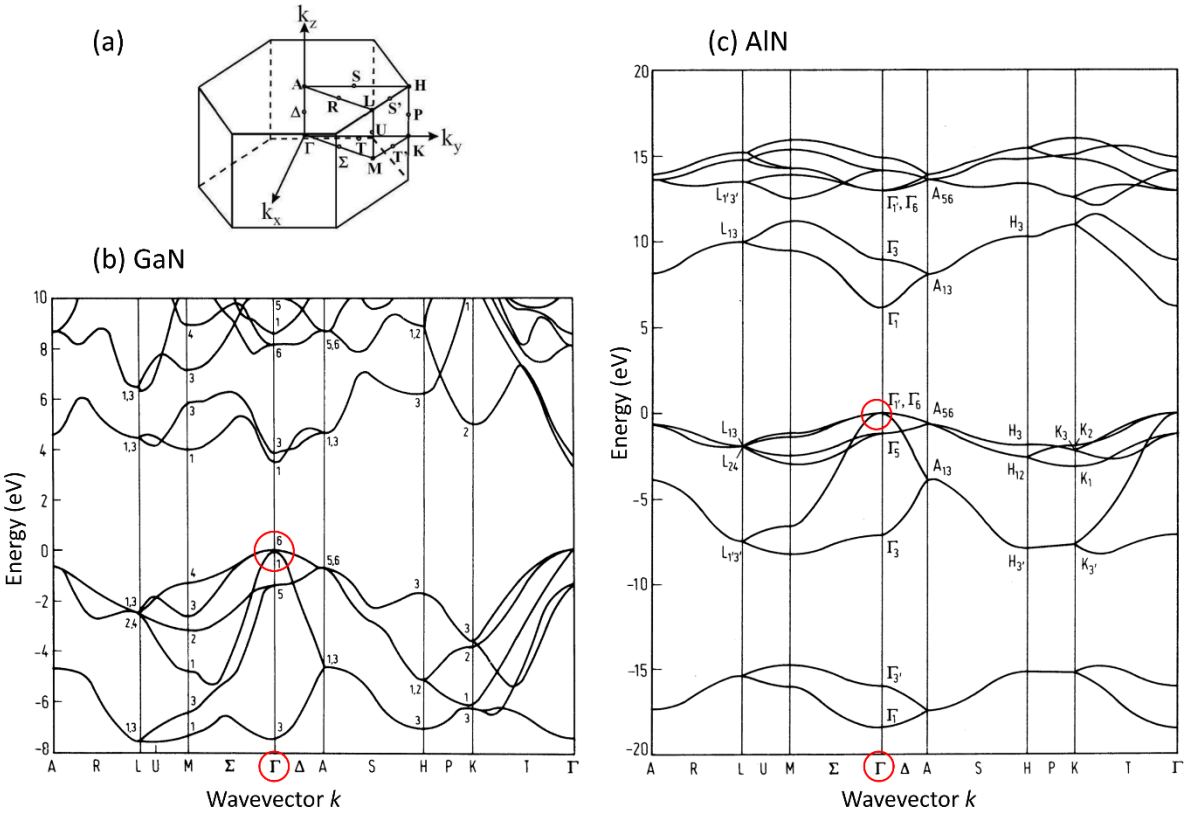

Figure 13 (a) First Brillouin zone of a wurtzite crystal **[44]**. Band structures of wurtzite (b) GaN **[46]** and (c) AlN **[48]**.

In wurtzite GaN, the valence band is non-degenerated at the Γ point, and splits in three subbands with different effective masses: the heavy-hole (subband A at Γ_9), light-hole (subband B at Γ_{7+}), and spin-orbit (subband C at Γ_{7-}), as illustrated in Figure 14. This is due to the asymmetry of the structure, the crystal field and the spin-orbit coupling. The effect of crystal field on the bands is represented in red. By adding the effect of spin-orbit coupling represented in blue, we obtain the final

band diagram in violet, and the resulting band diagrams with absolute energy values for GaN and AlN are represented in Figure 15. Especially, we notice that the magnitude of the crystal-field splitting in GaN and AlN leads to $\Gamma_1 < \Gamma_5$ in GaN, but $\Gamma_1 > \Gamma_5$ in AlN, which results in the spin-orbit hole having higher energy than the heavy hole in AlN, in contrast to GaN for which both the heavy hole and the light hole have higher energy than the spin-orbit hole. The valence band structures of GaN and AlN are represented in Figure 16.

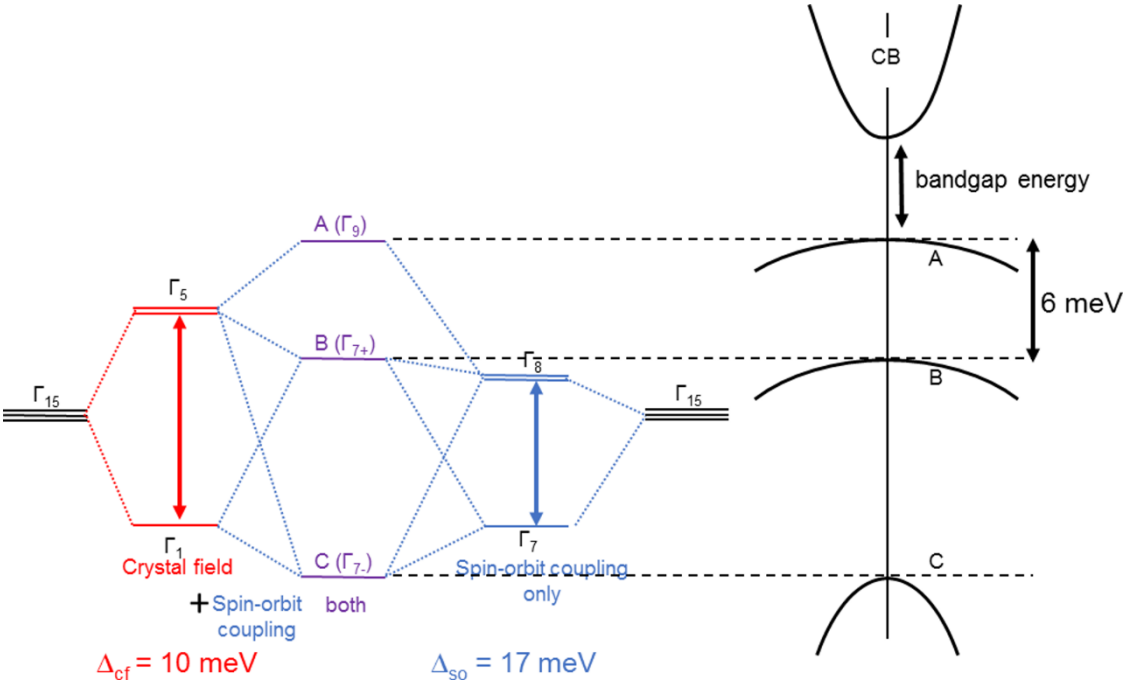

Figure 14 Schematic of the valence band splitting in wurtzite GaN. (Modified from **[49]**)

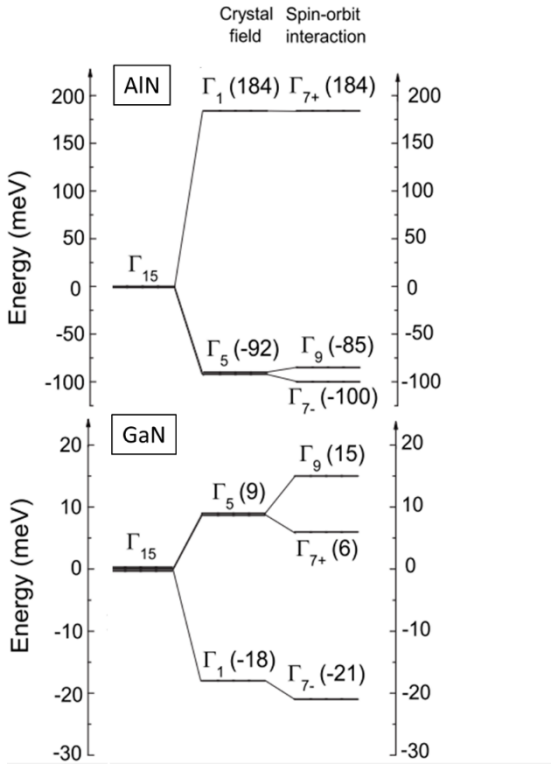

Figure 15 Characteristic splittings and shifts due to the crystal-field splitting and the spin-orbit interaction for AlN and GaN. The absolute energy values in meV are given between parenthesis. The threefold degenerate Γ_{15} level is used as energy zero. (Modified from **[50]**)

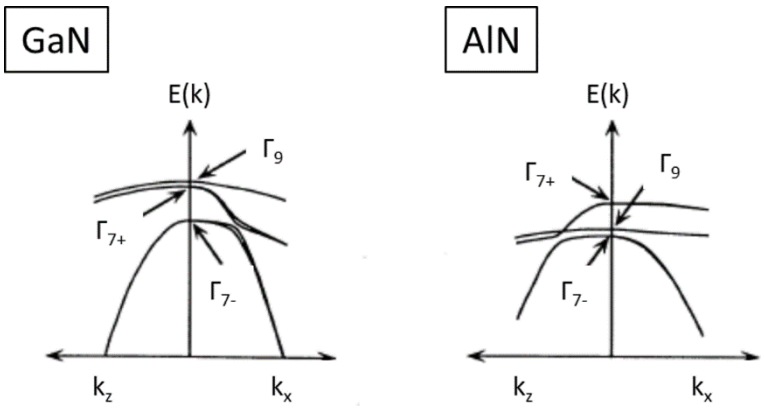

Figure 16 Valence band structure of GaN and AlN showing different effective masses along k_x and k_z.

1.1.3. Bandgap parameters

Good estimations of the bandgap parameters of GaN and AlN were established in the early 70s, with reference values used today listed in Table 3. Due to the temperature-dependent lattice expansion [51,52] and the electron-lattice interaction, the bandgap energy shows a dependence on temperature, which was first evaluated experimentally by absorption [53] and luminescence experiments [54] and can be described by the empirical Varshni equation:

$$E_g(T) = E_g(T = 0\ K) - \frac{\alpha_V T^2}{\beta_D + T} \qquad (25)$$

where α_V and β_D are the Varshni and Debye coefficients.

In ternary compounds ($Al_xGa_{1-x}N$), the bandgap dependence on the alloy composition is modeled using a quadratic polynomial whose linear coefficient is called the bowing parameter, *b*. This parameter accounts for the deviation from a linear interpolation. The variation of the bandgap energy versus the Al composition is thus given by:

$$E_g(x) = (1 - x)E_g(GaN) + xE_g(AlN) - b(1 - x)x \quad (26)$$

where the bowing parameter has value of b = 1-1.5 eV for AlGaN [55,56].

Table 3 Band parameters of GaN and AlN: bandgap energy at T = 0 K; Varshni parameters; electron and hole effective masses (m_0 being the nominal mass in vacuum).

	GaN	**AlN**
E_g (T = 0 K) (eV)	3.507 [34]	6.23 [34]
α_V (meV/K)	0.909 [34]	1.999 [34]
β_D (K)	830 [34]	1429 [34]
m^*_{e-}	0.2 m_0 [57]	(0.32-0.40) m_0 [34,58]
m^*_{h+}	1.25 m_0 [59]	1.44 m_0 [60]

1.1.4. Spontaneous polarization in wurtzite crystals

Due to the low symmetry of the wurtzite crystals, an intense polarization field along the <0001> direction is present in the GaN-based semiconductor heterostructures. Indeed, the barycenters of the positive and negative charges in a unit cell do not necessarily coincide, which results in the creation of an electric dipole along the <0001> direction. Since this spontaneous polarization depends on the cation-nitrogen bond length, the polarization in GaN and in AlN have different magnitudes. GaN has a larger <0001> anion-cation bond length *u* and a smaller *c/a* value compared to AlN, which results in smaller spontaneous polarization: -0.029 C/m^2 for GaN and -0.081 C/m^2 for AlN [35]. The spontaneous polarization of $Al_xGa_{1-x}N$ depends nonlinearly on the composition of the alloy and can be calculated as [61]:

$$P_{sp}(Al_xGa_{1-x}N) = xP_{sp}(AlN) + (1 - x)P_{sp}(GaN) + bx(1 - x) \quad (27)$$

where P_{sp} is the spontaneous polarization of the bulk materials and *b* is the bowing parameter. However, in this work, the best agreement between experimental measurements and simulations was found by neglecting the bowing parameter of the spontaneous polarization.

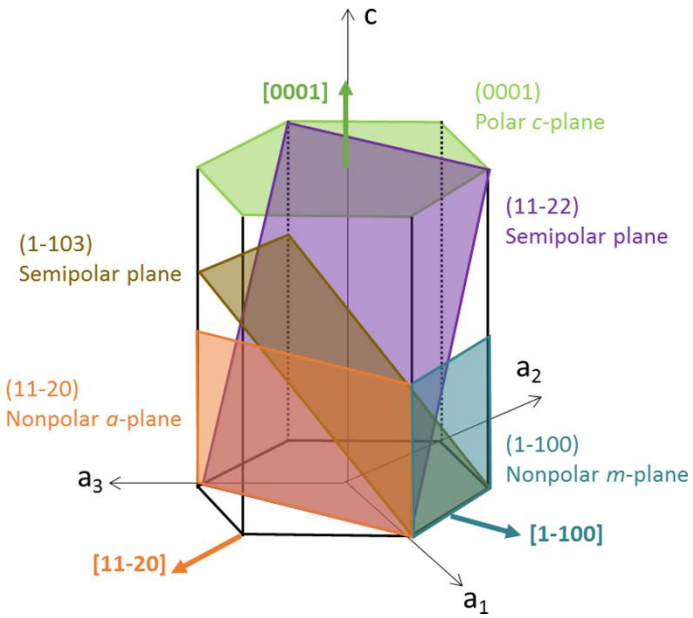

Figure 17 Description of the polar (0001), nonpolar (1-100) and (11-20), and semipolar (1-103) and (11-22) planes. (Modified from **[62]**)

As illustrated in Figure 17, crystallographic orientations that are perpendicular to the polarization vector (= *c* axis) are called nonpolar. The planes making an angle different than 0° and 90° with the *c* axis are called semipolar.

1.1.5. Optical phonons, Reststrahlen band and refractive index

Under optical excitation, the incident light can induce a collective excitation of the atoms in the crystal, resulting in lattice vibration. The quantum of lattice vibration is called a phonon. Because they have more than one atom in their smallest unit cell, wurtzite crystals exhibit two types of phonons: acoustic phonons and optical phonons, which are represented in Figure 18. Acoustic phonons are coherent movements of atoms of the lattice out of their equilibrium positions, they give rise to low-frequency vibrations in the range of sound. Optical phonons are out-of-phase movements of the atoms in the lattice. They give rise to high-frequency vibration that can interact with electromagnetic radiations.

Under light excitation, the strong interaction between the incident light and optical phonons results in the so-called Reststrahlen absorption, *i.e.* photons are absorbed and phonons are generated.

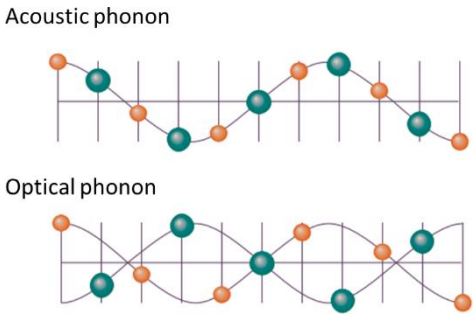

Figure 18 Schematic of the acoustic and optical phonon vibrations in a crystal.

The Group theory applied on wurtzite GaN with hexagonal symmetry predicts 8 phonon modes: 2 A_1, 2 E_1, 2 E_2 and 2 B_1 modes. The E_2 and B_1 modes are optic, but the E_2 mode cannot be seen by IR spectroscopy and the B_1 mode is not active [63]. This leaves the A_1 and E_1 modes which each have an acoustic and an optic vibration mode. We are interested in the optical phonon modes, which are decoupled into two modes: longitudinal and transversal. The longitudinal-optical (LO) and transverse-optical (TO) phonons with polarization parallel to the *c* axis constitute the A_1 modes, the LO and TO phonons with polarization perpendicular to the *c* axis constitute the E_1 modes, which is illustrated by Figure 19.

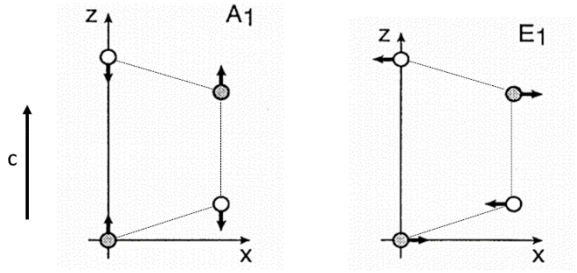

Figure 19 A_1 and E_1 optical phonon modes in wurtzite GaN (modified from **[64]**).

For wurtzite GaN and AlN, the A_1 and E_1 modes show a very small anisotropy, which enables to define effective average values for the LO and TO phonon frequencies. These phonon frequencies are located into the IR region, which is our region of interest. Considering the TO phonon frequency ω_{TO} and LO phonon frequency ω_{LO} intrinsic to the material, an incident light with frequency included in the region $[\omega_{TO}; \omega_{LO}]$ should enter in resonance with optical phonons, the process of optical phonon emission being coupled to strong light absorption. For GaN, we have $\omega_{LO} = 746\ \text{cm}^{-1}$ ($\approx$ 92.5 meV) and $\omega_{TO} = 559\ \text{cm}^{-1}$ ($\approx$ 69.3 meV) [28,65]. For AlN, we have $\omega_{LO} = 893\ \text{cm}^{-1}$ (≈ 111 meV) and $\omega_{TO} = 667\ \text{cm}^{-1}$ ($\approx$ 82.7 meV) [66]. Figure 20 shows the transmittance spectrum of a thick layer of GaN (250-µm thick free standing GaN). There are two main absorption regions, represented by a thick black line, and which are defined by the frequencies windows $[\omega_{TO}\text{-}\omega_{LO}]$ and $[2\omega_{TO}\text{-}2\omega_{LO}]$. It was demonstrated that the absorption can still be non-negligible for submicron layer thicknesses, and that both the first and second harmonic of the phonon frequencies lead to strong absorption by the material [67]. As a consequence, Reststrahlen absorption should be taken into account in the IR optical study of heterostructures grown on thick GaN free-standing substrates.

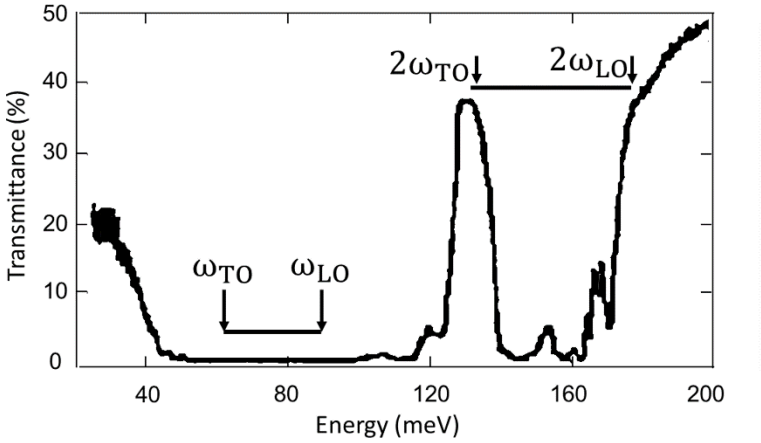

Figure 20 Transmittance of a 250-μm thick free-standing GaN film vs the energy of the incident light; $\boldsymbol{\omega_{TO}}$ and $\boldsymbol{\omega_{LO}}$ represent the TO phonon and LO phonon frequencies. (Reproduced from [67])

Table 4 Static and high-frequency dielectric constants of GaN and AlN at T = 300 K

	GaN	**AlN**
$\boldsymbol{\varepsilon_0}$ **(T = 300 K)**	8.9 [57]	8.5 [57]
$\boldsymbol{\varepsilon_\infty}$ **(T = 300 K)**	5.35 [57]	4.77 [57]

The dependence of GaN refractive index on the light frequency and optical phonons was studied in the IR and is described by [68]:

$$n^2(\omega) = \epsilon_\infty + \epsilon_\infty \frac{\omega_{LO}^2 - \omega_{TO}^2}{\omega_{TO}^2 - \omega^2 - i\Gamma\omega} \tag{28}$$

where ϵ_∞ is the dielectric constant of GaN at high frequency and $\Gamma = 10\ \mathrm{cm}^{-1}$ is the phenomenological damping coefficient of GaN for the phonon modes. It is represented for the FIR range in Figure 21. The refractive index of GaN in the visible range is 2.335.

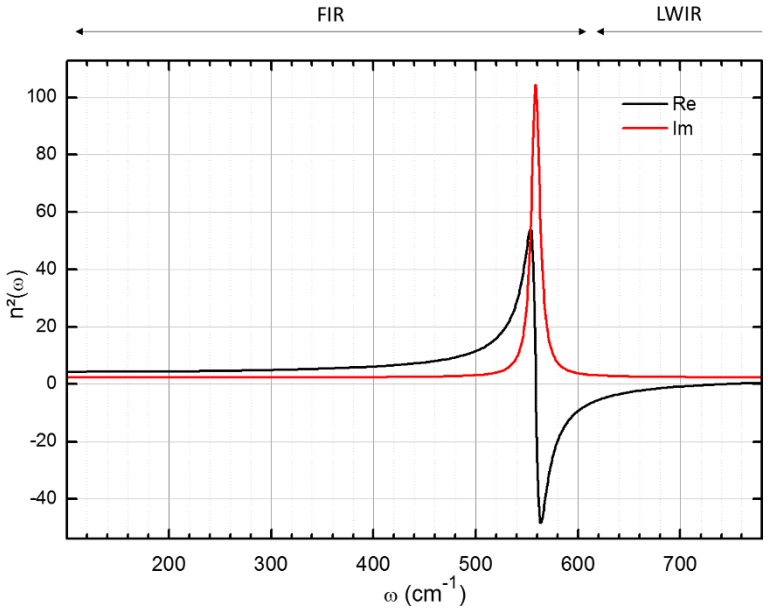

Figure 21 Real and imaginary parts of GaN refractive index in the FIR range.

1.2 Properties of III-nitride heterostructures

Now that we have established the basic knowledge on bulk III-nitride semiconductors, we can focus on the structural and electronical properties resulting from the stacking of different semiconductor materials in what is called a heterostructure. As illustrated by Figure 22, we consider a layer of material *A* sandwiched between two layers of material *B*, with the bandgap energy of *A* being smaller than the bandgap energy of *B*. In the case of GaN/AlN, the band offset presents a type I configuration, meaning that in the configuration in Figure 22, the electrons and holes are both confined in the material with the smaller bandgap. Several values for the GaN/AlN conduction band offset are reported in the literature, with ΔEc(GaN/AlN) = 1.5-2.1 eV [69,70]. In this work, we will use the value ΔEc(GaN/AlN) = 1.8 eV [71].

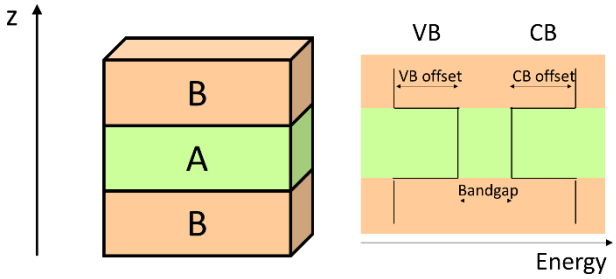

Figure 22 Example of a type I double heterostructure and its band diagram. VB refers to the valence band, CB refers to the conduction band.

1.2.1. Lattice mismatched heterostructures: strain, relaxation and extended defects

When stacking together two materials of different lattice constant, a mechanical stress is imposed in the obtained heterostructure, which in response undergoes strain relaxation, and eventually formation of structural defects.

Lattice deformation

The lattice-mismatched structure is either compressively strained, tensile strained, or relaxed (*i.e.* no strain, the lattices are unchanged for both materials), as illustrated by Figure 23.

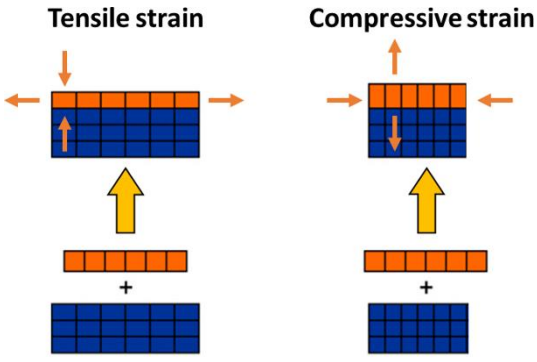

Figure 23 Illustration of tensile and compressive strains.

The deformation along the <0001> direction is $\varepsilon_z = (c - c_0)/c_0$ and the deformation in the plane perpendicular to the [0001] axis is $\varepsilon_x = \varepsilon_y = (a - a_0)/a_0$, where c_0 and a_0 are the in-plane and out-of-plane lattice parameters of unstrained bulk material, respectively. Accordingly to Hooke's law, the small stress σ_{ij} is related to the strain ε by:

$$\sigma_i = \sum C_{ij}\varepsilon_j \tag{29}$$

where C_{ij} is the stiffness or elastic constant tensor. In the case of wurtzite structure, due to the crystal hexagonal symmetry, the elastic constant tensor contains five independent coefficients, as described below:

$$C_{ij} = \begin{pmatrix} C_{11} & C_{12} & C_{13} & 0 & 0 & 0 \\ C_{12} & C_{11} & C_{13} & 0 & 0 & 0 \\ C_{13} & C_{13} & C_{33} & 0 & 0 & 0 \\ 0 & 0 & 0 & C_{44} & 0 & 0 \\ 0 & 0 & 0 & 0 & C_{44} & 0 \\ 0 & 0 & 0 & 0 & 0 & \frac{1}{2}(C_{11} - C_{12}) \end{pmatrix} \tag{30}$$

The values of elastic coefficients considered in this work for GaN and AlN are summarized in Table 5 [72,73].

Table 5 Elastic coefficients of GaN and AlN [72,73].

	C_{11} (GPa)	C_{12} (GPa)	C_{13} (GPa)	C_{33} (GPa)	C_{44} (GPa)
GaN	390	145	106	398	105
AlN	396	140	108	373	116

In the case of growth in the polar <0001> direction, there is no stress along <0001> (*i.e.* no shear stress) and the in-plane stress is uniform ($\sigma_x = \sigma_y$). In this biaxial stress configuration, equation (29) becomes:

$$\epsilon_y = \epsilon_x; \epsilon_z = -2\left(\frac{C_{13}}{C_{33}}\right)\epsilon_x \tag{31}$$

Strain relaxation and dislocations

In the case of lattice mismatched GaN/Al(Ga)N heterostructures, the strain related to the lattice distortion can be released either elastically by the undulation of the surface, or plastically by the introduction of defects in the epilayers. Several types of plastic relaxation are possible: crack propagation, which is commonly observed in III-nitrides under tensile stress, decohesion of the layer, which occurs in the case of compressive strain, and introduction of misfit dislocations (MDs), as illustrated by Figure 24. The MD threading through the structure defines threading dislocations (TDs). To describe the lattice deformation introduced by a dislocation, we use the Burgers vectors $\vec{b}$ shown in Table 6, which represent the magnitude and direction of the lattice distortion. The dislocations are either perfect or partial, where a partial dislocation is a decomposed form of an original perfect dislocation. In particular, Franck dislocations are immobile, they cannot move by gliding, in contrast to perfect dislocations.

Table 6 Dislocations observed in hexagonal structure. P: prismatic, B: basal, SS: stacking sequence.

Dislocations		
$\vec{b}$	Type	Character
1/3 <11-20>	a	Perfect
1/3 <11-23>	a+c	Perfect
<0001>	c	Perfect
1/3 <1-100>		Shockley partial
1/6 <20-23>		Frank-Shockley partial
1/2 <0001>		Frank partial

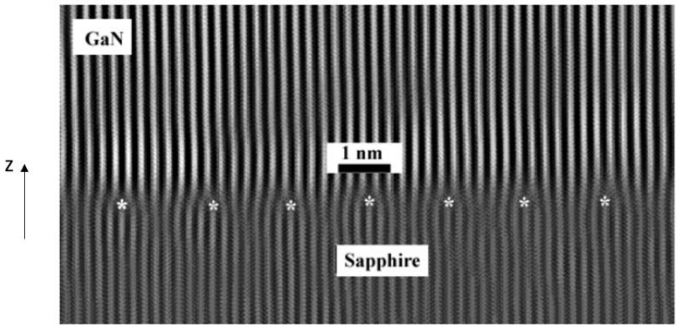

Figure 24 Fourier-filtered high-resolution transmission electron microscopy image showing misfit dislocations at a GaN/Sapphire interface. [74]

The formation and propagation of dislocations is associated to the material slip systems, which describe the set of symmetrically identical planes and associated family of directions for which dislocation motion can easily occur and lead to plastic deformation. In the case of nitride heterostructures grown along the [0001] axis, which is the predominant growth orientation in commercial devices, the most crystallographically favorable slip system, namely the (0001) basal plane with <11-20> {0002} slip directions, lies parallel to the heterointerfaces, which results in the resolved misfit stress on the main slip plane to be zero, and the formation of regular networks of MDs is thus hindered [75]. However, MDs can be detected at heterointerfaces when shear stress is intentionally or unintentionally induced by 3D growth [76,77], by crack formation [78,79], or in close proximity to V-defects (illustrated by Figure 25) [80]. Therefore, the relaxation mechanism depends not only on the structure itself, but also on the growth conditions.

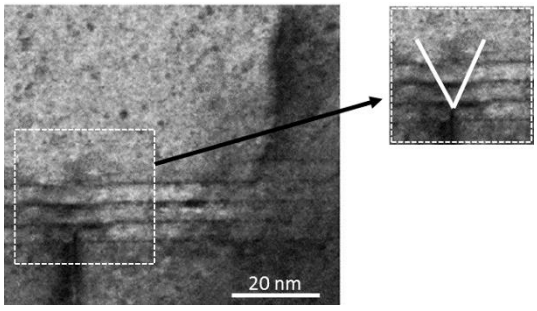

Figure 25 Scanning transmission electron microscopy bright field image of InGaN/GaN multi-quantum wells showing a V-defect **[74]**.

At the heterointerface with a substrate like sapphire or Si(111), GaN presents a high density of regularly-spaced 60° dislocations (type-B), formed due to the large mismatch. These 60° dislocations at the basal plane have the largest mobility of dislocation glide. They tend to bend in the growth direction, forming pure edge-type *a* or *a*+*c* dislocations (depending on their direction), as seen in Figure 26. In the *c*-plane orientation, the main dislocations are perfect TDs [81], with either edge, screw or mixed character (Burger vectors 1/3<11-20>, <0001> or 1/3<11-23>, respectively) [82], represented in Figure 26. Such TDs have their lines in the prismatic {11-20} or {1-100} planes. Edge-type dislocations make up the majority of the TD density in III-nitrides. An important characteristic of (0001) growth orientation is that the {11-20} and {1-100} planes contain the growth direction <0001> and constitute slip planes for the TDs. Therefore, as soon as they are formed, such dislocations can propagate until the surface of the epitaxial layer.

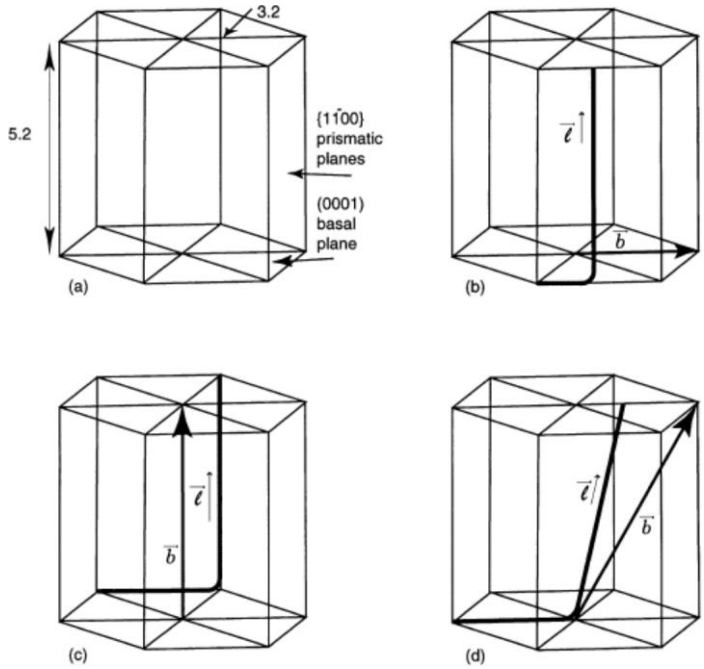

Figure 26 (a) Unit cell of wurtzite GaN. (b) Edge-type dislocation. (c) Screw-type dislocation. (d) Mixed-type dislocation. (Reproduced from **[83]**) The dislocations are represented by a thick black line.

Stacking faults and inversion domains

Stacking faults (SFs) [84–87] and inversion domains are also observed in III-nitride heterostructures [88,89]. Table 7 lists the SFs observed in hexagonal structures. A basal stacking fault (BSF) is an error in the ABABABA… hexagonal stacking sequence along the <0001> direction. They are known as intrinsic (I1 and I2) and extrinsic (E). Their stacking sequence (SS) and displacement vector ($\vec{R}$) are also given. For prismatic stacking faults (PSFs) the displacement $\vec{R}$ takes place out of the basal plane [90,91]. In GaN and AlN, two displacement vectors have been reported to characterize the PSFs in {11-20} planes [85,87,92]. In nitride layers grown along the *c*-axis, SFs are limited close to the interface with the substrate [93]. Figure 27 shows examples of SFs and inversion domains in GaN-based structures.

Table 7 Stacking faults in hexagonal structure. $\vec{R}$ is the displacement vector. P: prismatic, B: basal, SS: stacking sequence.

Stacking Faults		
$\vec{R}$	Type	SS or plane
1/3 <1-100>	B-I_1	AB<u>ABC</u>BCB
1/6 <20-23>	B-I_2	AB<u>ABCA</u>CA
1/2 <0001>	B-E	AB<u>ABCAB</u>AB
1/2 <1-101>	P	{11-20}
1/6 <20-23>	P	{11-20}

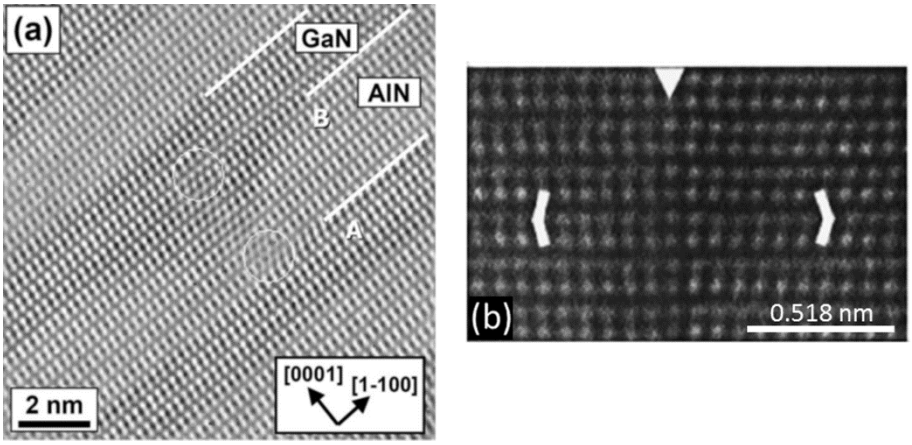

Figure 27 (a) High-resolution cross-sectional TEM image of a GaN/AlN heterostructure taken along the <11-20> zone axis and showing stacking faults **[94]**. (b) High-resolution electron microscopy image along the <11-20> zone axis showing {1-100} inversion domain boundaries in GaN grown on sapphire **[89]**.

Figure 28 describes the different types of stacking faults observed in Figure 27(a) as an example.

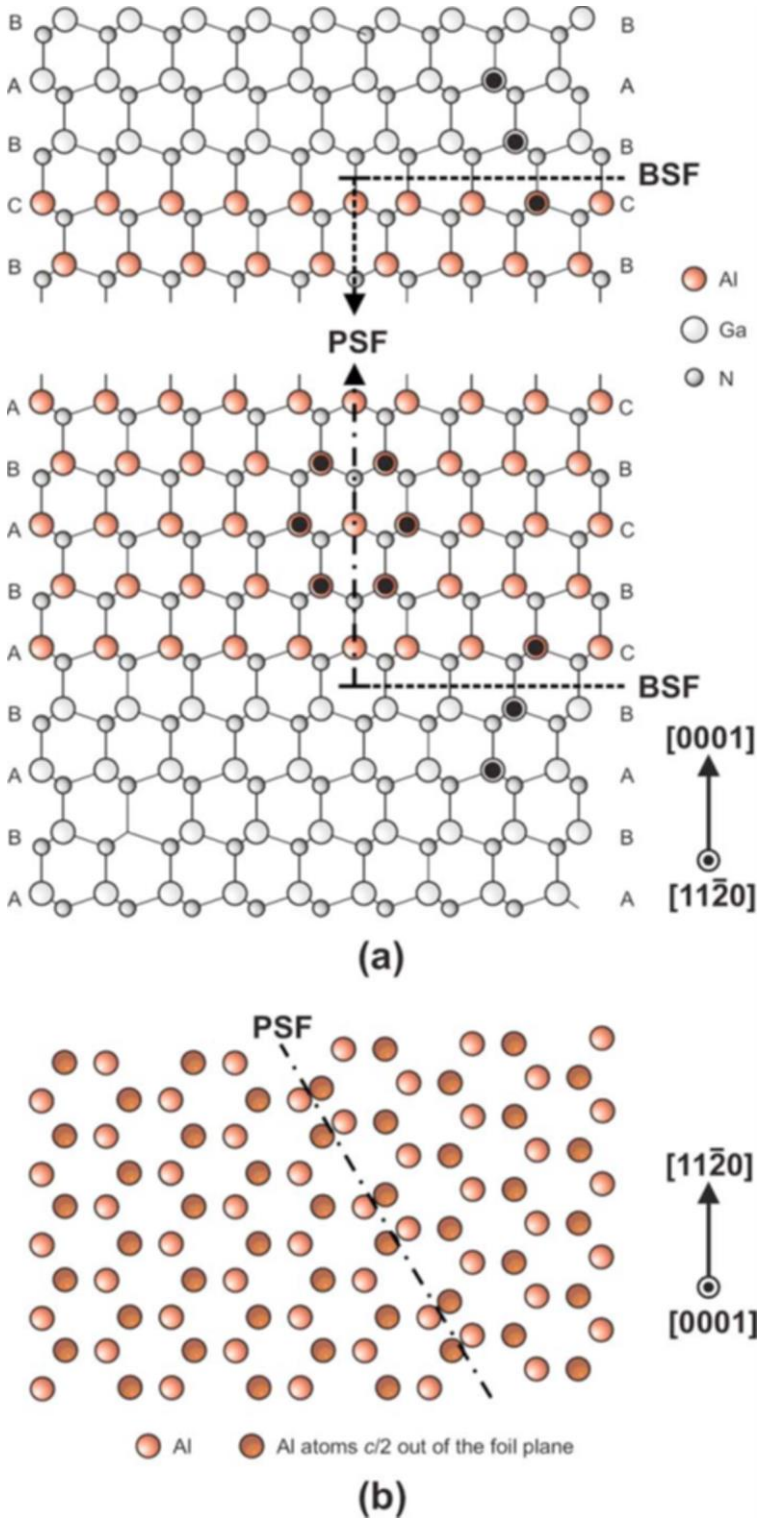

Figure 28 Schematic description of the defect structure observed in Figure 27 (a), projected along (a) the <11-20> zone axis and (b) the [0001] axis. [95]

1.2.2. Piezoelectric polarization

The presence of strain in the GaN/AlN system, associated to the lattice mismatch, results in the appearance of piezoelectric polarization. The piezoelectric polarization field, P_{pz}, is defined in the Cartesian system as a function of the piezoelectric constants e_{ij} and the strain field components ε_j:

$$P_{pz} = \sum e_{ij}\, \varepsilon_j \tag{32}$$

Due to crystal symmetry, there are only three independent piezoelectric constants e_{15}, e_{31}, and e_{33}:

$$P_{PZ} = \begin{pmatrix} 0 & 0 & 0 & 0 & e_{15} & 0 \\ 0 & 0 & 0 & e_{15} & 0 & 0 \\ e_{31} & e_{31} & e_{33} & 0 & 0 & 0 \end{pmatrix} \times \begin{pmatrix} \varepsilon_1 \\ \varepsilon_2 \\ \varepsilon_3 \\ \varepsilon_4 \\ \varepsilon_5 \\ \varepsilon_6 \end{pmatrix} \tag{33}$$

In subsection 1.2.1, we established the lattice deformation:

$$\epsilon_y = \epsilon_x; \epsilon_z = -2\left(\frac{C_{13}}{C_{33}}\right)\epsilon_x \tag{34}$$

Combining equations (33) and (34), the strain-induced piezoelectric polarization along the <0001> direction has its magnitude expressed as:

$$P_{pz} = 2\,\epsilon_z \left(e_{31} - e_{33}\frac{C_{13}}{C_{33}}\right) \tag{35}$$

and these in-plane and out-of-plane lattice constants are related by:

$$\frac{c - c_0}{c_0} = -2\frac{C_{13}}{C_{33}}\frac{a - a_0}{a_0} \tag{36}$$

which results in:

$$P_{pz} = 2\frac{a - a_0}{a_0}\left(e_{31} - e_{33}\frac{C_{13}}{C_{33}}\right) \tag{37}$$

The piezoelectric constants (e_{ij}) for GaN and AlN are listed in Table 8 [35,96,97]. The piezoelectric components for the alloys can be obtained by linear interpolation.

Table 8 Piezoelectric constants of GaN and AlN.

	e_{31} (C/m²)	e_{33} (C/m²)	e_{15} (C/m²)
GaN	-0.49 [35]	0.73 [35]	-0.3 [96]
AlN	-0.60 [35]	1.46 [35]	-0.48 [97]

1.2.3. Effect of polarization at heterointerfaces

The difference in the total macroscopic polarization across the heterointerface affects the band structure to a large extent. Taking the simple case of an epilayer grown on a bulk substrate, the difference in polarization across the interface is given by:

$$\Delta P = \Delta(P_{sp} + P_{pz}) = (P_{sp} + P_{pz})_{epilayer} - (P_{sp} + P_{pz})_{substrate} \tag{38}$$

The polarization difference results in a fixed charge density at the heterointerface. Figure 29 shows the polarization vectors and resulting $\pm\sigma_{pol}$ for different material/strain configurations, as well as the resulting band diagrams. Let us determine the sign of σ_{pol} for each case:

a) $\sigma_{pol} = P_{SP}(AlGaN) - P_{SP}(GaN) > 0$

b) $\sigma_{pol} = P_{PZ}(AlGaN) + P_{SP}(AlGaN) - P_{SP}(GaN)$

having $P_{SP}(\mathrm{AlGaN}) - P_{SP}(\mathrm{GaN}) > 0$, and $P_{SP}(AlGaN)$ and $P_{PZ}(AlGaN)$ being parallel (the parallel vectors point towards the same direction), we obtain $\sigma_{pol} > 0$.

c) $\sigma_{pol} = P_{PZ}(\mathrm{GaN}) + P_{SP}(\mathrm{GaN}) - P_{SP}(\mathrm{AlGaN})$

having $P_{SP}(\mathrm{GaN}) - P_{SP}(\mathrm{AlGaN}) < 0$, and $P_{SP}(GaN)$ and $P_{PZ}(GaN)$ being anti-parallel, we obtain $\sigma_{pol} < 0$.

If the charge sheet is positive ($+\sigma_{pol}$), free electrons will be attracted and will ultimately form a two dimensional electron gas (2DEG). Reciprocally, if the charge sheet is negative ($-\sigma_{pol}$), holes will accumulate at the interface.

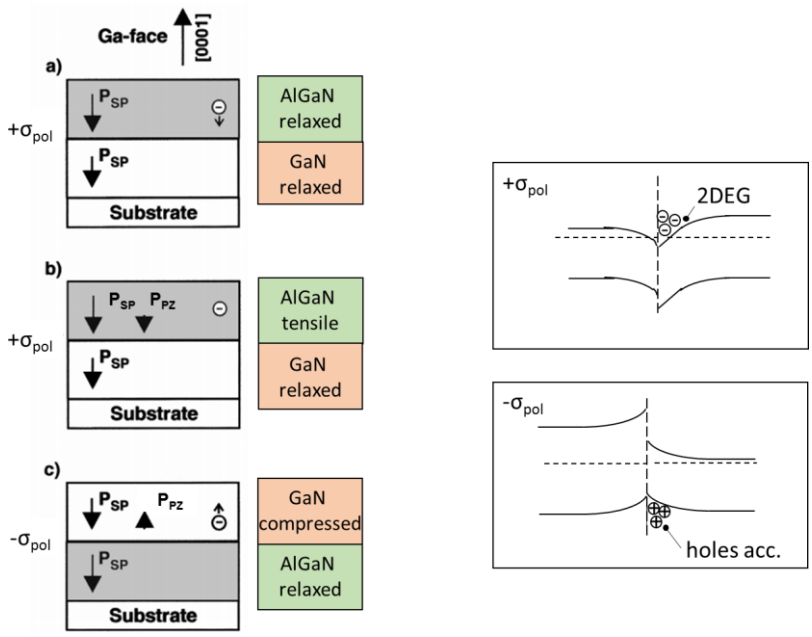

Figure 29 Polarization directions, sheet carrier densities and band diagrams in GaN and AlGaN for (a) unstrained GaN or AlGaN (b) tensile-strained AlGaN on a relaxed GaN buffer (c) compressively-strained GaN grown on a relaxed AlGaN buffer. (Modified from [98])

The consequences of the polarization-induced electric fields in III-N heterostructures on their optical and electrical properties are various and can be either exploited or compensated by our device design depending on the aimed application. As an example, the 2DEG formed at the GaN/AlGaN interface can be used to fabricate high electron mobility transistors (HEMTs) based on non-intentionally doped materials, and with sheet carrier concentrations comparable to those obtained when doping the channel [99]. This way, the mobility in not degraded by the doping-induced presence of ionized donors.

The effects of polarization can be eliminated by changing the growth orientation. Indeed, the high symmetry planes of wurtzite GaN at angles 39° and 90° off the <0001> direction are crystallographic directions for which polarization effects are either very small or zero [100]. The planes which satisfy these angles are the nonpolar *a* plane (11-20) and the nonpolar *m* plane (1-100) for 90°, and the semipolar planes (11-24) and (10-12) for 39°.

1.2.4. Quantum Confined Stark Effect

Following the above-described formation of sheet carrier densities at the GaN/AlN heterointerfaces, we therefore obtain fixed charges at the QW interfaces in the case of multi-quantum

wells (MQWs). The resulting electric field in the GaN well, F_{GaN}, and in the AlN barriers, F_{AlN}, can be calculated based on the conservation of the electric displacement vector along the growth direction, which is illustrated by the dotted line in Figure 30: the potential energies at the extremities of a period of the superlattice are equal [101]. This is expressed by the periodic boundary condition: $l_{GaN}F_{GaN} + l_{AlN}F_{AlN} = 0$. The electric fields are then expressed as:

$$\mathrm{F_{GaN}} = \Delta \mathrm{P} \frac{\mathrm{l_{AlN}}}{l_{GaN}\epsilon_{AlN} + l_{AlN}\epsilon_{GaN}} \tag{39}$$

$$\mathrm{F_{AlN}} = \Delta \mathrm{P} \frac{\mathrm{l_{GaN}}}{l_{AlN}\epsilon_{GaN} + l_{GaN}\epsilon_{AlN}} \tag{40}$$

where l_{AlN} and l_{GaN} are the barrier and well widths, ϵ_{AlN} and ϵ_{GaN} are the barrier and well dielectric constants.

The electric field in the GaN well causes what is known as the quantum confined Stark effect (QCSE): the first electron level e_1 in the conduction band and the first hole level h_1 in the valence band get closer in energy, which induces a redshift of the band-to-band transition energy e_1-h_1, as compared to square potential profiles [102]. As illustrated by Figure 30, QCSE also results in the spatial separation of electron and hole wavefunctions, which weakens the band-to-band oscillator strength, and therefore results in large radiative lifetimes.

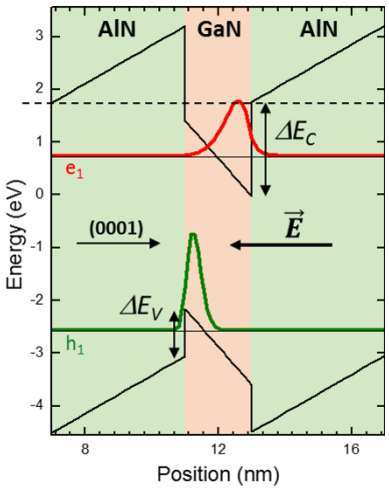

Figure 30 QCSE on the electron wavefunction (red) and the hole wavefunction (green) spatial separation, for a GaN/AlN (2 nm/ 4 nm) heterostructure, calculated using Nextnano[3]. The wavefunction represents the probability of presence of the carrier.

1.3 Intersubband transitions

Now that we have established the electronic properties of III-nitride heterostructures, we can focus on a specific type of electronic transitions of interest for IR optoelectronics: intersubband transitions.

The very first studies on ISB absorption date back to 1974, when Kamgar *et al.* recorded optical transitions between bound electronic levels in an accumulation layer on *n*-type Si(100) under FIR illumination [103]. Since then, Si space-charge regions and III-V surface layers were intensively studied and contributed to a better understanding of quantum confinement in thin-film structures, many-body effects, ISB absorption selection rules, oscillator strength and ISB absorption line shape

[104]. In 1977, Esaki and Sakaki suggested that the extrapolation of these principles to GaAs/AlGaAs MQWs should shift the transition wavelength to the MIR range [105], which lead to numerous experimental [106,107] and theoretical [108,109] studies and ultimately resulted in the first direct observation of ISB absorption by West and Eglash in 1985 in GaAs/$Al_{0.3}Ga_{0.7}As$ MQWs, measured at the Brewster angle [110]. Two years later, Levine *et al.* measured strong ISB absorption using for the first time a multipass waveguide configuration [111], and demonstrated the first QWIP [112,113]. In 1994, Faist *et al.* set a major breakthrough in the ISB technology with the development of the quantum cascade laser (QCL) as a replacement for the laser diode [114]. Since then, a great effort has been made in both fundamental and applied research on ISB transitions, which resulted in commercially available devices operating in the MIR and FIR. Nowadays, III-As material systems (like GaAs/AlGaAs) are the basis for ISB optoelectronics devices (emitters and photodetectors) that can be tuned from the MIR to the THz spectral ranges. However, the operation of such technologies is limited at shorter wavelengths (below 3 µm) due to the available conduction band offset and to the material transparency. Also, the small energy of LO-phonon (36 meV, 8.7 THz [115]) of GaAs limits the operating temperature of THz devices to the cryogenic range.

This is why III-nitride semiconductors started to attract much interest as an alternative material, due to their large bandgap and large conduction band offset (~ 1.8 eV for GaN/AlN [70,71,116]), allowing to develop ISB devices operating in the NIR spectral range, and especially in the telecom window (at 1.3-1.55 µm) [117–119]. Besides, GaN is transparent in a very large spectral region that covers almost the whole infrared window: it is transparent above 360 nm except for its Reststrahlen band between 9.6 and 19 µm (and possibly except for the 7.3-9 µm window where the absorption is attributed to the second order of the Reststrahlen band [67,120,121]). There is also an interest to push the III-nitride ISB technology towards longer wavelengths, especially to the THz frequency range. This spectral region has attracted attention due to potential applications in medical diagnostics, security screening, and quality control. GaAs-based QCLs have already demonstrated potential as THz sources in the 1.2–5 THz range, however their operating temperature and spectral range are limited by the LO phonon emission of GaAs (36 meV [115]) which is very close to the room temperature thermal energy (26 meV). GaN-based devices have the potential to operate at higher temperature in the whole THz spectral range due to a large LO-phonon energy of 92 meV.

1.3.1. Band structure of quantum wells in the envelope function approximation

We consider a QW grown in the direction *z*, and composed of a layer of material *A*, of thickness *L*, sandwiched into a barrier material *B*. The bandgap energy of *A* is considered smaller than that of *B*, and *L* is supposed to be small enough so that the electrons are confined in the material *A* in the growth direction *z*. To determine the band structure of the QW, we introduce the envelope function approximation, which is a very efficient and elegant tool that is widely used to predict the optical and electrical properties of semiconductor nanostructures [41]. It is basically a generalization of the k·p approximation, where the wavefunctions ϕ are considered as a sum of slowly varying envelop functions f that will modulate the material Bloch functions u, leading to:

$$\phi(\vec{r}) = \sum_{l} f_l^{A,B} u_{l,k_0}^{A,B}(\vec{r}) \tag{41}$$

This implies that the wavefunctions are described at each position as a k·p decomposition. The heterostructure presents an in-plane translational invariance, so that the wavefunctions can be

written as plane waves, and k_x and k_y are continuus and there is no propagation along *z*. The envelope functions can then be written as:

$$f(\overrightarrow{r_\perp}, z) = \frac{1}{\sqrt{S}} \exp\left(i\overrightarrow{k_\perp}\overrightarrow{r_\perp}\right) \chi(z) \tag{42}$$

where $\overrightarrow{k_\perp} = (k_x, k_y)$ is the in-plane wavevector, $\chi(z)$ is the projection of f along the *z* axis, *S* is the surface area in the *(x,y)* plane of the active region.

Simplified resolution: one band model

First, let us calculate the energy levels E_n inside the QW in the case of infinite barriers. We assume that the Bloch functions are the same in the barriers and the well, so that the Schrödinger equation can be derived only for the envelope function, which allows to isolate the eigenenergies E_n. Based on the effective mass approximation introduced in subsection 1.1.2, we can write the Schrödinger equation as follows:

$$-\frac{\hbar}{2m^*}\nabla^2.f(\vec{r}) + U(\vec{r})f(\vec{r}) = E_n f(\vec{r}) \tag{43}$$

where *U* is the crystal potential.

Considering a symmetric QW with infinite barriers, the resolution of the Schrödinger equation thus results in:

$$E_n(\vec{k}) = E_{n_0} + \frac{\hbar^2 \overrightarrow{k_\perp}^2}{2m^*} \tag{44}$$

where E_{n_0} depends on the potential profile *V(z)*. The obtained eigenvalues are:

$$\chi_n(z) = \sqrt{2/L}\sin(n\pi z/L) \text{ and } E_n(\overrightarrow{k_\perp}) = \frac{n^2\hbar^2\pi^2}{2m^*L^2} + \frac{\hbar^2\overrightarrow{k_\perp}^2}{2m^*} \tag{45}$$

where *L* is the QW thickness.

This result shows that due to the boundary conditions imposed by the heterostructure, the E_n energies are discrete. Since *L* is small, only a few values of E_n are allowed within the QW, and these energy values are largely spaced.

General resolution: two-band model

It is assumed that the envelop function is slowly varying compared to the Bloch function and that the Bloch functions are identical in both materials. We obtain:

$$\phi(\vec{r}) = \sum_l f_l^{A,B} u_{l,k_0}(\vec{r}) \tag{46}$$

The Hamiltonian is written as:

$$H = \frac{p^2}{2m_0} + U_A(\vec{r})Y_A + U_B(\vec{r})Y_B \tag{47}$$

where the functions $Y_A(z)$ and $Y_B(z)$ are equal to 1 in their respective layers and equal to 0 out of their layers.

Since the band edges are eigenfunctions of the Hamiltonian at k = 0, we can write:

$$\left(\frac{p^2}{2m_0} + U_A(\vec{r})Y_A + U_B(\vec{r})Y_B\right) u_{l,0}(\vec{r}) = \epsilon_{l,0}^{A,B} u_{l,0}(\vec{r}) \tag{48}$$

where the ϵ are the eigenvalues of this reduced Hamiltonian.

Similar to the k·p approximation, we use the relation between the momentum operator *p* and the momentum vector *p* (which may be obtained after a quite laborious derivation):

$$\mathrm{p}\left(\exp(\mathrm{i}\mathrm{k}_\perp \mathrm{r}_\perp)\,\chi_\mathrm{l}(\mathrm{z})\mathrm{u}_\mathrm{l}(\vec{\mathrm{r}})\right) = \left(\hbar \mathrm{k}_\perp - \mathrm{i}\hbar\frac{\partial}{\partial \mathrm{z}} + \mathrm{p}\right)\exp(\mathrm{i}\mathrm{k}_\perp \mathrm{r}_\perp)\,\chi_\mathrm{l}(\mathrm{z})\mathrm{u}_\mathrm{l}(\mathrm{r}) \tag{49}$$

and we can substitute p in the Hamiltonian as follows:

$$p \to \hbar k_\perp - i\hbar\frac{\partial}{\partial z} + p \tag{50}$$

where *p* acts only on the Bloch part of the wavefunction.

This leads to a set of differential equations $\mathrm{Du} = \epsilon \mathrm{u}$, where *D* is a matrix of elements:

$$D_{l,n} = \left(\epsilon_l^A Y_A + \epsilon_l^B Y_B + \frac{\hbar^2 {k_\perp}^2}{2m_0} - \frac{\hbar^2}{2m_0}\frac{\partial^2}{\partial z^2}\right)\delta_{l,n} + \frac{\hbar k_\perp}{m_0}\langle l|p_\perp|n\rangle - \frac{i\hbar}{m_0}\langle l|p_z|n\rangle\frac{\partial}{\partial z} \tag{51}$$

where $\delta_{l,n}$ is the delta function.

The two-band model is a fairly realistic model used to compute the conduction band energy states while accounting for the effect of the valence band as a whole on the conduction band, *i.e.* the valence subbands are replaced by one effective valence band. For simplicity, we neglect the free electron term $\frac{\mathrm{p}^2}{2\mathrm{m}_0}$ and we look at the states at $\mathrm{k}_\perp = 0$ which define the top of the valence band and bottom of the conduction band, so that we can consider V_A and V_B as V_c and V_v, the subscripts *v* and *c* referring to the valence and conduction bands). Equation (51) becomes:

$$\begin{cases} \mathrm{U_c(z)f_c} - \dfrac{\mathrm{i}\hbar}{\mathrm{m}_0}\left\langle \mathrm{u_{c,0}}\middle|\mathrm{p}\middle|\mathrm{u_{v,0}}\right\rangle\dfrac{\partial}{\partial \mathrm{z}}\mathrm{f_v} = \epsilon \mathrm{f_c} & (52) \\ -\dfrac{\mathrm{i}\hbar}{\mathrm{m}_0}\left\langle \mathrm{u_{c,0}}\middle|\mathrm{p^*}\middle|\mathrm{u_{v,0}}\right\rangle\dfrac{\partial}{\partial \mathrm{z}}\mathrm{f_c} + \mathrm{U_v(z)f_v} = \epsilon \mathrm{f_v} & (53) \end{cases}$$

From Equation (53), we have:

$$\mathrm{f_v} = \frac{1}{\mathrm{U_v(z)} - \epsilon}\frac{\mathrm{i}\hbar}{\mathrm{m}_0}\left\langle \mathrm{u_{c,0}}\middle|\mathrm{p^*}\middle|\mathrm{u_{v,0}}\right\rangle\frac{\partial}{\partial \mathrm{z}}\mathrm{f_c} \tag{54}$$

Replacing f_v in Equation (52), we obtain:

$$-\frac{\hbar^2\left|\left\langle \mathrm{u_{c,0}}\middle|\mathrm{p}\middle|\mathrm{u_{v,0}}\right\rangle\right|^2}{\mathrm{m}_0}\frac{\partial}{\partial \mathrm{z}}\frac{1}{\epsilon - \mathrm{U_v(z)}}\frac{\partial}{\partial \mathrm{z}}\mathrm{f_c} + \mathrm{U_c(z)f_c} = \epsilon \mathrm{f_c} \tag{55}$$

Recalling the definition of the Kane energy $\mathrm{E_P} = \frac{2}{\mathrm{m}_0}\left|\left\langle \mathrm{u_{c,0}}\middle|\mathrm{p}\middle|\mathrm{u_{v,0}}\right\rangle\right|^2$ and defining an energy-dependent effective mass:

$$\frac{1}{\mathrm{m}(\epsilon,\mathrm{z})} = \frac{1}{\mathrm{m}_0}\frac{\mathrm{E_P}}{\epsilon - \mathrm{U_c(z)}} \tag{56}$$

we obtain the Schrödinger-like equation:

$$-\frac{\hbar^2}{2}\frac{\partial}{\partial \mathrm{z}}\frac{1}{\mathrm{m}(\epsilon,\mathrm{z})}\frac{\partial}{\partial \mathrm{z}}\mathrm{f_c} + \mathrm{U_c(z)f_c} = \epsilon \mathrm{f_c} \tag{57}$$

This model is very useful to model the electronic states in the conduction band with the inclusion of the non-parabolicity of the bands. It is widely used in the study of ISB transitions.

1.3.2. Physics of intersubband transitions: selection rules

In this subsection, we introduce the basic physics principles and equations describing the ISB transitions. Again, we based ourselves on the work of Liu and Capasso [122], Bastard [123], and Faist [41].

ISB transitions are governed by so-called selection rules. We now formally detail the equations that lead to such properties. To do so, we work in the conduction band of a system composed of a QW sandwiched between two barriers and we use a single-particle approach. The QW growth direction is chosen to be *z*.

The QW is excited by an electromagnetic wave that may induce transitions between the two electronic states of the QW. The electric field component of the incident light is a plane wave $\vec{F}(\vec{r},t)$:

$$\vec{\mathrm{F}}(\vec{\mathrm{r}},\mathrm{t}) = \mathrm{F}_0\vec{\mathrm{e}}\cos\left(\vec{\mathrm{l}}.\vec{\mathrm{r}}-\omega\mathrm{t}\right) = \frac{\mathrm{F}_0}{2}\vec{\mathrm{e}}\left(\exp\left(\mathrm{i}\left(\vec{\mathrm{l}}.\vec{\mathrm{r}}-\omega\mathrm{t}\right)\right)+\exp\left(-\mathrm{i}\left(\vec{\mathrm{l}}.\vec{\mathrm{r}}-\omega\mathrm{t}\right)\right)\right) \quad (58)$$

where $\vec{e}$ is the polarization vector (it is the direction of the electric field, $\vec{\mathrm{e}} = \left(\mathrm{e_x},\mathrm{e_y},\mathrm{e_z}\right)$), $\vec{l}$ is the propagation vector, ω is the electric field pulsation.

Since $\vec{\mathrm{F}} = -\frac{\partial\vec{\mathrm{A}}}{\partial\mathrm{t}}$, the Hamiltonian can be expressed as a function of the potential vector $\vec{A}$:

$$\mathrm{H} = \frac{\left(\vec{\mathrm{p}}+\mathrm{q}\vec{\mathrm{A}}\right)^2}{2\mathrm{m}^*} = \frac{\mathrm{p}^2}{2\mathrm{m}^*}+\frac{\mathrm{q}}{2\mathrm{m}^*}\left(\vec{\mathrm{p}}.\vec{\mathrm{A}}+\vec{\mathrm{A}}.\vec{\mathrm{p}}\right)+\frac{\mathrm{q}^2}{2\mathrm{m}^*}\mathrm{A}^2 \quad (59)$$

where $\vec{p}$ is the total momentum operator of the excitation electric field, *q* is the elementary charge.

Using the Coulomb gauge $\nabla\vec{\mathrm{A}} = \vec{0}$ results in the commutation of $\vec{p}$ and $\vec{A}$. Also, considering a low intensity potential, we can neglect the term in A^2. We can thus isolate the time-dependent and the time-independent parts of the Hamiltonian:

$$\mathrm{H} = \mathrm{H}_0 + \frac{\mathrm{q}}{\mathrm{m}^*}\,\vec{\mathrm{A}}.\vec{\mathrm{p}} \quad (60)$$

where $\mathrm{H}_0 = \frac{p^2}{2m^*}$ does not depend on time and we define the interaction Hamiltonian H_{int}:

$$\mathrm{H_{int}}(\vec{\mathrm{r}},\mathrm{t}) = \frac{\mathrm{q}}{\mathrm{m}^*}\,\vec{\mathrm{A}}.\vec{\mathrm{p}} \quad (61)$$

Since $\vec{\mathrm{F}} = -\frac{\partial\vec{\mathrm{A}}}{\partial\mathrm{t}}$, $\vec{A}$ can be expressed as:

$$\vec{\mathrm{A}}\,(\vec{\mathrm{r}},\mathrm{t}) = \frac{\mathrm{F}_0}{\omega}\sin\left(\vec{\mathrm{l}}.\vec{\mathrm{r}}-\omega\mathrm{t}\right)\vec{\mathrm{e}} = \frac{\mathrm{iF}_0}{\omega}\exp\left(\mathrm{i}\left(\vec{\mathrm{l}}.\vec{\mathrm{r}}-\omega\mathrm{t}\right)\right)\vec{\mathrm{e}}+\mathrm{cst} \quad (62)$$

and we obtain:

$$\mathrm{H_{int}}(\vec{\mathrm{r}},\mathrm{t}) = \frac{\mathrm{iqF}_0}{\mathrm{m}^*\omega}\,\exp\left(\mathrm{i}\left(\vec{\mathrm{l}}.\vec{\mathrm{r}}-\omega\mathrm{t}\right)\right)\vec{\mathrm{e}}.\vec{\mathrm{p}} \quad (63)$$

where $\vec{e}$ and $\vec{p}$ are the polarization vector and momentum operators, respectively.

H_{int} represents the coupling between the electron and the electric field, which is a time-dependent perturbation that may induce transitions between the initial and final electronic states $|i>$ (of energy $\mathrm{E_i}$) and $|f>$ (of energy $\mathrm{E_f}$) of the QW.

The rate of these transitions (probability of transition per unit of time) can be described by the Fermi's golden rule (which is a straightforward consequence of the Schrödinger equation, solved to the lowest order):

$$\mathrm{W_{if}} = \frac{\pi}{2\hbar}\left|\langle\phi_\mathrm{f}|\mathrm{H_{int}}|\phi_\mathrm{i}\rangle\right|^2\delta(\mathrm{E_f}-\mathrm{E_i}-\hbar\omega_\mathrm{if}) \quad (64)$$

where ϕ and *E* are the wavefunction and energy of the quantum confined initial and final states, and $\hbar\omega_{if}$ is the energy of the radiation associated to the transition. The delta function δ represents the energy conservation condition.

Since we consider ISB transitions in the infrared range, there is a large difference between the light wavelength (≈ µm) and the lattice dimension (≈ nm). This is why we can use a dipole approximation and neglect the spatial dependence of $\vec{A}(\vec{r},t)$ inside the interaction Hamiltonian matrix element $\langle\phi_\mathrm{f}|\mathrm{H_{int}}|\phi_\mathrm{i}\rangle$, resulting in:

$$\langle\phi_f|H_{int}|\phi_i\rangle = \left\langle\phi_f\left|\frac{q}{m^*}\,\vec{A}.\vec{p}\right|\phi_i\right\rangle$$
$$= -\frac{q}{m^*}\frac{iF_0}{\omega}\vec{e}\exp\left(i\,\vec{l}.\vec{r}\right)\langle\phi_f(\vec{r})|\exp(i\omega t)\,\vec{e}.\vec{p}|\phi_i(\vec{r})\rangle \quad (65)$$

leading to the transition rate:

$$W_{if} = \frac{\pi}{2\hbar}\frac{q^2F_0^2}{m^{*2}\omega^2}|\langle\phi_f|\vec{e}.\vec{p}|\phi_i\rangle|^2\delta(E_f - E_i - \hbar\omega_{if}) \quad (66)$$

The derivation of the transition rate allows to determine the selection rules of the ISB transitions.

We can write the wavefunctions as products of a Bloch function $u(r)$ (and the ensemble of the Bloch functions form a basis) and an envelope function $f(r)$:

$$\phi_i = f_i(r)u_\nu(r) \quad (67)$$
$$\phi_f = f_f(r)u_{\nu'}(r) \quad (68)$$

where ν and ν' subscripts refer to the band indices of the initial and final states of the transition, respectively, and *i* and *f* subscripts refer to the subband indices of the initial and final states of the transition, respectively. *i* and *f* subscripts are the quantum numbers. We obtain:

$$\langle\phi_f|\vec{e}.\vec{p}|\phi_i\rangle = \langle f_f u_{\nu'}|\vec{e}.\vec{p}|f_i u_\nu\rangle = i\hbar\int f_f^* u_{\nu'}^*\frac{\partial(f_i u_\nu)}{\partial t}\partial r^3$$
$$= i\hbar\int f_f^* u_{\nu'}^*\left[\frac{\partial f_i}{\partial t}u_\nu + \frac{\partial u_\nu}{\partial t}f_i\right]\partial r^3 \quad (69)$$

In the slowly varying envelope function approximation, we consider that the variation of $f(r)$ is much slower than that of $u(r)$. We obtain:

$$\langle\phi_f|\vec{e}.\vec{p}|\phi_i\rangle = i\hbar\int f_f^*\frac{\partial f_i}{\partial t}\partial r^3\int u_{\nu'}^* u_\nu\,\partial r^3 + i\hbar\int f_f^* f_i\,\partial r^3\int u_{\nu'}^*\frac{\partial u_\nu}{\partial t}\partial r^3$$
$$= \langle f_f|\vec{e}.\vec{p}|f_i\rangle\langle u_{\nu'}|u_\nu\rangle + \langle f_f|f_i\rangle\langle u_{\nu'}|\vec{e}.\vec{p}|u_\nu\rangle$$
$$= \langle f_f|\vec{e}.\vec{p}|f_i\rangle\delta_{\nu\nu'} + \langle f_f|f_i\rangle\langle u_{\nu'}|\vec{e}.\vec{p}|u_\nu\rangle \quad (70)$$

The two terms have very different character:

- $\langle f_f|f_i\rangle\langle u_{\nu'}|\vec{e}.\vec{p}|u_\nu\rangle$ represents the band-to-band transition from band ν to band ν'.
- $\langle f_f|\vec{e}.\vec{p}|f_i\rangle\delta_{\nu\nu'}$ represents the ISB transition and is non-zero when two envelope states are taken from the same band (*i.e.* $\nu = \nu'$). The ISB transition is thus governed by $\langle f_f|\vec{e}.\vec{p}|f_i\rangle$.

Let us focus on the ISB transition. We assume the same Bloch functions for the well and the barrier, meaning that the lattices are the same, and we can then work only on the envelope functions. As stated before (equation (42)), we have:

$$f_i(r_\perp, z) = \frac{1}{\sqrt{S}}\exp\left(i\overrightarrow{k_\perp}\overrightarrow{r_\perp}\right)\chi_i(z) \quad (71)$$

where $\overrightarrow{k_\perp} = (k_x, k_y)$ is the in-plane wavevector, $\chi_i(z)$ is the projection of f_i along the *z* axis. This is also true for f_f: $f_f(\overrightarrow{r_\perp}, z) = \frac{1}{\sqrt{S}}\exp\left(i\overrightarrow{k'_\perp}\overrightarrow{r_\perp}\right)\chi_f(z)$ and $\overrightarrow{k'_\perp} = (k'_x, k'_y)$

Writing $\vec{e}.\vec{p} = p_x\overrightarrow{e_x} + p_y\overrightarrow{e_y} + p_z\overrightarrow{e_z}$, $\|\vec{e}\| = 1$, the matrix element $\langle f_f|\vec{e}.\vec{p}|f_i\rangle$ is:

$$\langle f_f|\vec{e}.\vec{p}|f_i\rangle = \frac{1}{S}\int \exp\left(-i\overrightarrow{k'_\perp}\overrightarrow{r_\perp}\right)\chi_f^*(z)\left[p_x\overrightarrow{e_x}+p_y\overrightarrow{e_y}+p_z\overrightarrow{e_z}\right]\exp\left(i\overrightarrow{k_\perp}\overrightarrow{r_\perp}\right)\chi_i(z)\,\partial r^3$$
$$= \frac{1}{S}\Big[\int \exp\left(-i\left(\overrightarrow{k_\perp}-\overrightarrow{k'_\perp}\right)\overrightarrow{r_\perp}\right)\chi_f^*(z)\chi_i(z)p_x\overrightarrow{e_x}\,\partial r^3$$
$$+\int \exp\left(-i\left(\overrightarrow{k_\perp}-\overrightarrow{k'_\perp}\right)\overrightarrow{r_\perp}\right)\chi_f^*(z)\chi_i(z)p_y\overrightarrow{e_y}\,\partial r^3$$
$$+\int \exp\left(-i\left(\overrightarrow{k_\perp}-\overrightarrow{k'_\perp}\right)\overrightarrow{r_\perp}\right)\chi_f^*(z)\chi_i(z)p_z\overrightarrow{e_z}\,\partial r^3\Big]$$
$$= \frac{1}{S}\langle\chi_f|\chi_i\rangle\Big[\int \exp\left(-i\left(\overrightarrow{k_\perp}-\overrightarrow{k'_\perp}\right)\overrightarrow{r_\perp}\right)\partial y\,p_x\,\partial x\overrightarrow{e_x}$$
$$+\int \exp\left(-i\left(\overrightarrow{k_\perp}-\overrightarrow{k'_\perp}\right)\overrightarrow{r_\perp}\right)\partial x\,p_y\,\partial y\,\overrightarrow{e_y}\Big]$$
$$+\frac{1}{S}\int \exp\left(-i\left(\overrightarrow{k_\perp}-\overrightarrow{k'_\perp}\right)\overrightarrow{r_\perp}\right)\partial x\,\partial y\int \chi_f^*(z)p_z\chi_i(z)\,\partial z\overrightarrow{e_z} \qquad (72)$$

Since $\exp\left(-i\left(\overrightarrow{k_\perp}-\overrightarrow{k'_\perp}\right)\overrightarrow{r_\perp}\right) = \exp\left(-i\left((k_x-k'_x)x-(k_y-k'_y)y\right)\right)$ and $p=\hbar k$ in 1D, we obtain:

$$\langle f_f|\vec{e}.\vec{p}|f_i\rangle = \frac{1}{S}\langle\chi_f|\chi_i\rangle\Big[\int \exp\left(i\left(k_y-k'_y\right)y\right)\partial y\int p_x\exp(-i(k_x-k'_x)x)\,\partial x\overrightarrow{e_x}$$
$$+\int \exp(-i(k_x-k'_x)x)\,\partial x\int p_y\exp\left(i(k_y-k'_y)y\right)\partial y\overrightarrow{e_y}\Big]$$
$$+\frac{1}{S}\int \exp\left(-i\left(\overrightarrow{k_\perp}-\overrightarrow{k'_\perp}\right)\overrightarrow{r_\perp}\right)\partial x\,\partial y\int \chi_f^*(z)p_z\chi_i(z)\,\partial z\overrightarrow{e_z}$$
$$= \frac{1}{S}\langle\chi_f|\chi_i\rangle\Big[\int \exp\left(i\left(k_y-k'_y\right)y\right)\partial y\int(-\hbar(k_x$$
$$-k'_x))\exp(-i(k_x-k'_x)x)\,\partial x\overrightarrow{e_x}$$
$$+\int \exp(-i(k_x-k'_x)x)\,\partial x\int \hbar\left(k_y-k'_y\right)\exp\left(i\left(k_y-k'_y\right)y\right)\partial y\overrightarrow{e_y}\Big]$$
$$+\frac{1}{S}\int \exp\left(-i\left(\overrightarrow{k_\perp}-\overrightarrow{k'_\perp}\right)\overrightarrow{r_\perp}\right)\partial x\,\partial y\int \chi_f^*(z)p_z\chi_i(z)\,\partial z\overrightarrow{e_z} \qquad (73)$$

Since $\exp(-i(k_x-k'_x)x)$ and $\exp\left(i\left(k_y-k'_y\right)y\right)$ are two periodic functions, their integral is zero except if $k_x=k'_x$ and $k_y=k'_y$, respectively. However if $k_x=k'_x$ and $k_y=k'_y$ then $(k_x-k'_x)\exp(i(k_x-k'_x)x)=0$ and $\left(k_y-k'_y\right)\exp\left(i\left(k_y-k'_y\right)y\right)=0$, respectively. This leaves:

$$\langle f_f|\vec{e}.\vec{p}|f_i\rangle = \frac{1}{S}\int \exp\left(-i\left(\overrightarrow{k_\perp}-\overrightarrow{k'_\perp}\right)\overrightarrow{r_\perp}\right)\partial x\,\partial y\int \chi_f^*(z)p_z\chi_i(z)\,\partial z\overrightarrow{e_z} \qquad (74)$$

Since $\exp\left(-i\left(\overrightarrow{k_\perp}-\overrightarrow{k'_\perp}\right)\overrightarrow{r_\perp}\right)$ is a periodic function, we have $\int \exp\left(i\left(\overrightarrow{k'_\perp}-\overrightarrow{k_\perp}\right).\overrightarrow{r_\perp}\right)\partial r^3 = 0$ except if $\overrightarrow{k_\perp}=\overrightarrow{k'_\perp}$.

This results in: $\frac{1}{S}\int \exp\left(i\left(\overrightarrow{k'_\perp}-\overrightarrow{k_\perp}\right).\overrightarrow{r_\perp}\right)\partial x\,\partial y = \delta_{k_\perp,k'_\perp}$ and we obtain:

$$\langle f_f|\vec{e}.\vec{p}|f_i\rangle = \delta_{k_\perp,k'_\perp}\int \chi_f^*(z)p_z\chi_i(z)dz\ \overrightarrow{e_z} \qquad (75)$$

and the transition rate is:

$$W_{if} = \frac{\pi}{2\hbar}q^2E_0^2\delta_{k_\perp,k'_\perp}|\langle\chi_f(z)|p_z|\chi_i(z)\rangle|^2\delta(E_f-E_i-\hbar\omega_{if}) \qquad (76)$$

In conclusion, only the *z*-component of the electric field couples to the ISB transition. This is the polarization selection rule:

Only light polarized in the direction of confinement (z) can induce ISB transitions.

This has strong experimental consequences. Especially, the polarization selection rule allows to distinguish ISB absorption from all other absorption processes. Also, it complicates the

measurement of light absorption for example at a normal incidence, which is why a number of geometries were developed to measure ISB absorption in QWs, as illustrated by Figure 31. In this work, the 2D heterostructures are measured using the multi-pass A configuration [41].

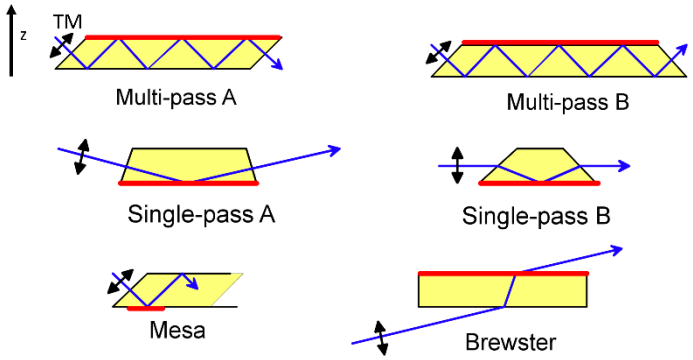

Figure 31 Experimental geometries allowing the measurement of ISB transitions. (Reproduced from **[41]**)

It is worth mentioning that in the case of general QWs with several possible energy states, a symmetric potential profile results in the heterostructure Hamiltonian having a defined parity. As a consequence, the wavefunctions are symmetric, which results in the matrix element being zero for wavefunctions with same parity (*i.e.* with both their quantum numbers either odd or even).

1.3.3. Scattering processes

An electron in an excited subband can recombine to the lower subband (*i.e.* relax) through a large variety of processes: spontaneous emission (of a photon), inelastic scattering by emission of a phonon, elastic scattering by an impurity or interface roughness, or electron-electron scattering. In practice, this carrier scattering results in the optical transitions always having a finite spectral linewidth, usually represented by a Lorentzian function. The contribution of each of these scattering processes to the ISB absorption linewidth was formulated by Ando [124,125] and calculations were developed and experimentally verified on GaAs QWs by Unuma *et al.* [126,127]. As opposed to the case of band-to-band transitions, the radiative emission of photon is not (by far) the dominant relaxation mechanism for ISB transitions.

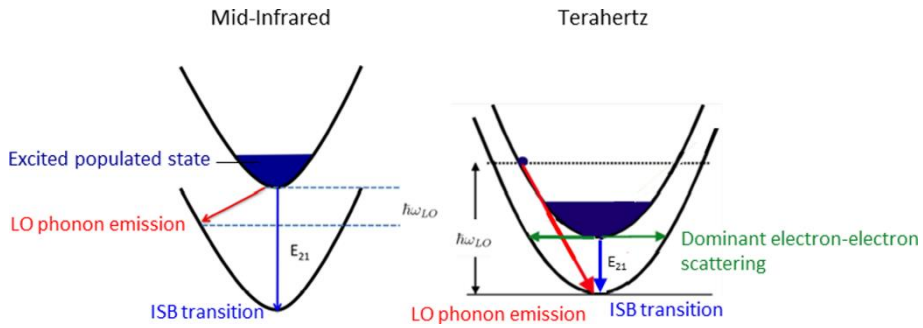

Figure 32 Schematic description of relevant scattering mechanisms in the two different cases: the transition energy is larger than the LO phonon energy (short-wavelength and mid-infrared) or the transition energy is smaller than the LO phonon energy (THz). (Modified from [41])

To emit optical phonons, electrons require a threshold energy of $\hbar\omega_{LO}$. This is why different behaviors are observed depending on whether the subband separation E_{12} is larger or smaller than $\hbar\omega_{LO}$, as illustrated in Figure 32. When the energy of the transition is larger than the LO phonon

energy $\hbar\omega_{LO}$, the dominant channel of carrier relaxation from the excited energy level is the scattering by optical phonon, which typical time constant is about 1 ps, leading to excited carrier lifetimes of about 1 ps. In contrast, in the case of a transition energy smaller than $\hbar\omega_{LO}$, optical phonon scattering may be forbidden depending on the temperature and the electron densities, and the lifetimes are then controlled by the competition between optical phonon emission and the other processes. Typically, optical phonon scattering by thermally-excited electrons will always dominate at temperatures above 60 K (the electrons are thermally excited and naturally relax through the emission of an optical phonon, which is a very rapid, sub-ps, process), electron-electron scattering and interface roughness scattering will be the strongest scattering mechanisms below 60 K, depending on the structure and on the electron density. The scattering by emission of an acoustic phonon can be significant only for extremely low electron densities and for systems with very little impurities. The typical lifetimes are ≈ 10 ps at low temperature.

Inelastic LO-phonon scattering

As a simple approach well verified in nitrides, the LO-phonon scattering is considered dominated by the interaction between the electron and the piezoelectric potential created by the local lattice deformation. Also, the optical phonon is supposed to have very little dispersion, and therefore can be assumed monoenergetic [128]. In this approach, an electron with an initial wavevector k_i and energy E_i in the upper subband scatters to the lower subband at k_f, thus losing (or gaining in the case of optical phonon absorption) an energy equal to $\hbar\omega_{LO}$ in the process, which is illustrated by Figure 33, where *Q* is the momentum exchanged in the process.

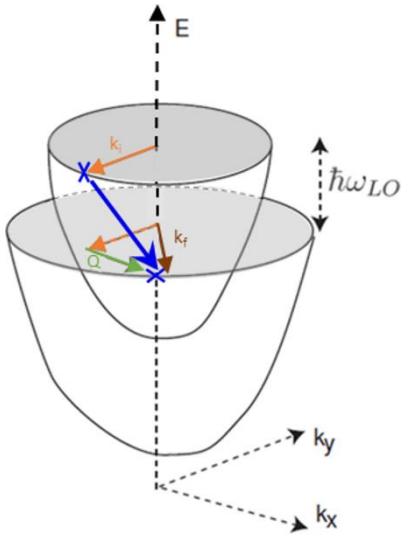

Figure 33 Scattering by an optical phonon between two subbands. (Modified from [41])

By applying the Fermi's golden rule on the envelope functions, the scattering rate can be calculated, resulting in an estimation of the electron lifetime due to optical phonon emission. As a consequence, a strong reduction of the ISB lifetime (*i.e.* rapid relaxation with emission of phonon, of the order of sub-ps) is predicted when the two states are spaced resonantly with the optical phonon.

Quasi-elastic electron-electron scattering

Electron-electron scattering is a quasi-elastic scattering process in which two electrons exchange energy and momentum, while still respecting the conservation of the total energy and of the total momentum. As a result, this process can only thermalize a carrier population but not cool it down. As illustrated in Figure 34, the different electron-electron scattering processes are:

- $2,2 \rightarrow 2,2$ and $1,1 \rightarrow 1,1$, which are scattering processes within a single subband, which help establishing a thermal equilibrium within the subband.
- $2,1 \rightarrow 2,1$ and $1,2 \rightarrow 1,2$, which tend to equilibrate the temperatures of the two subbands.
- $2,2 \rightarrow 1,1$ and $2,2 \rightarrow 2,1$, which tend to transfer the electrons from the upper to the lower subbands. The $2,2 \rightarrow 1,1$ process is the dominant electron-electron scattering, and we note that the $2,2 \rightarrow 2,1$ scattering is forbidden by parity in a symmetric structure [129]. The computation of the $2,2 \rightarrow 1,1$ electron-electron scattering rate by [130] demonstrates the linear dependence of the scattering rate on the electron density, and its inverse dependence on the ISB transition energy. As a result, electron-electron scattering is expected to play a significant role only for structures with very little impurities at low temperature.

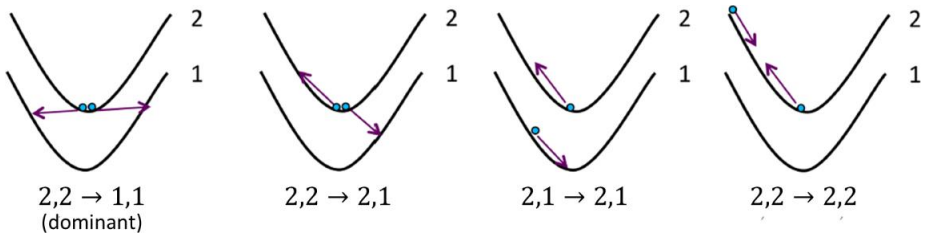

Figure 34 The different electron-electron scattering processes.

Elastic ionized impurity scattering and interface roughness scattering

Elastic scattering between subbands can occur whenever the translational invariance of the subband within the plane of the QW is lost, which may be induced by the collision with an ionized impurity or by an interface step. Ionized impurity scattering is the strongest scattering mechanism limiting the low-temperature mobility even when having very little impurities. The ionized impurity scattering rate was shown to be significant only for relatively large doping densities, with a time constant down to 1 ps [122,131].

Besides, the ISB transitions spectral linewidth was also reported to be sensitive to interface roughness scattering with significant effect for QW widths < 100 Å [132], but not to alloy scattering (to which electron mobility is sensitive) [133].

Also, if ISB transitions are usually described using a single-particle approach (as done in this manuscript), their description as a collective phenomenon (*i.e.* using the concept of plasma) results in a much better understanding of the contribution of scattering processes to spectral broadening when dealing with high electron densities [134], which is developed in the following subsection.

1.3.4. Doping and many-body effects

To be able to observe ISB absorption, the ground electronic state of the conduction band needs to be populated with electrons. To do so, we n-dope the semiconductor: we introduce impurities

in the semiconductor, which replace the original atom and set additional free electrons in the conduction band. Therefore, doping is an essential parameter for device design, and the possible requirement of high doping densities makes it necessary to consider the effects of electron-electron interactions. A great effort was made to study ISB transitions in the presence of dense electron plasma [135–137], and a large deviation of the ISB energy is expected for heavily doped structures [138].

The electron-electron interaction effects on the ISB transition energy and broadening are called many-body effects, and can be classified in two groups: the effects on the energy levels (namely the exchange interaction and direct Coulomb interaction) and the effects on the transition energy (namely the depolarization shift and exciton shift). In practice, these many-body effects are stronger for smaller transition energies, *i.e.* for larger QW widths. Accounting for all these many-body effects, the ISB transition energy $\mathrm{E_{if}^{final}}$ can be estimated as:

$$\mathrm{E_{if}^{final}} = \widetilde{\mathrm{E}}_{\mathrm{if}} - \mathrm{E_{exch}} - \mathrm{E_{dir}} \tag{77}$$

where $\widetilde{\mathrm{E}}_{\mathrm{if}}$ is the combination of depolarization and exciton shifts, $\mathrm{E_{exch}}$ is the exchange interaction energy, $\mathrm{E_{dir}}$ is the direct Coulomb interaction energy.

Depolarization shift and exciton shift

The depolarization shift α, also called plasmon screening, and the exciton shift β were shown to be the two main terms that can modify the ISB transition energy from the initial state $|i>$ to the final state $|f>$ from its nominal value E_{if} to [104,139–141]:

$$\widetilde{\mathrm{E}}_{\mathrm{if}} = \mathrm{E_{if}}\sqrt{1+\alpha-\beta} \tag{78}$$

where $\alpha, \beta > 0$.

As the external radiation (external electric field) excites the electron from the ground state to the excited state, the radiation also interacts with the other electrons coming from the doping of the structure. These electrons act as a plasma, and each single electron feels an effective electric field that is thus different from the external electric field. The electron gas screens the external electric field. This results in the modulation of the carrier density and in the increase of the transition energy, which is called a plasmon shift [136]. The depolarization shift can be estimated as [142]:

$$\alpha = \frac{2\mathrm{e}^2\mathrm{n_s}}{\epsilon_{\mathrm{R}}\epsilon_0\mathrm{E_{if}}}\int_{-\infty}^{+\infty}\left[\int_{-\infty}^{\mathrm{z}}\phi_{\mathrm{f}}(\mathrm{z}')\phi_{\mathrm{i}}(\mathrm{z}')\,\mathrm{dz}'\right]^2\mathrm{dz} \tag{79}$$

where n_s is the 2D density of charge, e is the electron charge, ϵ_0 is the electric permittivity, ϵ_R is the dielectric constant in GaN, ϕ_i is the wavefunction of the state $|i>$. The depolarization shift increases the transition energy and is important only for high electron densities and/or small transition energies.

The exciton shift accounts for the Coulomb interaction between the excited electron and the quasi-hole left in the ground state [137]. The exciton shift reduces the transition energy and is expressed as [143,144]:

$$\beta = -\frac{2\mathrm{n_s}}{\mathrm{E_{if}}}\int_{-\infty}^{+\infty}\phi_{\mathrm{f}}(\mathrm{z})^2\phi_{\mathrm{i}}(\mathrm{z})^2\mathrm{dz}\,\frac{\partial \mathrm{U_{xc}}[\mathrm{n(z)}]}{\partial \mathrm{n(z)}} \tag{80}$$

where U_{xc} is the exchange-correlation potential:

$$\mathrm{U_{xc}} = -\left(\frac{9\pi}{4}\right)^{\frac{1}{3}}\frac{2}{\pi \mathrm{r_s}}\frac{\mathrm{e}^2}{8\pi\epsilon_{\mathrm{R}}\epsilon_0 \mathrm{a}^*}\left[1+\frac{\mathrm{B}}{\mathrm{A}}\mathrm{r_s}\ln\left(1+\frac{\mathrm{A}}{\mathrm{r_s}}\right)\right] \tag{81}$$

where $a^* = \frac{\epsilon_R a_B m_0}{m^*}$ is the exciton Bohr radius, $r_s = \left[\frac{4\pi}{3} a^{*3} n(z)\right]^{-1/3}$ is dimensionless and characterizes the electron gas, a_B is the Bohr radius, $A = 21$, $B = 0.7734$.

Exchange interaction and direct Coulomb interaction

The exchange interaction accounts for the repulsion between electrons with parallel spin, which results from the Pauli principle: since the electron with the same spins avoid each other, the energy of electron-electron repulsion is reduced. It thus mainly affects the ground highly-populated state by lowering its energy, which ultimately results in a total blueshift of the ISB transition energy (and a redshift of the band-to-band transition). When the excited states can be considered unpopulated (at typical doping densities < 10^{19} cm^{-3}), the exchange interaction effect is negligible. However at high doping levels, the exchange interaction between the ground state subband and the excited states subbands must be accounted for. This is illustrated by Figure 35.

The exchange interaction E_{exch} between an electron in the ground state and the rest of the electrons within the same subband is given by [145,146]:

$$E_{exch} = -\frac{e^2}{2\epsilon_R} \int_0^{k_f} \frac{d^2k'}{(2\pi)^2} \int \frac{\exp(-q|z-z'|)}{q} |\chi_i(z')|^2 |\chi_i(z)|^2 \, dz \, dz' \qquad (82)$$

where $q = |k - k'|$ and $k_f = \sqrt{2\pi n_s}$.

Assuming that χ_i is strongly localized in the well, the leading term involves $q|z - z'|$ which is small. Then by considering the first two terms of the Taylor series expansion of the exponential term, we obtain [145]:

$$E_{exch}(k) \cong -\frac{e^2 k_f}{4\pi\epsilon_R\epsilon_0} \left[\frac{2\mathbf{E}\left(\frac{k}{k_f}\right)}{\pi} - 0.32\left(\frac{k_f}{k_L}\right) \right] \qquad (83)$$

where $k_L = \pi/L$, L is the QW thickness, **E** is the elliptic integral function.

High doping levels resulting in the population of the excited state require to take into account the exchange interaction between the subbands. The exchange interaction between an electron in the ground subband $|i>$ and the ensemble of electrons in the excited subband $|j>$ is given by [145,146]:

$$E_{exch} = -\frac{e^2}{2\epsilon_R} \int_0^{k_f} \frac{d^2k'}{(2\pi)^2} \int \frac{\exp(-q|z-z'|)}{q} \chi_j^*(z')\chi_i(z')\chi_i^*(z)\chi_i(z) \, dz \, dz' \qquad (84)$$

Since χ_i and χ_j are orthogonal, the leading term of the Taylor series expansion of the exponential term is zero. The next leading term is estimated by taking $\chi_j(z) = \sqrt{\frac{2}{L}}\sin(2k_L z)$ within the well and $\chi_j(z) = 0$ out of the well. We obtain [145,146]:

$$E_{exch} \cong -\frac{e\sqrt{2\pi n_s}}{4\pi\epsilon_R\epsilon_0} \, 0.18 \sqrt{\frac{2n_s}{\pi}} \qquad (85)$$

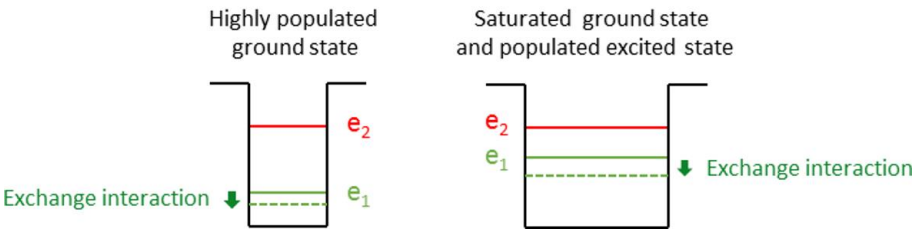

Figure 35 Schematic representation of the exchange interaction in the case of interaction within the same subband and of interaction between subbands.

The direct Coulomb interaction, on the other hand, accounts for the electrostatic potential resulting from the difference between the spatial distribution of the charges and the spatial distribution of the ionized donors. Usually, it is relatively weak when doping the QWs but quite large when doping the barriers. In the latter case, the electrons are transferred from the barrier to the well, which leads to a strong modification of the potential, called doping modulation and results in an increase of the electron mobility and a reduction of the ISB absorption linewidth (due to the suppression of impurity scattering) [122]. This is illustrated by Figure 36.

For QW doping densities where only the ground-state is being populated, the direct Coulomb interaction E_{dir} is expressed as:

$$\mathrm{E_{dir}} = \frac{3\mathrm{n_s e^2}}{8\epsilon_R\epsilon_0 {\mathrm{k_L}}^2 \mathrm{L}} \tag{86}$$

In this case, the direct Coulomb interaction E_{dir} tends to screen the electric field but is dominated by the exchange interaction.

At high doping densities, the direct Coulomb interaction between electrons in excited states and electrons in the ground-state is expressed as:

$$\mathrm{E_{dir}} = \frac{\mathrm{n_S e^2}}{4\epsilon_R\epsilon_0 {\mathrm{k_L}}^2 \mathrm{L}} \tag{87}$$

Generally in this case, the direct Coulomb interaction is negligible.

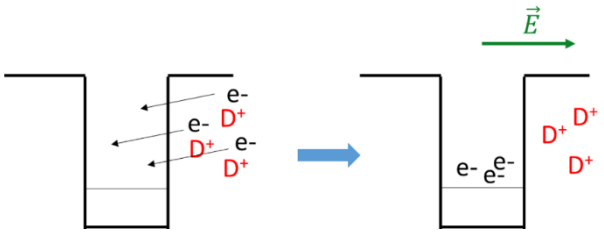

Figure 36 Schematic representation of the direct Coulomb interaction in the case of doping in the barriers. The electrons tunnel towards the QW and the spatial separation between electrons (e-) and ionized donors (D^+) creates an electrostatic potential $\vec{E}$ across the structure.

1.3.5. Intersubband transitions in GaN/AlGaN heterostructures

In this subsection, we review the previous work done on ISB transitions in GaN/AlGaN polar, semipolar and nonpolar heterostructures [8,119,147–153].

Polar heterostructures

Starting by the NIR range, the first observation of ISB absorption in GaN/AlGaN QWs was published in 1999 for wavelengths above 2.8 µm [154]. ISB absorption at shorter wavelengths was then observed at 1.75 µm [155] and then around the telecommunication wavelength 1.55 µm [156] in 2000. Since then, room temperature ISB absorption was demonstrated in nitride-based QWs and QDs by many research groups in Europe, Asia and the US.

In GaN/AlN, the $e_1 \rightarrow e_2$ ISB transition can be tuned in the 1.0 to 3.5 µm range by changing the QW thickness from 1 nm to 7 nm [71,157–164]. By using AlGaN instead of AlN for the barriers, it is possible to extend the ISB technology towards longer wavelengths: to the MIR up to 10 µm [135,165–169]. However, for large QW widths (> 5 nm), the first two quantum confined electronic states are trapped in the triangular part of the QW potential resulting from the internal electric field. This leads to a saturation of the value of the $e_1 \rightarrow e_2$ ISB transition energy.

To further reduce the ISB transition energy, two main alternatives are considered. The first one consists in engineering the band diagram of the polar heterostructure to approach a square potential profile in the QWs. This solution was suggested by Machhadani *et al.* [170] and further developed by Beeler *et al.* [171–173]. Figure 37 shows one of the proposed structures, which allowed to demonstrate FIR ISB absorption between 1.9 and 5.6 THz [171]. The second one involves the replacement of the usual polar *c*-oriented GaN by GaN in alternative crystallographic orientations where the intensity of the internal electric field in reduced (semipolar GaN) or null (nonpolar GaN).

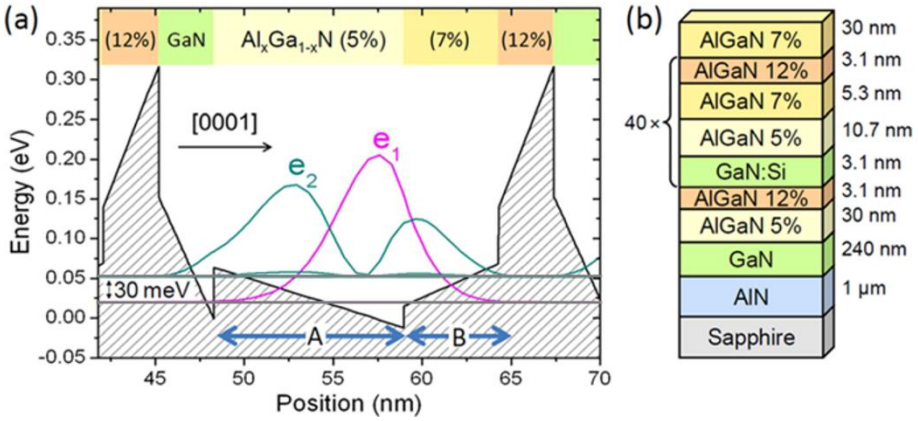

Figure 37 Band diagram (a) and structure (b) proposed by Beeler *et al.* for a THz *c*-plane GaN/AlGaN heterostructure with a quasi-square potential profile in the wells. (Reproduced from **[171]**)

In terms of devices, the first prototypes of nitride-based ISB devices were room-temperature multi-Tbit/s all-optical switches operating at 1.5 µm [174]. The demonstration of strong electron coupling in GaN/AlN double QWs [175] led to the development of the first charge-transfer GaN-based ISB electro-optical modulators [176]. Regarding detectors, the first III-nitride photovoltaic and photoconductive QWIPs and QD IR photodetectors were demonstrated in 2003 [177,178] and 2006

[179–181], respectively, for operation in the NIR, and in 2010 for operation in the FIR [170]. Regarding emittive devices, NIR ISB luminescence from GaN/AlN QWs [182–184] and QDs [185] was detected. The demonstration of the concept of quantum cascading in III-nitrides through the development of QD-based quantum cascade photodetectors (QCDs) operating in the 1.5-2.0 μm spectral range [186,187] has opened prospects for the development of QCLs.

Semipolar heterostructures

As illustrated in Figure 38, semipolar GaN/AlN MQWs exhibit quasi-square potential band profiles with symmetric wavefunctions, due to the reduced electric field [100,188], in the range of 0.5-0.6 MV/cm in the QWs for the (11–22) plane [189,190]. From the experimental viewpoint, ISB absorption had not been shown from semipolar crystal planes until relatively recently. Starting in 2008, NIR ISB absorption in the range of 1.5 to 3.75 μm was reported on semipolar (11–22)-oriented GaN/AlN MQWs, as illustrated in Figure 39 [189,190]. However, in semipolar structures, the reduction in the internal electric field resulted in a redshift of the ISB energy when compared with polar QWs with the same dimensions. ISB absorption in (11-22) GaN/AlGaN MQWs could not be extended to the MIR and FIR ranges, due to strong alloy fluctuation within the AlGaN ternary alloy [190]. Finally, very recent work on (20-2-1) GaN resulted in the demonstration of a THz QWIP with a detection peak at 10.1 THz [191].

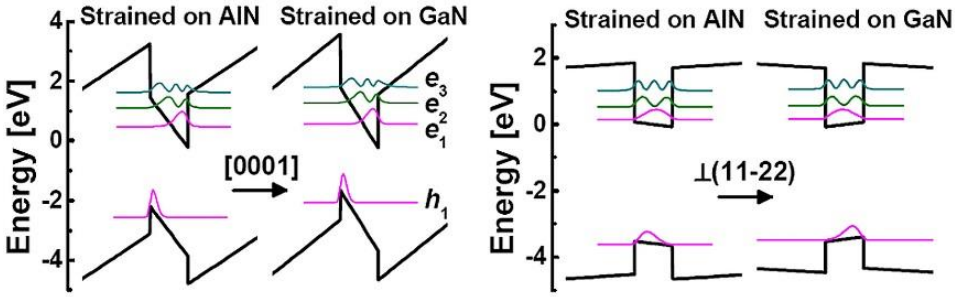

Figure 38 Band diagram of (0001)- and (11-22)-oriented GaN/AlN (2.5 nm/ 5 nm) MQWs assuming structures fully-strained on AlN and on GaN. (Modified from [192])

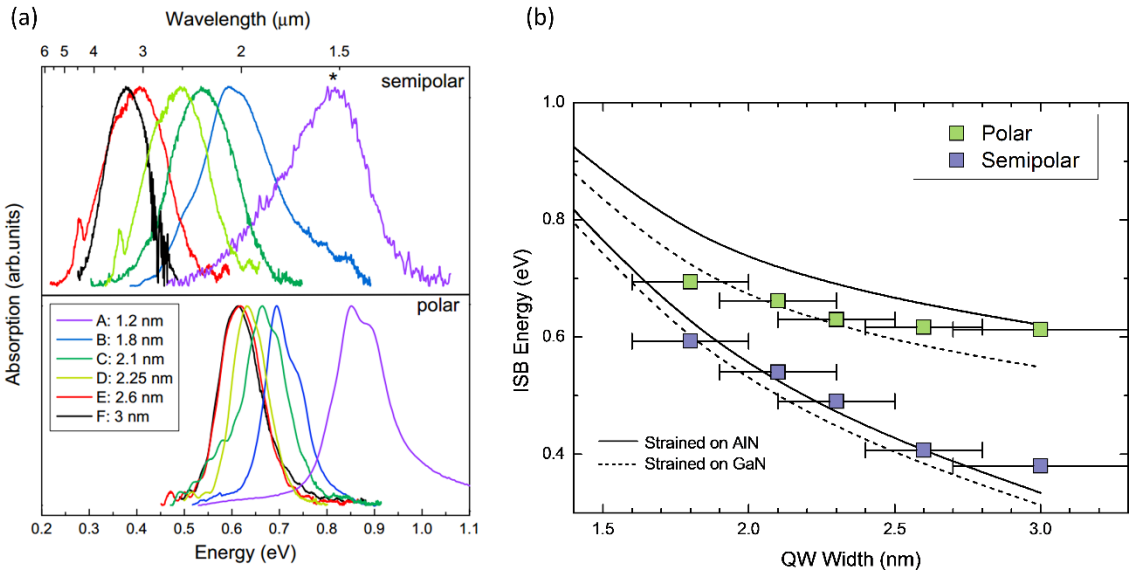

Figure 39 (a) ISB absorption spectra for semipolar (11-22) (top) and polar (bottom) GaN/AlN QWs with different well thicknesses, indicated in the legend box. The spectrum labeled with a star was obtained by photoinduced absorption measurement, all the others were measured by Fourier transform infrared spectroscopy. (b) Calculated and measured ISB absorption energy versus well thickness for semipolar and polar QWs. (Modified from [190])

Nonpolar heterostructures

ISB absorption in nonpolar GaN-based heterostructures was first observed in 2003 in *a*-plane GaN:Si/AlN MQWs grown on *r*-plane sapphire, showing ISB absorption at $\lambda \approx 2.1$ µm with a full width at half maximum (FWHM) of 120 meV [193]. The recent availability of high-quality free-standing nonpolar GaN substrates has encouraged research on nonpolar orientations, and in particular the growth of *m*-plane MQWs has been intensively studied since 2013 [194–196]. Especially, QWIPs in the MIR on *m*-plane GaN substrates were demonstrated at 7.5 and 9 µm in 2013 [197]. As illustrated by Figure 40, FIR ISB absorption in *m*-plane heterostructures was also demonstrated in 2014 [198], as well as resonant tunneling capabilities [199], confirming their potential to develop THz optoelectronics devices. At the beginning of my PhD thesis, NIR and MIR ISB absorption in nonpolar *m*-plane MQWs had not been shown yet, and the relaxation mechanisms within such structures had not been fully assessed.

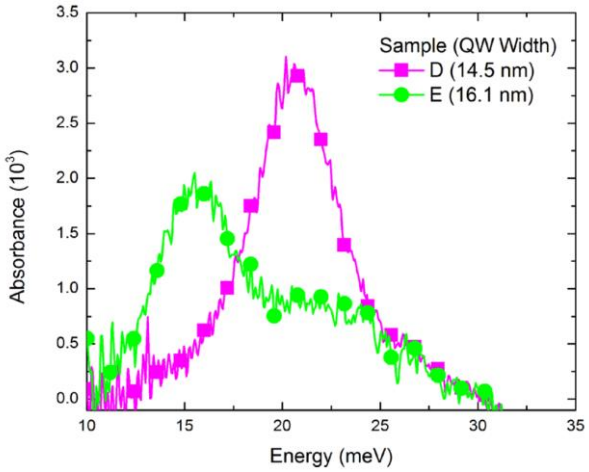

Figure 40 TM-polarized FIR ISB absorbance spectra. (Reproduced from [198])

Lovely MBE
Best oven for young atoms
Naked eye can't see

Chapter 2.
Methods

In this chapter, we describe the simulation tools and experimental techniques used in this work. We first introduce the simulation software. We then detail the different substrates we used and introduce plasma-assisted molecular beam epitaxy, as well as reflection high-energy electron diffraction, used as a real-time in-situ characterization technique. Finally, we focus on material characterization techniques: optical properties are assessed by photoluminescence and Fourier transform infrared spectroscopy, the morphology of the samples is analyzed by atomic force microscopy and scanning electron microscopy, and the sample structure is verified by x-ray diffraction and transmission electron microscopy.

2.1. Simulations

This thesis contains a study of nanostructures based on III-nitride semiconductors, particularly on GaN, AlN and their ternary alloy AlGaN. The simulations of the strain states, band diagrams, and electronic levels were performed using the Nextnano^3 software [29], taking into account the presence of spontaneous and piezoelectric polarization, with the material parameters listed in Table 9. In the case of 2D layers (*i.e.* 1D simulations), the 8x8 k.p Schrödinger-Poisson solver was used self-consistently. The k.p theory model overcomes the assumption of parabolic band structures that are usually considered for convenience at the bottom of the conduction band and the top of the valence band. By incorporating this non-parabolicity, differences in ISB energy of up to 25% can be observed with respect to with the effective-mass approximation [71].

As GaN/AlN is a lattice mismatched system with an in-plane lattice mismatch of 2.5%, the effect of strain and lattice relaxation will define both the device functionality and the band structure. Additionally, *c*-plane GaN/AlGaN heterostructures are very sensitive to the piezoelectric fields, which makes the calculation of the strain state crucial for understanding the electric fields and therefore the band profiles. In such polar structures, the strain state has two main effects on the band diagram: first, it modifies the materials bandgap, second, it modifies the piezoelectric polarization within the material. This induces changes in both the band-to-band and the ISB transition energies.

Table 9 Material parameters used in the theoretical calculations.

Parameters (units)	[ref.]		GaN	AlN
Lattice constants (nm)	[34][150][149][147][146][151][150][153][152][140][139]	*a*	0.3189	0.3112
		c	0.5185	0.4982
Spontaneous polarization ($C.m^{-2}$)	[35]		-0.029	-0.081
Piezoelectric constants ($C.m^{-2}$)	[35]	e_{13}	-0.49	-0.60
		e_{33}	0.73	1.46
Elastic constants (GPa)	[72,73]	C_{11}	390	396
		C_{12}	145	140
		C_{13}	106	108
		C_{33}	398	373
Dielectric constants	[200]		10	8.5
Luttinger parameters	[201]	A_1	-5.947	-3.991
		A_2	-0.528	-0.311
		A_3	5.414	3.671
		A_4	-2.512	-1.147
		A_5	-2.510	-1.329
		A_6	-3.202	-1.952
		A_7	0	0
		$E_P^{\parallel}$ (eV)	14	17.3
		$E_P^{\perp}$ (eV)	14	16.3
Deformation potentials (eV)	[200]	a_{c1}	-4.6	-4.5
		a_{c2}	-4.6	-4.5
		D_1	-1.70	-2.89
		D_2	6.30	4.89
		D_3	8.00	7.78
		D_4	-4.00	-3.89
		D_5	-4.00	-3.34
		D_6	-5.66	-3.94
Band offset (eV)	[71]		1.8	

For 3D calculations, we used the effective mass approximation, so that the simulations would converge at useful spatial resolutions. We note that Nextnano[3] does not completely incorporate many-body effects, so that only the screening of the internal electric fields is taken into account for calculations at high dopant densities.

2.2. Substrates

During my PhD, growth of the polar structures was performed on foreign substrates (GaN-on-sapphire, AlN-on-sapphire, or GaN-on-Si(111) templates). In contrast, nonpolar structures were exclusively grown on bulk GaN, since the growth of nonpolar III-nitrides on foreign substrates results in a high density of stacking faults [74,202,203].

2.2.1. Sapphire-based substrates

Sapphire is the most widely used substrate for GaN heteroepitaxy, in spite of the large lattice mismatch (about 30%). Different crystalline orientations of sapphire can be used to obtain the different crystallographic orientations of GaN. Polar GaN grows on *c*-sapphire, but with an in-plane rotation of 30° with respect to sapphire lattice, which reduces the lattice mismatch to 13.9%.

When choosing a substrate for infrared applications, two requirements must be taken into account: the transparency window (NIR and SWIR regions) and the dislocation density. In general, sapphire-based substrates present lower dislocation densities than silicon-based templates. However, their transparency range is spectrally narrower. Figure 41 shows the transmittance spectra of sapphire-based and Si(111)-based substrates in the SWIR and MIR. Sapphire-based templates are transparent in the SWIR but have a cut-off at ≈ 6 µm. We used AlN-on-sapphire templates to grow Si- and Ge-doped polar GaN/AlN MQWs with ISB absorption in the SWIR (section 3.3), and GaN-on-sapphire templates to grow the reference GaN/AlN polar MQWs with ISB absorption in the SWIR (section 4.3).

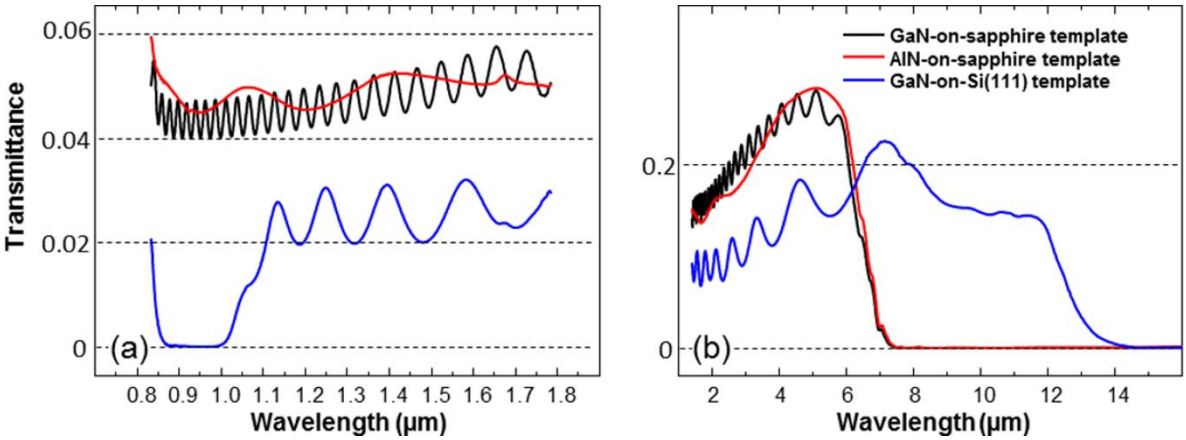

Figure 41 Transmittance spectra of sapphire-based and Si(111)-based substrates in the (a) SWIR and (b) MIR, measured by Fourier transform infrared spectroscopy. (Reproduced from **[204]**)

The AlN-on-sapphire templates used in this work were deposited by metalorganic vapor phase epitaxy by Dowa Electronics Materials Co., Ltd. They consist of 1.0 ± 0.1 µm-thick AlN(0001) on *c*-plane sapphire. The FWHM of the ω-scan measured by x-ray diffraction around the (0002) reflection is smaller than 150 arcsec, and the dislocation density is ~10^9 cm^{-2}. Figure 42, presents an atomic force microscopy (AFM) view of the substrate surface, characterized by the presence of atomic terraces, the root-mean-square roughness being around 0.42 nm.

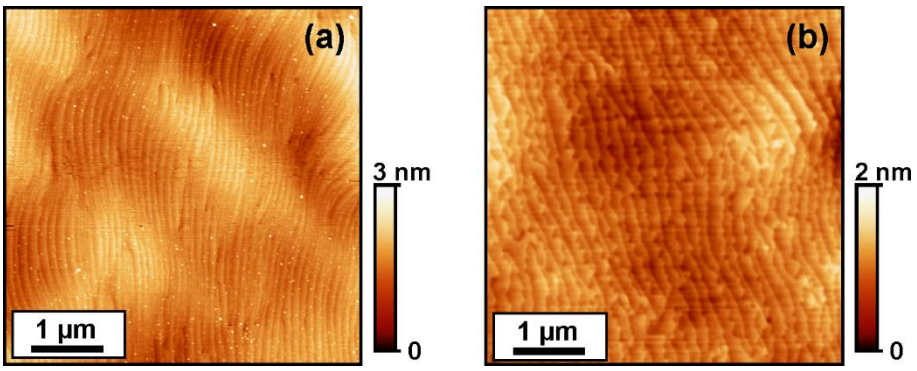

Figure 42 Typical AFM images of the (a) GaN-on-sapphire templates and (b) AlN-on-sapphire templates used in this work. (Modified from **[205]**)

The n.i.d GaN-on-sapphire templates used in this work were deposited by metalorganic chemical vapor deposition by Lumilog. They consist of 3.5 µm-thick GaN(0001) on *c*-plane sapphire. The dislocation density is ~4×10^{8} cm^{-2}. The top epilayer presents an atomically smooth surface, with an RMS roughness around 0.66 nm.

2.2.2. GaN-on-Si(111) substrates

Silicon substrates present many advantages for the growth of GaN templates: low-price wafers, large-scale production capability, good thermal stability under GaN growth conditions. Eventhough the thermal expansion coefficient of GaN is more than twice as large as that of Si (5.6×10^{-6} K^{-1} compared to 2.6×10^{-6} K^{-1}), which favors the formation of cracks in the template during the cooling down process after growth, several companies are today able to produce crack-free GaN-on-Si(111) thanks to a complex buffer layer containing GaN/AlGaN heterostructures. As illustrated by Figure 41, the GaN-on-Si(111) templates we used are IR-transparent, with the exception of the Reststrahlen band of GaN. In this work, we used GaN-on-Si(111) templates to grow the reference GaN/AlGaN polar MQWs with ISB absorption in the MIR (section 4.4).

The GaN-on-Si(111) templates consist of a 4µm-thick commercial HEMT epitaxial structure, as described in Figure 43, grown by metalorganic vapor phase epitaxy on floating-zone Si(111) by Dowa Electronics Materials Co., Ltd. The resistivity of the Si substrate is > 6000 Ω.cm, the average FWHM of the rocking curves around the (0002) and (10-12) reflections are ~856 arcsec and ~1700 arcsec, respectively. An AFM image of the substrate surface is shown in Figure 44.

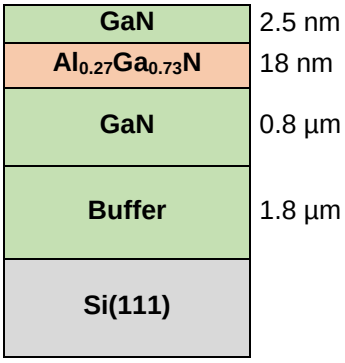

Figure 43 Schematic description of the GaN-on-Si(111) templates used in this work.

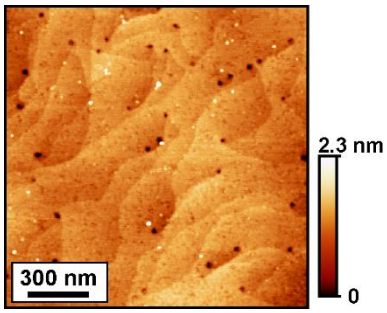

Figure 44 AFM image of the GaN-on-Si(111) templates used in this work. (Reproduced from **[205]**)

2.2.3. *a*- and *m*-plane free-standing GaN substrates

The nonpolar *a*- and *m*-plane substrates that we used consist of semi-insulating (s.i.) free-standing GaN sliced along nonpolar surfaces from *c*-oriented GaN boules synthesized by hydride vapor phase epitaxy (HVPE) by Nanowin (Suzhou Nanowin Science and Technology Co. Ltd). The use of semi-insulating substrates, rather than n-doped GaN, is a requirement to ensure transparency in the FIR range, as illustrated in Figure 45.

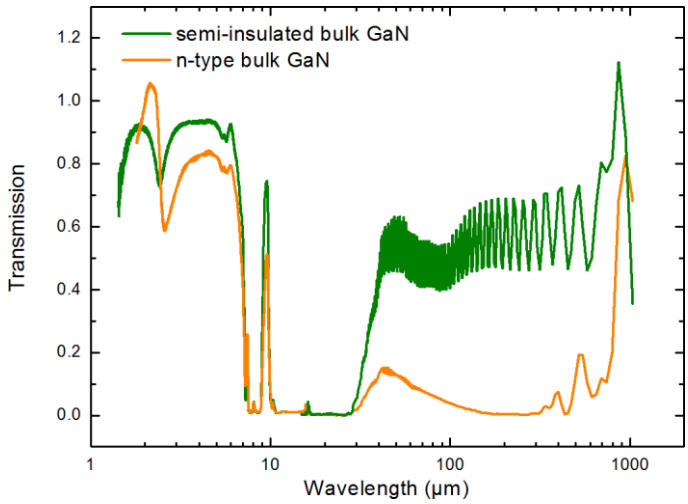

Figure 45 Transmission spectra of semi-insulated and n-doped free-standing GaN substrates.

Their miscut is smaller than ± 0.5°. At the beginning of my PhD thesis, the nonpolar substrates dimensions were 3.0 × 10.0 mm, for a thickness of 350 ± 25 µm. Their resistivity is > 10^6 Ω.cm. They have a dislocation density < 5×10^6 cm^{-2}. At the end of my PhD, the *m*-plane substrates dimensions were 5.0 × 20.0 mm. AFM images of the *a*-plane and *m*-plane substrates are shown in Figure 46, with RMS surface roughness of 0.20 nm and 0.18 nm, respectively.

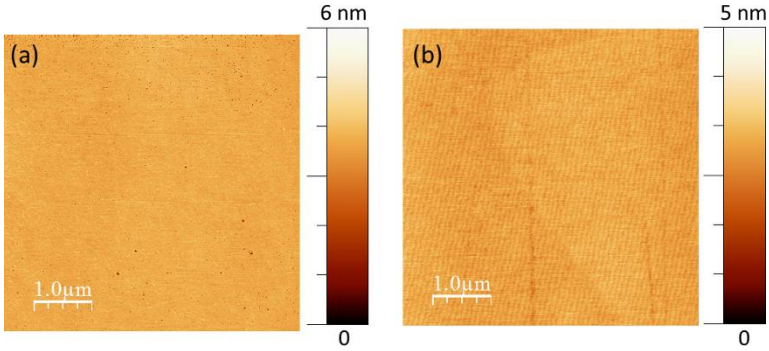

Figure 46 Typical AFM images of the (a) *a*-plane and (b) *m*-plane free-standing substrates used in this work.

2.3. Growth by plasma-assisted molecular beam epitaxy

2.3.1. Epitaxial growth

The term "epitaxy" describes the physical deposition of a monocrystalline film on a monocrystalline substrate, with conservation of a certain lattice alignment. In the particular case of homoepitaxy, the substrate and epilayer are of same material. The epitaxial growth process depends not only on the thermodynamic properties of the surface but also on the adatoms kinetics [206–208]. The temperature of the substrate is a key parameter which defines and activates the kinetic processes taking place at the growing surface. As illustrated by Figure 47, these different possible atomistic processes are: adsorption, diffusion, nucleation, incorporation and desorption.

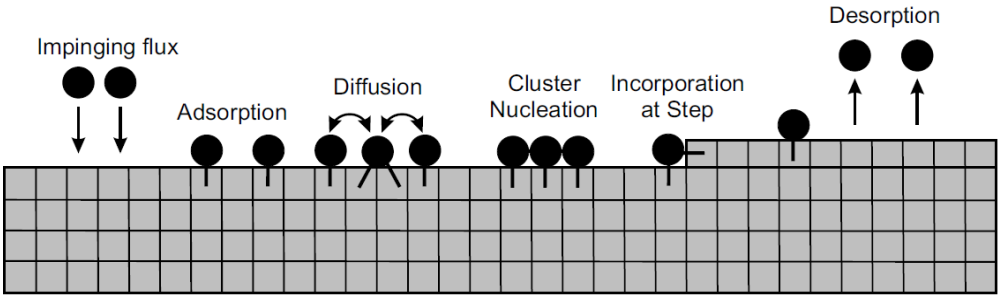

Figure 47 Atomistic processes that can occur at the surface during the growth.

Depending on the growth conditions, the behavior of surface processes varies due to the different adatoms mobility, defined by their diffusion length and lifetime. As illustrated by Figure 48, the growth modes can be described as a function of this parameter:

- Multi-layer growth: short diffusion length results in the nucleation of multi-layer-thick clusters, ultimately forming a rough surface.
- Layer-by-layer growth: the increased diffusion length results in the nucleation of monolayer (ML) clusters, with monolayers completed one by one.

- Step-flow growth: the long diffusion length gives the adatoms enough mobility to reach the step edges, which are often energetically favorable incorporation sites.

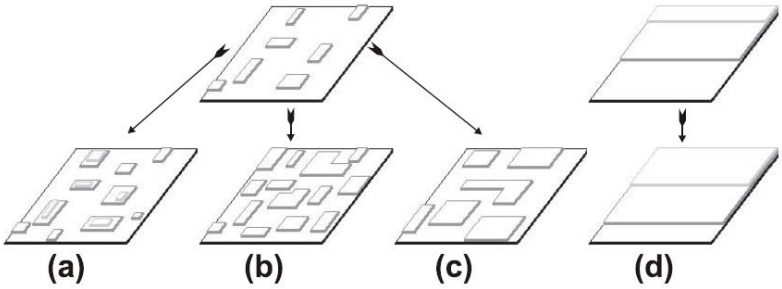

Figure 48 Growth modes as a function of the adatom mobility: (a) multi-layer growth, (b) and (c) layer-by-layer growth, (d) step-flow growth.

The growth of an epilayer on a substrate of different material is referred to as heteroepitaxy. In that case, various growth modes can be observed as illustrated by Figure 49, depending on the lattice mismatch, surface free energy, and dislocations formation energy:

- Volmer-Weber: for materials presenting a large lattice mismatch, the material tries to keep much of the surface uncovered without wetting.
- Franck van der Merwe (FvdM): 2D growth occurs. The misfit strain during the growth can be released by the formation of dislocations.
- Stranski-Krastanov (SK): the material initially wets the surface, but eventually forms 3D islands over the 2D wetting layer after a critical height.

Figure 49 Possible heteroepitaxy growth modes: (a) Volmer-Weber (b) Franck van der Merwe (c) Straski-Krastanov.

2.3.2. Plasma-assisted molecular beam epitaxy

It is possible to grow III-nitrides with many different instruments. In Table 10, we give a comparative overview of the typical systems used to grow GaN, AlN and their alloys, including metalorganic vapor phase epitaxy (MOVPE) / metalorganic chemical vapor deposition (MOCVD), HVPE, molecular beam epitaxy (MBE) and reactive sputtering.

Table 10 List of techniques used to grow GaN and AlN and their specifications.

Technique	Principle	Precursors	Growth temperature	Results
MOVPE/ MOCVD	Chemical reaction	Mixtures NH_3 and $(CH_3)_3M$, M being In, Ga, or Al [209]	1000-1100°C [210–212]	High growth rate (1-3 µm/h) and excellent material quality and control over layer thickness and doping.
HVPE	Physical deposition	GaCl, NH_3 [213]	1000-1050°C [210,214–216]	Very high growth rate (up to 100 µm/h). Possibility to synthesize mm-thick GaN crystal boules to slice free-standing wafers [217].
MBE	Physical deposition	High purity metals and N_2 or NH_3	600-800 [218]	Low growth rate (0.2-1 µm/h), excellent control over layer composition and thickness. Real-time in-situ control.
Reactive sputtering	Physical deposition	High purity metals or III-nitride blanks and N_2	300-750°C	Lower crystal quality but deposition is possible on any substrate and in large surfaces [219].

In this work, all samples were grown by plasma-assisted MBE. MBE is one of the most advanced single crystal thin film deposition techniques, invented in the late 1960s at the Bell Telephone Laboratories by A. Y. Cho and J. R. Arthur [220]. The MBE technique consists in the thermal evaporation of the desired materials and dopants under ultra-high vacuum. The rather low growth temperature in MBE (compared to HVPE or MOCVD/MOVPE) and the ultra-high vacuum environment result in several advantages of MBE compared to other growth techniques, like:

- A good control over layer thickness due to the low growth rate (less than 1 ML/s), and reduced interdiffusion effects. This results in excellent interface and surface morphology.
- A precise control of the beam fluxes.
- The possibility to synthesize a wide range of ternary and quaternary alloys, even alloys that are barely miscible under thermodynamic equilibrium.
- A high dopant incorporation.
- The possibility to use in-situ real-time characterization by reflection high-energy electron diffraction (RHEED).

In our particular case of III-nitride growth, MBE also offers the possibility to change the material polarity depending on the substrate or buffer layer, and makes it unnecessary to activate the Mg-dopant thanks to the hydrogen-free growth environment.

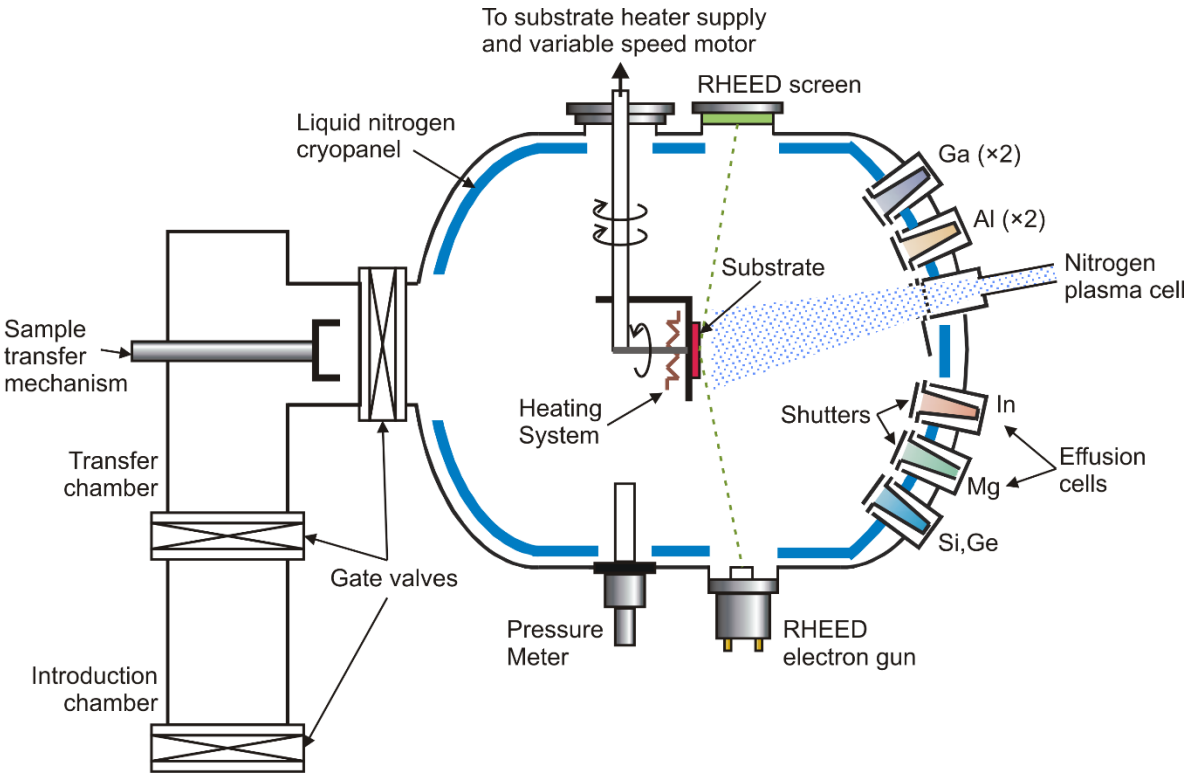

Figure 50 Schematic of the plasma-assisted MBE we used.

Figure 50 shows a schematic of the MBE set-up we used during my thesis. The main building blocks are the introduction chamber, transfer chamber and growth chamber. In order to load the samples, the introduction chamber is opened under a nitrogen flux and then evacuated up to 10^{-9} mbar. The transfer chamber is a transfer module permanently kept at a pressure of about 10^{-10} mbar. The growth takes place in the growth chamber, which is initially evacuated to about 10^{-11} mbar by a cryogenic pump combined with the cryogenic cooling down of the chamber walls with liquid nitrogen. The growth in this type of system occurs under a nitrogen pressure of about 5×10^{-6} mbar.

In the plasma-assisted MBE of III-nitrides, the active nitrogen is obtained by cracking high-purity molecular nitrogen (6N5) with a radiofrequency plasma source. Our MBE was equipped with an automatic N plasma source HD25 supplied by Oxford Applied Research, described in Figure 51. Since N_2 molecules are not reactive with Ga and cannot be thermally dissociated, the high-purity N_2 is introduced into a pyrolytic boron nitride cavity, where the plasma of mono-atomic nitrogen is generated by inductively-coupled radio-frequency excitation. The plasma is constantly monitored through an optical feedback loop.

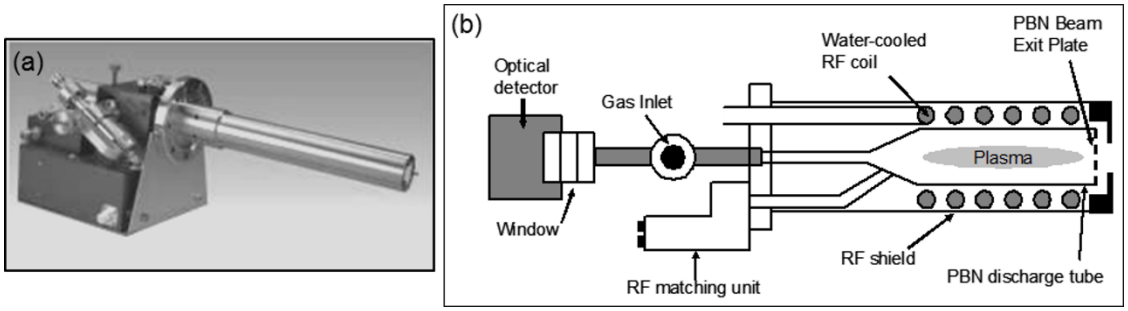

Figure 51 (a) Photograph and (b) schematic of the nitrogen plasma cell.

As illustrated by Figure 52, the molecular beams of Al, Ga, Si and Ge are generated from high-purity solid metals loaded in effusion cells, which consist of a crucible surrounded by heating coils. By raising up the temperature of the effusion cells, the sources are evaporated, and a mechanical shutter in front of every effusion cell is used to interrupt or start the beam flux (*i.e.* stop or start the doping and deposition).

A molybdenum sample holder (molyblock), on which the substrate is In-glued, is fixed on an axis manipulator which allows to automatically rotate and heat the substrate. Indeed, the substrate rotation is necessary to obtain homogeneity in the layer thickness and composition.

The MBE growth chamber being at ultra-high vacuum and its walls being cooled down with liquid nitrogen, the only heat locations are the effusion cells and the substrate, which is held at a suitable temperature (typically ~720°C in our case). The ultra-high vacuum ensures the beam nature of the flow of evaporated atoms and molecules from the hot effusion cells towards the hot substrate, *i.e.* the mean free path is much longer than the distance between the source cells and the substrate. The evaporation rate is controlled by setting the cell temperature. The atoms deposit and crystallize by reacting with the substrate. Under these conditions, the crystal growth is far from thermodynamic equilibrium, and is mostly governed by the kinetics of the surface processes.

As a result, the growth parameters are the substrate temperature, the effusion cells temperature, the chamber pressure, and the N-cell power.

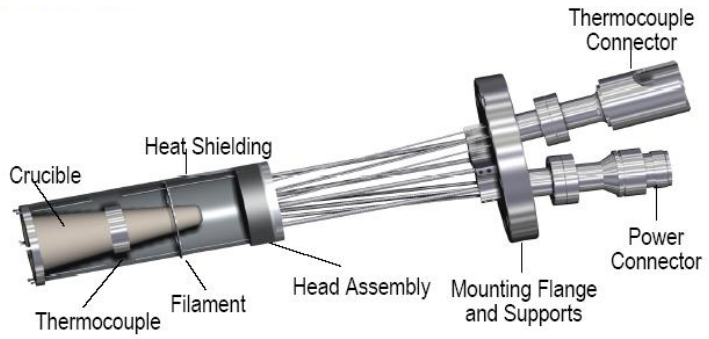

Figure 52 Description of a standard effusion cell.

2.3.3. Reflection high-energy electron diffraction

The ultra-high vacuum environment makes it possible to use an electron beam to diffract on the growing sample surface and this way obtain real-time information on the growing surface structure. RHEED is a characterization technique which presents the advantage of being in-situ and real-time. Electrons are emitted by a hot filament, which is excited by a 1.5 A current, and accelerated under high-voltage (typically 32 kV in our system). The electron beam strikes the sample at a grazing angle, and then impinges on a fluorescent phosphor screen mounted opposite to the electron gun. The obtained image displayed on the screen is the Fourier transform of the lattice interacting with the beam. A schematic description of the RHEED measurement is shown in Figure 53. The radius of the Ewald sphere is much larger than the separation of the reciprocal rods, and the intersection of the sphere and rods results in a streaky, rather than spotty, diffraction pattern.

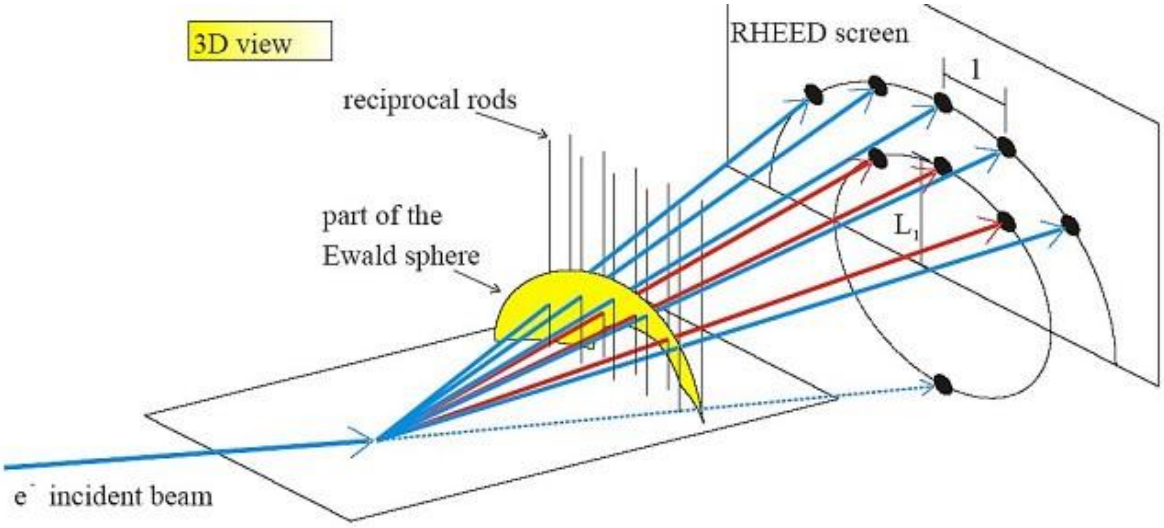

Figure 53 Schematic description of the RHEED measurement principle.

Information on the growing surface structure can then be extracted from the obtained diffraction pattern. The in-plane lattice constant can be calculated following: $\mathbf{d_u = L\lambda_0/t}$, where d_u is the interplanar distance, L is the distance between the surface normal and the screen, λ_0 is the electron wavelength (λ_0 = 0.124 Å), t is the distance between two streaks on the screen display. The 2D or 3D nature of the surface morphology and a qualitative estimation of the crystal quality can be obtained. Finally, the growth rate can be measured under layer-by-layer growth conditions, since the change in density of atoms at the growth front results in an oscillatory variation of the RHEED intensity. In the case of a flat surface, *i.e.* the layer at the surface is complete, the coverage θ is minimum (0) or maximum (1), the RHEED intensity is maximum. Starting with a minimum coverage θ = 0, we describe the procedure to determine the growth rate, as illustrated by Figure 54. Once the coverage increases and reaches θ = 0.5, the roughness is maximum and the intensity is at its lowest. At θ = 0.75, the intensity recovers as the space in-between the nucleating sites gets filled. The surface flattens at θ = 1, reaching again a maximum RHEED intensity. The RHEED intensity oscillation period corresponds to the growth of a single layer. We note that the calibration of the growth rate and the control of the alloy composition and thickness of the layers are done using this RHEED feature.

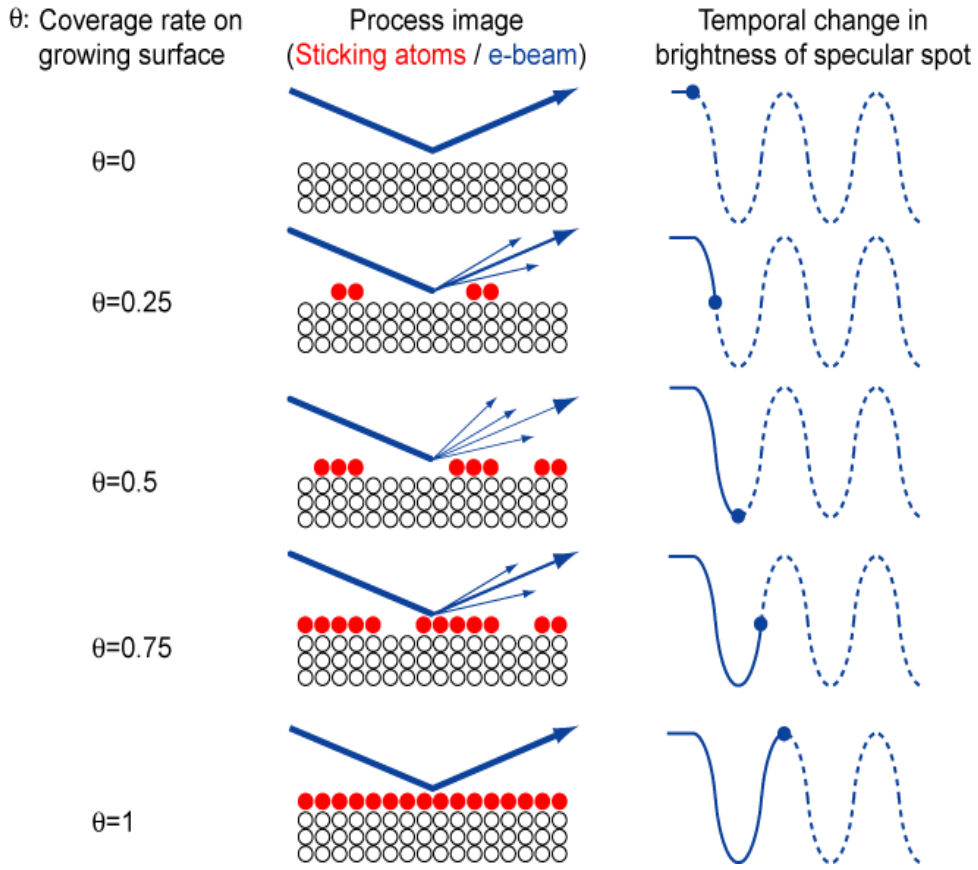

Figure 54 Schematic description of the procedure to determine the growth rate from the variation of the RHEED intensity.

2.3.4. Growth of polar GaN, AlN and AlGaN

In this thesis, we will study polar *c*-plane as well as nonpolar *a*- and *m*-plane heterostructures (*i.e.* with the *c*-axis in the growth plane). At the beginning of my PhD thesis, the plasma-assisted MBE growth of 2D polar GaN structures with smooth surfaces has already been much investigated and mastered. Regarding nonpolar growth though, high-quality free-standing nonpolar GaN substrates had just been made available. As a consequence, research had until then turned its interest towards the growth on semipolar planes to reduce the internal electric field [221], instead of developing nonpolar ISB technologies. In this work, after checking that the growth conditions of polar and nonpolar structures were compatible (cf. section 4.2), the growth of nonpolar structures was done on the same molyblock and simultaneously to the growth on a *c*-plane substrate, using the RHEED of the polar surface as a reference and real-time in-situ control means.

The growth of *c*-plane GaN by plasma-assisted MBE is extensively discussed in the literature [222–224]. Three generic types of surface reactions are reported, among which the precursor-mediated model is considered to best explain the process of GaN layer formation occurring during the plasma-assisted MBE growth of III-nitrides [225]. In Figure 55, we show a schematic representation of this process.

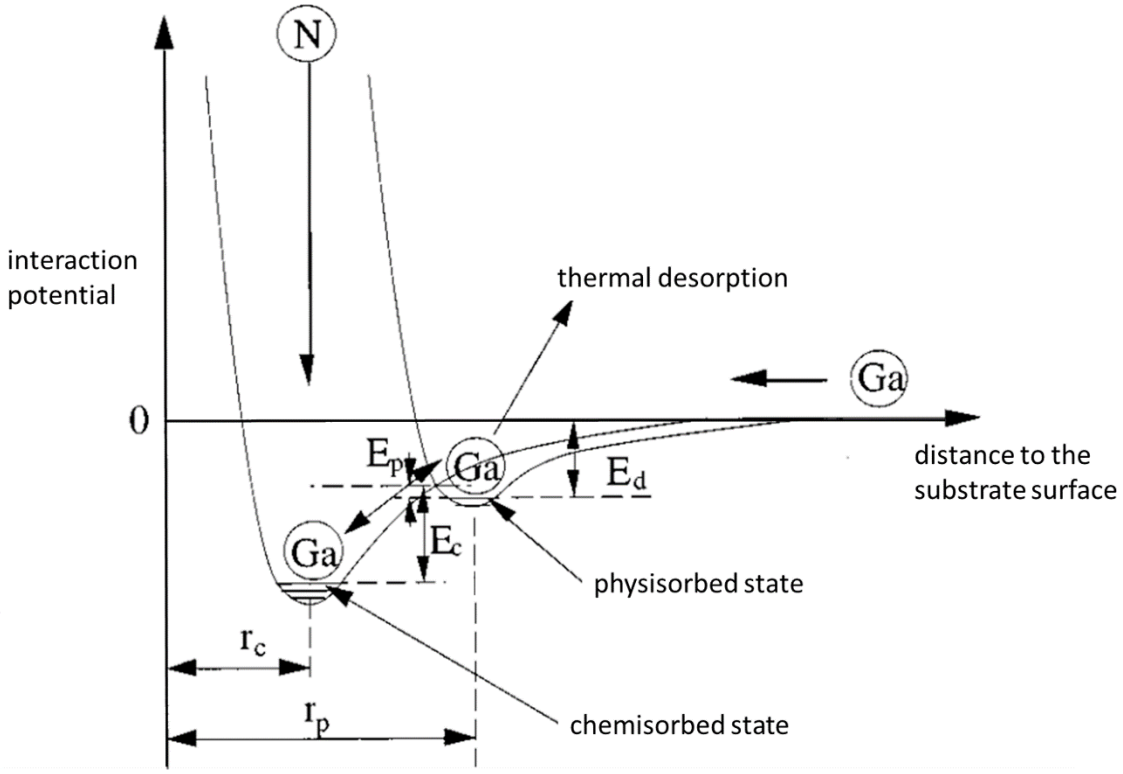

Figure 55 Schematic representation of the process occurring during a GaN layer growth. (Reproduced from **[226]**)

The impinging atomic nitrogen adhere to the growing surface, which is called adsorption. The impinging Ga atoms are also adsorbed but in weakly bound state. On the one hand, some of the Ga adatoms can be moved from this state to a chemisorbed state through the formations of new chemical bonds at the surface. On the other hand, some of the Ga adatoms as well as some of the chemisorbed Ga atoms can be transferred to a physisorbed state, where the electronic structure of the adatom is barely modified, and then be thermally desorbed from the surface. When a chemisorbed Ga atom meets an N atom, a GaN layer is formed.

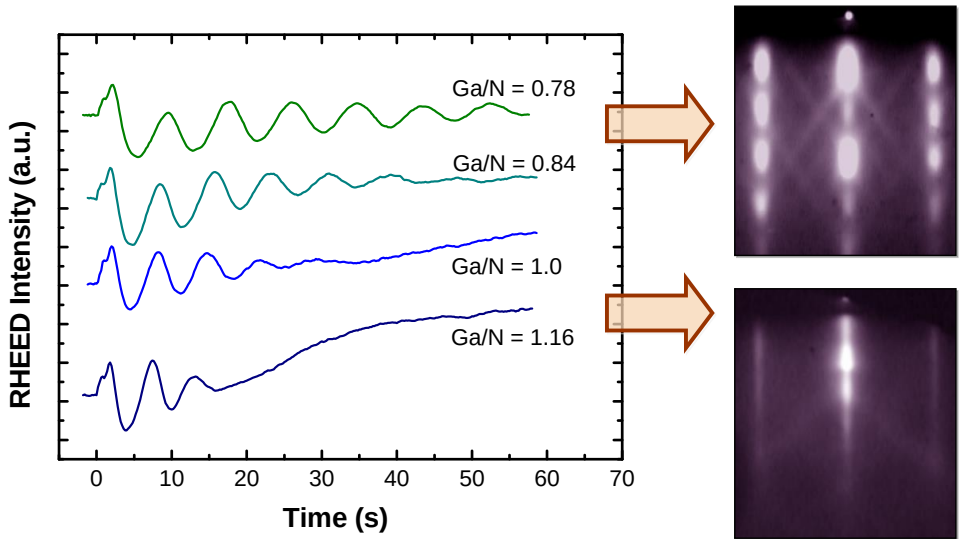

Figure 56 RHEED intensity oscillations and pattern at different III/V ratios.

The growth kinetics is determined by the control of the metal-to-nitrogen (III/V) flux ratio and the substrate temperature. As illustrated by Figure 56, GaN deposition under N-rich conditions occurs in a layer-by-layer mode, which starts with RHEED oscillations that attenuate as the surface roughness increases. After a few nanometers, the RHEED becomes spotty and the samples are facetted with a high surface roughness. As a result, the deposition of 2D GaN layers requires Ga-rich conditions. However, high Ga flux lead to the formation of metal droplets on the surface, which is also detrimental to the layer quality. To obtain GaN layers with smooth surface morphology, it is thus necessary to perform the deposition under slightly Ga-rich conditions. At growth temperatures which allow a certain Ga desorption rate, a Ga adlayer with a thickness independent of the Ga flux can be stabilized at the growing surface,. Thanks to the slight Ga excess, this Ga adlayer forms a laterally-contracted biatomic Ga layer, illustrated by Figure 57, which minimizes the (0001) surface energy and postpones the potential plastic and elastic relaxations, allowing to obtain smooth 2D GaN layer growth [224,227].

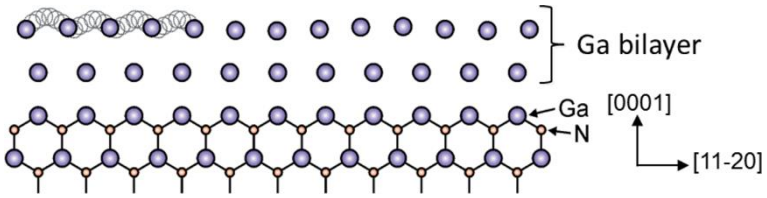

Figure 57 Schematic representation of the laterally-contracted Ga bilayer model **[228]**.

From ref. [222], there is a correlation between the Ga flux and the Ga coverage of the surface at a fixed substrate temperature. Using the RHEED, it is possible to quantify the amount of Ga adsorbed on a GaN epilayer by analyzing the Ga desorption transients. For this study, the GaN surface is first exposed for a short time to a Ga flux and a N flux to perform GaN growth. Then both fluxes are shuttered and the RHEED intensity is recorded during the Ga desorption from the GaN surface. The experiment is repeated for a fixed N flux and different Ga fluxes. After data processing, four regimes can be distinguished, as illustrated by Figure 58:

- Regime A: a small quantity of Ga is present on the GaN surface for a GaN growth rate $\Phi < 0.3$ ML/s.
- Regime B: less than 1 ML of Ga at the growth front is remained (0.3 ML/s $< \Phi < 0.5$ ML/s).
- Regime C: a bilayer of Ga (~2.4 MLs) at the growth front is formed for flux between 0.5 ML/s and 1 ML/s.
- Regime D: the system reaches the Ga accumulation regime (much Ga excess), leading to the formation of metal droplets for flux > 1 ML/s.

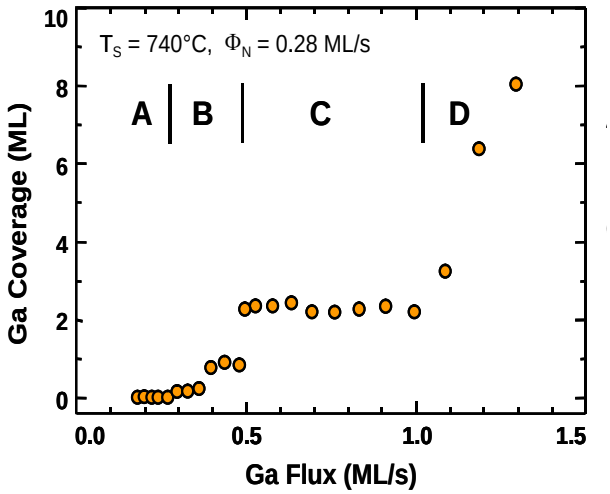

Figure 58 Ga coverage on top of the GaN(0001) surface as a function of the Ga flux. (Reproduced from **[204]**)

Figure 59 shows the Ga flux dependence on the substrate temperature. To keep a certain amount of Ga on the growing surface, the Ga flux should be increased as the growing surface temperature is raised up. Smooth GaN layers with atomic steps can be obtained during Ga-rich growth in the Ga bilayer regime. In practice, the optimum growth conditions correspond to the region of regime C at the limit with regime D, where a Ga bilayer is formed and Ga is close to accumulating at the surface.

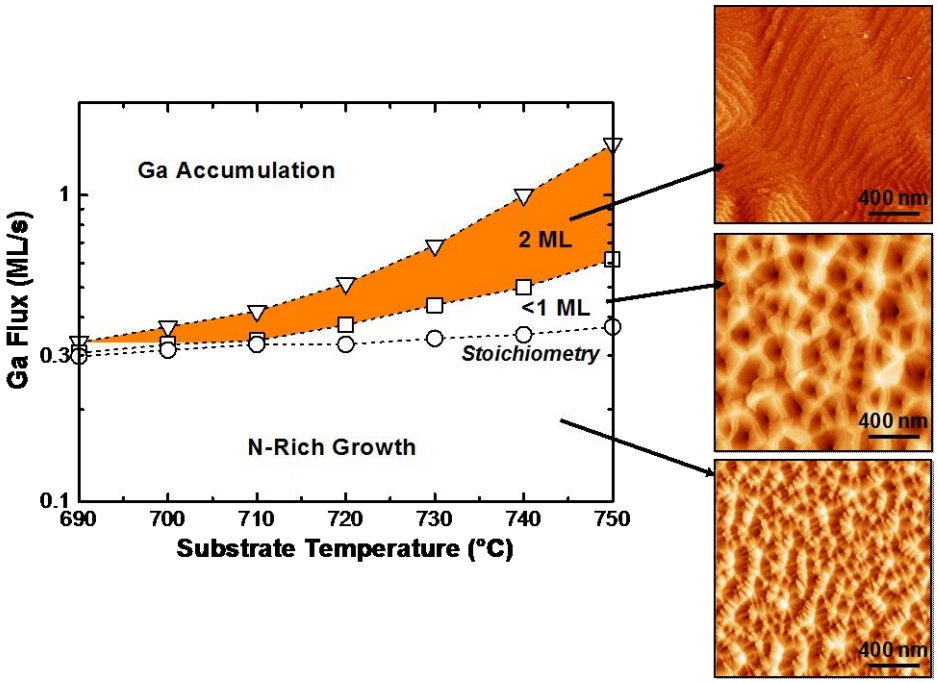

Figure 59 Ga coverage regimes as a function of both substrate temperature and impinging Ga flux.

The 2D growth of smooth *c*-plane AlN layers also requires metal-rich conditions. In case of Al excess on top of the epilayer, the RHEED pattern will show two extra lines along the <11-20> azimuth, which points to an Al layer with a smaller in-plane lattice constant compared to AlN. However, Al cannot be desorbed at the standard GaN growth temperatures (substrate temperature

~700°C). This is why a growth interruption under N is needed to eliminate any accumulated Al. Smooth AlN can also be deposited under stoichiometric growth conditions with excess of Ga on the growing interface in order to minimize the surface energy. The Ga – N bond is weaker than the Al – N bond, which is the reason why Al is preferentially incorporated.

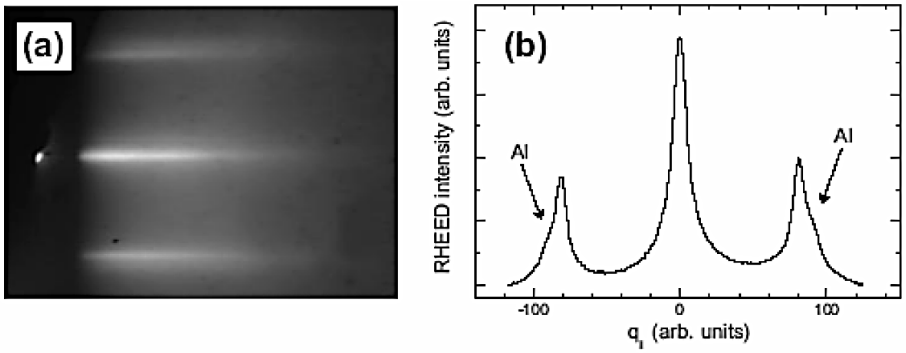

Figure 60 (a) RHEED pattern of an Al-rich AlN surface (azimuth <11-20>). (b) Intensity profile along the <11-20> direction. The extra streaks due to the Al excess are indicated by the arrows. (Reproduced from **[229]**)

The 2D growth of smooth *c*-plane AlGaN layers also requires Ga-rich conditions [230,231]. For Al contents < 50%, it is possible to obtain a layer-by-layer growth mode under slightly Ga-rich conditions. As the sticking coefficient of Al is unity (meaning that 100% of the Al atoms impinging on the surface adsorb onto the surface), we fixed the Al/N ratio at the required Al content and Ga is used in excess, to obtain a surfactant effect that favors 2D growth. For Al contents > 40%, it is necessary to decrease the substrate temperature to maintain a 2D growth. Reducing the growth temperature allows to balance the different diffusion barriers of Al, Ga and N.

2.3.5. Growth of semipolar and nonpolar GaN, AlN and AlGaN

From the previous subsections, the growth of 2D GaN(0001) with the best properties is achieved under the self-regulated regime of the Ga bilayer, right before Ga accumulation. To perform growth on a different crystallographic orientation, it is thus assumed that such a Ga excess is also needed. In the case of semipolar GaN(11-22), the maximum Ga coverage that can be stabilized on the surface without Ga accumulation is about 1.05 ± 0.10 ML, and the accumulation regime is reached at a lower Ga flux than in the case of GaN(0001) [232]. This is shown by Figure 61.

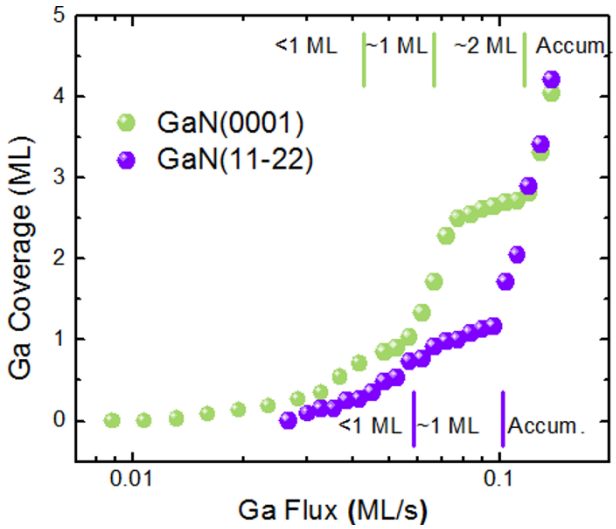

Figure 61 Ga coverage of polar GaN(0001) and semipolar GaN(11-22) surfaces in function of the Ga flux. (Modified from **[232]**)

Regarding nonpolar materials, studies on the growth process of *a*- and *m*-plane GaN were carried out. According to the PhD work of S. Founta (2007), the maximal Ga coverage that can be stabilized on the surface of *a*-plane GaN is less than 1 ML, and self-regulated growth conditions equivalent to the Ga bilayer on GaN(0001) do not exist for plasma-assisted MBE growth of *a*-plane GaN. Based on the PhD work of B. Amstatt (2008), a self-regulated Ga adlayer of 2 ± 0.3 ML can be stabilized on the surface of *m*-plane GaN. Compared to GaN(0001), this bilayer regime is shifted towards higher Ga flux, meaning that it requires higher Ga-rich conditions.

At the beginning of my PhD thesis, high-quality free-standing nonpolar GaN substrates were made available and were used in this work, allowing to obtain better structural quality as compared to heteroepitaxy of nonpolar GaN on foreign substrates.

2.4. Characterization techniques

In this section, all characterization techniques used in this work are described. It includes the ones I used (atomic force microscopy, high-resolution x-ray diffraction, photoluminescence, Fourier transform infrared spectroscopy, Hall effect) and some that I did not use personally, but are important for the interpretation of the results (scanning and transmission electron microscopy, cathodoluminescence).

2.4.1. Atomic force microscopy

The surface morphology of the grown samples was assessed by atomic force microscopy (AFM) in the tapping mode, using a Dimension 3100 system. The obtained images were processed using the WSXM free software [233]. The schematic of the AFM setup is illustrated in Figure 62.

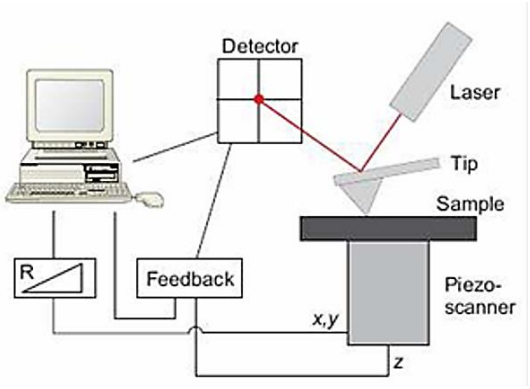

Figure 62 Schematic of the AFM setup.

The probe tip is integrated into a cantilever which is sensitive to the forces between the sample surface and the tip. In the tapping mode, the cantilever is forced to oscillate at its resonant frequency $\omega_0 = \sqrt{\alpha_3/\mathrm{m}}$, α_3 being a constant, m being the cantilever mass. The probe lightly "taps" on the surface during the scanning, making the contact between the surface and the bottom of its swing. In this mode, the gradient of the force $\left(\frac{\partial F}{\partial z}\right)$ affects the oscillation frequency which becomes $\omega = \omega_0\sqrt{1 - \frac{1}{k}\frac{\partial F}{\partial z}}$. When the tip approaches the surface, the oscillation amplitude decreases rapidly. By maintaining a constant oscillation amplitude, a constant tip-sample interaction is maintained, and an image of the surface morphology is obtained.

The minimum force that can be detected is $\left(\frac{\partial F}{\partial z}\right)_{min} = \frac{1}{A_{osc}}\sqrt{\frac{4B_d\alpha_3 kT}{\omega_0 Q}}$, where A_{osc} is the root mean-square (RMS) oscillation amplitude, B_d is the detection bandwidth, $Q = \Delta\omega/\omega$ is the quality factor of the resonance.

2.4.2. High-resolution x-ray diffraction

X-ray diffraction (XRD) is a non-destructive tool used to characterize the structure of ordered materials. In this work, the structural quality and thickness of the epitaxial layers were assessed using:

- a Seifert XRD 3003 PTS-HR diffractometer with a beam concentrator in front of a 2- or 4- bounce Ge(220) monochromator and a 0.15° long plate collimator in front of the detector (samples of sections 4.3, 4.4)
- a PANalytical X'Pert PRO MRD system (samples of sections 3.1, 3.2, 4.5, 4.6) in collaboration with J. Schörmann (Justus-Liebig-Universität Giessen, Germany)
- a Rigaku Smartlab x-ray diffractometer system with a 4-bounce Ge(220) monochromator and a 0.114° collimator in front of the detector (samples of sections 3.1, 4.5, 4.6, 4.7), illustrated by Figure 63.

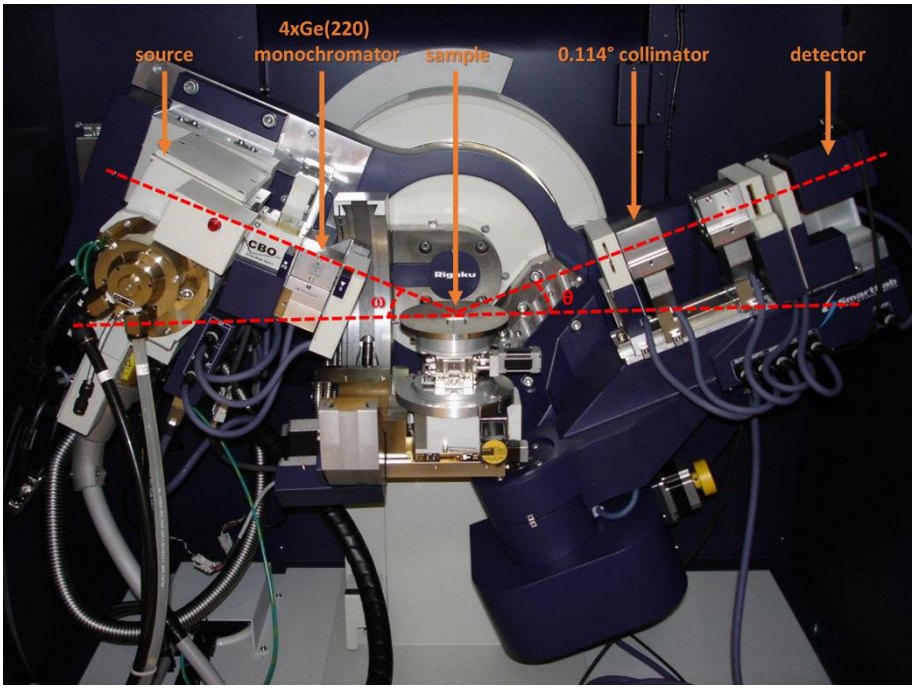

Figure 63 The Rigaku Smartlab system in the used configuration.

The x-ray source is an evacuated tube in which electrons are emitted from a heated tungsten filament and accelerated by an electric potential (~40 kV) to finally impinge on a Cu target. The x-ray wavelength is $\lambda_{XRD} = 0.154056$ nm and corresponds to the $k_{\alpha 1}$ emission line of Cu. The x-ray beam coming out from the source is reflected and converted into a parallel beam by a parabolic mirror. A beam of parallel (0.01° divergence) and monochromatic x-rays is incident on a crystal at the angle ω_i, which is the angle between the sample plane and the incident beam. Since the crystal has a periodic structure, we can apply the Bragg's law: $2d \sin \omega_i = n\lambda_{XRD}$, where n is an integer and d is the interplane spacing. A highly parallel and monochromatic incident x-ray beam is achieved by using one or two monochromators each consisting of two Ge(220) monocrystals. So called "2-crystal" or "4-crystal" scheme (-n, +n, +n, -n) results in an x-ray beam with a wavelength spread $\Delta\lambda_{XRD}/\lambda_{XRD} = 2.2 \times 10^{-5}$ and divergence $\Delta\Theta = 0.0033°$.

The sample is placed on a monocrystalline Si plate to minimize the background noise. However, the sample surface rarely corresponds to the epitaxial planes due to the substrate miscut. In order to choose a proper plane family, we need to align the epilayers plane with the optical axis of the setup, as illustrated in Figure 65. To do so, the sample position is precisely controlled with 4 possible angular rotation mechanisms: 3 sample's rotations (ω, φ, χ) and 1 detector's rotation (2θ), as described in Figure 64.

The detector aperture is 2°, which can be reduced by inserting slides in order to enhance the resolution, which in turn reduces the intensity.

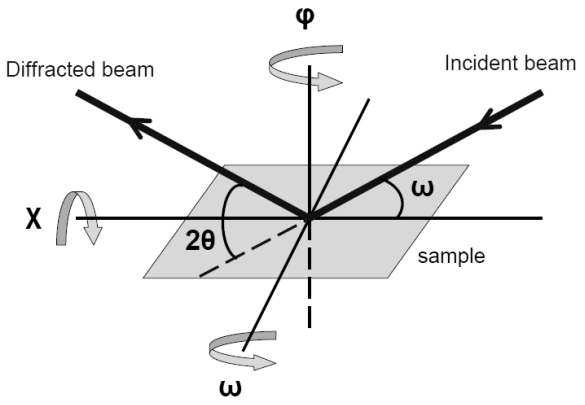

Figure 64 Schematic of all the rotation angles: ω is the angle defined by the incident beam and the sample surface, φ is the angle of in-plane rotation, χ is the angle of off-plane rotation, and θ is the angle defined by the detector direction and the sample surface.

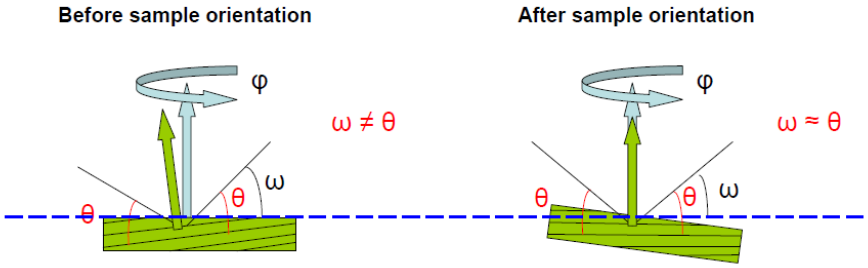

Figure 65 Schematic of the sample orientation: after orientation, the atomic planes normal is parallel to the φ-axis.

To obtain high-resolution XRD (HR-XRD), a 0.114° collimator or a Ge(220)x2 analyzer, to measure either nonpolar or polar samples respectively, is placed between the sample and the diffracted beam, it improves the angular precision of the diffracted beam (<0.001°). In this configuration, the direct beam intensity is higher than 10^6 counts per second (cps) and the noise is about 1 cps.

In this work, we will measure ω-2θ scans, ω-scans and reciprocal space maps. The MQWs period P_{MQW} can be extracted from the angular separation of two MQW satellites in the ω-2θ scans:

$$P_{MQW} = \frac{\pm n\lambda_{XRD}}{2(\sin\theta_{\pm n} - \sin\theta_0)} \quad (88)$$

where θ_0 and $\theta_{\pm n}$ are the zero-order and ±m-order MQW satellites.

Information on the mosaicity and crystalline quality of the structures can be extracted from the ω-scans (also called "rocking curves"), measured at a fixed value of 2θ. The lower the ω-scan FWHM the better the crystalline quality. And the strain states can be extracted from the reciprocal space maps. It is important to note that the XRD provide information on the average periodic structure. To obtain local information (like an estimation of local thickness fluctuations), transmission electron microscopy is used.

2.4.3. Photoluminescence

Photoluminescence (PL) spectroscopy is a non-destructive tool for probing the ground electronic states in a semiconductor structure. To obtain PL from the probed sample, the material

must be excited by a laser with an energy exceeding the semiconductor bandgap. The absorption of light in the sample results in a transfer of electrons from the valence to the conduction band. The return to equilibrium occurs via non-radiative processes (phonon emission) or radiative processes (photon emission). The absorption and carrier relaxation mechanisms must respect the energy and momentum conservation rules, and since III-nitride materials have direct bandgaps, both the photon absorption and emission conserve the momentum, *i.e.* phonons are not required to assist the process. Besides energy bandgap, PL spectroscopy can provide information about the electron and hole confinement states in the QWs, the presence of donor and acceptor levels in the bandgap due to the presence of impurities, defects in the material or alloy inhomogeneities. The broadening of the PL peak also gives information on the crystal quality.

Figure 66 shows a schematic of the PL measurement setup used in this work. The excitation of III-nitride structures was mostly performed by a continuous-wave frequency-doubled Ar laser (λ_{PL} = 244 nm) with an excitation power around 100 µW focused on a spot with a diameter of ≈ 100 µm. The emission from the sample was collected by a Jobin Yvon HR460 monochromator equipped with an ultraviolet-enhanced charge-coupled device (CCD) camera.

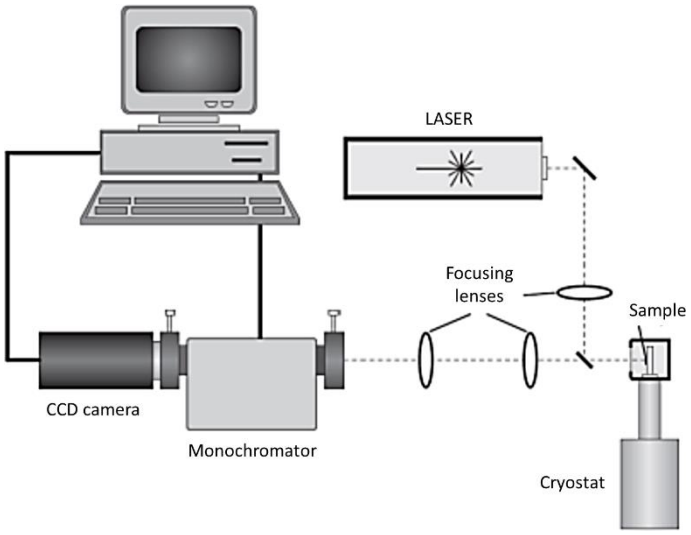

Figure 66 Schematic of the PL setup.

Time-resolved PL (TRPL) was also used to study carrier relaxation processes (section 3.2). In that case, the material is excited by a laser pulse and we analyze the evolution of the PL emission intensity in function of time. The excitation source was a frequency-tripled Ti:sapphire excitation laser (λ_{TRPL} = 270 nm) with a pulse width of 200 fs. This laser was equipped with a cavity damper section with a base pulse repetition rate of 54 MHz. This allowed the period between pulses to be varied from 20 ns to 5 µs. The excitation power was about 500 µW. The luminescence was dispersed by a Jobin Yvon Triax320 monochromator and was detected by a Hamamatsu C−5680 streak camera.

In both PL and TRPL experiments, the samples were mounted on a cold finger of a He cryostat.

2.4.4. Fourier transform infrared spectroscopy

Fourier transform infrared spectroscopy (FTIR) is a spectroscopy technique using IR light to assess the absorption, emission or photoconductive properties of semiconductor heterostructures. The equipment used in this work is a Bruker V70v spectrometer, used in the transmission mode and

represented in Figure 67. It is equipped with an interferometer, sources, beamsplitters (BS) and detectors to cover the whole IR spectrum. During measurement, the whole setup can be kept under vacuum at ~10^{-1} mbar. This allows to avoid absorption lines from the atmosphere: air humidity and CO_2 mostly, as illustrated in Figure 68.

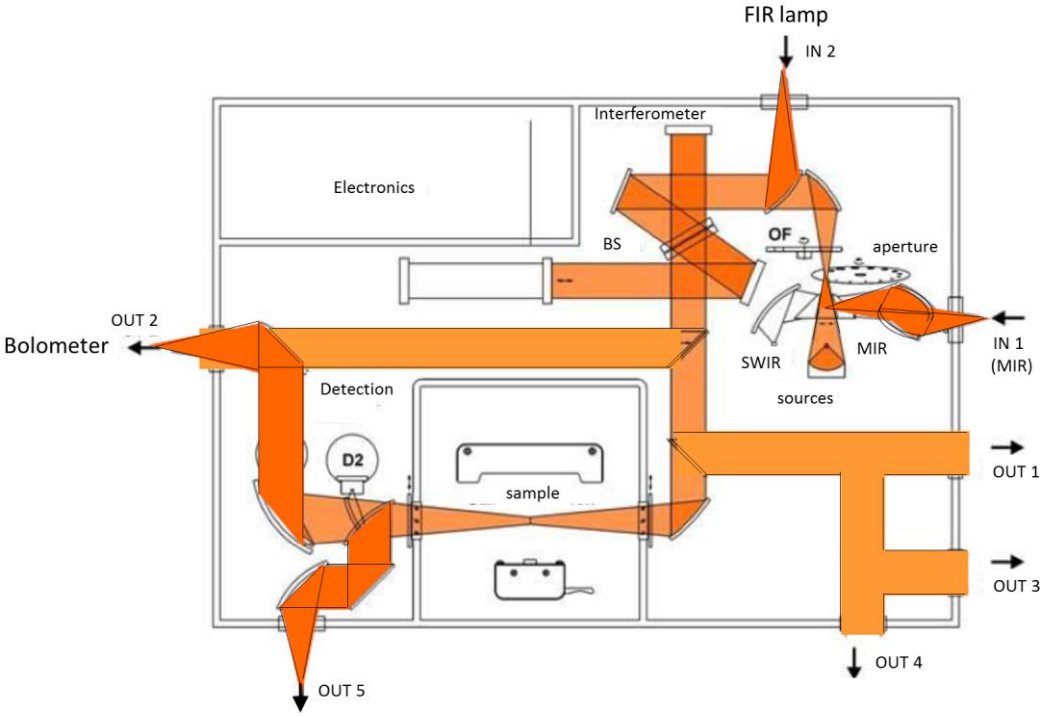

Figure 67 Schematic of the FTIR setup in the transmission mode.

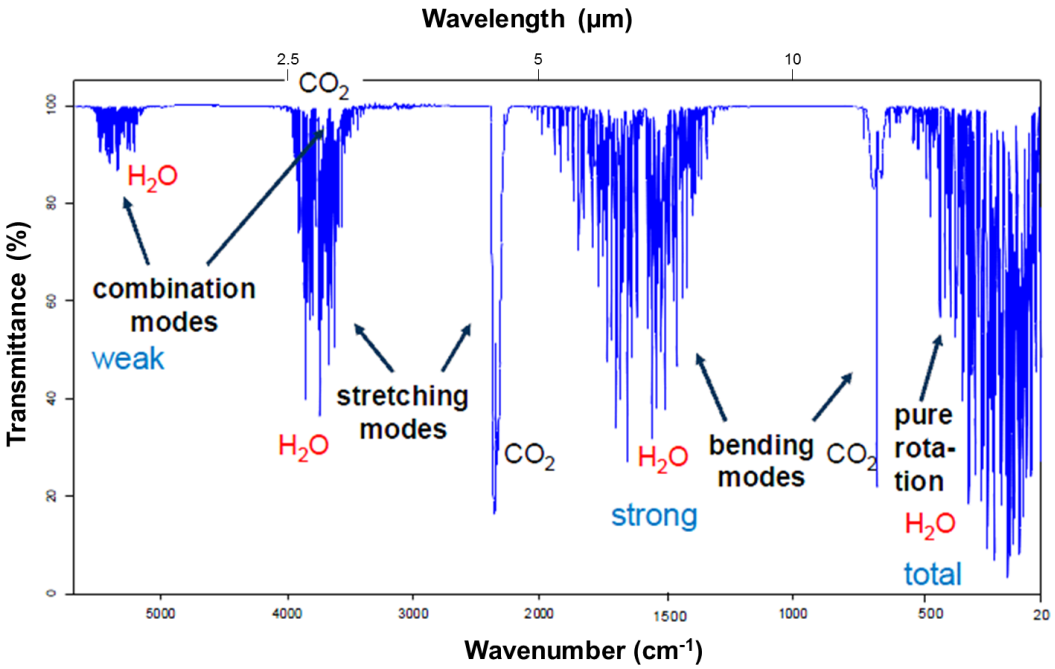

Figure 68 Atmosphere absorption lines in the IR window.

To discern between the TE and the TM polarized light, we choose the polarizer and beam-splitter adapted to the targeted IR region. For characterization in the SWIR and MIR ranges, it was equipped with a halogen lamp source, a CaF2 or a KBr beamsplitter, respectively, and a liquid

nitrogen-cooled mercury-cadmium-telluride detector. For characterization in the FIR, we used a mercury lamp source, a Si beam splitter and a helium-cooled Si bolometer.

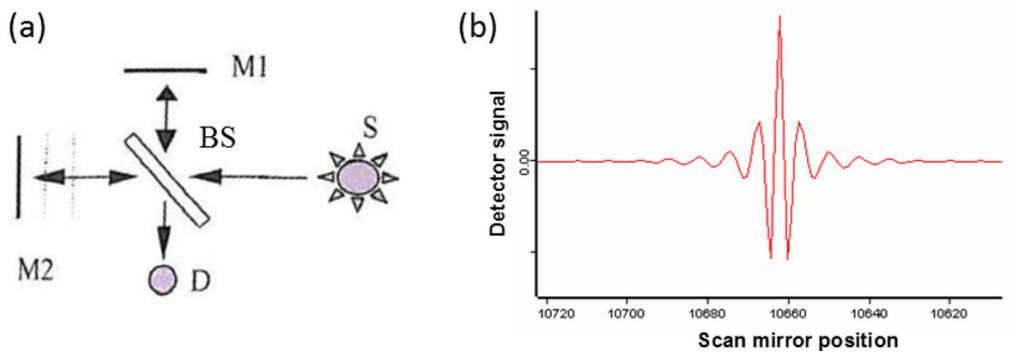

Figure 69 (a) Schematic of the Michelson interferometer (b) Interferogram displayed by the detector.

The working principle of the FTIR spectrometer is based on the Michelson interferometer, represented in Figure 69 (a). In consists of a source (S), a detector (D), a beam splitter (BS), a fixed flat mirror (M1) and a moving flat mirror (M2). Ideally, the beam splitter transmits 50% of the incident radiation and reflects the other 50%. That way, the beam splitter separates the source IR light into two optical beams: one is transmitted through and reflects off of the flat fixed mirror M1, and the other one reflects off of the beam splitter to the mirror with constantly moving mechanism M2. The beams reflected from the mirrors M1 and M2 are recombined at the beam splitter. As the moving mirror M2 travels back and forth, various wavelengths of light go in and out of phase. By recording the signal received by the detector at different precise intervals, the raw data for the interferogram is generated, as shown in Figure 69 (b). The main peak of highest intensity corresponds to the interference of two beams with zero optical path difference. The reduction of the distance between the fringes when the path difference is increased makes them more difficult to see. The interferogram is then converted into an absorption spectrum using Fast Fourier Transform algorithm.

In the FTIR though, the flat mirrors are replaced by cube corner mirrors. These mirrors are practically immune to mirror tilt, as shown in Figure 70, allowing the interferometer to have a stable permanent alignment. This way, the light can recombine precisely at the beam splitter, and the stability, resolution, spectral quality, and thus signal-to-noise ratio are maximized.

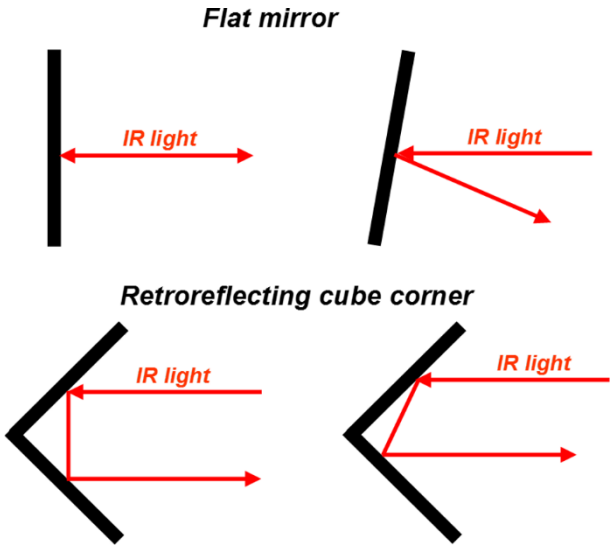

Figure 70 Effect of mirror tilt on a flat mirror and on a cube corner mirror.

To measure FTIR spectroscopy, we must take into account the selection rules for ISB transitions explained in section 1.3.2. The ISB absorption being associated only with light polarized perpendicular to the QWs, the samples must be prepared in a special geometry.

The samples facets were mirror-polished at 45° when using bulk GaN or sapphire-based substrates, and at 30° when using Si-based substrates. Also when it was not already the case (sapphire-based and Si-based templates), the back face of the samples was mirror-polished. This polishing form a multipass waveguide configuration allowing 4-5 interactions of the incident light with the active region. For characterization in the FIR range, two pieces of each sample were polished and placed face-to-face on the cold finger of a helium liquid-cooled cryostat to increase the signal-to-noise ratio. In the case of SWIR and MIR characterization, only one piece of each sample was polished and simply placed on the sample holder of the FTIR sample compartment. Figure 71 illustrates these configuration in the case of a 45° polishing.

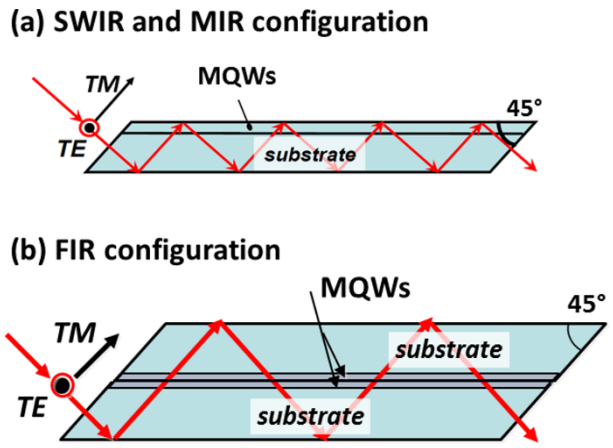

Figure 71 Multipass waveguide configurations in the case of 45° polishing for measurements (a) in the SWIR and MIR and (b) in the FIR.

2.4.5. Hall effect

Hall effect measurements were used to calibrate the doping densities in reference GaN:Si and GaN:Ge layers. Basically, the Hall effect can be observed when the combination of a magnetic field through a sample and a current along the length of the sample creates an electrical current. This resulting electrical current is perpendicular to both the magnetic field and the current. An illustration is shown in Figure 72. Due to the Lorentz force, this generates a transverse voltage in the semiconductor material, and the voltage is perpendicular to both the magnetic field and the current.

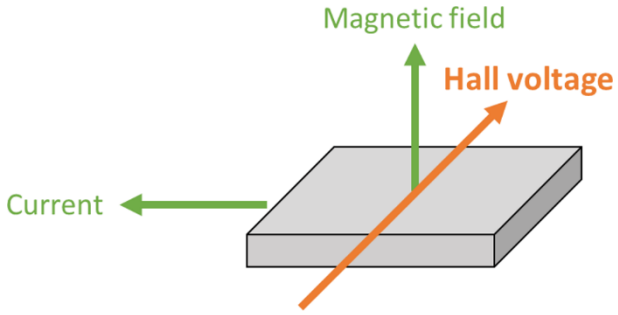

Figure 72 Illustration of the Hall effect

2.4.6. Scanning electron microscopy

Scanning electron microscopy (SEM) is a microscopy technique based on the interaction of an electron beam and the scanned surface of a sample. The particularity of electron microscopy compared to optical microscopy is the much higher resolution, due to the smaller electrons wavelength (about 0.1 nm). Information about the sample's surface morphology is obtained. In this work, the measurements were performed in collaboration with J. Lähnemann using a Zeiss Ultra 55 microscope.

2.4.7. Transmission electron microscopy

Transmission electron microscopy (TEM) is a microscopy technique based on the transmission of an electron beam through a sample. The measurements in this work were performed in collaboration with C. Bougerol in an FEI Titan Ultimate microscope operated at 200 kV.

Several TEM techniques were used and gave access to different types of information:

- High-resolution TEM (HR-TEM): heavier atoms and thicker regions appear darker. The high resolution makes it possible to reach the atomic scale. However, no direct interpretation of the images can be done due to the influence of thickness and defocus.
- High angle annular dark field scanning transmission electron microscopy (HAADF-STEM): the contrast in the image is due to the chemical nature of the atoms (proportional to $Z^{1.7}$, Z being the atomic mass). There is no diffraction contrast, it is possible to reach the atomic scale, and we can directly interpret the images.
- Energy-dispersive x-ray spectroscopy (EDX): used to perform a quantitative analysis of the samples chemical composition. It is used for elements heavier than Carbon, and offers a resolution of ≈ 100 eV. However it is sensitive to thickness effects.

If the observation is non-destructive, the samples need to be prepared so that its thickness does not exceed 300 nm to allow the electron beam to pass through. In this work, the planar samples were prepared by focus ion beam (FIB) and the nanowires were directly scratched from the substrate with a holey carbon TEM grid.

2.4.8. Cathodoluminescence

Cathodoluminescence (CL) is the photon emission from a material excited by a high-energy electron bombardment beam. The sample is placed in an electron microscope system and the photoemission is collected for each excitation point. As a result, the spatial resolution is limited by the exciting electron beam, and is around 10 nm in our equipment. However, our materials being semiconductors makes it possible for excitons to diffuse and for secondary electrons to contribute to the excitation. This result in the excitation points being defined with a lower spatial resolution than ideally considered. To limit these diffusion effects, the acceleration voltage needs to be kept at a rather low value.

In this work, measurements were performed in collaboration with J. Lähnemann to assess the homogeneity of the planar MQWs structures, in an FEI Inspect F50 fitted with a homemade CL system, using an acceleration voltage of 5 kV and a current of about 10 pA. The emission from the sample was collected by a parabolic mirror and thereby focused onto a Horiba Jobin Yvon iHR550 monochromator equipped with a CCD with an integration time of 1 s per spectrum.

Growing. Watching. Hope
Will be caught with IR light
At MBE's will

Chapter 3.
Germanium and silicon doping

In this chapter, we assess the effect of doping on the structural and optical properties of polar c-plane GaN/AlGaN multi-quantum wells, designed to show intersubband absorption in the short-wavelength, mid- and far-infrared ranges. We first explain the issues related to silicon doping, and then introduce germanium as an alternative dopant. As an example of the interest of germanium doping, we study its effect on the optical characteristics of GaN/AlN nanowires. Finally, we compare the optical and structural properties of c-plane GaN/AlGaN multi-quantum wells doped with different concentrations of silicon and of germanium.

Introduction for Newbies: To allow ISB transitions, the ground confined state of the quantum well needs to be populated with electrons. Therefore, it is necessary to n-dope the active region, by introducing the dopant either in the barriers or in the wells. The first issue of this chapter concerns the nature of the dopant. Silicon is the most commonly used n-type dopant in GaN, but it comes with several limitations which could be overcome by using germanium instead. We need to determine in what extent germanium doping of GaN would be relevant for our application. To do so, in the first part of this chapter, we assess the possibility of using germanium as a dopant for GaN, and study the screening of the internal electric field in Ge-doped GaN/AlN nanowires as an example. The second issue of this chapter concerns the dopant concentration. On the one hand, "high" doping densities are required to obtain enough carriers and efficient ISB absorption. On the other hand, too high dopant concentrations may lead to the formation structural defects and the degradation of the optical properties due to many-body effects. Looking for the optimum doping density, we have studied the structural and optical properties of polar *c*-plane GaN/AlGaN heterostructures with ISB absorption in the short-wavelength and mid-infrared, for different doping densities of silicon and germanium.

For the study of germanium as an alternative dopant for GaN (section 3.1), I performed XRD measurements and helped with the MBE growth, working in collaboration with A. Ajay (MBE growth, Hall effect, PL measurements), M. Jiménez-Rodriguez (AFM), and J. Schörmann (XRD). The complete study was published in "Ge doping of GaN beyond the Mott transition", A. Ajay *et al.*, J. Phys. D: Appl. Phys. **49** 445301 (2016) [234].

For the study of the screening of the electric field in Ge-doped GaN/AlN NW heterostructures (section 3.2), I was in charge of the PL measurements, and worked in collaboration with M. Beeler (TRPL measurements and simulations). The samples were grown at the University of Giessen, under the supervision of Prof. Martin Eickhoff. The complete study was published in "Long-lived excitons in GaN/AlN nanowire heterostructures", M. Beeler *et al.*, Phys. Rev. B **91**, 205440 (2015) [235].

For the study of Ge and Si-doped *c*-GaN/Al(Ga)N MQWs with ISB transitions in the near- and mid-infrared (sections 3.3 and 3.4), I was in charge of the PL, FTIR and XRD measurements, and worked in collaboration with A. Ajay (MBE growth), who also helped me with the FTIR measurements.

3.1. Germanium as an alternative dopant for GaN

Silicon has been the preferred n-type dopant for wurtzite GaN so far, even though it contributes to the formation of edge-type dislocations and leads to an increase in tensile stress [236–238]. Tensile strain is particularly problematic when growing GaN on silicon substrates, because the mismatch between their thermal expansion coefficients favors the generation of cracks [239]. In addition, Si doping densities exceeding 10^{19} cm^{-3} induce surface roughening and eventually crack propagation [237]. Concerning the doping of NW structures with Si, the radial distribution of Si is inhomogeneous, with a tendency to migrate towards the sidewalls [240], and high doping levels degrade the NW morphology [241]. This is why germanium has been recently introduced as an alternative to Si as n-type dopant for GaN, with the possibility for higher doping densities [237,238].

Ge and Si have theoretical activation energies of 31.1 meV and 30.8 meV, respectively [242]. Structurally, the ionic radius of a Ge atom is similar to that of Ga, and the metal-nitrogen bond length changes by only 1.4% with Ge, compared to 5.5% with Si [243]. For these reasons, the Ge occupancy of the Ga lattice site is expected to induce far less lattice distortion compared to Si.

Successful Ge-doping of GaN using HVPE [244,245] and MOVPE have been demonstrated [246–249], and recent results confirm the possibility of reaching high carrier concentration in GaN on Si(111) substrates without producing any additional tensile stress [238,248]. Using plasma-assisted MBE, free carrier concentrations up to 4×10^{20} cm^{-3} were reported in thin films [250,251], and Ge-doped NWs achieving significant dopant levels (up to 3.3×10^{20} cm^{-3}) and metallic conductivity were demonstrated [252,253].

However, at the beginning of my PhD work, extensive understanding of the effect of Ge-doping on the growth kinetics and on the optical and electrical properties of GaN:Ge was still needed to be able to use efficiently Ge as a dopant. As explained in Chapter 2, the growth of two-dimensional GaN by plasma-assisted MBE is associated to the presence of a Ga bilayer on top of the growing surface [222]. The presence of dopants can disturb the formation and behavior of this Ga bilayer, with direct consequences on the structural quality of the grown sample. For instance, Si has no effect on the growth kinetics, whereas the segregation of Mg on the growing surface hinders the formation of the bilayer, which ultimately leads to a reduction of the range of acceptable Ga fluxes to achieve two-dimensional growth of GaN [254–256].

3.1.1. Effect on the growth kinetics of GaN

As detailed in Chapter 2, non-intentionally doped (n.i.d.) GaN is grown by plasma-assisted MBE under slightly Ga-rich conditions, with the formation of a self-regulated Ga bilayer on top of the growing surface [222]. To assess the effect of the Ge flux on the growth kinetics, we studied the Ga desorption process from the (0001) surface of GaN:Ge during a growth interruption, which provides direct information on the thickness of the Ga adlayer during growth. To do so, we measured the RHEED intensity transient generated by the Ga desorption during a growth interruption (shuttering the Ge, Ga and N cells simultaneously) after deposition of 7 nm of GaN:Ge, and repeated the experiment for various Ge fluxes [234]. After each measurement, we grew 7 nm of n.i.d. GaN and recorded the Ga desorption transient from the undoped surface as a reference.

During the above-described experiment, the growth rate was 0.5 ML/s, *i.e.* 450 nm/h. The growth temperature was T_s = 720°C, verified by measurement of the Ga desorption time from the GaN (0001) surface [160], the Ge cell temperature was varied from T_{Ge} = 720°C to T_{Ge} = 1000°C.

For these experiments, the Ga flux was set around 0.7 ML/s, which ensured a dynamically stable Ga bilayer during the growth while working at the limit of Ga accumulation (note that Ga accumulation on the growing surface takes place when increasing the Ga flux only by 7%).

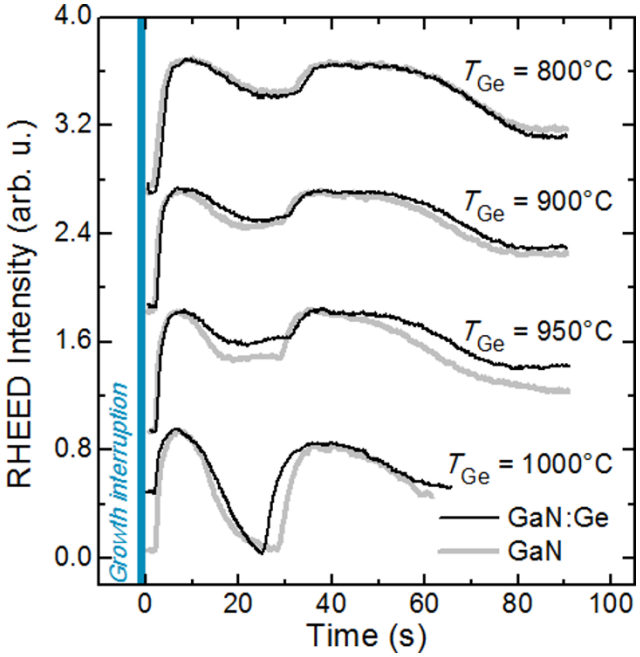

Figure 73 RHEED intensity oscillations during the Ga desorption after the growth of non-intentionally doped GaN and of GaN:Ge for different Ge cell temperatures. (Modified from ref. **[234]**)

Figure 73 presents the RHEED intensity transient generated by the Ga desorption, recorded after the growth of n.i.d GaN, and after the subsequent growth of Ge-doped GaN, for T_{Ge} = 800°C, 900°C, 950°C and 1000°C. The growth was interrupted at time t = 0. As we can see on the measurements for undoped GaN (our reference), the shape of the RHEED transient during Ga desorption can change during the growth. This can be due to a modification of the surface morphology during the growth, a change in the position of the sample, a change in the angle of incidence of the RHEED electron beam, or the choice of the analyzed section of the RHEED pattern (which indeed is the same for all measurements in this study). In contrast, variations of the desorption time, *i.e.* the duration of the transient, are due to changes in the sample temperature or in the amount of Ga accumulated on the surface. When comparing the two measured RHEED transients at a fixed Ge cell temperature under our experimental conditions, the drifts due to substrate temperature and relative position of the RHEED and the surface are negligible, and the differences are only due to the surface morphology and amount of Ga on the surface. This is not true if we compare the transients associated to different temperatures of the Ge cell, due to both the necessary delay between measurements, and the difficulty to guarantee that the relative position of RHEED and sample surface remain stable during long runs (minutes).

As shown in Figure 73, for each Ge cell temperature, the RHEED intensity first increases sharply at the growth interruption, which indicates that there is no accumulation of Ga, which would lead to the formation of droplets or clusters. Then, for all values of T_{Ge}, the evolution of the RHEED intensity after the growth interruption presents two distinct oscillations in both cases of growth with and without Ge. Comparing the RHEED transients with and without Ge, the difference in the time to the first inflection point is lower than 1 s, which corresponds to a difference in the Ga coverage during growth lower than 0.5 ML. This is why we can conclude that the presence of a Ge flux does not affect

the RHEED intensity transients, *i.e.* Ge incorporation does not disturb the Ga kinetics on the GaN (0001) growth surface.

3.1.2. Effect on the structural quality

Following these experiments, we grew 675 nm-thick Ge-doped GaN thin films on 1 µm-thick AlN-on-sapphire templates, under the described growth conditions and for various values of T_{Ge}, as detailed in Table 11. As illustrated in Figure 74, all samples present monoatomic terrasses and hexagonally-shaped hillocks, characteristic of plasma-assisted MBE-grown GaN, without observation of cracks or pits. For all the samples, the RMS roughness measured in 5 × 5 µm^2 AFM images is 0.9 ± 0.3 nm and the density of hillocks is (1.0 ± 0.6) × 10^6 cm^{-2}. We can hence conclude that there is no significant effect of Ge doping on the surface morphology, in contradiction to SEM observations reported in [250].

Table 11 Description of the samples under study: temperature of the Ge cell during growth and free carrier concentration measured by Hall Effect.

Sample	T_{Ge} (°C)	Free carrier concentration (× 10^{18} cm^{-3})
E3495	720	0.78 ± 0.07
E3496	760	1.0 ± 0.1
E3482	800	2.4 ± 0.2
E3483	850	13 ± 1
E3484	875	31 ± 3
E3480	900	68 ± 7
E3485	925	150 ± 20
E3481	950	260 ± 30
E3487	1000	670 ± 70
E3488	(n.i.d.)	

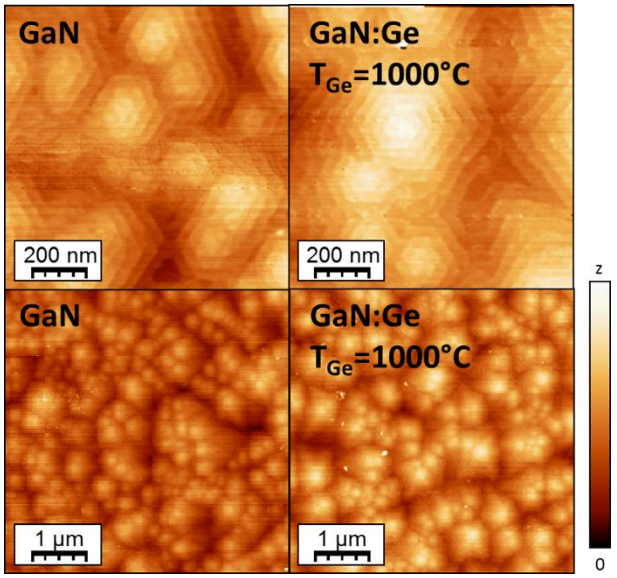

Figure 74 AFM images of n.i.d. and Ge-doped GaN thin films. [Modified from **[234]**]

We further assessed the samples structural quality by HR-XRD. The average strain of the GaN *c* lattice parameter extracted from the ω-2θ scans of the (0002) GaN reflection was ε_{zz} = 0.22 ± 0.07%, without any clear trend as a function of the Ge density. This tensile strain along *c*

results from the compressive in-plane strain imposed by the AlN substrate, in good agreement with [227]. The FWHM of the ω-scans of the (0002) reflection of GaN:Ge remain in the 190 ± 110 arcsec range, without any systematic influence of Ge-doping. Instead, the broadening of the ω-scans follows the same variation trend as the corresponding AlN substrates, *i.e.* the GaN mosaicity depends more on the substrate quality than on the Ge-doping density.

3.1.3. Effective dopant incorporation

Hall Effect measurements at 300 K were performed to assess the effective incorporation of Ge, and free carrier concentrations of up to $n_{3D} = 6.7 \times 10^{20}$ cm^{-3} were obtained for the sample grown with the highest Ge cell temperature (T_{Ge} = 1000°C).

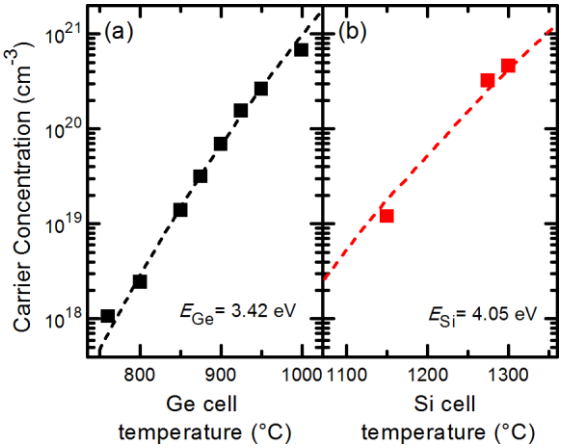

Figure 75 (a) Free carrier concentration measured by Hall effect as a function of the Ge cell temperature. The dashed line is a fit to Eq. (89) (b) For reference, free carrier concentration as a function of the Si cell temperature. (Modified from **[234]**)

As illustrated in Figure 75 (a), the free carrier concentration scales exponentially with T_{Ge} in the range of T_{Ge} under study, following:

$$n_{3D} \propto \exp(-E_{Ge}/kT_{Ge}) \qquad (89)$$

where E_{Ge} = 3.42 eV [257] is the thermal evaporation energy of Ge, and k is the Boltzmann constant. The fit is plotted in dashed line. This is also true for Si doping, as illustrated in Figure 5(b), with E_{Si} = 4.05 eV [257]. From the good agreement between the obtained fits and the experimental data, we can consider that the free carriers result only from the incorporation of Ge and Si, respectively.

We also notice that during the study, the Si cell temperature remains below the Si melting point (at 1414 °C), whereas the melting point of Ge (at 938.2 °C) is crossed, yet without showing any effect on the free carrier concentration measurement.

3.1.4. Effect on optical properties

The PL emission spectra were measured at 5 K and at room temperature, and are shown in Figure 76 (a) and (b), respectively. The PL spectra at 5 K of n.i.d GaN show near-band-edge excitonic emission around 3.515 eV, blue-shifted with respect to the theoretical value (in the range of 3.470 eV in bulk GaN) due to the in-plane compressive strain induced by the AlN substrate. At both low and

room temperatures, increasing the Ge concentration induces first a redshift (T_{Ge} = 720 to 800°C) consistent with the bandgap renormalization (BGR) [258] due to electron–electron and electron–ion interactions. Further increasing the carrier concentration (T_{Ge} = 850 to 1000°C) causes a blueshift of the PL emission energy due to the Burstein–Moss effect (BME) [259]: the lower energy states in the conduction band become significantly filled, and the Fermi level lies inside the conduction band. We also observe a broadening of the spectrum, in agreement with its definition by the product of the Kane density of states for the conduction band and the Fermi–Dirac distribution. Our observations are similar to the description in [260], which used HVPE grown-GaN doped with Si in the range of 8.7×10^{17} cm^{-3} to 1.4×10^{19} cm^{-3}, and MOVPE grown-GaN doped with Ge in the range of 3.4×10^{19} cm^{-3} to 1.6×10^{20} cm^{-3}.

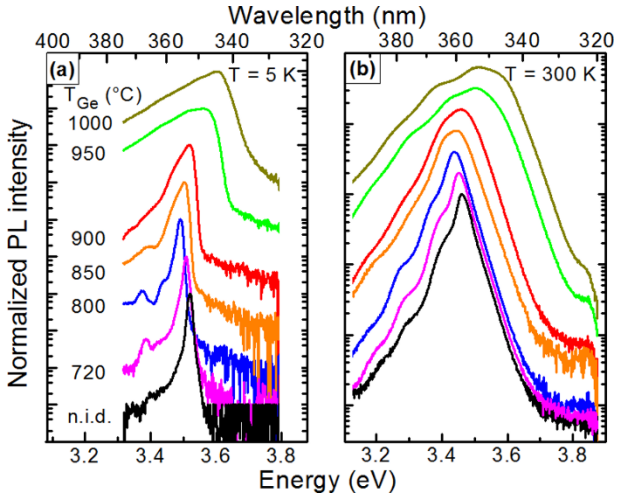

Figure 76 PL spectra at (a) 5 K and (b) 300 K. The spectra are normalized and vertically shifted for clarity. (Modified from **[234]**)

3.1.5. Conclusions

From this study, we can conclude that the presence of a Ge flux (with a Ge cell temperature up to 1000°C) during the growth of GaN does not affect the Ga kinetics. Ge-doped GaN thin films were grown and showed carrier concentration varying linearly with the Ge cell temperature, in the range from 7.8×10^{17} cm^{-3} to 6.7×10^{20} cm^{-3}. For all these carrier concentrations, the surface morphology of the samples was similar to that of n.i.d. GaN thin films. Furthermore, Ge incorporation showed to have no influence on the mosaicity of the structure. Optically, the evolution of the PL emission from Ge-doped GaN thin films as a function of the Ge concentration is consistent with theoretical calculations taking into account the BGR and the BME. For all these reasons, Ge appears as a promising alternative to Si as an n-type dopant for GaN grown by plasma-assisted MBE.

3.2. Application: screening of the electric field in Ge-doped GaN/AlN nanowires

As a first example of the relevance of Ge doping, we studied the effect of Ge-doping of GaN/AlN nanodisks in GaN NWs on the internal electric field, assessed via the measurement of the PL energy and radiative recombination time [235]. In such structures, the use of Ge as n-type dopant has the advantage of not having any significant influence on the NW aspect ratio even for high doping

levels (3.3×10^{20} cm^{-3}), whereas Si was proven to migrate towards the NW surface and decrease the doping efficiency [101,253,261].

GaN/AlN NW heterostructures can display PL decay times of the order of the microsecond due to the internal electric field associated to spontaneous and piezoelectric polarization [35,101]. Such long decay times persist up to room temperature thanks to the efficient exciton confinement resulting from the large band offset (~1.8 eV in the conduction band). Thus, excitons in nanodisks are isolated from dislocations and other non-radiative recombination centers.

The decay time is associated to the spatial separation of the electron and hole wavefunctions. Therefore, the screening of the internal electric field by free carriers should lead to a reduction of the recombination time. In this chapter, this phenomenon is described in the case of Ge-doped GaN/AlN NW heterostructures with different doping levels.

3.2.1. Sample description and experimental details

The samples under study are N-polar GaN/AlN NWs grown catalyst-free by plasma-assisted MBE under N-rich conditions on floating-zone Si(111) substrates at a temperature of ~790°C. The growth rate was 390 nm/h. They consist of a n.i.d. GaN NW base (length 600 nm, radius 25-40 nm) followed by 40 periods of GaN:Ge/AlN (nominally 4 nm/4 nm) nanodisks, and a 20 nm-thick n.i.d. GaN cap layer [262]. The free carrier concentration in these samples was estimated from time-of-flight secondary ion mass spectroscopy (ToF-SIMS) measurements in reference Ge-doped GaN NW samples. Table 12 details the structural characteristics of the GaN/AlN NWs under study.

Table 12 Characteristics of the GaN/AlN NWs: doping density, GaN/AlN period extracted from HR-XRD measurements, values of the E_a and α_2 parameters in Eq. (92) extracted from the fits in Figure 78 (b).

Sample	Doping density ($\times 10^{20}$ cm^{-3})	Period from HR-XRD (nm)	E_a (meV)	α_2
N40	(n.i.d.)	7.5 ± 0.2	40 ± 10	9 ± 2
N60	0.9	7.6 ± 0.2	54 ± 10	31 ± 2
N70	1.7	7.4 ± 0.2	53 ± 10	42 ± 2
N80	3.7	7.4 ± 0.2	68 ± 10	131 ± 2

As illustrated by Figure 77, HAADF-STEM, HR-TEM and HR-XRD measurements were performed, showing a perfect epitaxy consecutively achieved between the two materials. The images show no trace of GaN-AlN interdiffusion. However, Figure 77 (c) shows the presence of an AlN shell with a thickness roughly equal to the size of the barrier. This shell is generated by direct deposition of the impinging Al atoms due to the low Al diffusion length at the considered growth temperature. Also, the GaN/AlN interfaces often present {1-102} facets close to the NW sidewalls, highlighted by a white dashed line, which is due to the plane bending phenomena related to the elastic strain relaxation. From the HR-XRD measurements, illustrated by Figure 77 (d), estimations of the superlattice periods were obtained (7.4-7.6 ± 0.2 nm), consistent with the local views provided by the microscopy images.

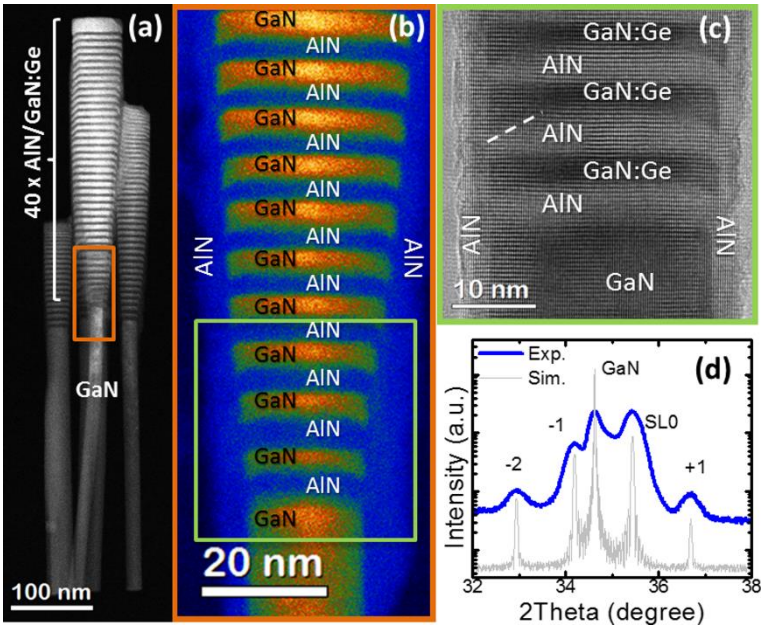

Figure 77 (a) HAADF-STEM image of the GaN/AlN NW heterostructures. The dark layers correspond to the AlN barriers and the bright layers correspond to the GaN disks. (b) Zoom into the squared region in (a) displayed in temperature color code. (c) HR-TEM image of the first three GaN:Ge disks (near the GaN stem). The dashed line highlights the presence of facets. (d) HR-XRD ω−2θ scan around the (0002) reflection of sample N70, and corresponding simulation. The simulation is down shifted for clarity. (Reproduced from **[235]**)

3.2.2. Photoluminescence study

In a first experiment, PL measurements were performed with a continuous-wave frequency-doubled Ar excitation laser (λ_{PL} = 244 nm), with an excitation power around 50 µW focused on a spot with a diameter of ~100 µm, giving a power density of about 7 kW/m². The emission from the sample was collected by a Jobin Yvon HR460 monochromator equipped with an ultraviolet-enhanced CCD camera.

As illustrated by Figure 78 (a), the low-temperature PL energy blueshifts and the spectra are broadened for increasing dopant concentrations. This is attributed to the screening of the internal electric field by the free carriers [262,263]. Figure 78 (b) shows that the normalized integrated PL intensities remain almost constant up to about 100 K, and drop to 20-40% of their maximum value at room temperature. This behavior is characteristic of GaN/AlN NWs, in contrast to planar structures which generally exhibit a PL quenching of several orders of magnitude at room temperature [1,264–266].

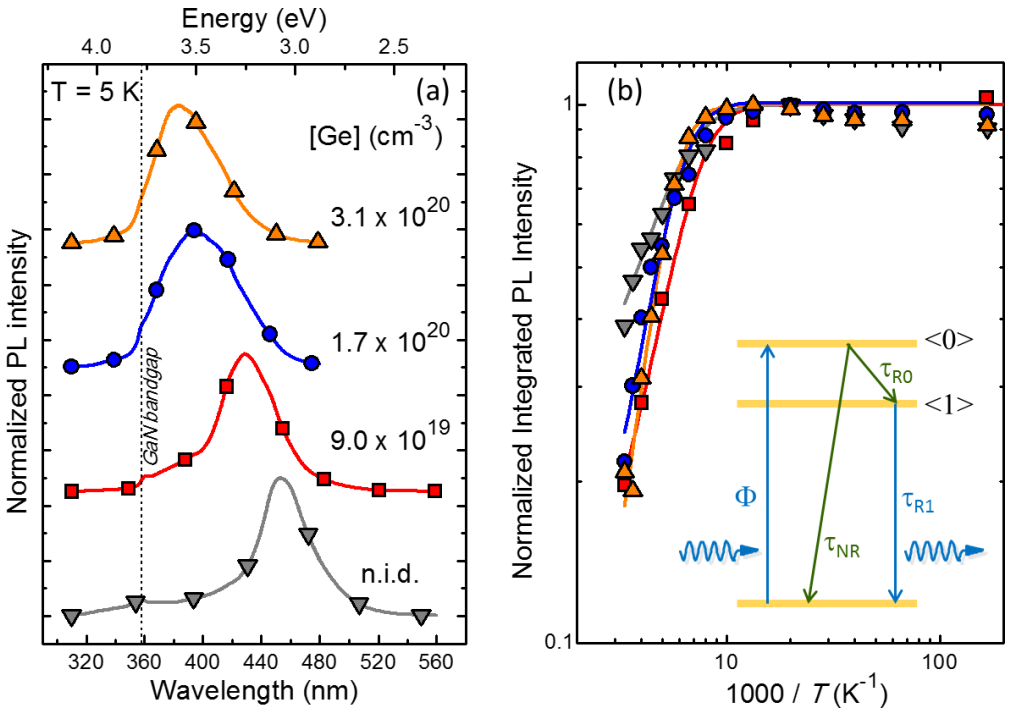

Figure 78 Low temperature PL spectra for different doping concentrations. Spectra are normalized and vertically shifted for clarity. (b) Normalized integrated PL intensity of the samples shown in (a) as a function of temperature. Solid lines are fits to Eq. **(92)**. Inset: Simplified three-level model of the PL dynamics. (Modified from **[235]**)

In a second experiment, time-resolved PL was performed using a frequency-tripled Ti:sapphire excitation laser (λ_{TRPL} = 270 nm) with a pulse width of 200 fs, to measure the PL decay and this way study the radiative recombination times. This laser was equipped with a cavity damper section with a base pulse repetition rate of 54 MHz. This allowed the period between pulses to be varied from 20 ns to 5 µs. The excitation power was about 500 µW. The luminescence was dispersed by a Jobin Yvon Triax320 monochromator and was detected by a Hamamatsu C−5680 streak camera.

We start by identifying the relevant time constants by analyzing the recorded spectra. As a typical example, Figure 79 (a) shows the low-temperature time-resolved evolution of the PL spectra emitted from sample N70 ([Ge] = 1.7×10^{20} cm^{-3}). The PL emission presents a redshift of 45 nm during the first ~60 ns before the setting of a steady-state, as illustrated in Figure 79 (b). This spectral shift is systematically observed in all the samples and decreases from 0.1 to 0.3 eV for increasing doping concentrations.

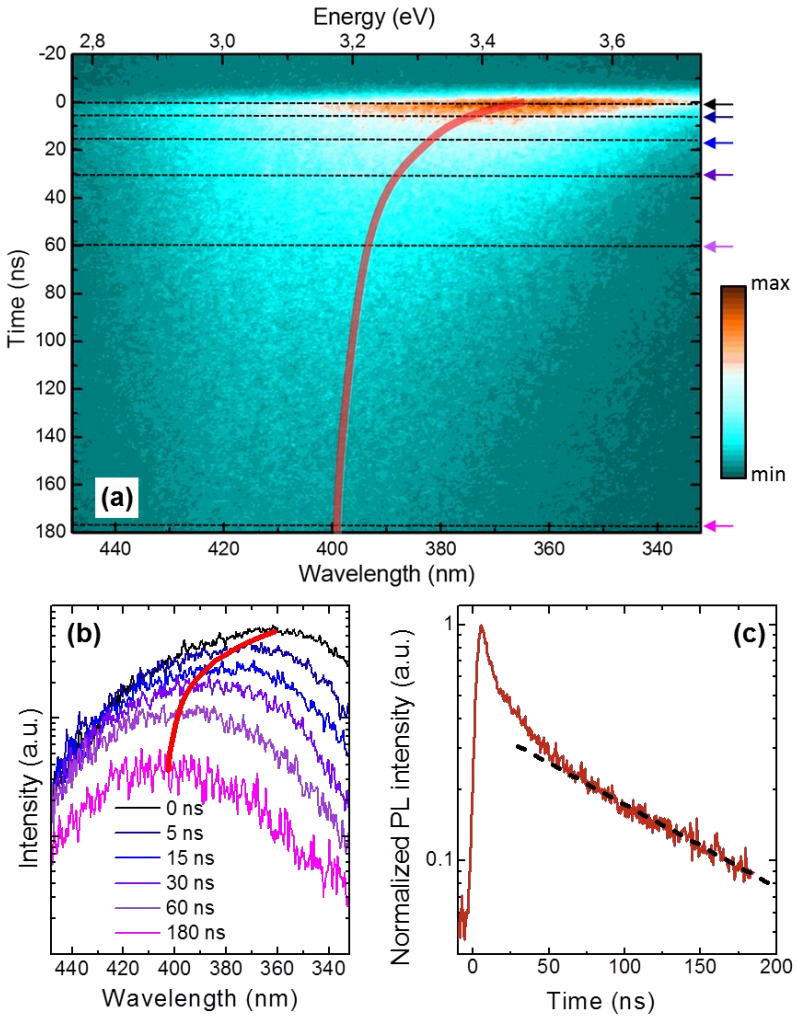

Figure 79 (a) Time-resolved PL spectra for sample N70 (doped with [Ge] = 1.7×10^{20} cm^{-3}). The red line follows the intensity maximum as a function of time. (b) Evolution of the PL spectra as a function of time. The time of maximum intensity is taken as t = 0. The spectra are acquired with a time integration window of 0.4 ns. The red line follows the intensity maximum. (c) Evolution of the PL peak intensity as a function of time. The dashed black line is an exponential fit to the PL decay for times longer than 60 ns. (Reproduced from **[235]**)

In Figure 79 (a) and (b), the red line indicates the evolution of the maximum PL intensity as a function of time. Following this trajectory, we obtain the intensity decay in Figure 79 (c). Comparing Figure 79 (b) and (c), the initial redshift during the first ~60 ns is associated to a nonexponential drop of the PL intensity, which is then followed by an exponential decay. These PL dynamics are qualitatively the same for all the samples regardless of the doping concentrations. The initial redshift and nonexponential behavior are attributed to the perturbation of the band structure by the laser excitation (namely the screening of the polarization fields) and to band-filling [267]. This is why the time constant of the exponential decay regime (indicated by the dashed black line in Figure 79 (c)) is the only relevant parameter to the study of the original band structure, after dissipation of the perturbation induced by the laser excitation.

In Figure 80 (a), we show the low-temperature PL decay (maximum PL intensity as a function of time) for the NW heterostructures with different dopant concentrations. Focusing on the exponential decay, we observe a huge drop of the decay time with increasing Ge concentration: the

n.i.d. sample displays a decay time of the order of the µs, while the decay times for higher dopant concentrations are in the order of the hundreds of ns.

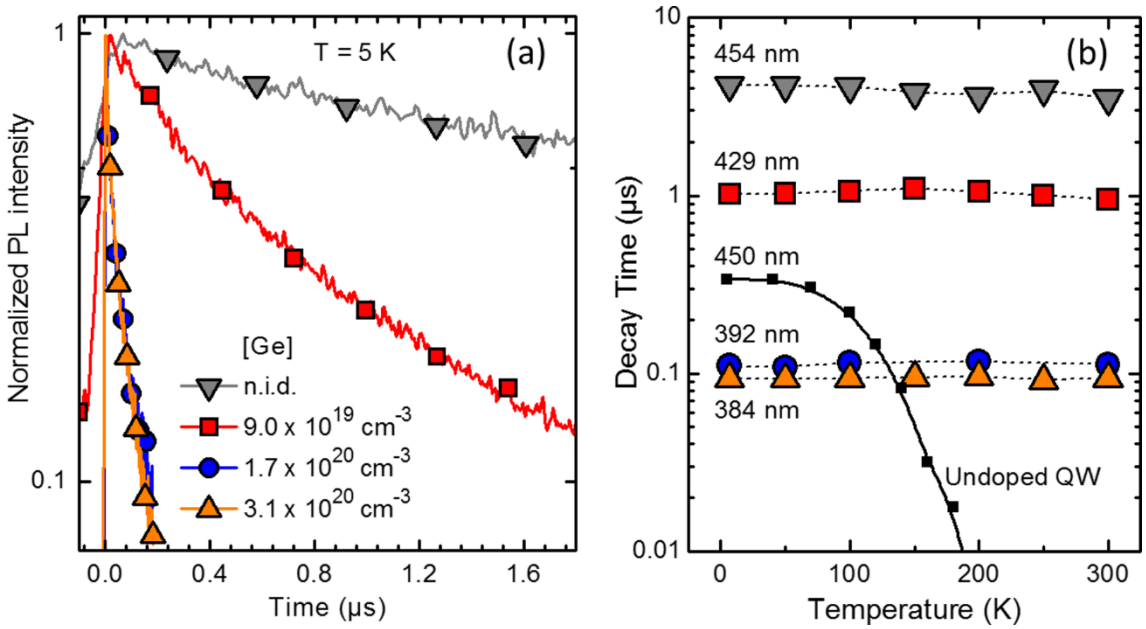

Figure 80 (a) Low-temperature PL decay for NWs with different doping concentrations. (b) PL decay characteristic times extracted from the exponential part of the PL decays [similar to Figure 79 (c)], plotted as a function of temperature. The emission wavelengths are indicated in the figure. Superimposed, PL decay times of an n.i.d. GaN/AlN QW emitting at approximately the same wavelength that the n.i.d. NWs. (Modified from **[235]**)

It should be noted that the decay times measured in our NWs are orders of magnitude longer than shown in the literature [263,268], where the measured PL decay times were even shorter than for equivalent QW structures. This can be explained when comparing the measurement procedures: in Refs. [263,268], the decay times were estimated from measurements exciting with a pulse repetition rate of 78 MHz (time between pulses = 12.8 ns). Based on the data from Ref. [41], the PL from undoped (highest doped) samples would have only dropped to about 60% (14%) of the maximum value before the next laser pulse hit. From their data, a 1/*e* decay time can be extracted assuming exponential relaxation. However, our experiments shows that the initial relaxation is strongly nonexponential due to the screening of the electric field induced by the laser pulse. With the lower excitation power, after 12.8 ns none of the samples have entered the exponential regime (indicated by the dashed black line in Figure 79 (c)), and only the most heavily doped sample would have recovered from the initial blueshift induced by the laser. We therefore conclude that the measurements in Ref. [263] provide information mostly about the recovery of the screening of the internal fields induced by the measuring laser. This is in agreement with the dependency of the decay time (and the spectral shift) on laser power reported by Hille *et al.* [263].

In Figure 80 (b), we plotted the evolution of the characteristic PL decay time as a function of temperature, where the relaxation times were extracted from the exponential decay profiles as indicated in Figure 79 (c). In all cases, the PL decay times remain constant (±10%) in the full range 10−300 K, as previously observed in the case of Stransky-Krastanov GaN/AlN quantum dots [269]. In contrast, temperature-dependent time-resolved measurements of GaN/AlN QW samples show a decrease in relaxation time over this temperature range by several orders of magnitude, as described

in Ref. [269]. This demonstrates that the 3D confinement in the nanodisks efficiently suppresses thermally activated non-radiative recombination channels up to room temperature.

From this latest conclusion, we attribute the thermal quenching at 100 K of the integrated PL intensity in Figure 78 (b) to carrier losses, occurring during the relaxation process of the hot photoexcited carriers in state $\langle 0 \rangle$ to the exciton ground state. In the inset of Figure 78 (b), we schematically describe the three-level model which can be used as a simplified view of this process.

In steady-state conditions, the carrier generation rate, Φ_c, is equal to the sum of the non-radiative recombination rate and the relaxation rate to the exciton emitting state $\langle 1 \rangle$ as follows:

$$\Phi_c = \frac{n_0}{\tau_{NR}} + \frac{n_0}{\tau_{R0}} \tag{90}$$

where n_0 is the optically excited population at the $\langle 0 \rangle$ level, and τ_{NR} and τ_{R0} are the characteristic times associated to the non-radiative processes and to the relaxation to the exciton emitting state, respectively.

Since the PL decay is constant with temperature (*i.e.* no non-radiative recombination channels can be thermally activated), we can neglect non-radiative recombination once the excitons are trapped in the nanodisk, and the PL intensity (I) can be described as:

$$I = \frac{n_1}{\tau_{R1}} = \frac{n_0}{\tau_{R0}} = \frac{\Phi_c}{1 + \frac{\tau_{R0}}{\tau_{NR}}} \tag{91}$$

where n_1 is the population of the exciton emitting state in the nanodisk and τ_{R1} is the associated characteristic time.

Assuming that the photogeneration (Φ_c) is constant with temperature, and that non-radiative processes from state $\langle 0 \rangle$ are thermally activated (since the PL quenching is due to carrier losses during the relaxation process to the ground state), the PL intensity as a function of temperature, I (T), can be described as:

$$I(T) = \frac{I(T = 0)}{1 + \alpha_2 \exp(-\frac{E_a}{kT})} \tag{92}$$

where E_a represents the activation energy of the non-radiative process in state $\langle 0 \rangle$, kT is the thermal energy, and α_2 is a constant coefficient.

Solid lines in Figure 78 (b) are fits of the experimental data to Eq. (92). The extracted values of E_a and α_2 are summarized in Table 12. We observe an increase in both parameters with increasing doping concentration, which reveals an increased probability of non-radiative processes with increasing carrier density.

The strong acceleration of the PL decay with increasing Ge concentration shows that the Ge-doping-induced screening of the electric field in the nanodisks is drastically defining the radiative carrier lifetime. The magnitude of this effect is much larger than previously reported for GaN QWs [135,269], And we measured that the low-temperature PL lifetimes of n.i.d. nanodisks are much longer than for n.i.d. QWs emitting approximately at the same wavelength. This indicates a much larger electron-hole separation in space in the nanodisks, which implies a different electric field distribution.

3.2.3. Calculation of the electric field distribution

To understand the electric field distribution leading to this giant screening effect, we carried out 3D calculations of the NW strain state, band diagram and quantum confined states using the Nextnano[3] software with the material parameters described in [160]. The NW was defined as a hexagonal prism consisting of a 50-nm-long GaN stem followed by a sequence of 10 AlN/GaN stacks and capped with 18 nm of GaN. The radius of the GaN base was 20 nm, the growth axis was [000−1], and the sidewall faces were {1−100} planes. The structure was defined on a GaN substrate, to provide a reference in-plane lattice parameter. The GaN stem and the AlN/GaN heterostructure were laterally surrounded by an AlN shell, and the whole structure was embedded in a rectangular prism of air, which permits the deformation to reduce elastic energy. Surface states were modeled as a negative surface charge density of 2×10^{12} cm^{-2} at the air/semiconductor interfaces [270]. The presence of {1−102} facets in the AlN sections was also taken into account, as illustrated in Figure 81 (a), which shows a cross-section view along <1-100> of three nanodisks in the stack.

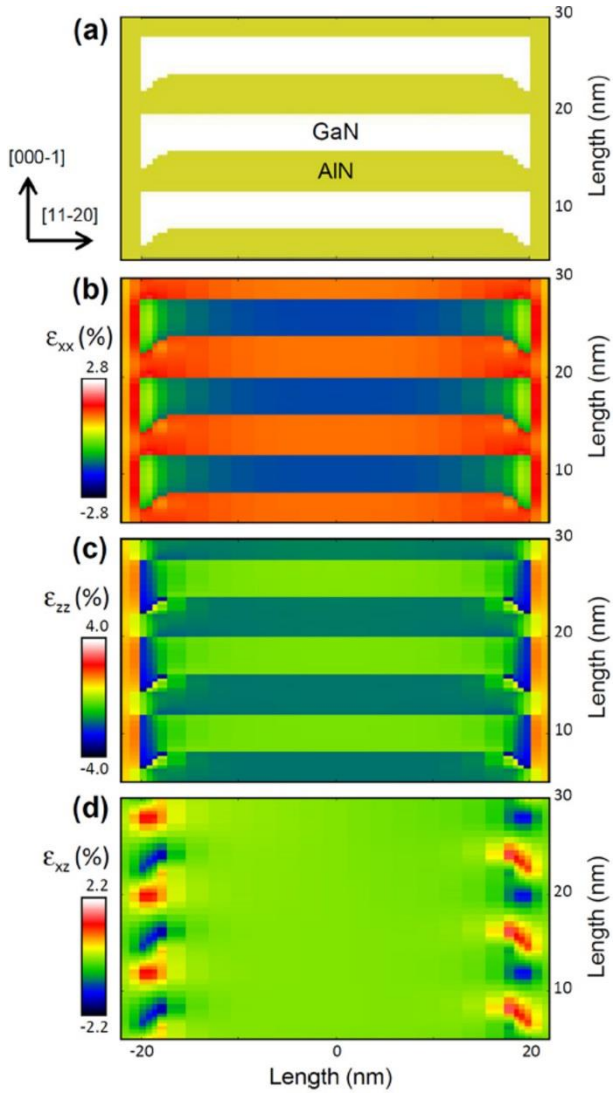

Figure 81 (a) Schematic representation of three GaN/AlN nanodisks in the center of the nanowire heterostructures. The structure is viewed along the <1−100> direction. White areas correspond to GaN and yellow areas correspond to AlN. (b) Calculation of the ε_{xx} strain component (strain along <11−20>) for these

same disks. (c) Calculation of the ε_{zz} strain component (along <000–1>). (d) Calculation of the ε_{xz} shear strain component.

The 3D strain distribution was calculated by minimizing the elastic energy and applying zero-stress boundary conditions at the surface. The effect of doping on the strain distribution was neglected following [237,248]. Figure 81 (b) and (c) display cross-sectional views along direction <1-100> of the strain components along the <11−20> direction, ε_{xx}, and <0001> direction, ε_{zz}, for three nanodisks in the stack. Regarding the ε_{xx} component, the center of the disk is compressed by the AlN sections (ε_{xx} = −1.29%) and there is an elastic relaxation close to the sidewalls. In contrast, the ε_{zz} strain component is almost zero (ε_{zz} = −0.025%) along the center of the nanodisk, however the GaN gets significantly compressed near the sidewalls due to the presence of the AlN shell (up to ε_{zz} = −2.2%). The radial inhomogeneous strain results in nonzero ε_{xz} and ε_{yz} shear strain components (*i.e.* strain along the *c* axis, represented by the z axis in Figure 81), as illustrated in Figure 81 (d) for ε_{xz}. Using the equation (33) of subsection 1.2.2 describing the piezoelectric polarization field in function of the piezoelectric constants and the deformation of the crystal, this leads to a radial piezoelectric polarization associated to the nonzero e_{15} piezoelectric constant in the wurtzite lattice. On the other hand, this particular strain distribution results also in an increase of the GaN band gap by ~120 meV when moving from the center of the nanodisk to the sidewalls (data obtained using the deformation potentials from Ref. [200]).

Using the obtained NW 3D map of polarization as an input, we classically solve the nonlinear Poisson equation, and calculate the 3D band structure of the NW. Finally, solving the Schrödinger equation in a quantum region covering one nanodisk and the AlN barriers on top and bottom of the nanodisk, we obtain the eigenfunctions, as illustrated by Figure 82.

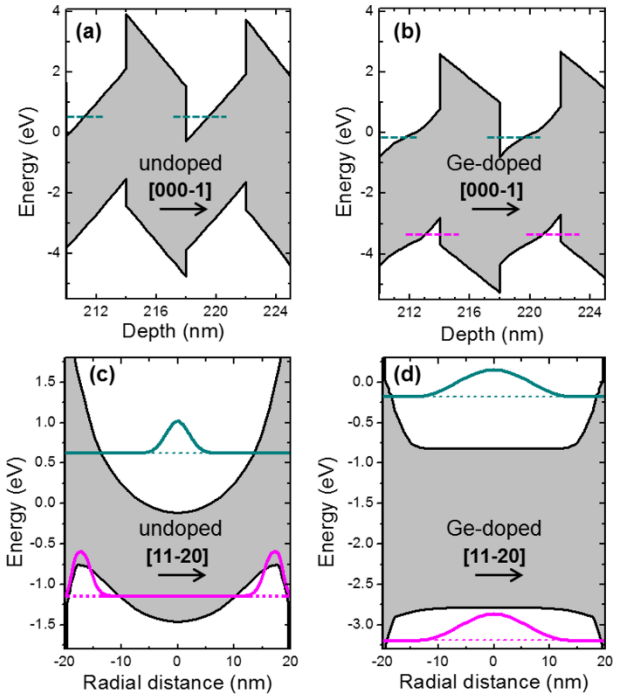

Figure 82 (a)–(d) Calculation of the conduction and valence band profiles and first electronic levels of electrons (blue) and holes (pink). (a), (b) Conduction and valence band profiles along [000−1] taken at the center of the NW, for (a) undoped nanodisks and (b) Ge-doped nanodisks (N_D = 1.7×10^{20} cm^{-3}). The ground electron and hole levels are indicated by dashed lines. In (a), the ground hole level is not indicated because the value of the squared wavefunction along the center of the NW is zero. (c), (d) Radial conduction and valence band profiles

for the (c) undoped and (d) Ge-doped nanodisk in the center of the stack. Note that the conduction band was taken at the bottom of the disk, while the valence band was taken at the top of the disk. The squared wavefunctions of the ground electron and hole states are indicated in the figures. (Modified from **[235]**)

Figure 82 (a) and (b) show the axial conduction and valence band profiles (along the [000-1] growth axis), along the center of the NW for (a) undoped nanodisks and (b) doped nanodisks with an *n*-type dopant concentration $N_D = 1.7\times10^{20}$ cm^{-3}. In both cases, the polarization-induced internal electric fields results in a sawtooth profile with the electron levels shifted towards the bottom of the nanodisk. In the doped NW, carrier screening results in a reduction of the internal axial electric field from 5.9 to 2.5 MV/cm.

Figure 82 (c) and (d) show the radial conduction and valence band profiles (along the [11-20] axis) for (c) undoped nanodisks and (d) doped nanodisks with $N_D = 1.7\times10^{20}$ cm^{-3}. In both cases, the conduction (valence) band profile was taken at the bottom (top) interface of the nanodisk. The squared wavefunctions of the first electron and hole levels are also represented, in blue and pink respectively. In the case of undoped nanodisks, the band bending induced by the AlN shell pushes the electrons towards the center of the NW (blue wavefunction in Figure 82 (c)), while the radial valence band profile has local maxima near the NW sidewalls (pink wavefunction in Figure 82 (c)). This is in agreement with calculations by [271] and [272], and we can conclude that in addition to the polarization-induced vertical separation of electron and holes, the 3D geometry of the nanodisks contributes to extend the radiative recombination lifetime, when comparing to the case of QWs. We note that the strain-induced enlargement of the GaN bandgap at the ~5 nm closest to the nanodisk sidewalls contributes to separate the carriers, especially the holes, from the core/shell interface. The presence of {1-102} facets at the top interface of the AlN sections, which enlarges the GaN disks close to the surface, does not have a significant effect on the radial location of the hole. This is because the spontaneous and piezoelectric polarization shifts the hole towards the top of the GaN nanodisk. However, these facets modify the electron wavefunctions, which results in a shift of the band-to-band transition by ~300 meV.

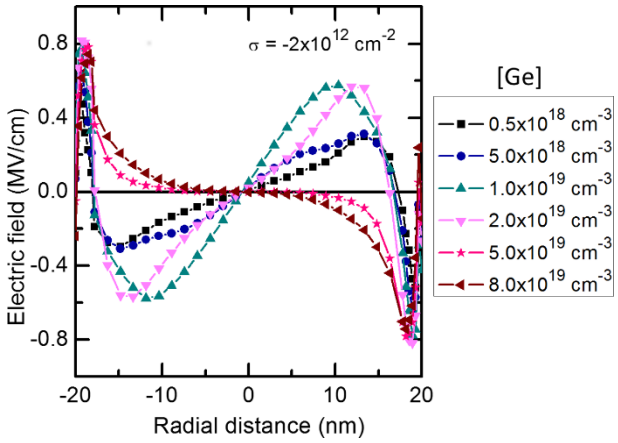

Figure 83 Calculation of the electric field along [11-20] at the top of the nanodisk for various doping concentrations in the nanodisks, with surface charges at a concentration of $\sigma = -2\times10^{12}$ cm^{-2}. (Modified from **[235]**)

Figure 83 shows the calculation results of the lateral electric field (along [11-20]) considering the presence of negatively charged surface states. At low dopant concentrations (below 10^{19} cm^{-3}), the electric field along the [11-20] axis at the top GaN/AlN interface presents a maximum value of

~0.6 MV/cm, which is one order of magnitude smaller than the axial field (along [000-1]). When increasing the doping concentration, we observe a screening of the lateral electric field. As seen in Figure 82 (d), this is causing both a spatial broadening of the electron wavefunction and a shift of the hole wavefunction towards the center of the NW, ultimately leading to the radial alignment of the electron and hole wavefunctions. This improvement of the electron-hole wavefunction overlap explains the drastic decrease of the radiative recombination lifetime. Besides, a positive electric field implies that it points in the [11−20] direction. The transition of the hole towards the center of the NW takes place for a doping concentration around 3.35×10^{19} cm^{-3}, which corresponds to the transition to a zero-field in the radial direction, namely when the sign of the electric field sees a crossover. A null electric field was seen 17 nm from the center of the wire.

Therefore, the radial misalignment of the electron and hole wavefunctions is a determining factor for the band-to-band dynamics in GaN/AlN nanodisks. At low dopant concentrations, the radial electron-hole separation leads to radiative lifetimes which are significantly longer than for GaN/AlN QWs emitting at the same wavelength. Increasing the dopant concentration results in screening of the electric field, which leads to a radial centralization of the hole, *i.e.* an alignment of the electron and hole wavefunctions, which results in a large decrease in the radiative lifetime.

3.2.4. Conclusions

We studied 40-period GaN/AlN NWs with the GaN nanodisks doped with different Ge concentrations. Our goal was to assess the screening effect of Ge-doping on the internal electric field. The internal electric field leads to the spatial separation of electron and holes, extending the decay time that reaches the order of the µs for n.id. structures. The carrier lifetime is expected to decrease with increasing doping, due to the screening of the electric field by free carriers.

By measuring TRPL, we observed a huge drop in the carrier lifetimes with increasing Ge-doping. Interestingly, carrier lifetimes were measured longer in NWs than in QWs with similar width, and the screening effect was much larger in NWs than in QWs with similar width. The long relaxation times in GaN/AlN NWs are explained as the result of the presence of internal electric fields in the nanodisks, with an axial component in the range of a few MV/cm associated to spontaneous and piezoelectric polarization, and a radial component associated to the radial variation of lattice strain. Simulations show that at low dopant concentrations, a large electron-hole separation in both axial and radial directions is present. The relatively weak radial electric field (10 times smaller than the axial electric field) is rapidly screened by Ge doping, leading to the radial and axial centralization of the hole underneath the electron. This bidirectional Ge-doping induced giant screening leads to a large decrease of the radiative lifetime, by about 2 orders of magnitude, in addition to the luminescence blueshift.

From these results, we can conclude that Ge-doping has the advantage over Si not only of not altering the NWs aspect ratio thanks to a homogeneous diffusion in the layers, but also of having a huge screening effect on the internal electric field, allowing to efficiently tune the radiative recombination times in these structures.

3.3. Ge-doped GaN/AlN MQWs with ISB transitions in the Short-Wavelength Infrared

Device development requires fine tuning of the carrier concentration in the QWs for the population of the ground quantum electronic level. This is why in this section we focus on the study of doping in GaN/AlN MQWs designed for ISB absorption in the SWIR. As a consequence of the promising properties obtained in GaN layers doped with Ge, we compare the performance of heterostructures doped with Ge and doped with Si.

3.3.1. Sample structure

The structures consist in 25 periods of GaN/AlN (2 nm/3 nm) MQWs, designed to show ISB absorption at 0.71 eV (1.77 µm), and grown on AlN-on-sapphire substrates. The GaN QWs are homogeneously doped with Si or Ge, with the doping densities described in Table 13, and the heterostructures are capped with 30 nm of AlN to avoid surface charges effects. Figure 84 shows a sketch of the structure as well as the obtained band diagram.

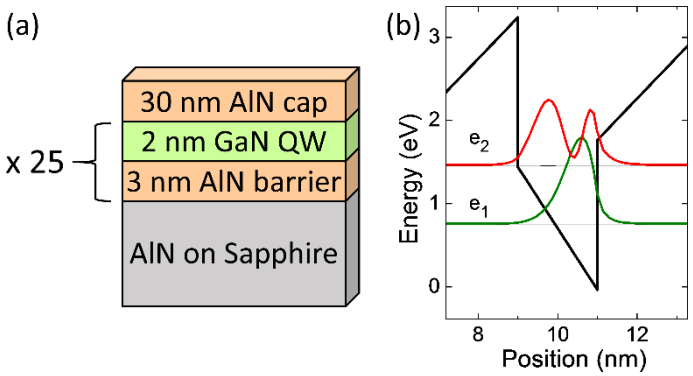

Figure 84 (a) Sketch of the GaN/AlN MQWs structure. (b) Band diagram calculated using the Nextnano[3] software.

Table 13 Structural and optical characteristics of the samples under study: nature of the n-type dopant; doping density; HR-XRD measured MQWs period; broadening of the ω-scan of the (002) XRD reflection measured for the MQWs and the substrate; PL peak energy; measured ISB transition energy; normalized broadening (broadening in energy divided by the absorption peak energy) of the ISB absorption spectrum; ISB absorption per pass.

Dopant	Sample	Doping density ($\times 10^{12}$ cm^{-2})	XRD period (nm)	XRD FWHM MQW (°)	XRD FWHM AlN (°)	PL peak energy (eV)	ISB energy (eV)	Norm. broaden-ing	ISB abs. per pass (%)
Si	E3522	1	4.77	0.199	0.056	3.39	0.71	0.12	2.1
Ge	E3523	1	4.81	0.167	0.046	3.41	0.72	0.13	1.8
Si	E3524	4	4.85	0.180	0.061	3.52	0.83	0.13	8.9
Ge	E3525	4	4.78	0.154	0.058	3.46	0.76	0.15	6.6
Si	E3588	10	4.25	0.176	0.057	3.68	0.86	0.22	9.5
Ge	E3587	10	4.36	0.149	0.063	3.56	0.82	0.11	8.6

The periodicity of the samples was analyzed by HR-XRD, using the setup described in subsection 2.4.2. Figure 85 shows the ω-2θ scan of the (002) reflection of the Si-doped E3588 and

Ge-doped E3587 samples. The MQW period extracted from the intersatellite distance in the ω-2θ scans are summarized in Table 13. Samples E3522 to E3525 show a periodicity in agreement with the original design, with a deviation below 5%. In contrast, samples E3587 and E3588, which were not grown with the rest of the series, show a deviation of 15% with respect to the design. Also, the FWHM of the rocking curves was measured for the substrate and the MQW zero-order reflection (MQW 0 peak in Figure 85), providing information on the sample mosaicity. The average broadening for Si-doped MQWs is $0.19 \pm 0.01°$ whereas the average broadening for Ge-doped MQWs is $0.16 \pm 0.01°$, which indicates that for similar substrate quality, Ge-doping systematically results in structures with better mosaicity than when using Si-doping. This is consistent with our expectations, the ionic radius of a Ge atom being similar to that of Ga, and the metal-nitrogen bond length changing by only 1.4% with Ge, compared to 5.5% with Si [243], allowing the Ge occupancy of the Ga lattice site to induce far less lattice distortion compared to Si.

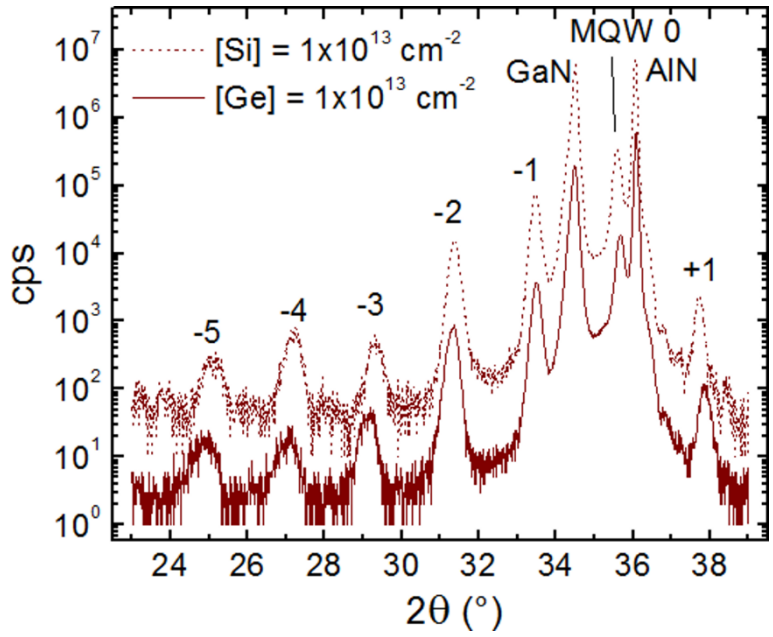

Figure 85 XRD ω-2θ scans of the (002) reflection of samples E3587 and E3588.

3.3.2. Optical characterization

To assess the band-to-band properties of the MQWs, the PL spectra of all the samples were measured at 5 K. The results in terms of emission energy are shown in Table 13, and the obtained spectra are displayed in Figure 86. In both cases of Ge- and Si-doping, the spectra present a multipeak structure due to monolayer fluctuations of the well thickness [71]. Increasing the dopant density induces a blueshift of the PL energy as well as a broadening of the emission peak, which is due to the BME (band filling effect described in section 3.1.4) [259]. The total energy shift and the energy broadening are similar for both dopants.

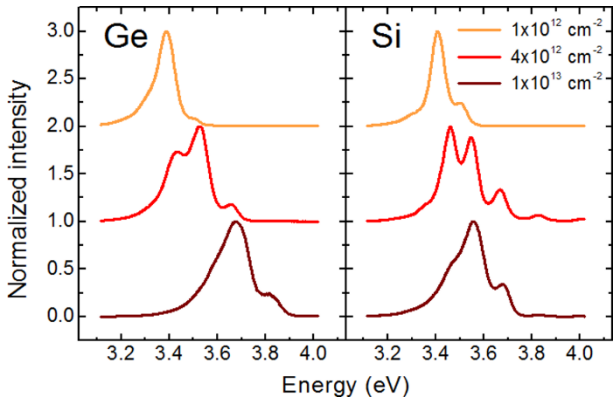

Figure 86 PL spectra of the Ge-doped and Si-doped samples measured at 5 K.

To assess the ISB properties of the samples, the ISB absorption in the SWIR range was measured at room temperature by FTIR spectroscopy. The ISB nature of the transition was set because absorption was observed when exposing the sample to TM-polarized light and not when exposing it to TE-polarized light. In Figure 87, the obtained TM-polarized spectra are normalized by division by the respective TE-polarized spectra. As explained in the PL case, the multipeak structure of the spectra is due to monolayer thickness fluctuations in the wells [71]. The ISB absorption energies for the various samples are presented in Table 13. The lowest-doped structures show ISB absorption in agreement with the simulations. As expected, they are blueshifted when increasing the doping concentration, which is due to many-body effects (namely exchange interaction and depolarization shift). The magnitude of these effects is similar for both dopants. However, in the case of Si-doping, increasing the doping density leads to a stronger broadening of the absorption peak, which is not the case for Ge-doping where the widening effect is much reduced.

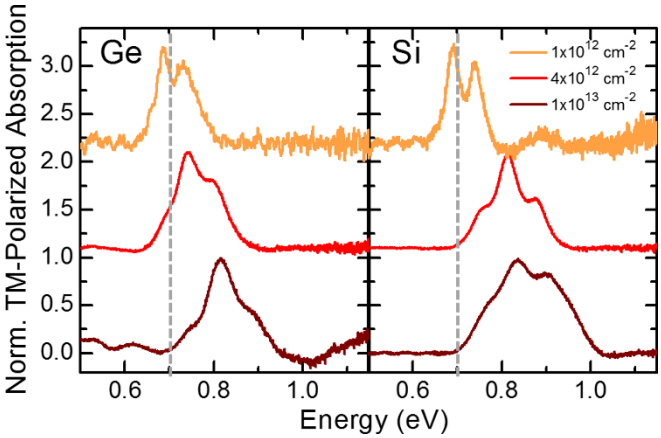

Figure 87 TM-polarized ISB absorption of the Ge- and Si-doped samples measured at room temperature. The dashed lines indicate the theoretical ISB absorption energy at 0.71 eV.

3.3.3. Conclusions

In summary, we have grown 25 period-GaN/AlN (2 nm/3 nm) MQWs designed to show ISB absorption at 0.71 eV (1.77 µm), where the GaN QWs were homogeneously doped with silicon or germanium with different doping densities. Structurally, the Ge-doped structures showed better mosaicity than those Si-doped. For both dopants, increasing the doping density results in a blueshift of the PL energy and a broadening of the peak, which is due to the combination of screening and band

filling effects. However, no dependence of these band-to-band properties on the dopant nature was observed. When increasing the doping concentrations, the spectral broadening of the ISB absorption was larger in the case of Si-doping, while the measured energy shift was similar for both dopants.

3.4. Ge-doped GaN/AlGaN MQWs with ISB transition in the Mid-Infrared

In this section, we replace AlN by AlGaN in the barriers and enlarge the QW widths and therefore extend the study to the MIR range. Again, we compare the GaN/AlGaN MQWs performance when doped with Si and with Ge.

3.4.1. Sample structure

The structures consist in 30 periods of GaN/$Al_{0.2}Ga_{0.8}N$ (4 nm/3 nm) MQWs, designed to show ISB absorption at 164 meV (7.6 µm) and grown on GaN-on-Si(111) substrates. The 2-nm center region of the GaN QWs are homogeneously doped with Si or Ge, with the doping densities described in Table 14, and the heterostructures are capped with 30 nm of $AlGa_{0.2}N$ to avoid surface charges effects. Figure 88 shows a sketch of the structure as well as the band diagram.

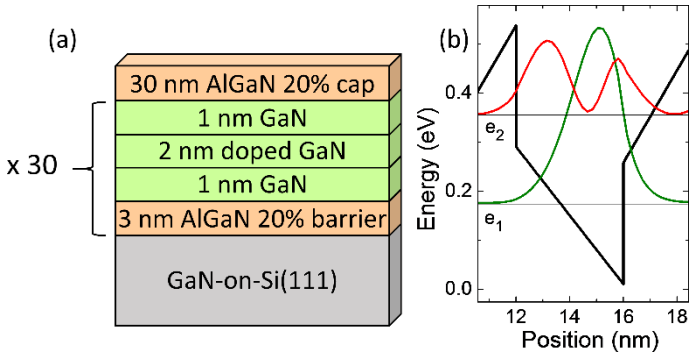

Figure 88 (a) Sketch of the GaN/AlGaN MQWs structure. (b) Band diagram calculated using the Nextnano[3] software.

Table 14 Structural and optical characteristics of the samples under study: nature of the n-type dopant; doping density; broadening of the ω-scan of the (002) XRD reflection measured for the MQWs and the substrate; PL peak energy; measured ISB transition energy; normalized broadening (broadening in energy divided by the absorption peak energy) of the ISB absorption spectrum; ISB absorption per pass.

Dopant	Sample	Doping density ($\times 10^{12}$ cm^{-2})	XRD FWHM MQW (°)	XRD FWHM GaN (°)	PL peak energy (eV)	ISB transition energy (meV)	ISB Norm. broaden-ing	ISB abs. per pass (%)
Si	E3576	1	0.190	0.212	3.46	249	0.18	4.7
Ge	E3579	1	0.188	0.209	3.46	272	0.22	4.1
Si	E3577	4	0.187	0.210	3.48	289	0.40	5.8
Ge	E3580	4	0.185	0.210	3.47	276	0.30	7.4
Si	E3578	10	0.189	0.206	3.48	278	0.65	14.6
Ge	E3582	10	0.187	0.204	3.55	269	0.34	16.0

The periodicity of the MQWs was verified by HR-XRD and all the samples showed a periodicity of about 7 nm with less than 5% deviation. Their structural quality was evaluated by

measuring the FWHM of the rocking curves for the substrate and the MQW zero-order reflection around the (002) reflection. As shown in Table 14, no dependence of the samples structural quality on neither the dopant nature nor the doping density was observed.

3.4.2. Optical characterization

The band-to-band properties of the MQWs were assessed by measuring their low-temperature PL, with the results in Figure 89. When increasing the Ge-doping density, we observe a blueshift of the PL energy as well as an asymmetric widening of the PL peak towards the low-energy side. In contrast, increasing the Si-doping density induced only a slight blueshift of the PL energy, but introduced a certain asymmetry of the PL peak, without any significant broadening.

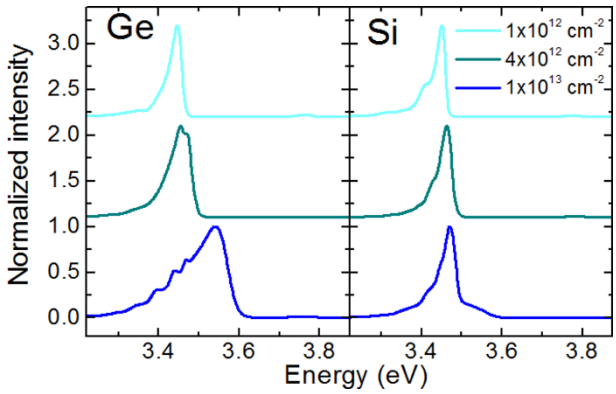

Figure 89 PL spectra of the Ge-doped and Si-doped samples measured at 5 K.

The structures were designed to show ISB absorption at 0.164 eV. To assess their ISB properties, the samples were measured by FTIR at room temperature. As shown in Table 14 and illustrated by Figure 90, all samples present a TM-polarized absorption spectrum where the peak energy is blueshifted from this value. When increasing the Ge-doping density, the ISB absorption peak energy is almost constant and the peak spectral broadening is enlarged by 54%. When increasing the Si-doping density, the peak energy undergoes a blueshift of about 20 meV between the lowest and highest doping levels, which is due to many-body effects (namely exchange interaction and depolarization shift), and the ISB absorption peak broadening is multiplied by a factor of 3.6. We also calculated the magnitudes of ISB absorption per pass for the different doping levels, and as shown in Table 14, they were found to be comparable for similar doping densities of Si and Ge.

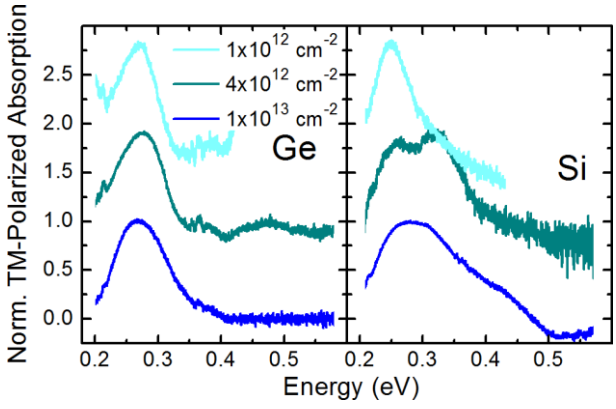

Figure 90 TM-polarized ISB absorption of the Ge- and Si-doped samples measured at room temperature.

3.4.3. Conclusions

As a conclusion, Ge-doping offers a slightly better mosaicity in the case of high lattice mismatched structures like GaN/AlN MQWs when compared to Si-doping, but the change is negligible in GaN/AlGaN MQWs where the lattice mismatch is reduced. When increasing the Ge doping density, the ISB absorption peak energy shift and widening are very slight (about 3 meV shift). When increasing the Si doping density, the ISB absorption peak undergoes a stronger broadening and blueshifts of about 20 meV, which is stronger than in the case of Ge-doping, and which is due to the combination of depolarization shift and scattering by ionized impurities.

3.5. Conclusions on the use of Ge as a dopant

We started by studying the consequences of Ge-doping on the GaN growth process through the characterization of Ga desorption from the GaN surface. We concluded that even for Ge cell temperatures up to 1000°C, the presence of a Ge flux during the growth of GaN did not affect the Ga kinetics. Then, we grew Ge-doped GaN thin films with carrier concentrations in the range of 7.8×10^{17} cm^{-3} to 6.7×10^{20} cm^{-3}. They showed high quality surface morphology similar to that of n.i.d. GaN thin films. Moreover, the mosaicity of the structure was not affected by Ge incorporation. Optically, the evolution of the PL emission from Ge-doped GaN thin films as a function of the Ge concentration was in agreement with theoretical calculations taking into account the BGR and the BME. From these results, we concluded that Ge constitutes a possible alternative to Si as an n-type dopant for GaN grown by plasma-assisted MBE.

As a first example of the relevance of Ge doping, we studied GaN/AlN NWs, in which the GaN nanodisks had been doped with Ge. We assessed the screening effect of Ge-doping on the internal electric field of the structures via the measurement of the PL energy and radiative recombination time. By measuring TRPL, we observed a huge drop in the carrier lifetimes with increasing Ge-doping. The screening effect was much larger in NWs than in QWs with similar width while the carrier lifetimes were measured longer in NWs than in QWs with similar width. Simulations were run and showed that at low dopant concentrations, a large electron-hole separation in both axial and radial directions was present in the NWs. Then, by increasing the Ge doping, the relatively weak radial electric field (10 times smaller than the axial electric field) got rapidly screened, leading to the radial and axial centralization of the hole underneath the electron. This bidirectional Ge-doping induced giant screening lead to a large decrease of the radiative lifetime, by about 2 orders of magnitude, in addition to the luminescence blueshift. From these results, we concluded that, in contrast to Si-doping, Ge-doping had the advantage not only of not altering the NWs aspect ratio thanks to a homogeneous diffusion in the layers, but also of having a huge screening effect on the internal electric field, allowing to efficiently tune the radiative recombination times in these structures.

We then turned towards 2D GaN/AlGaN MQWs. We designed and grew 25 period-GaN/AlN (2 nm/3 nm) MQWs with ISB absorption at 0.71 eV (1.77 µm) and 30-periods GaN/$AlGa_{0.2}N$ (4 nm/3 nm) MQWs with ISB absorption at 164 meV (7.6 µm). The GaN QWs were homogeneously doped with Si or Ge with different doping densities. Structurally, the Ge-doped GaN/AlN MQWs showed better mosaicity than those doped with Si. In contrast, the GaN/AlGaN MQWs, for which the lattice mismatch is already reduced, showed no structural difference as a function of the dopant nature. No clear dependence of the band-to-band properties on the dopant nature was observed in any of the

cases. Regarding the optical properties, both for GaN/AlN and GaN/AlGaN, the ISB absorption peak blueshifted in energy and widened for increasing doping levels, which is due to the combination of depolarization shift and scattering by ionized impurities.

Infrared photons
Don't get trapped in stacking faults
I need you all out

Chapter 4.
Nonpolar orientation

In this chapter, we study the possibility to use nonpolar orientations of GaN to obtain heterostructures without internal electric field, which is a major hurdle to extend the operation range of GaN-based intersubband devices towards the far-infrared. We start by introducing our motivation to work with nonpolar GaN. Then we detail the growth conditions of our structures. We continue by presenting two possible nonpolar planes, *a* and *m*, and we justify our choice to work with the *m* orientation through the comparative study of *a*- vs *m*- plane GaN/AlN multi-quantum-wells showing intersubband transition in the short-wavelength infrared range. The study is then extended to *m*-plane GaN/AlGaN multi-quantum wells with intersubband transitions in the mid- and far-infrared.

Introduction for Newbies: So far, research has mostly focused on the polar *c* plane orientation of GaN. However, this crystallographic orientation comes with the complicating factor of a polarization-induced electric field, resulting in a band diagram with triangular potential profiles in the quantum wells, instead of symmetric square wells. Among other consequences, this electric field increases the carrier confinement in the wells and ultimately hampers the extension of the GaN/AlGaN heterostructures towards the far-infrared range (small transition energies of the order of the meV). Nonpolar orientations are free from such a polarization-induced electric field and may be an alternative. To validate this approach, we need first to decide which nonpolar orientation would be the best to work with in terms of structural and optical performance. Then, we need to determine whether or not structures grown in this nonpolar orientation can outperform their polar *c*-plane counterparts for applications in the different regions of the infrared spectrum. To do so, the quantum well width must be adapted to the targeted spectral range.

For the comparative study of *a* vs *m* plane MQWs (section 4.3), I was in charge of AFM, XRD, and FTIR measurements, and conclusions were attained in collaboration with M. Beeler (design, MBE growth, PL measurements), C. Bougerol (TEM), and J. Lähnemann (SEM). The complete study was published in "Intersubband transitions in nonpolar GaN/Al(Ga)N heterostructures in the short and mid-wavelength infrared regions", C. B. Lim *et al.*, J. Appl. Phys. **118**, 014309 (2015) [273].

For the study of GaN/AlGaN MQWs with ISB transitions in the MIR (section 4.4), I performed the design, MBE growth, AFM, XRD, PL and FTIR measurements, and the work was performed in collaboration with C. Bougerol (TEM), J. Lähnemann (SEM) and A. Ajay (temperature-dependent PL). The complete study was published in "Intersubband transitions in nonpolar GaN/Al(Ga)N heterostructures in the short and mid-wavelength infrared regions", C. B. Lim *et al.*, J. Appl. Phys. **118**, 014309 (2015) [273].

For the study of GaN/AlGaN MQWs with ISB transitions in the FIR (section 4.5), I designed and grew the samples, and measured XRD and FTIR. Results were completed in collaboration with A. Ajay (AFM, temperature-dependent PL), J. Schörmann, who helped me with the XRD measurements, C. Bougerol and B. Haas (TEM) and J. Lähnemann (CL measurements). The complete study was published in "Nonpolar *m*-plane GaN/AlGaN heterostructures with intersubband transitions in the 5–10 THz band", C. B. Lim *et al.*, Nanotechnology **26**, 435201 (2015) [274].

For the study of the effect of Si doping on GaN/AlGaN MQWs with ISB transition in the FIR (section 4.6), I was in charge of the design and MBE growth, calculation of the many-body effects, XRD, temperature-dependent PL, and FTIR measurements. The study was completed in collaboration with A. Ajay (AFM and help with the PL measurements) and C. Bougerol (TEM). The complete study was published in "Effect of doping on the far-infrared intersubband transitions in nonpolar *m*-plane GaN/AlGaN heterostructures", C. B. Lim *et al.*, Nanotechnology **27**, 145201 (2016) [275].

For the comparative study of Si vs Ge doping of *m*-plane GaN/AlGaN MQWs with ISB transition in the FIR (section 4.7), I realized design and MBE growth, XRD and FTIR measurements, in collaboration with C. Bougerol (TEM).

4.1. Introduction

As mentioned at the beginning of this chapter, the presence of polarization-induced internal electric fields in polar materials increases the carrier confinement in the wells, which is illustrated in Figure 91 (a). As a result, the energy distance between the quantum confined states saturates as the QW width increases. Figure 91 (b) shows how the piezoelectric component of the electric field renders the ISB absorption energies more sensitive to the strain state of the QWs, making it necessary to develop complex designs to extend the *c*-plane GaN-based ISB technology to the FIR [170,171].

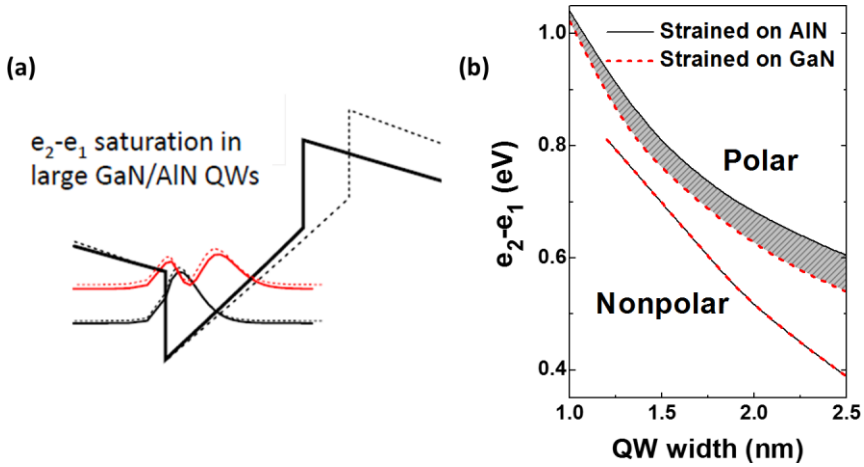

Figure 91 (a) Saturation of the energy distance in the QW as its width increases. (b) Dependence of the ISB transition energy in polar and nonpolar MQWs with different strain states.

The use of QWs grown along nonpolar crystallographic orientations, like the *m*-plane {1–100} or the *a*-plane {11–20} is an alternative to obtain heterostructures without internal electric field [221]. At the beginning of my PhD, high-quality free-standing nonpolar GaN substrates had just been made available. Before that, first experimental results in nonpolar materials were obtained at Bell Labs by heteroepitaxy of *a*-plane GaN:Si/AlN MQWs on *r*-plane sapphire by plasma-assisted MBE showing ISB optical absorption at $\lambda \approx 2.1$ µm with a FWHM of 120 meV [193]. The possibility to perform homoepitaxy of nonpolar GaN resulted in much interest and rapid progress on the growth and development of nonpolar GaN-based ISB. As a successful result, Technion demonstrated *m*-plane QWIPs consisting of $In_{0.095}Ga_{0.905}N/Al_{0.07}/Ga_{0.93}N$ (2.5 nm/56.2 nm) and $In_{0.1}Ga_{0.9}N/GaN$ (3 nm/50 nm) MQWs grown on free-standing *m*-GaN fabricated by the university of California and Santa Barbara, showing photocurrent peaks at 7.5 µm and 9.3 µm, respectively, at 14 K [197]. In

view of these promising results, we decided at the beginning of my PhD thesis to evaluate the potential of the nonpolar GaN/AlGaN technology for applications in the IR spectral range.

4.2. Growth conditions

As a first step, we need to verify that the growth conditions on *c*-plane, *m*-plane and *a*-plane GaN are compatible. To confirm the compatibility of the *c*-plane and *m*-plane GaN growth, we study the Ga adsorption process to GaN surface of both orientations, using free-standing *m*-GaN as well as on *c*-GaN-on-sapphire (for reference). Based on [222,229], we assess the Ga coverage of the GaN surface in function of the impinging Ga flux. The experiment was first performed on *c*-GaN at a substrate temperature $T_s \approx 723°C$. The Ga desorption transients were recorded as a function of the Ga flux by varying the temperature of the Ga cell in steps of 2 degrees. Then, to ensure the same substrate temperature for the *c*-plane and for the *m*-plane substrates, we entered both substrates mounted on the same molyblock and we adjusted the substrate heating to obtain the same Ga desorption from *c*-GaN as previously obtained. Then we shifted the RHEED beam to the *m*-GaN substrate to perform the second experiment as a function of the Ga flux.

The measurement of the Ga coverage proceeds as follows. First, we expose the GaN surface to a Ga flux for a certain time (30s – 1 min), long enough to be sure that the RHEED intensity is stable. This stability implies that we have a constant Ga coverage on the GaN surface, which is only possible if the impinging Ga flux, Φ_{Ga_i}, is equal to the desorbing flux, Φ_{Ga_d}. Then the Ga cell is shuttered, and we record the variation of the RHEED intensity during the resulting Ga desorption transient. We assume that at the moment of shuttering the cell ($t = 0$), the desorption flux is still equal to the impinging flux, $\Phi_{Ga_d}(t = 0) = \Phi_{Ga_i}$. We also assume that at any time, $\Phi_{Ga_d}(t)$ depends only on the Ga coverage on the surface c(t) and on the substrate temperature, which is constant all along the experiment. Therefore, during the desorption process, the variation of the coverage can be expressed as:

$$dc(t) = -\Phi_{Ga_d}(t)dt$$

Around $t = 0$, the equation can be written:

$$dc(t) = -\Phi_{Ga_i}dt$$

Then, if we compare a certain transient (1) with another one measured with an impinging Ga flux only slightly lower (2), we can extract the variation in the Ga coverage from the variation in the desorption time, Δt:

$$c^{(1)} - c^{(2)} = -\left(\Phi_{Ga_i}^{(1)} - \Phi_{Ga_i}^{(2)}\right)\Delta t$$

Integrating from very low Ga fluxes, *i.e.*:

$$c(\Phi_{Ga}) = \int_0^{\Phi_{Ga}} \partial c,$$

it is possible to reconstruct the variation of the Ga coverage as a function of the Ga flux.

The transients recorded for different Ga fluxes are illustrated in Figure 92. We observe various regimes where the desorption time is constant, *i.e.* the Ga coverage remains stable independently of the impinging Ga flux (within that window).

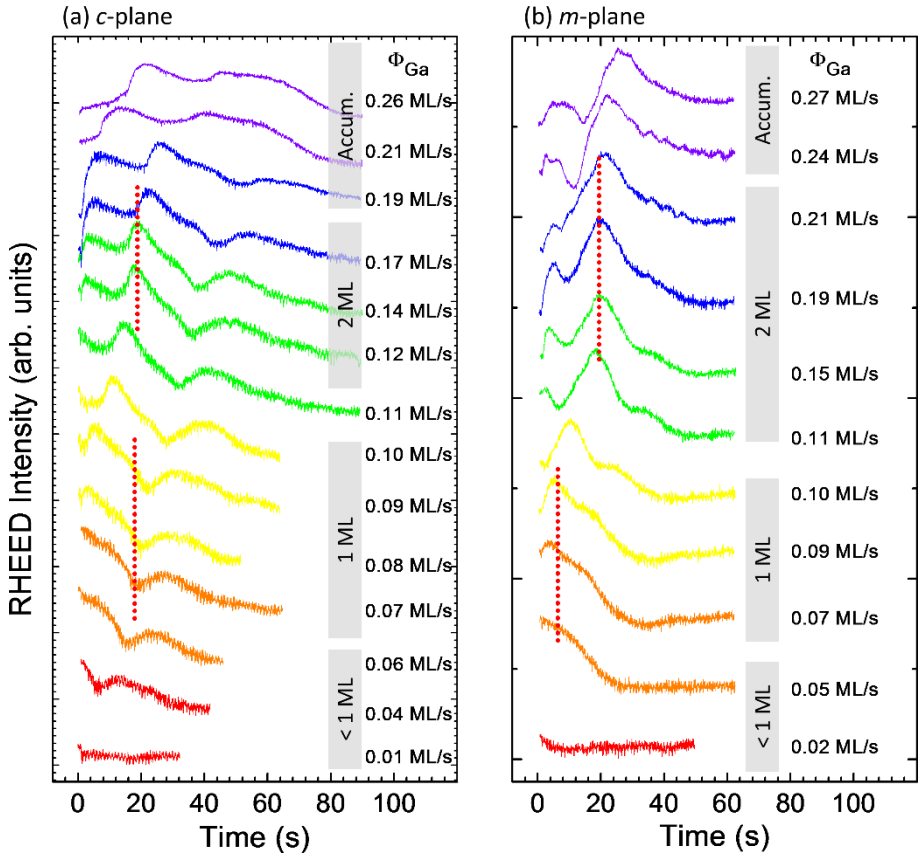

Figure 92 RHEED intensity of the Ga desorption transient for different Ga flux (Ga cell temperature indicated on the right side of the figure) for (a) the *c*-plane GaN (b) the *m*-plane GaN. The dashed lines indicate equivalent states of desorption.

The result of the calculation of the Ga coverage as a function of the impinging Ga flux is plotted in Figure 93 for *c*- and *m*-GaN. As described in subsection 2.3.4 (where the Ga coverage of the GaN surface was studied during GaN growth instead of Ga flux exposure), four regimes are distinguished in both cases of *c*- and *m*-GaN:

- Regime A: a small quantity of Ga is present on the GaN surface for a GaN growth rate about $\Phi < 0.046$ ML/s.
- Regime B: less than 1 ML of Ga at the growth front is present for a GaN growth rate $0.046 < \Phi < 0.095$ ML/s.
- Regime C: a bilayer of Ga (~2.7 MLs for *c*-GaN, ~2.6 MLs for *m*-GaN) at the growth front is formed for flux 0.12 ML/s $< \Phi <$ 0.18 ML/s for *c*-GaN and 0.10 ML/s $< \Phi <$ 0.23 ML/s for *m*-GaN.
- Regime D: the system reaches the Ga accumulation regime (much Ga excess), leading to the formation of metal droplets for flux larger than 0.18 ML/s and 0.23 ML/s for *c*- and *m*-GaN, respectively.

The different regimes of growth are indicated in Figure 92, where we see that the 1 ML and 2 ML coverages correspond to the stability windows of the desorption transients.

The stability windows are very similar for both crystallographic orientations (equivalent of ± 3°C of the Ga cell temperature), which proves that compatible growth conditions exist to obtain smooth 2D growth in the bilayer regime. The slight shift of the growth windows between the substrates is most probably due to a slight difference in the temperatures of the substrates mounted on the same molyblock during the experience of Ga desorption from *m*-plane, which is explained by

the different nature (*i.e.* different thermal conductivity) of the substrates (*c*-GaN-on-sapphire vs bulk *m*-GaN).

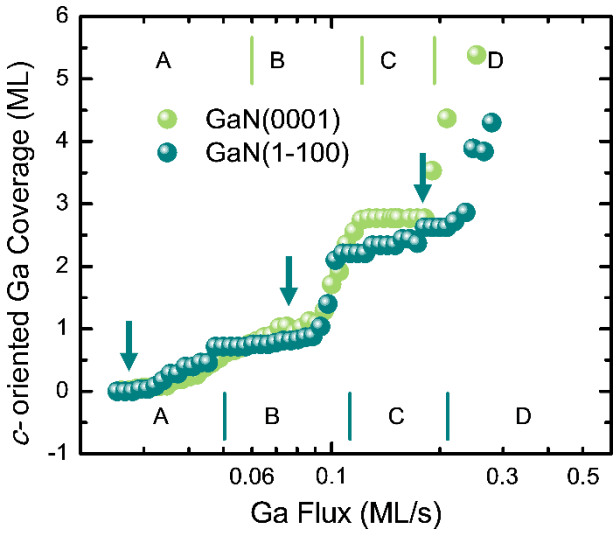

Figure 93 Absolute Ga surface coverage as a function of the impinging Ga flux for *c*-GaN and *m*-GaN.

As shown by Figure 94, *c*-plane and *m*-plane GaN both grow smoothly (similar RMS roughness ≈ 0.8 nm) under the same Ga-rich conditions, which is supported by the literature [222,276,277].

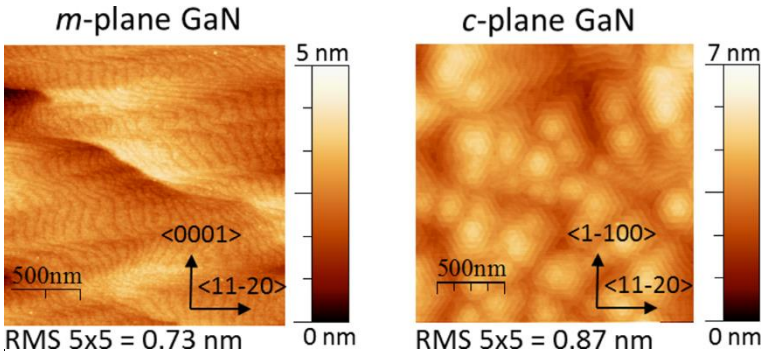

Figure 94 AFM images of *m*-plane and *c*-plane GaN grown in the same Ga-rich conditions.

However, as illustrated in Figure 95, it was not possible to obtain such smooth surfaces when growing under these conditions on the *a*-orientation of GaN.

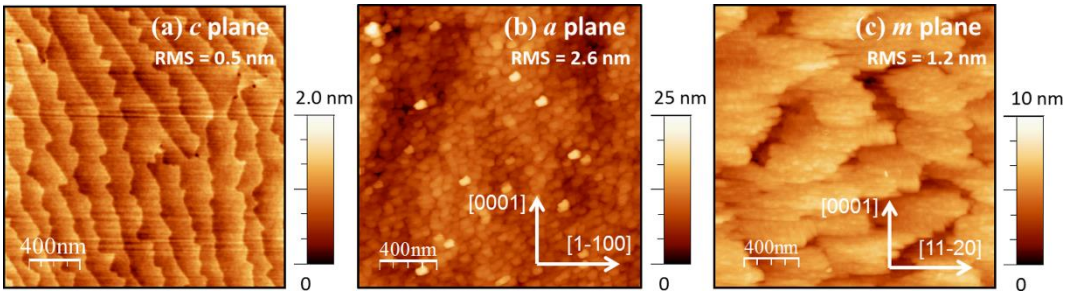

Figure 95 AFM images of (a) *c*-plane (b) *a*-plane (c) *m*-plane (2.5 nm/3.5 nm) GaN/AlN MQWs grown simultaneously under Ga-rich conditions on GaN-on-sapphire and bulk *a*- and *m*-GaN, respectively.

4.3. Choice of a nonpolar orientation: *a* vs *m* plane GaN/AlN MQWs

To choose the best option between the nonpolar *a* and *m*- planes, we compare GaN/AlN MQWs grown simultaneously on *a*- and *m*-GaN substrates as well as on the reference polar *c*-plane. The samples were designed to display ISB transitions in the SWIR region. Indeed, compared to the FIR, this spectral range simplifies the IR optical characterization: FTIR measurements can be performed at room temperature and using a simple liquid-nitrogen-cooled mercury-cadmium-telluride detector. We compare the nonpolar structures in terms of mosaicity, surface roughness, PL linewidth and intensity, and ISB absorption.

4.3.1. Sample description

A series of 40-period GaN/AlN MQWs was grown at a substrate temperature T_s = 720°C with a growth rate of 0.4 ML/s (≈360 nm/h). Samples were grown along the *m*-, *a*- and *c*- crystallographic directions simultaneously, using *a*-and *m*-plane free-standing s.i. GaN substrates and *c*-plane 1-µm-thick AlN-on-sapphire templates all placed on the same molyblock. As explained in Chapter 4.2, this comparison is possible because each of the three crystallographic planes grows two-dimensionally under Ga-rich conditions in plasma-assisted MBE. The structures were designed to show ISB absorption in the 292-795 meV range (1.4-4.2 µm). As an illustration, a sketch of the structures and the band diagram of one of the designs are shown in Figure 96. The QWs were homogeneously doped with Si at a concentration of ≈1×10^{19} cm^{-3}. The geometry of the samples and their characterization results are summarized in Table 15. As an illustration, Figure 97 shows an HR-TEM image of a few QWs in the center of sample E3303m.

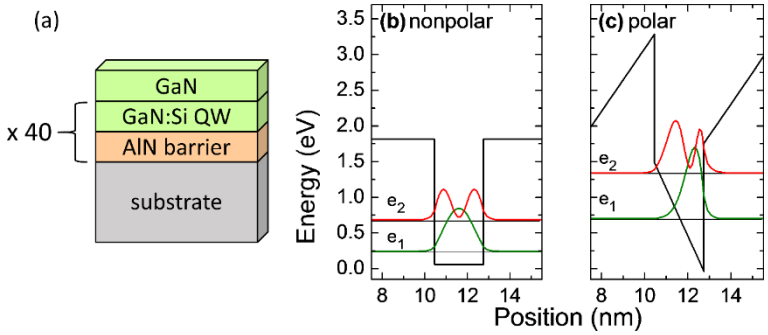

Figure 96 (a) Sketch of the MQW structure. Conduction band diagram of a QW in the center of the active region of sample E3304 grown on (b) nonpolar (c) polar substrate, with the two first electron confined energy levels (e_1, e_2) and their electron wavefunction. Calculations were performed using Nextnano^3 software. (Modified from **[278]**)

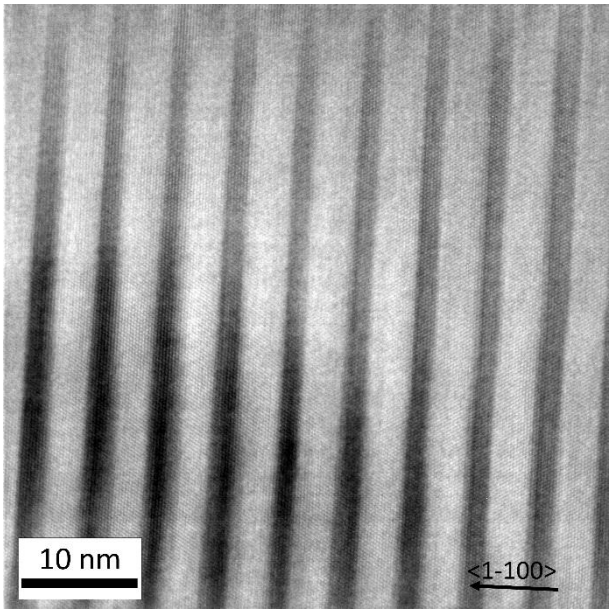

Figure 97 : HR-TEM image of sample E3303m taken along <0001> zone axis. (Reproduced from **[278]**)

Table 15 Structural and optical characteristics of the GaN/AlN MQWs: QW thickness (t_{QW}); MQW period measured by XRD; broadening of the ω-scan of the (3-300) XRD reflection in the *c* and *a* directions ($\Delta\omega_c$ and $\Delta\omega_a$, respectively) for *m*-oriented samples and substrates, and of the ω-scan of the (11-20) XRD reflection in the *c* and *m* directions ($\Delta\omega_c$ and $\Delta\omega_m$, respectively) for *a*-oriented samples and substrates; tilt between the MQW and the GaN substrate towards the *c* and *a* directions ($\delta\omega_c$ and $\delta\omega_a$, respectively) for *m*-oriented samples, and towards the *c* and *m* directions ($\delta\omega_c$ and $\delta\omega_m$, respectively) for *a*-oriented samples; strain state in the 3 perpendicular directions *m*, *a* and *c* (ε_m, ε_a, and ε_c respectively); PL peak energy and intensity normalized with respect to E3303m; simulated and measured ISB transition energy.

Sample	t_{QW} (nm)	XRD Period (nm)	XRD FWHM MQW (°)	XRD FWHM GaN (°)	Tilt MQW/GaN (°)	Strain (%)	PL peak energy (eV) [norm. int.]	Sim. / Meas. ISB transition (meV)
E3303m	1.5	5.1	$\Delta\omega_c = 0.33$ $\Delta\omega_a = 0.39$	$\Delta\omega_c = 0.028$ $\Delta\omega_a = 0.028$	$\delta\omega_c = 0.20$ $\delta\omega_a = 0.04$	$\varepsilon_m = 0.38\pm0.15$ $\varepsilon_a = -1.03\pm0.40$ $\varepsilon_c = -0.36\pm0.40$	3.8 [1]	712 / 799
E3304m	2.3	5.9	$\Delta\omega_c = 0.44$ $\Delta\omega_a = 0.30$	$\Delta\omega_c = 0.037$ $\Delta\omega_a = 0.040$	$\delta\omega_c = 0.08$ $\delta\omega_a = 0.015$	$\varepsilon_m = 0.44\pm0.15$ $\varepsilon_a = -0.50\pm0.40$ $\varepsilon_c = -0.17\pm0.40$	3.8 [0.94]	437 / 578
E3305m	3.1	6.7	$\Delta\omega_c = 0.45$ $\Delta\omega_a = 0.29$	$\Delta\omega_c = 0.026$ $\Delta\omega_a = 0.032$	$\delta\omega_c = 0.05$ $\delta\omega_a = 0.01$	$\varepsilon_m = 0.41\pm0.15$ $\varepsilon_a = -0.63\pm0.40$ $\varepsilon_c = -0.23\pm0.40$	3.7 [0.58]	296 / 425
E3303a	1.5	5.1	$\Delta\omega_c = 0.28$ $\Delta\omega_m = 0.72$	$\Delta\omega_c = 0.030$ $\Delta\omega_m = 0.030$	$\delta\omega_c = 0.16$ $\delta\omega_m = 0.00$	$\varepsilon_a = 0.33\pm0.15$ $\varepsilon_m = -0.56\pm0.40$ $\varepsilon_c = -0.62\pm0.40$	3.9 [0.56]	712 / 815
E3304a	2.3	5.9	$\Delta\omega_c = 0.53$ $\Delta\omega_m = 0.40$	$\Delta\omega_c = 0.019$ $\Delta\omega_m = 0.023$	$\delta\omega_c = 0.29$ $\delta\omega_m = 0.015$	$\varepsilon_a = 0.32\pm0.15$ $\varepsilon_m = -0.42\pm0.40$ $\varepsilon_c = -0.09\pm0.40$	3.7 [0.24]	431 / 755
E3305a	3.1	6.7	--	--	--	--	3.7 [0.11]	296 / --
E3303c	1.5	5.1	--	--	--	--	3.7 [0.014]	814 / 815
E3304c	2.3	5.9	--	--	--	--	3.2 [0.008]	657 / 731
E3305c	3.1	6.7	--	--	--	--	3.0 [0.003]	603 / 624

4.3.2. Structural characterization

To evaluate their structural quality, the surface morphology of the samples was assessed by SEM and AFM. On a large scale, the SEM images of the nonpolar samples show smooth surfaces with cracks propagating along the *c* axis, with an average distance between cracks of ≈ 10 µm, resulting in {11-20} or {1-100} facets for *m*- or *a*-oriented samples, respectively. In the polar case, cracks propagation occurs when GaN/Al(Ga)N heterostructures are grown under tensile strain. In this case, cracks are isotropically distributed and present vertical {1-100} facets [279,280]. Due to the anisotropy of the nonpolar lattices, relaxation along the *c* and the *a/m* directions must be analyzed independently.

Cracks propagating along the in-plane axis *m* have been described in *a*-AlN grown on *a*-plane 6H-SiC [281], which was explained as due to the tensile strain along the *c* axis (-1.1% lattice mismatch) in combination with a lack of low-energy slip systems available for plastic relaxation. However, in a highly compressed configuration (with larger mismatch such as *a*-GaN on *r*-sapphire having +1.2% and +16.1% lattice mismatch along *c* and *m*, respectively), cracks are observed to propagate preferentially along the *c* axis [282,283]. In the case of *m*-AlGaN, cracks propagating along the in-plane axis *a* have been reported [284,285]. For the samples under study, we can see on the SEM images that the cracks appeared once the surface features were formed, showing that these cracks did not develop during the growth, but instead during the cooling process, as a result of the temperature-dependent GaN/AlN lattice mismatch [51].

On the AFM scale, the RMS surface roughness measured in the 5×5 µm² image was 1.1 ± 0.2 nm, 2.0 ± 0.6 nm, and 3.7 ± 1.2 nm for *c*-, *m*-, and *a*-plane samples, respectively. The *m*-plane growth systematically resulted in smoother surfaces than *a*-plane growth.

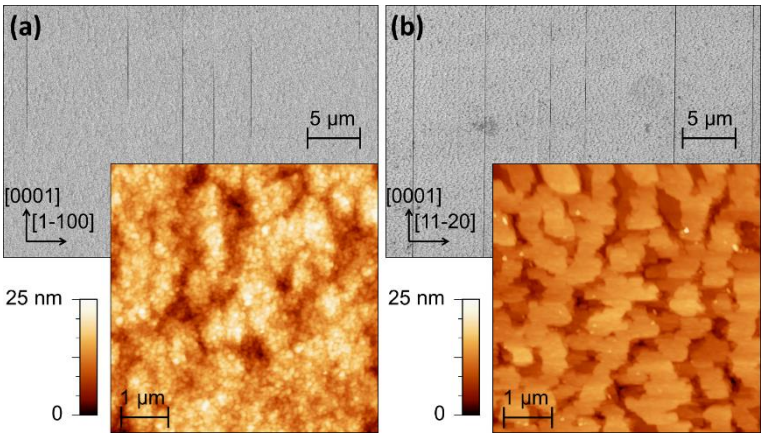

Figure 98 SEM and AFM images of GaN/AlN (3.1/3.6 nm) MQWs grown on (a) *a*-plane and (b) *m*-plane. Note that the crystallographic axis are the same for both the SEM and AFM images. (Reproduced from **[273]**)

The periodicity and strain state of the samples were analyzed by HR-XRD. Figure 99 shows the ω-2θ scans of the (3-300) reflection of the *m*-plane samples and of the (11-20) reflection of two *a*-plane samples, with the QW thicknesses indicated on the right side of the figure. Table 15 summarizes the MQW period extracted from the inter-satellite distance in the ω-2θ scans. The FWHM of the rocking curves were measured for the substrate and the MQW zero-order reflection (MQW0 peak on Figure 99) in the *c* and *a* (respectively *c* and *m*) directions for the *m*-oriented (respectively *a*-oriented) samples, which provides information on the sample mosaicity in the measured direction.

Comparing the values in Table 15, it appears that the *m*-plane MQWs exhibit better crystalline quality than the *a*-plane structures.

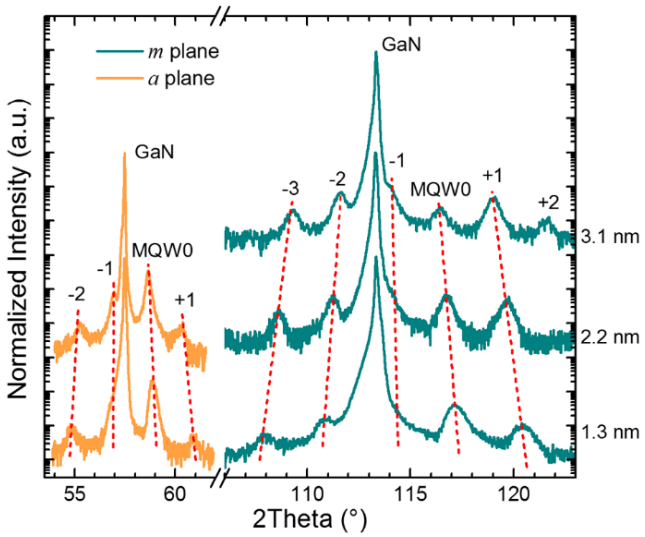

Figure 99 XRD ω-2θ scans of the (3-300) reflection of samples E3303m, E3304m, and E3305m and the (11-20) reflection of samples E3303a and E3304a. The corresponding QW thicknesses are indicated at the right side of the figure. (Reproduced from **[273]**)

To assess the MQW strain state, reciprocal space maps were measured. Figure 100 illustrates the results for sample E3304m, where the (3-300) (*i.e.* oriented along *c*), (3-302) (*i.e.* with the *c*-axis in the diffraction plane), and (3-2-20) (*i.e.* with the *a*-axis in the diffraction plane) reflections were considered. The reciprocal space is presented using the GaN substrate as a reference. In Figure 100 (b), we observe a shift in q(0001) (projection of the reciprocal space vector along [0001]) of the MQW (3-300) reflection with respect to the substrate, which reveals a tilt of the epitaxial structure. The tilt angles towards the in-plane directions ($\delta\omega_c$ and $\delta\omega_a$ for *m*-oriented samples, and $\delta\omega_c$ and $\delta\omega_m$ for *a*-oriented samples) are summarized in Table 15. Taking the measured tilt into account, the strain states along the *a*, *m* and *c* axis can be described as $\varepsilon_p = \frac{p-p_r}{p_r}$, where ε_p is the strain along the axis *p* (*a*, *m* or *c*), *p* is the measured lattice parameter along this axis, and p_r is the theoretical value of *p* assuming that the structure is relaxed. Using the lattice parameters of Vurgaftman *et al.*[34] and Wright *et al.*[72] (a_{GaN} = 3.1891 Å; a_{AlN} = 3.112 Å; c_{GaN} = 5.1850 Å; c_{AlN} = 4.980 Å), the lattice mismatch between AlN and GaN is –2.4% in the *a* and *m* directions and –3.9% in the *c* direction. The larger mismatch along *c* explains the larger tilt towards this direction (0.05° to 0.29°). This tilt is a way to relax the in-plane lattice mismatch, and thus to reduce the number of dislocations necessary to release the strain.[286]

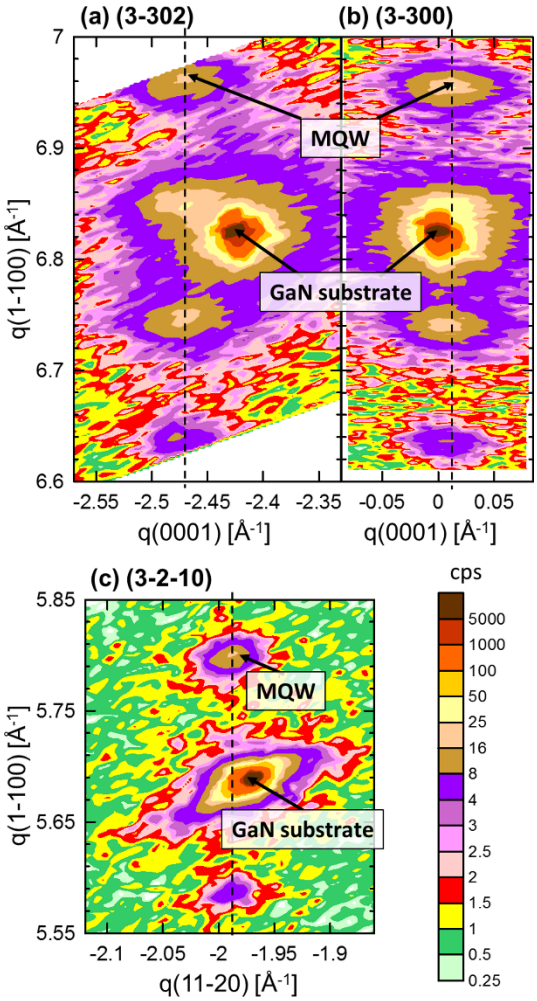

Figure 100 Reciprocal space maps of sample E3304m around the asymmetric reflections (a) (3-302) with the *c*-axis in the diffraction plane and (c) (3-2-10) with the *a*-axis in the diffraction plane, and the symmetric reflection (b) (3-300) oriented along *c*. (Reproduced from **[273]**)

Figure 101 presents the values of strain extracted from the reciprocal space maps, compared with the in-plane lattice mismatch between the GaN substrates and the relaxed MQWs (considered as a relaxed AlGaN alloy with the average Al composition of the structure). The positive (negative) values of strain correspond to compressive (tensile) strain. Due to the lattice mismatch, all the structures undergo in-plane tensile strain, and as a result of Hooke's law, they are compressively strained in the growth direction. In the case of *m*-oriented samples, all the MQWs are about 50% relaxed along the in-plane *a* axis, whereas almost full relaxation is observed along *c*. This strong relaxation along *c*, *i.e.* parallel to the crack propagation axis, points to the presence of extended defects in the structure.

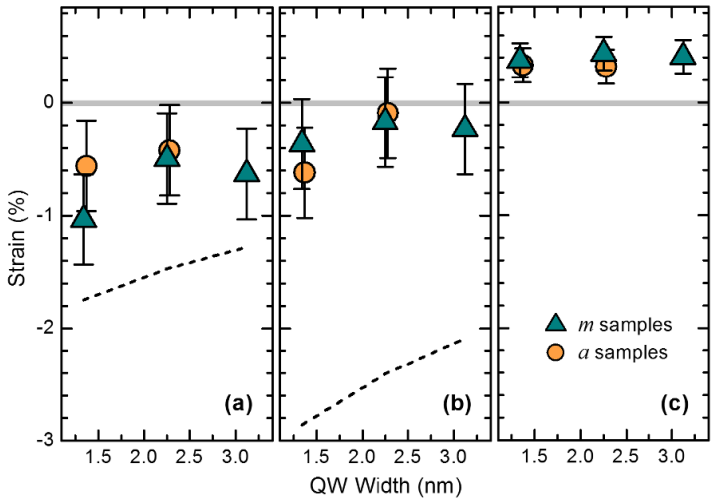

Figure 101 Strain state of the MQWs extracted from the XRD measurements. (a) In-plane lattice parameter *a* (*m* samples) or *m* (*a* samples). (b) In-plane lattice parameter *c*. (c) Out-of-plane lattice parameter. Dashed lines indicate the lattice mismatch between a relaxed AlGaN layer with the average Al concentration of the MQW and the GaN substrate. (Reproduced from **[273]**)

To visualize the defect structure in these *m*-plane MQWs, HAADF-STEM was performed. Figure 102 shows a cross-section view along *a* of the GaN substrate/MQW interface of sample E3304m, with AlN barriers. We observe the generation of a high density of stacking faults (SFs) which initiates at the very interface and propagate to the sample surface. The observed strain relaxation appears to be associated to the partial dislocations that limit the stacking faults. The presence of this defect structure, which relaxes the elastic energy, explains the absence of cracks propagating along the in-plane axis *a*.

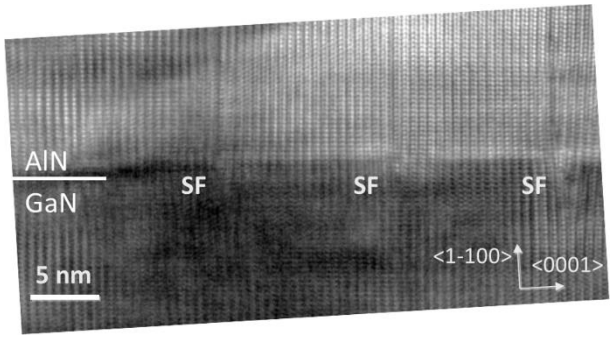

Figure 102 : HR-TEM image of the GaN substrate/MQW interface in sample E3304m viewed along <11-20>, displaying a high density of stacking faults. (Reproduced from **[287]**)

As a conclusion of the above-presented structural characterization, the *m*-plane MQWs exhibit smoother surface, better mosaicity and crystalline quality than the *a*-plane structures.

4.3.3. Optical characterization

To assess the band-to-band properties of the MQWs, the PL spectra of all the samples were measured at low temperature (T = 5 K), with the results in terms of emission wavelength and intensity

summarized in Table 15. As an illustration, Figure 103 (a) shows the spectra of samples E3304c, E3304m and E3304a. For all samples, the *c*- and *a*- orientations systematically lead to broader emission peaks than those measured for the *m*-orientation. In addition, the PL from *m*-plane samples is twice as intense as that from *a*-plane, and more than twenty times as intense as that from *c*-plane QWs, whose PL is quenched due to the quantum confined Stark effect.

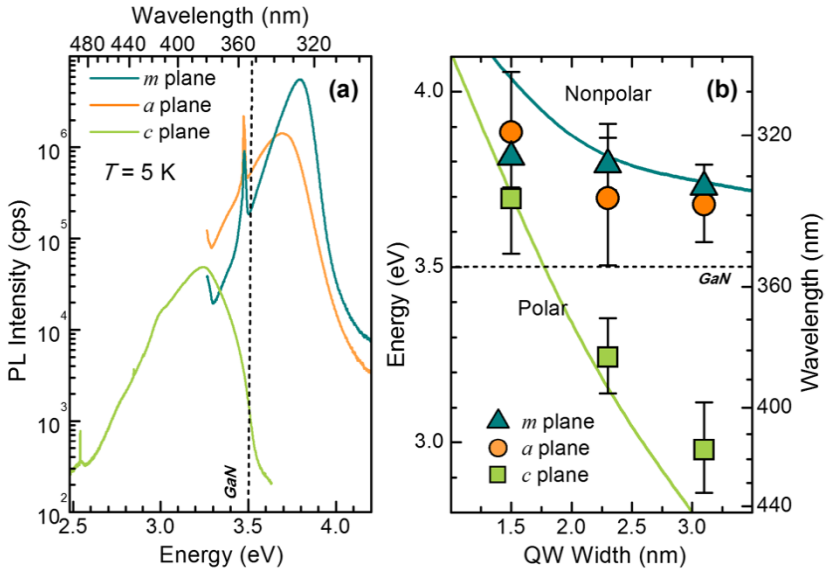

Figure 103 (a) PL spectra of samples measured at low temperature (T = 5 K). (b) PL peak energies as a function of the QW width. Error bars correspond to the FWHM of the PL peaks. Solid lines are theoretical calculations assuming that the in-plane lattice parameters of the MQWs correspond to those of a relaxed AlGaN alloy with the average Al composition of the structure. Dashed lines mark the location of the GaN bandgap. (Reproduced from **[273]**)

In Figure 103 (b), the PL peak emission energies are compared with theoretical calculations assuming that the in-plane lattice parameters correspond to those of an AlGaN ternary alloy with an Al composition equal to the average Al content of the MQW. For nonpolar samples, their luminescence is systematically above the GaN band gap, confirming the absence of internal electric field. For the *c*-plane samples, the emission energy shifts below the GaN band gap when increasing the well width. In general, the emission energies are in agreement with the theoretical calculations. The deviation from the calculations observed for the smallest QWs (E3303) is attributed to carrier localization in thickness fluctuations in such small QWs (the thickness of a GaN monolayer being ≈ 0.25 nm).

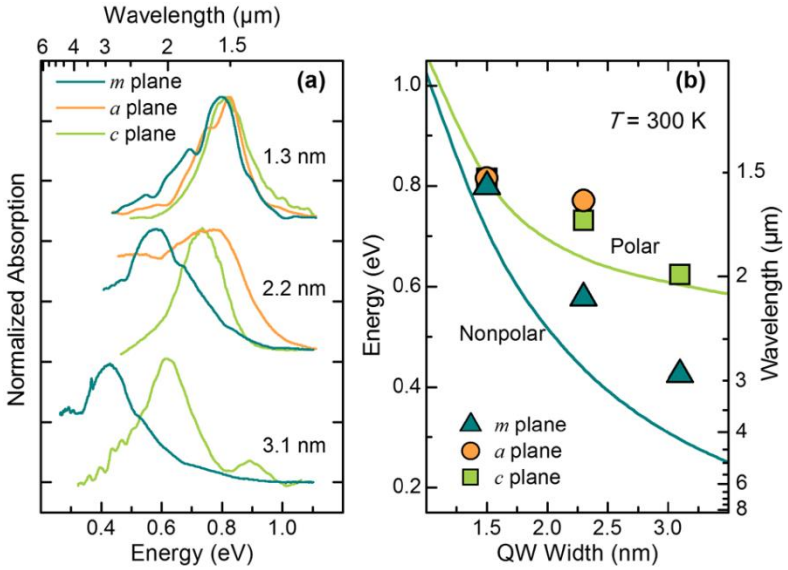

Figure 104 (a) TM-polarized ISB absorption of the samples measured at room temperature. Data are normalized and vertically shifted for clarity. The corresponding QW thicknesses are indicated on the right side. (b) ISB energies as a function of the QW width. Solid lines correspond to theoretical simulations assuming that the in-plane lattice parameters of the MQWs correspond to those of a relaxed AlGaN alloy with the average Al composition of the structure. (Reproduced from **[273]**)

To assess the ISB properties of the samples, the ISB absorption in the SWIR range was measured at room temperature by FTIR spectroscopy. The ISB nature of the transition is set because absorption is observed in the case of TM-polarized light, and no absorption is observed under TE-polarized light illumination. To identify the ISB transition energy in the samples, the TE transmission spectra were divided by the respective TM transmission spectra, and the results are presented in Figure 104 (a) and Table 15. As expected, the absorption energy is red-shifted when increasing the QW width. In the case of nonpolar MQWs, the absence of the internal electric field results in a redshift of the ISB energy, in comparison to *c*-plane structures, where the triangular potential profile in the wells contributes to the separation of the quantized electron levels. A similar result was observed in the case of semipolar (11-22) MQWs due to the reduction of spontaneous and piezoelectric polarizations [190]. The TM polarized absorption of nonpolar *a*-plane sample E3304a undergoes a significant broadening and deviation from the calculations, and no ISB absorption was observed for sample E3305a. In contrast, nonpolar *m*-plane samples exhibit an absorption linewidth similar to that of polar MQWs absorbing at the same wavelengths.

The difference between simulations and experimental results on ISB absorption peak energies may have several origins, namely the strain state, many-body effects, or fluctuations in layer thickness:

- In our calculations, we assume that the in-plane lattice parameter of the MQW corresponds to the one of relaxed AlGaN with the average alloy composition of the structure. A variation of the strain state has a significant influence on the ISB energy in the case of *c*-plane QWs [160], due to the piezoelectric component of the internal electric field. In contrast, in semipolar and nonpolar crystallographic orientations, the effect of the strain state is negligible [189].
- Because of the high doping level, many-body effects result in a blueshift of the transition, which can reach about 30 meV for the doping levels under study in the SWIR and MIR [288]. The effect is comparable in polar and nonpolar structures.

– In polar structures the internal electric field renders the ISB transition energies more sensitive to QW thickness fluctuations compared to nonpolar structures. In 2-nm-thick polar QWs, a variation of the QW thickness by 0.25 nm may shift the ISB energy by 100 meV (typical interface roughness in the range of ±0.25 nm). In contrast, in 2-nm-thick nonpolar QWs, a variation of the QW thickness by 0.25 nm shifts the ISB energy by less than 50 meV. The typical thickness fluctuations observed in HR-TEM images of nonpolar GaN/AlN QWs being as high as ±1 nm might explain the deviation from the expected energies.

4.3.4. Conclusions

In summary, we have grown 40-period GaN/AlN MQWs with various GaN QW widths, with the QWs doped with Si, designed to show ISB absorption in the SWIR range. To allow their comparison, each design was grown simultaneously on 3 substrates: a bulk nonpolar *a*-plane GaN substrate, a bulk nonpolar *m*-plane GaN substrate and polar *c*-plane GaN template. Compared to nonpolar *a* plane samples, *m*-plane structures display better results in terms of mosaicity, surface roughness, PL linewidth and intensity, and ISB absorption. Furthermore, the *m*-plane GaN/AlN MQWs showed ISB absorption in the 1.5-2.9 µm range, covering the whole SWIR spectrum, with performance comparable to polar *c*-plane MQWs.

4.4. *m*-plane GaN/AlGaN MQWs with ISB transition in the Mid-Infrared

Based on the results of chapter 4.3, we now analyze the possibility to cover the MIR spectral region with nonpolar *m*-plane GaN/AlGaN MQWs.

4.4.1. Sample description

To obtain ISB transition in this spectral range, we enlarge the QW widths, and we replace the AlN barriers by AlGaN (*i.e.* decrease the Al composition of the barrier) with a twofold purpose: reducing the lattice mismatch in the MQW and approaching the excited level in the QW to the continuum to mimic the band diagram of a QWIP by reducing the band offset. A sketch of the designed structures is shown in Figure 105. Four *m*-plane structures were designed to display ISB transitions between the ground conduction band level and the first excited level ($e_1 \rightarrow e_2$) in the 186-356 meV (3.4-6.7 µm) range, using the QW thicknesses and Al contents in the barriers summarized in Table 16. The samples consist of 50-period GaN/AlGaN MQWs with Al composition between 26% and 44%, and with each design being grown simultaneously on an *m*-plane free-standing s.i. GaN substrate and on a *c*-plane GaN-on-Si(111) template placed on the same molyblock. The barriers were chosen to be 22.6 nm thick, in order to prevent coupling between QWs even in the largest QWs. The QWs were Si-doped with $[Si] \approx 2\times10^{19}$ cm^{-3} for samples E3399, E3401, and E3402. Sample E3403 was doped with $[Si] \approx 8\times10^{18}$ cm^{-3}. The MQWs structures were capped with ≈ 100 nm GaN.

In this spectral range, we must keep in mind that the use of bulk GaN as a substrate sets an additional limit for characterization. Even though the GaN Reststrahlen band spans from 9.6 µm to 19 µm, absorption in the range of 6.7 µm to 9 µm has been observed in bulk GaN substrates with carrier concentrations $<10^{16}$ cm^{-3}, and was attributed to the second harmonic of the Reststrahlen band [67,120,121]. Figure 105 shows the band diagrams of the *m*-plane MQWs, together with those of

structures with the same dimensions but grown along the *c* direction. In the case of nonpolar samples, two quantum confined states only are allowed in the well and the upper states are at the top of the barrier. In the case of polar samples, the upper states e_3 e_4 are also allowed in the well, making it theoretically possible to observe more than one ISB transition. In the case of the *c*-oriented MQWs studied in this work, characterization of ISB absorption in the spectral range between 6.7 µm and 9 µm is possible due to the use of floating-zone silicon substrates, as previously demonstrated [169].

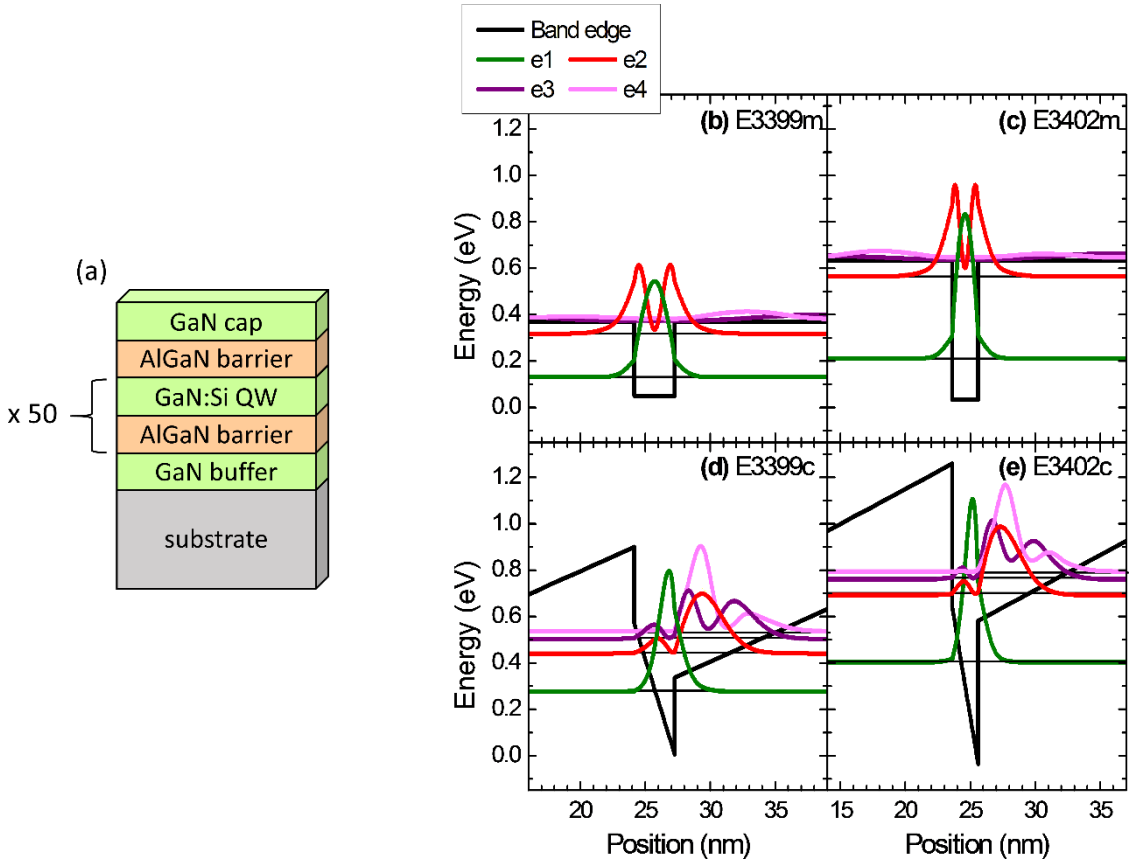

Figure 105 (a) Sketch of the MQW structure. Conduction band diagram with first four energy levels and electron wavefunctions of a QW in the center of the active region of samples (b) E3399m, (c) E3402m, (d) E3399c, and (e) E3402c. (Modified from **[273]**)

Table 16 Structural and optical characteristics of the GaN/AlGaN samples: QW thickness (t_{QW}); MQW period measured by XRD; Al composition in the barrier (x_B); PL peak energy; simulated and measured first ($e_1 \rightarrow e_2$), second ($e_1 \rightarrow e_3$) and third ($e_1 \rightarrow e_4$) ISB transition energies. (*) Thickness extrapolated from XRD measurements of other samples in the same series.

Sample	t_{QW} (nm)	XRD Period (nm)	x_B (%)	PL peak energy (eV)	Simul. ($e_1 \rightarrow e_2$) / Meas. ISB transition (meV)	Simul. ($e_1 \rightarrow e_3$, $e_1 \rightarrow e_4$) / Meas. ISB transition (meV)
E3399m	3.1	25.7 (*)	26	3.60	186 / 222	--
E3401m	2.8	25.4 (*)	31	3.64	223 / 213	--
E3403m	2.5	25.1 (*)	35	3.39	261 / 251	--
E3402m	2.0	24.6 (*)	44	3.40	356 / 308	--
E3399c	3.1	25.7 (*)	26	3.61	162 / 188	227, 256 / 270
E3401c	2.8	25.4	31	3.68	200 / 209	264, 294 / 319
E3403c	2.5	25.1	35	3.41	226 / 241	292, 323 / 326
E3402c	2.0	24.6	44	3.46	290 / 286	358, 387 / 378

4.4.2. Structural characterization

As a first evaluation of the structural quality, the surface morphology was assessed by AFM and SEM, as illustrated in Figure 106 for sample E3399m. Similar to the SWIR samples, SEM images of the nonpolar samples reveal cracks propagating along the *c*-axis. However, the distance between cracks increased to ≈15-30 µm, in comparison with ≈ 10 µm for GaN/AlN MQWs. At the AFM scale, all the nonpolar samples in Table 16 present similar morphology: large-scale (5×5 µm² to 10×10 µm² images) roughness in the range of 7-15 nm with features elongated along the <11-20> direction, whereas at a smaller scale (1×1 µm² images) the surfaces are smooth, with RMS roughness in the 1-2 nm range.

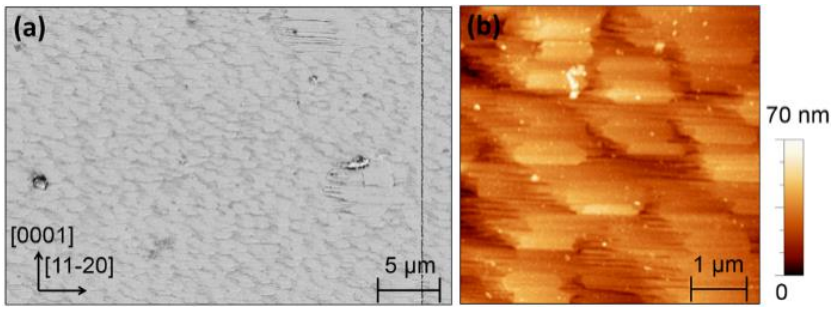

Figure 106 Typical (a) SEM and (b) AFM images of the GaN/AlGaN MQWs in Table 16. Note that the crystallographic axis are the same for both images. Measurements correspond to sample E3399m. (Reproduced from **[273]**)

This reduction in the crack density compared to the previous GaN/AlN MQWs points to a modification of the distribution of extended defects in the structure. Figure 107 displays a HAADF-STEM cross-section view along *a* of sample E3402m, with AlGaN barriers. In addition to the stacking fault network, the barriers present dark horizontal areas (arrows in Figure 107). These features are identified as AlN-rich clusters, in agreement with [289], in which similar Al-rich elongated clusters are observed in *m*-plane GaN/AlGaN heterostructures grown under N-rich conditions.

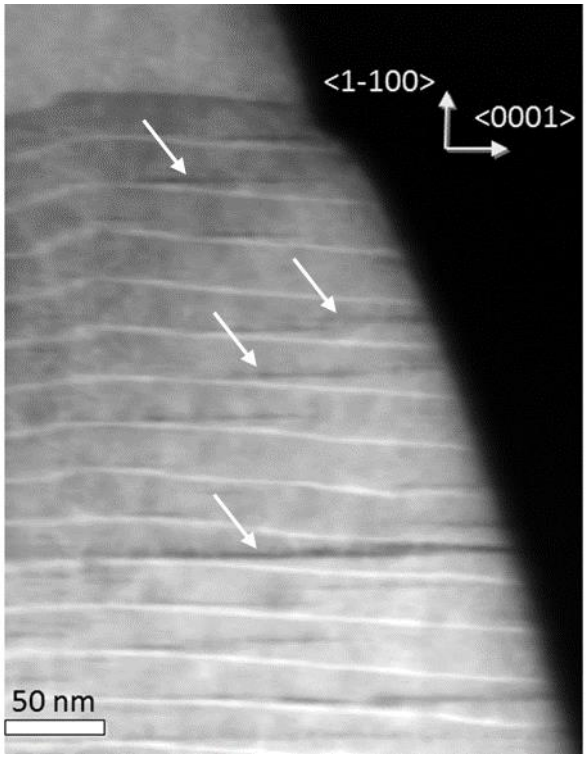

Figure 107 HAADF-STEM image of a sample E3402m viewed along <11-20>. Layers with dark and bright contrast correspond to the AlGaN barriers and GaN QWs respectively. (Reproduced from **[287]**)

The periodicity, strain state and mosaicity of sample E3402m were further analyzed by XRD. To assess the MQW strain state, we measured various reciprocal space maps for sample E3402m (the error bars of this technique were too large to extract reliable conclusions in samples with lower Al composition). The calculated strain components are ε_m = 0.03±0.15%, ε_a = –0.43±0.40%, and ε_c = –0.27±0.40%. Compared to the relaxed lattice mismatch between the GaN/$Al_{0.44}Ga_{0.56}N$ MQW and the GaN substrate (–0.98% in the *a* and *m* directions and –1.6% in the *c* direction), they confirm a certain relaxation in spite of the large error bars of the measurement. The FWHM of the rocking curves of the MQW reflection were $\Delta\omega_c$ = 0.28° and $\Delta\omega_a$ = 0.22°, pointing to a significant improvement of the MQW crystalline quality with respect to the GaN/AlN MQWs (see Table 15) thanks to the reduced lattice mismatch.

4.4.3. Optical characterization

The PL spectra of the samples were measured at low temperature, as illustrated by Figure 108 (a). In Figure 108 (b), the PL emission energies are compared with theoretical calculations as a function of the QW width. For the *c*-plane samples, the luminescence is systematically below the GaN bandgap due to the internal electric field, and it exhibits superimposed oscillations due to Fabry-Perot interferences. For nonpolar samples, the emission remains above the GaN band gap energy. In both cases, decreasing the QW width leads to a redshift of the PL energy, with emission energies in agreement with the calculations.

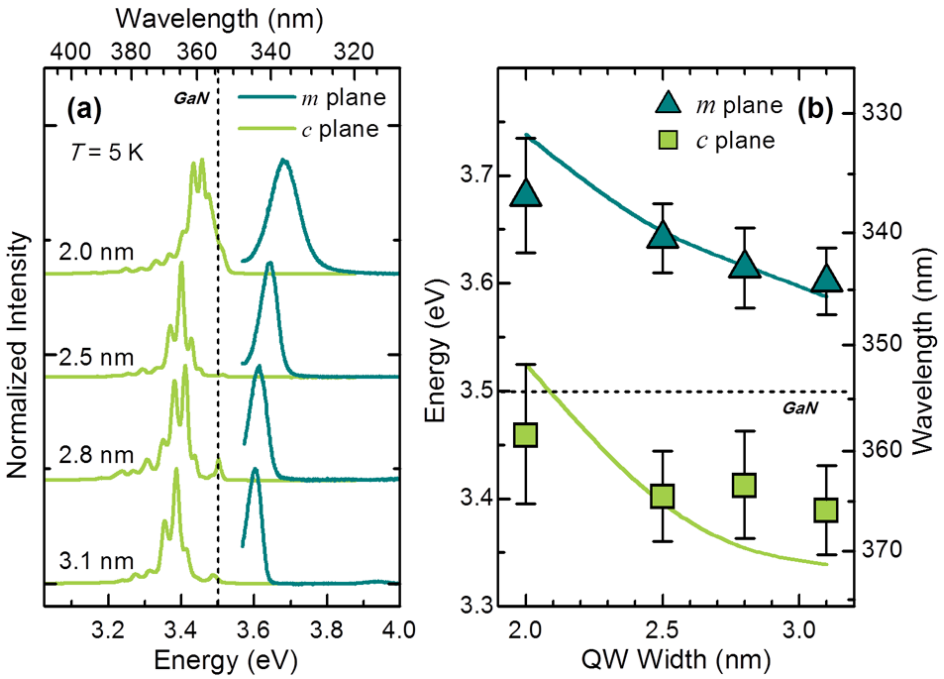

Figure 108 (a) PL spectra of the *m*- and *c*-plane GaN/AlGaN MQWs in Table 16 measured at low temperature. Data are normalized and vertically shifted for clarity. The corresponding QW thicknesses are indicated on the left side. (b) PL peak energies as a function of the QW width. Error bars correspond to the FWHM of the PL emission. Solid lines are theoretical calculations of the band-to-band transition assuming that the in-plane lattice parameters of the MQWs correspond to those of a relaxed AlGaN alloy with the average Al composition of the structure. Dashed lines mark the location of the GaN band gap. (Reproduced from **[273]**)

We also measured the variation of the luminescence with temperature, which presents the behavior that is illustrated Figure 109 for an *m*-plane typical sample (E3399m). The fit represented in red solid line was calculated following [290]:

$$I = \frac{I_0}{1 + \alpha_1 \exp\left(-\frac{E_a}{kT}\right)} \tag{93}$$

where I is the PL intensity, I_0 the PL peak intensity, α_1 is a constant parameters, E_a is the activation energy, *k* is the Boltzmann constant, and T is the sample temperature during the measurement. From this fit, we obtain an activation energy of $E_a = 12.3 \pm 3$ meV. This is in agreement with literature, where an activation energy of 15 ± 3 meV was found for GaN/AlN MQWs [266].

The PL intensity drop from low temperature to room temperature is less than one order of magnitude, which is rather characteristic of quantum dots systems, where the 3D confinement reduces the effect of non-radiative recombination centers[265,266,291–293]. In *c*-plane samples with similar characteristics, the PL intensity drop can reach several orders of magnitude [265,294,295]. Looking at the TEM images, the carrier localization that leads to thermal stability of the PL in *m*-plane structures can be assigned to the thickness inhomogeneity of the QWs, which can generate some lateral carrier confinement.

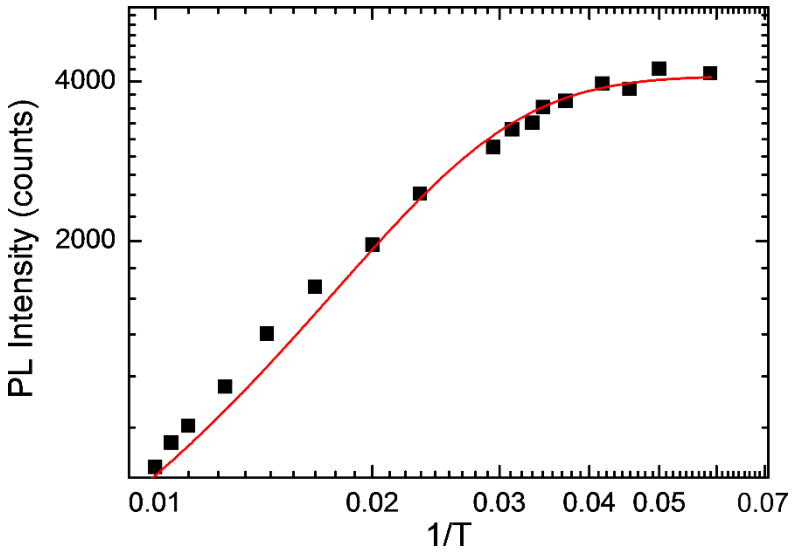

Figure 109 PL peak intensity versus temperature and fit to equation (93) for sample E3399m.

The ISB absorption in the MIR range was measured at room temperature by FTIR spectroscopy. To identify the ISB transition in the samples, the substrate transmission spectrum was divided by the respective TM transmission spectra, with the results displayed in Figure 110 (a) and (b).

In nonpolar structures, increasing the QW width leads to a redshift of the ISB energies from 308 to 213 meV (4.0 to 5.8 µm), in agreement with calculations as shown in Figure 110 (c). The deviation observed in the sample with the largest QWs (calculated transition at 186 meV) is attributed to the proximity of the second order of the Reststrahlen band at 184 meV (6.7 µm), which sets the onset of substrate absorption [shadowed area in Figure 110 (a) and (c)]. These results complete the work of The University of Tokyo [296], which has recently demonstrated room-temperature MIR ISB absorption in the range from 256 meV to 295 meV (4.20 to 4.84 µm) in *m*-plane GaN/$Al_{0.5}Ga_{0.5}N$ MQWs grown by MOCVD on free-standing *m*-GaN substrates. The same group also recently studied the temperature-dependence of MIR ISB absorption in *m*-GaN/AlGaN MQWs [297]. They showed that these nonpolar structures had a stable temperature behavior compared to polar ones, which would be advantageous to develop ISB devices operating over a wide range of temperatures.

For all polar samples, two absorption peaks are observed. The peak at lower energy corresponds to the ($e_1 \rightarrow e_2$) transition, whereas the higher energy peak is assigned to ISB transitions involving upper states ($e_1 \rightarrow e_3$, $e_1 \rightarrow e_4$), as previously observed in GaN/AlN QWs [298]. In symmetric structures, the $e_1 \rightarrow e_3$ transition is forbidden due to parity, whereas $e_1 \rightarrow e_4$ is allowed. However, both transitions are possible in asymmetric polar QWs, and the second peak might hence correspond to the combination of both transitions.

In this series of samples, the absorption in *m*- and *c*-oriented MQWs is located in the same spectral range, both theoretically and experimentally. This coincidence is due to the choice of the Al content in the barriers, which determines the energetic location of e_2 in the *c*-plane structures. Increasing the Al content of the barriers would introduce only slight corrections to ($e_1 \rightarrow e_2$) in *m*-plane MQWs, but it would induce a major blueshift of this transition in the *c*-plane MQWs due to the internal electric field.

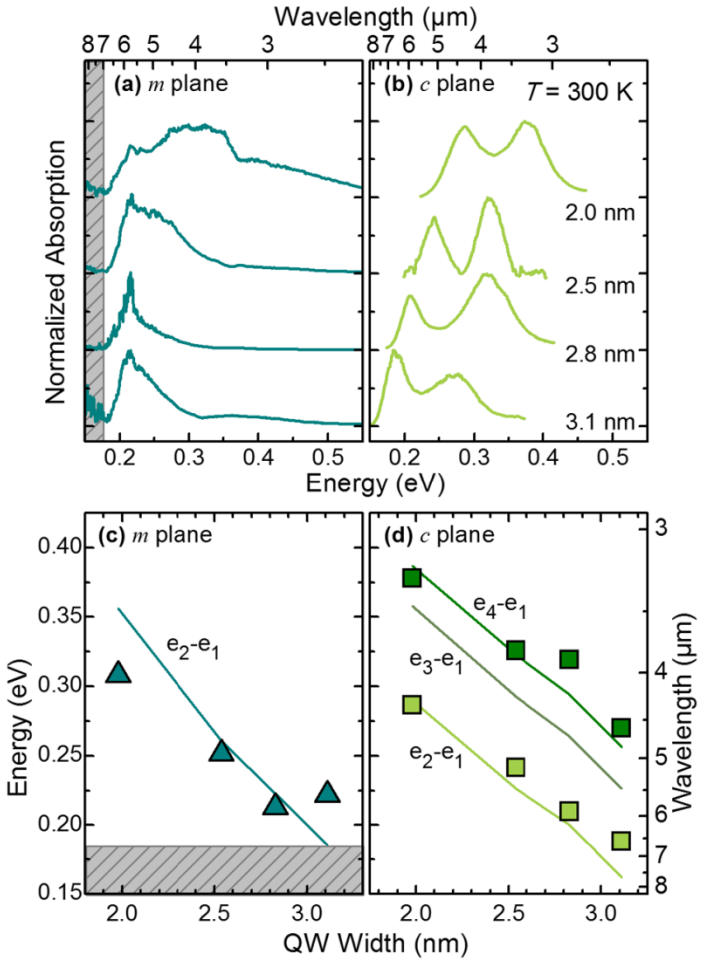

Figure 110 TM-polarized ISB absorption spectra for (a) the *m*-plane and (b) *c*-plane GaN/AlGaN MQWs in Table 16 measured at room temperature. Data are normalized and vertically shifted for clarity. The corresponding QW thicknesses are indicated on the right side. ISB energies as a function of QW width for all (c) *m*-plane and (d) *c*-plane samples. Solid lines are theoretical calculations assuming that the in-plane lattice parameters of the MQWs correspond to those of an AlGaN alloy with the average Al composition of the structure. Note that the calculations represented as a function of the well width do not follow a linear trend since two parameters (Al composition of the barriers and QW width) are changed in the simulations. Shadowed areas in graphs (a) and (c) mark the second order of the Reststrahlen band of GaN. (Reproduced from **[273]**)

4.4.4. Conclusions

In summary, we have designed and grown 50-period *m*-oriented (nonpolar) and *c*-oriented (polar) GaN/AlGaN MQWs with various QW widths and Al composition in the barriers, chosen so that the MQWs would show ISB absorption in the MIR range. With the replacement of AlN barriers by AlGaN barriers, we aimed at reducing the lattice mismatch in the structure. Reducing the Al composition of the structure lead to reducing the density of cracks. However we still observe stacking faults, and the AlGaN barriers present AlN-rich clusters. Nevertheless, we have demonstrated that the ISB absorption in these *m*-plane GaN/AlGaN MQWs can be tuned in the range of 4.0-5.8 μm, the longer wavelength being set by the second order of the GaN Reststrahlen band when using bulk substrates.

4.5. *m*-plane GaN/AlGaN MQWs with ISB transition in the Far-Infrared

We now extend the study to the FIR range and analyze the possibility to cover this spectral region with nonpolar *m*-plane GaN/AlGaN MQWs.

4.5.1. Sample description

Concerning the sample design, we enlarge the QW widths to obtain ISB absorption in the FIR range. Also, we reduce the Al composition of the AlGaN barriers below 10% to both reduce the lattice mismatch in the structure and keep the two lowermost electronic levels confined in the QWs and the third electronic level close to the continuum. This design should guarantee the confinement of the two lowermost states in the well, which should ensure the observation of ISB transition. The samples under study consist of 40-period *m*-plane GaN/AlGaN MQWs, with thick barriers around 20 nm to avoid coupling between the wells. The QW widths are chosen to display ISB absorption in the range of 4.8-8 THz (19.7-33 meV). The GaN wells were homogeneously doped with silicon at a concentration of 3×10^{18} cm^{-3} and, to prevent surface effects, the MQW structures were capped with a 50 nm AlGaN layer with the same Al content as the barriers. Table 17 summarizes the *m*-plane MQWs architectures, and Figure 111 shows the calculated band diagram of sample E3419m, along with a sketch of the sample structure.

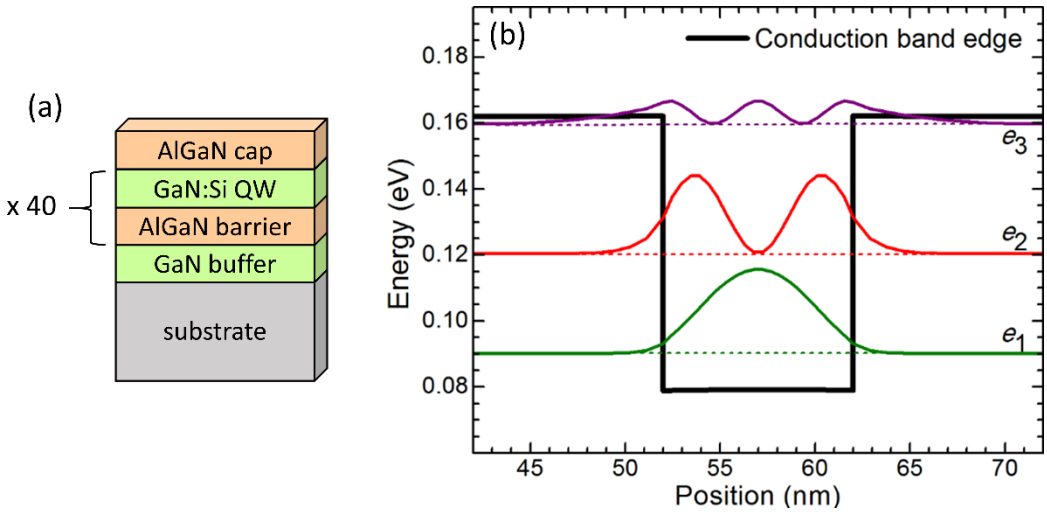

Figure 111 (a) Sketch of the sample structure. (b) Conduction band diagram with the three first electronic states and their square wavefunctions of a QW in the center of the active region of sample E3419m. (Modified from **[274]**)

Table 17 Structural and optical characteristics of the *m*-plane GaN/AlGaN MQWs: QW and barrier thickness (t_{QW} and t_B, respectively); Al composition of the barriers (x_B); MQW period measured by HR-XRD; FWHM of the ω-scan of the (3-300) x-ray reflection of the MQWs and of the GaN substrate, measured in the *c* and *a* directions ($\Delta\omega_c$ and $\Delta\omega_a$, respectively); simulated ISB transition energy; measured ISB transition energy window and central energy.

Sample	t_{QW} (nm)	t_B (nm)	x_B (%)	Period (nm)	ω-scan FWHM MQW (arcsec)	ω-scan FWHM GaN (arcsec)	Sim. ISB transition energy (meV)	Meas. ISB transition energy window (meV)	Meas. ISB transition central energy (meV)
E3420m	9.5	21.7	8	31.2	$\Delta\omega_c = 35$ $\Delta\omega_a = 34$	$\Delta\omega_c = 34$ $\Delta\omega_a = 39$	33	[13.4 – 37.4]	25.4
E3419m	10.0	18.5	7.5	28.5	$\Delta\omega_c = 38$ $\Delta\omega_a = 35$	$\Delta\omega_c = 35$ $\Delta\omega_a = 36$	30.5	[18.1 – 36.1]	27.1
E3424m	10.4	21.2	7.5	31.6	$\Delta\omega_c = 22$ $\Delta\omega_a = 31$	$\Delta\omega_c = 24$ $\Delta\omega_a = 39$	30.3	[6.3 – 36.3]	21.3
E3423m	12.9	21.1	6	34.1	$\Delta\omega_c = 38$ $\Delta\omega_a = 28$	$\Delta\omega_c = 42$ $\Delta\omega_a = 29$	19.7	[7.9 – 33.9]	20.9

4.5.2. Structural characterization

As a first assessment of the structural quality, Figure 112 displays a typical AFM image of this series (the example corresponds to sample E3420m), showing a smooth surface morphology with an RMS roughness of 0.32 nm, and clearly resolved monoatomic steps. However, a few cracks (between 1 and 5 cracks within an overall distance of 5 mm) propagating along the *a* direction (in contrast with the previous *m*-plane series where cracks were propagating along the *c* direction) are observed in nanostructures with a total MQW thickness above 1.2 µm and an average Al composition around 5%, which is in agreement with Ref. [285]. This is consistent with the higher tensile stress along the *c* direction (GaN/AlN lattice mismatch = 3.9%) with respect to the in-plane *a* direction (GaN/AlN lattice mismatch = 2.4%).

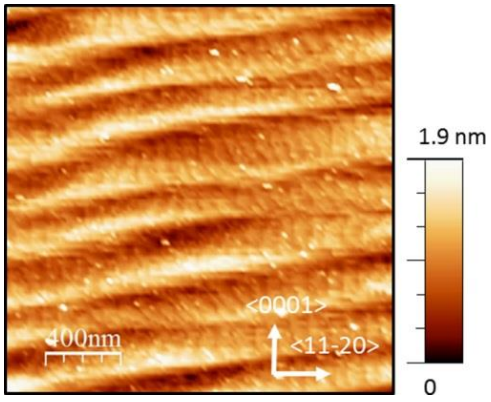

Figure 112 AFM image of sample E3420m showing smooth surface morphology (RMS = 0.32 nm) with monoatomic steps. (Reproduced from **[287]**)

To further evaluate their structural quality, the samples were analyzed by HAADF-STEM and HR-TEM. Figure 113 (a) and (b) show cross-section HAADF-STEM images of sample S2, viewed along (a) <0001> and (b) <11-20>. The images show the flatness of the QW interfaces along

the two perpendicular directions. Furthermore, no dislocations or stacking faults appear in the epitaxial layers, which was further confirmed by HR-TEM measurements.

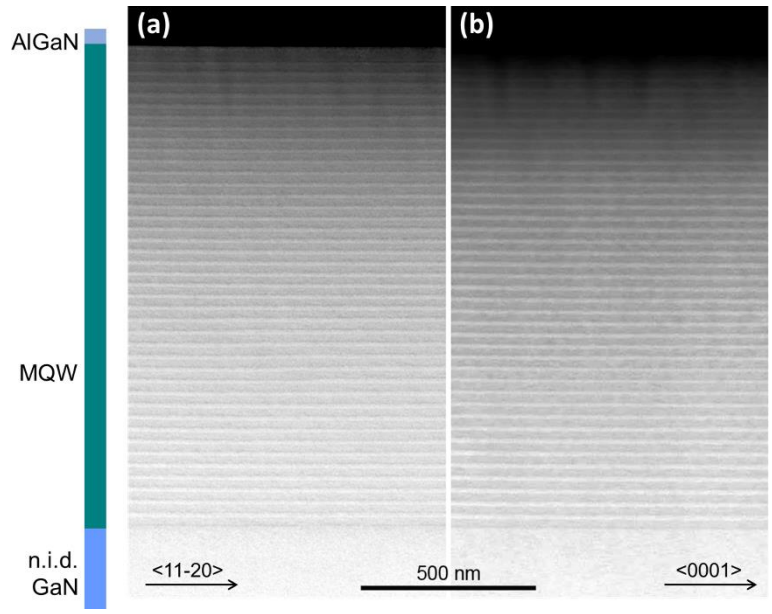

Figure 113 Cross-section HAADF-STEM images of sample E3419m viewed (a) along <0001>, and (b) along <11-20>. Layers with dark and bright contrast correspond to the AlGaN barriers and GaN QWs, respectively. (Modified from **[274]**)

Figure 114 (a) presents a HAADF-STEM view of two GaN QWs in the middle of the same sample. The AlGaN barriers have an inhomogeneous contrast with dark lines parallel to the QW interfaces. This contrast is assigned to alloy inhomogeneity along the growth axis, as confirmed by the absence of extended defects in the high-resolution image Figure 114 (b). From the intensity profile extracted from Figure 114 (a), the alloy fluctuations in the barriers can reach ± 30% of the average concentration. This fluctuation has been qualitatively confirmed by EDX, as illustrated Figure 115.

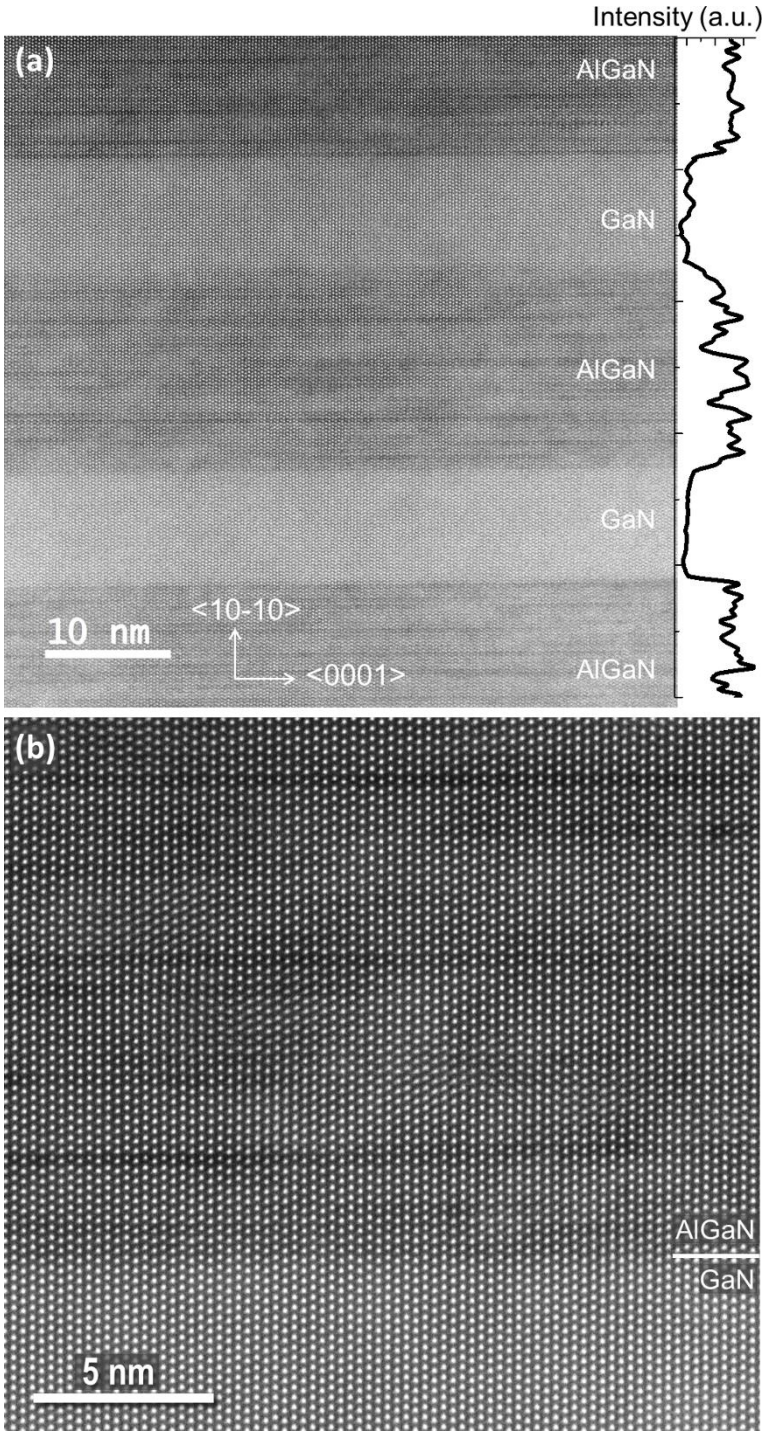

Figure 114 Layers with dark and bright contrast correspond to the AlGaN barriers and GaN QWs, respectively. (a) Cross-section HAADF-STEM image of sample E3419m viewed along <11-20> and intensity profile along <0001>. (b) High-resolution HAADF-STEM image of the barrier/QW interface showing that the variations of contrast in the image are not associated to structural defects. (Reproduced from **[274]**)

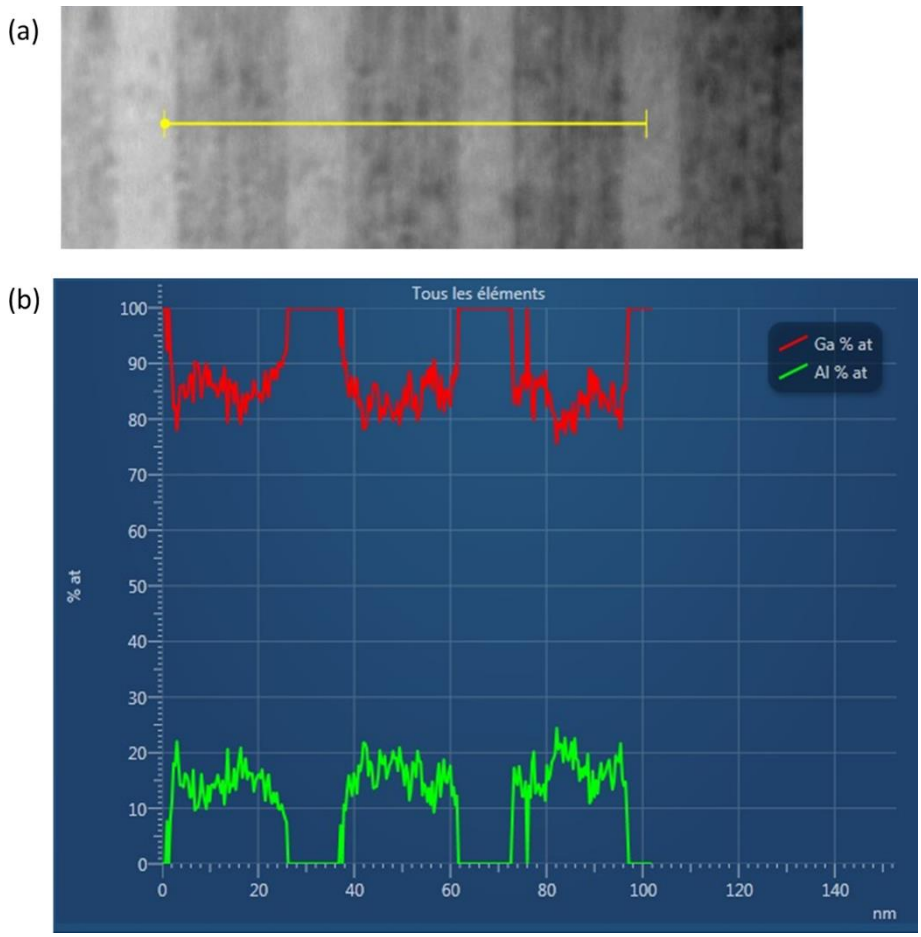

Figure 115 (a) STEM-HAADF image of sample E3419m with zone axis <11-20>, where the contrast is related to the atomic number. (b) EDX profile along the growth direction *m*, showing an alloy fluctuation of ± 30% of the average concentration in the barriers.

The periodicity of the MQWs was measured by HR-XRD. Figure 116 presents ω-2θ scans along the (3-300) reflection of samples E3420m and E3423m, together with simulations, assuming that the quantum structures are fully strained on the GaN substrate. Table 17 summarizes the MQW periods extracted from the inter-satellite distance in the HR-XRD measurements. The FWHM of the ω-scans were measured for the substrate and the MQW zero-order (3-300) reflection with the *c*-axis and the *a*-axis in the plane of diffraction ($\Delta\omega_c$ and $\Delta\omega_a$, respectively). Both $\Delta\omega_c$ and $\Delta\omega_a$ remain in the 30 ± 8 arcsec range for all the MQWs, and these values are similar to those measured for the substrate reflections. This is consistent with the absence of epitaxially-generated defects in the TEM images.

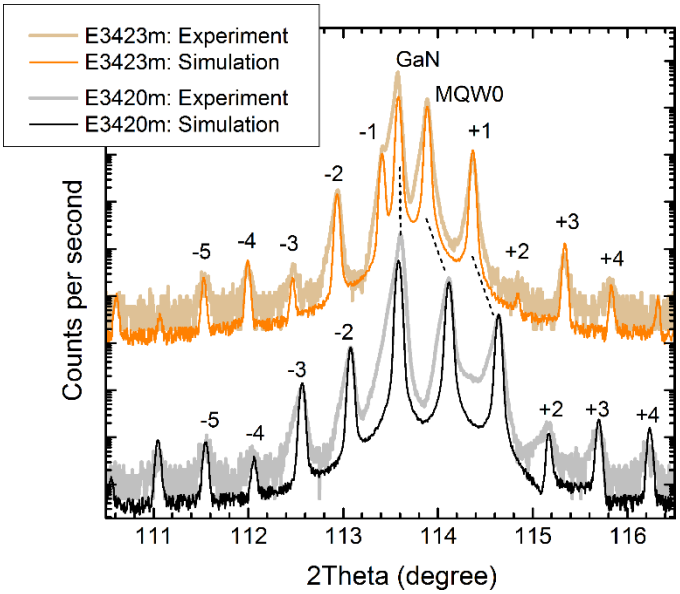

Figure 116 HR-XRD ω-2θ scans of the (3-300) reflection of samples E3420m and E3423m. Simulations assume the structures fully strained on the GaN substrate. (Reproduced from **[274]**)

4.5.3. Optical characterization

To assess the quality and homogeneity of the MQW stack, a spectral line-scan of the cathodoluminescence (CL) was recorded on a cross-section of sample E3419m cleaved along the growth direction *m*. Figure 117 shows the obtained spectral map, along with a sketch of the corresponding sequence of layers. While the s.i. GaN substrate does not yield a discernable emission for the used excitation conditions and integration time, the n.i.d. GaN buffer layer also grown by plasma-assisted MBE presents an emission peak between 3.471 and 3.478 eV, corresponding to donor-bound and free excitons in unstrained GaN, respectively [299]. Following the growth axis, the MQWs show a slightly broader emission with the peak energy continuously shifting from 3.484 to 3.497 eV from the bottom to the top of the MQW stack, while the intensity of the peak remains almost constant. Such a minor shift of the emission energy in this thick (1.15 µm) 40-period MQW stack confirms the excellent homogeneity of the heterostructures. This change in emission energy may be related to fluctuations of the QW thickness (there is no indication of such a gradient in the broadening of the reflection peaks in HR-XRD ω-2θ scans or in HR-TEM images taken at various points along the structure) or of the strain state. Finally, the AlGaN capping layer is visible as an extra emission peak centered around 3.61 eV.

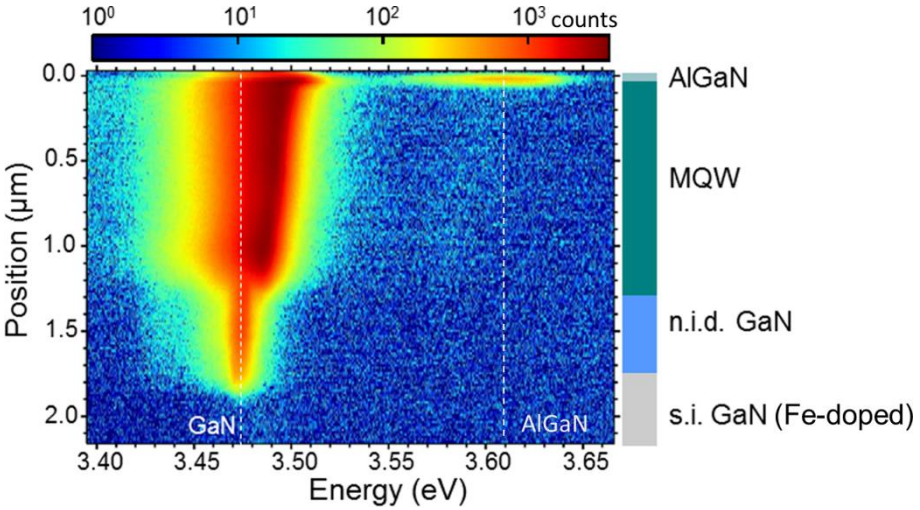

Figure 117 CL spectral line-scan on the cross-section of sample E3419m measured at T = 5 K. The intensity is color-coded on a logarithmic scale. The sketch on the right side shows the corresponding sequence of layers. (Modified from **[275]**)

We performed temperature-dependent PL measurements on these samples. Figure 118 (a) shows the typical PL spectrum obtained for this low-Al-content MQW series, for different temperatures. The low temperature spectrum is dominated by the excitonic line associated to the MQW, together with its LO phonon replicas. At high energy, the emission from the AlGaN cap layer is visible, but it is rapidly quenched for increasing temperatures. In Figure 118 (b), we show the variation of the MQW PL peak intensity versus temperature. Two periods of decay are distinguished. We can calculate the corresponding activation energies E_a and E_b extracted from the formula:

$$I = \frac{I_0}{1 + \alpha_1 \exp\left(-\frac{E_a}{kT}\right) + \beta_1 \exp\left(-\frac{E_b}{kT}\right)} \quad (94)$$

where I is the PL intensity, I_0 the PL peak intensity, α_1 and β_1 are constant parameters, *k* is the Boltzmann constant, and T is the sample temperature during the measurement.

The MQW line shows a low activation energy (E_a = 4.6±0.3 meV) at lower temperatures and a higher activation energy (E_b = 43±5 meV) at higher temperatures.

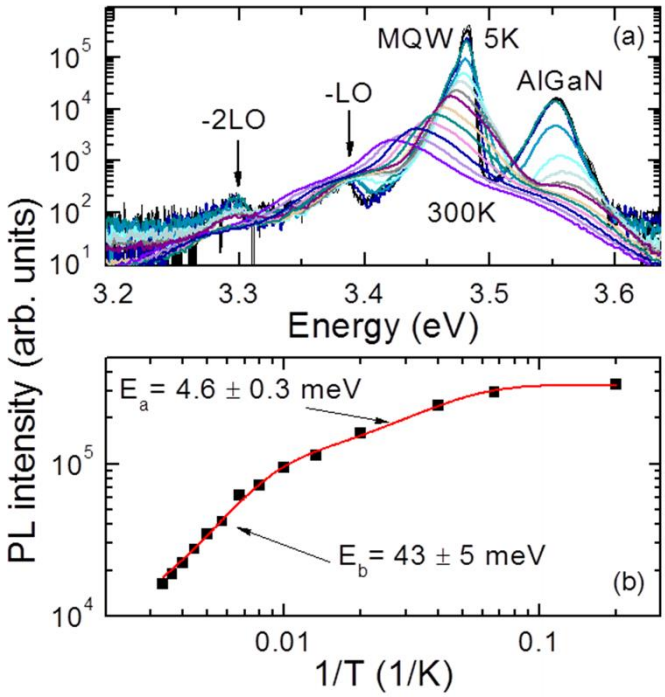

Figure 118 (a) Variation of the PL spectrum of sample E3423m as a function of temperature, from 5K to 300K. (b) Variation of the PL intensity of the MQW-related PL peak with temperature. Squares correspond to the experimental data and the red solid line correspond to the fit to equation (94). (Reproduced from **[287]**)

To probe the ISB absorption of the MQWs, characterization by FTIR spectroscopy was performed at 5 K. Using sample E3419m as an example, Figure 119 (a) illustrates typical TE- and TM-polarized THz transmission measurements, and Figure 119 (b) compares the same transmission spectrum for TM-polarized light with that of the substrate. As shown in the magnified view in the inset of Figure 119 (a), the apparent noise superimposed on all the spectra is an oscillation with nearly-regular periodicity in energy, which is assigned to a Fabry-Pérot interference. Using the refractive index of GaN in the FIR range from Ref. [68], the cavity length associated to the interference is ≈ 350 μm, corresponding to the overall thickness of the samples. The transmission spectra for TE-polarized light present additional Fabry-Pérot oscillations associated to the MQW layers. In contrast, the transmission spectrum for TM-polarized light exhibits a broad dip, in the 3-8 THz range in the case of sample E3419m, which is assigned to ISB absorption, following the polarization selection rule. In the inset of Figure 119 (b), we plot the normalized broadening of the absorbance (energy broadening divided by the central energy) as a function of the doping density in the MQWs. Hollow square symbols are extracted from Ref. [198], and the full round symbol corresponds to this work.

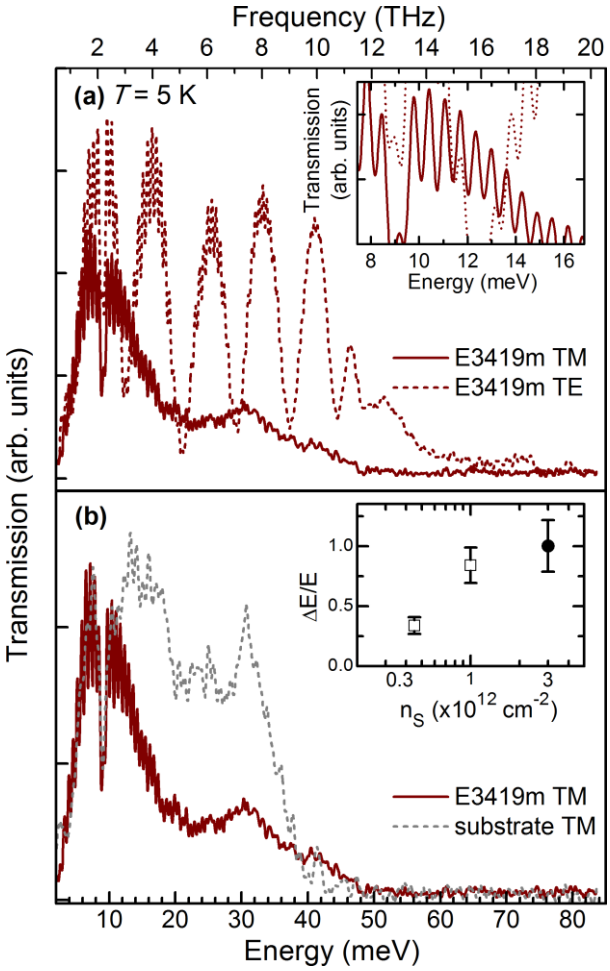

Figure 119 (a) Transmission spectra of TM and TE-polarized light of sample E3419m measured in the THz range. Inset: Magnification of the transmission spectra showing Fabry-Pérot oscillations. (b) Transmission spectra of TM-polarized light of sample E3419m and of the substrate, measured in the THz range. Inset: Normalized broadening of the absorbance as a function of the doping density in the MQWs. Hollow square symbols are extracted from Ref. **[198]**, and the full round symbol corresponds to this work. (Reproduced from **[274]**)

We define the normalized absorbance as $A = 1 - \frac{TM_{MQW}}{TM_{sub}}$, where TM_{MQW} and TM_{sub} are the TM-polarized transmission of the MQWs and of the substrate, respectively. Figure 120 presents the normalized absorbance of the samples under study for TM-polarized light, extracted from the transmission measurements. TM-polarized absorption is observed over a broad spectral window of normalized bandwidth close to 1, whose extreme values and central energy are summarized in Table 17. The central energy decreasing from 27.1 to 20.9 meV (6.5 to 5 THz) as the QW width increases is consistent with the trend of the simulations. The broad absorption bands are consistent with the doping density in the QWs of around $n_S = 3\times10^{12}$ cm^{-2}, *i.e.* at least three times higher than in Ref. [198], as illustrated in the inset of Figure 119 (b). The samples show ISB absorption ranging from 6.3 to 37.4 meV (1.5 to 9 THz), providing experimental evidence that ISB transitions in GaN MQWs can cover the THz spectral range forbidden to GaAs. These results complete the work of Purdue University [198], which has recently demonstrated THz ISB absorption (15.6-26.1 meV) in *m*-plane GaN/AlGaN MQWs. The obtained absorption peaks were also broad (the largest normalized broadening was 0.84) and were reduced by up to 40% by dividing the doping density by a factor 2 and inserting undoped spacer regions between the QWs and the barriers.

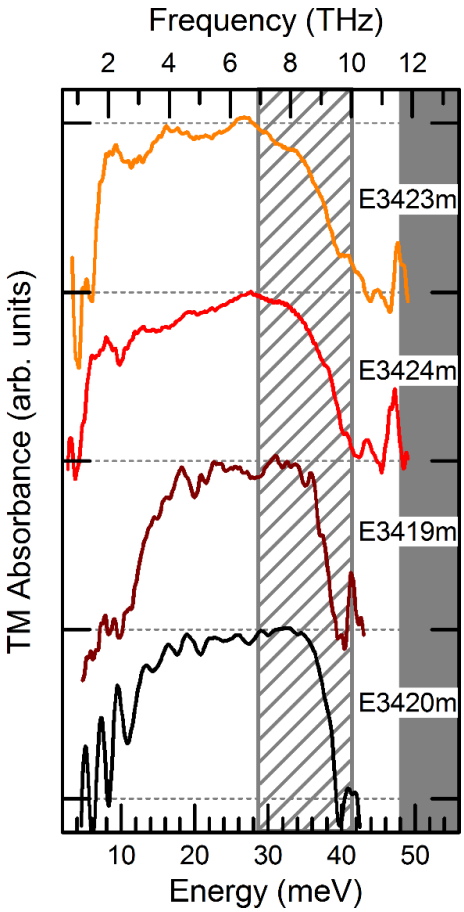

Figure 120 Normalized absorbance of TM-polarized light for the samples under study in the THz range. Data are vertically shifted for clarity. The striped and shadowed areas represent the phonon absorption bands of GaAs and GaN, respectively. (Reproduced from **[274]**)

4.5.4. Conclusions

In summary, we have designed a series of nonpolar *m*-plane GaN/AlGaN MQWs by varying the QW thicknesses and Al compositions to separate the two confined electronic levels by 20–33 meV (corresponding to 4.8–8 THz transitions), and decouple these transitions from the neighboring wells. These low-Al-composition MQWs (Al composition in the AlGaN alloy below 10% and average Al concentration in the MQW below 6%) displayed flat and regular layers in the two perpendicular in-plane directions *a* and *c*, and a very good crystalline quality. Extended defects like stacking faults or dislocations, were not present. Only when the total MQW thickness exceeded 1.2 µm, we observed cracks propagating along the *a* direction. Inhomogeneities of the Al composition in the barriers were observed along the growth axis *m*. Optically, the structures showed low-temperature ISB absorption in the 6.3 to 37.4 meV (1.5 to 9 THz) range, providing an experimental demonstration of the possibility for GaN to cover a large part of the 7–10 THz band forbidden to GaAs-based technologies. However, the demonstrated ISB absorption are spectrally broad, with a normalized bandwidth close to 1, which is attributed to the high Si doping density ($n_s = 3\times10^{12}$ cm^{-2}). Based on this result, we further study the effect of Si doping density on such FIR structures in the following section.

4.6. Effect of Si doping density on Far-Infrared *m*-plane GaN/AlGaN MQWs

High Si-doping levels are known to perturb significantly the IR absorption spectrum. In the SWIR, the exchange interaction (dominant many-body mechanism) leads to a blueshift of the ISB transitions in *c*-plane GaN/AlN MQWs [159]. In the MIR, using *c*- and *m*-plane GaN/AlGaN MQWs, high doping levels lead to the broadening of the ISB transition. Also, the expected redshift due to the screening of the internal electric field is over-compensated by the blueshift induced by exchange interaction and the now dominant depolarization [135].

In this section, we assess the effect of Si doping on the low-temperature ISB absorption of nonpolar *m*-plane GaN/AlGaN MQWs designed for ISB absorption in the THz range.

4.6.1. Sample description

In this study, samples consisted of *m*-plane 40-period GaN/AlGaN MQWs all with the same structure (10 nm GaN / 18.5 nm $Al_{0.075}Ga_{0.925}N$) based on the design of sample E3419m. As described in the previous section, at low doping levels, there should be only two electronic levels confined in the QWs separated by ~30 meV (7.3 THz). A 300 nm thick, n.i.d. GaN buffer layer was grown by plasma-assisted MBE prior to the heterostructures, and the MQW structures were capped with 50 nm of AlGaN using the same Al content as for the barriers (see sketch of the structure in Figure 111 (a)). The GaN wells were homogeneously doped with silicon, at concentrations increasing from 1×10^{11} cm^{-2} to 3×10^{12} cm^{-2}. The list of samples is presented in Table 18.

Table 18 Structural and optical characteristics of the *m*-plane GaN/AlGaN MQWs: Si doping concentration; FWHM of the ω-scan of the (3-300) x-ray reflection of the MQWs and of the GaN substrate measured with the *c* direction in the diffraction plane; FWHM of the MQW PL emission at T = 5 K; measured ISB transition energy; ISB absorption per pass.

Sample	Si doping concentration ($\times 10^{12}$ cm^{-2})	ω-scan FWHM MQW (arcsec)	ω-scan FWHM GaN (arcsec)	PL at T = 5 K FWHM (meV)	Measured ISB transition energy (meV)	ISB absorption per pass (%)
E3445m	3	23	22	10.3	35.5	9.1
E3447m	1	44	33	5.2	28.2	10.0
E3448m	0.3	20	19	4.0	31.0	7.3
E3449m	0.1	35	35	6.3	27.6	2.9

4.6.2. Structural characterization

Since we basically reproduced sample E3419m with same or lower values of Si doping densities, we expect to see similar structural features as for the previous series of samples. We analyzed sample E3448m by HR-TEM and HAADF-STEM. As expected, cross-section images of the stack viewed along the <11-20> and <0001> zone axis do not show any extended defects (neither dislocations nor stacking faults) generated during the epitaxial process over an in-plane length of ≈ 2 μm. Again, in the magnified HAADF-STEM image in Figure 121, the variations of contrast are associated to compositional changes in the alloy. This alloy inhomogeneity in the AlGaN barriers appears as small shadowed areas with a typical diameter of 2–5 nm.

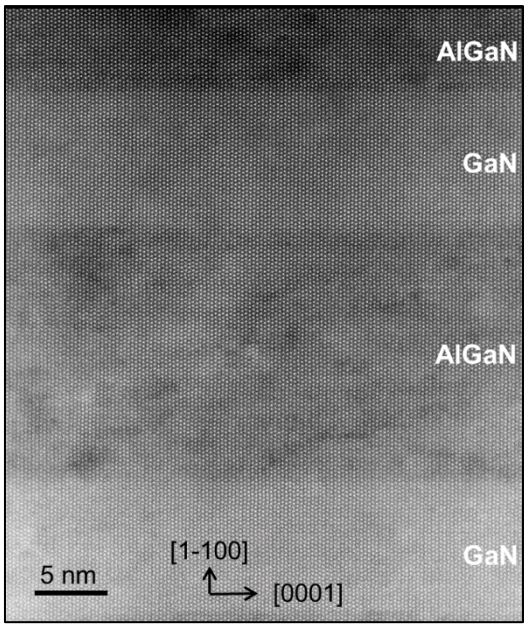

Figure 121 Cross-section HAADF-STEM images of sample E3448m, viewed along the <11-20> zone axis showing two QWs in the middle of the stack. Clear areas correspond to GaN, darker contrast reveals the presence of aluminum. (Modified from **[275]**)

The period of the MQWs was verified by ω–2θ scans of their (3-300) x-ray reflection, illustrated by Figure 129. To get an idea of the mosaicity of the epitaxial layers, the FWHM of the rocking curves was measured with the *c* direction in the diffraction plane, which is the case where the lattice mismatch is maximum, for both the substrate and the zero-order MQW (3-300) reflection. As shown in Table 18, the FWHM of the MQW reflection remains in the range of 20–44 arcsec, obtaining similar values to those of their respective substrates regardless of the doping level. This result is consistent with the absence of epitaxially-induced defects in the microscopy images.

4.6.3. Optical characterization

Temperature-dependent PL was measured for all the samples. As an example, the normalized spectra for E3448m are presented in Figure 122 (a). The spectra present two main emission lines, the low-energy line around 3.48 eV associated to the band-to-band excitonic transition in the MQW, and the high-energy line around 3.55 eV associated to the emission from the AlGaN cap layer. Taking into account the penetration depth of the laser (excitation at 244 nm) and the geometry of the sample,

the PL emission originates only from the cap layer and the two topmost QWs. The FWHM of the GaN peaks at low temperature are in the range 4.0–10.3 meV, as summarized in Table 18. When increasing the temperature, the integrated intensity of the GaN peak for all samples decreases only by a factor 30.

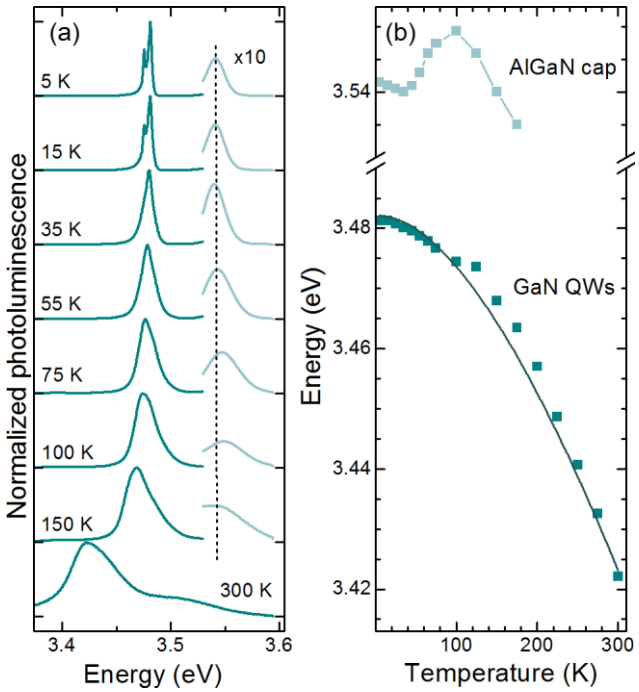

Figure 122 (a) Temperature-dependent PL spectra measured for sample E3448m. Data are vertically shifted and the AlGaN peaks (light blue) are magnified by a factor 10 for clarity. (b) Temperature-dependent energy of GaN and AlGaN band-to-band transitions in sample E3448m and fit to the Varshni law. (Modified from **[275]**)

Figure 122 (b) depicts the evolution with temperature of the MQW and AlGaN PL peak energies for sample E3448m. The thermal shift of the MQW transition is well described by the Varshni law, $E_{PL}(\mathrm{T}) = E_{PL}(\mathrm{T}=0) - \frac{\alpha_V \mathrm{T}^2}{\mathrm{T}+\beta_D}$, with a transition energy at 0 K $E_{PL}(\mathrm{T}=0) = 3.48$ eV and the Varshni and Debye coefficients α_V = 0.590 meV/K and β_D = 600 K, respectively, which is in complete agreement with the temperature-induced bandgap quenching in *c*-GaN/AlN MQWs described by Gačevic *et al.* [266]. On the other hand, the AlGaN presents a marked S-shaped behavior, characteristic of AlGaN alloys [231,300]. The first blueshift up to about 100 K is attributed to the transition from localized to extended bandtail states. Such localization could originate from variations of thickness, interface roughness, or alloy inhomogeneity. In our case, the TEM images revealed sharp interfaces and regular QWs. In addition, having so large QWs makes a variation of thickness unlikely to induce such localization. However the TEM images have shown alloy fluctuations, this is why the origin of the inhomogeneous potential distribution leading to exciton localization is assigned to the alloy inhomogeneity. For temperatures above 100 K, the emission redshifts following the semiconductor band gap.

For a better understanding, Figure 123 shows an illustration of the thermally-induced transition from a localized state of the exciton to a free exciton. On the left, we show the variation of the excitonic transition with temperature, with two distinct zones: above 100 K the PL energy follows

the Varshni law, and below 100 K the transition is strongly red-shifted due to localization. On the right, we show a sketch of the band diagram in an area with allow fluctuation. At low temperatures (1), the alloy inhomogeneity lead to the formation of local minima in the energy diagram (circled in red), where the exciton gets localized. Then, the increase in temperature (2) results in an increase of the exciton energy, until reaching the state of a free exciton (here at 100 K).

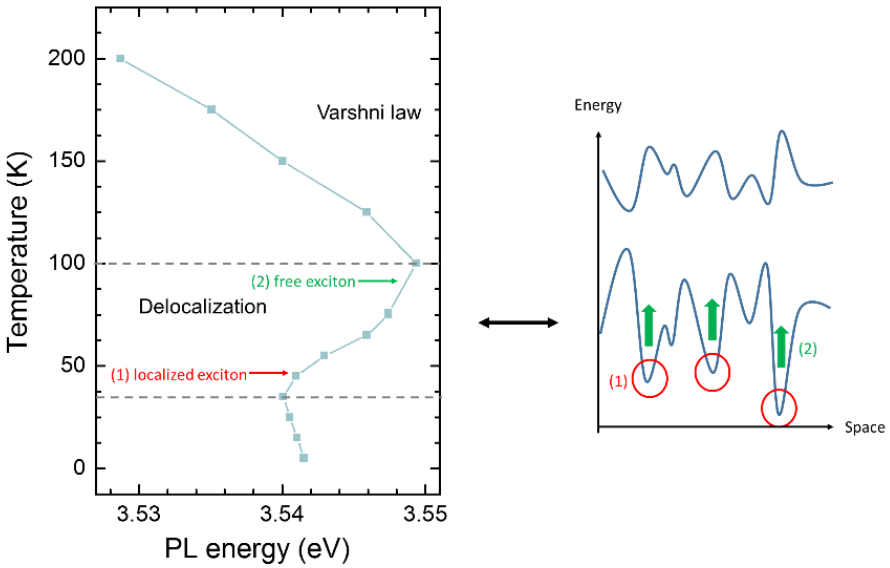

Figure 123 Illustration of the temperature-induced transition from a localized state of the exciton to a free exciton. Left: Temperature-dependent energy of the AlGaN band-to-band transition for sample E3448m. Right: Illustration of the delocalization process on an energy diagram scheme in the reciprocal space.

Comparing the measurements at low temperature with the low-temperature transition energy predicted by the Varshni law, we can estimate the exciton localization energy, $E_{Loc,}$ as illustrated in Figure 124. We first performed a fit of the experimental data for temperature above 100 K (temperature from which the exciton is free) to the Varshni law (which describes the behavior of a free exciton). Then we extrapolated this fit to the temperatures from 0 to 200 K, to obtain the energy of the free exciton state. The difference between this value and the measured PL peak energy at low temperature is the localization energy, and the estimated localization energies for all the samples are plotted in Figure 125.

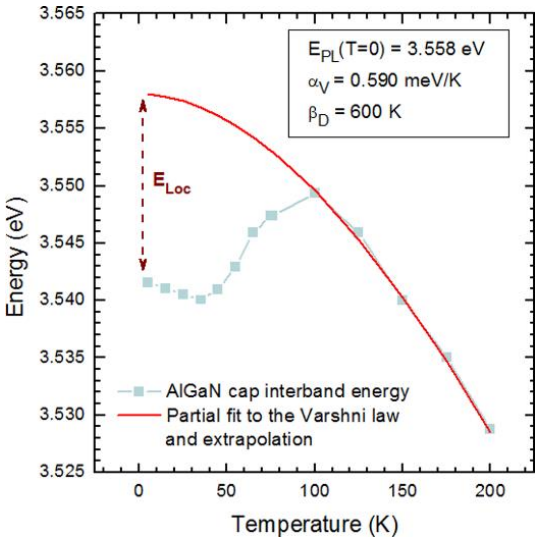

Figure 124 Estimation of the localization energy E_{Loc} for sample E3448m. The dotted line corresponds to the measured band-to-band transition energy of the AlGaN cap layer. The red solid line corresponds to the fit to the Varshni law for temperatures above 100 K (range between brackets), extrapolated to the full range of temperatures.

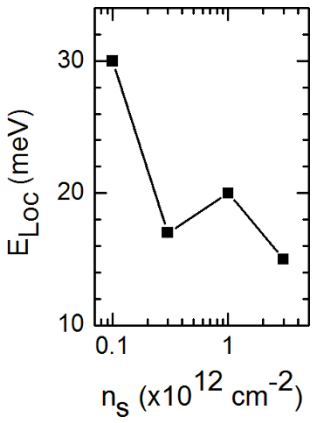

Figure 125 AlGaN cap exciton localization energy as a function of doping density. (Modified from **[275]**)

The value of E_{Loc} for the sample with the lowest doping level is roughly twice as large as typical values in *c*-plane AlGaN with similar alloy composition [231,300]. Increasing the doping density results in a higher Fermi level, which increases the amount of carriers in the AlGaN cap layer, filling the AlGaN energy states and reducing the localization energy.

We turn now to the ISB properties of these MQWs. To probe the ISB absorption, FTIR spectroscopy was performed at 5 K. Figure 126 (a) shows the normalized TM-polarized absorbance spectra. By dividing the absorbed intensity ratio by the number of light reflections (≈ 6) in the multipass waveguide, we estimate the ISB absorption per pass with the results in Table 18. Increasing the doping density results in higher absorption which saturates when the Fermi level approaches the first excited electron state e_2. Indeed, using the equation (95), the Fermi level is calculated to reach e_2 for a doping concentration $n_s \approx 2.3\times10^{12}$ cm^{-2}:

$$n_s = \frac{m_{eff} E_{21}}{\pi \hbar^2} \tag{95}$$

Where m_{eff} is the electron effective mass in GaN, E_{21} is the transition energy, and $\hbar$ is the reduced Planck constant.

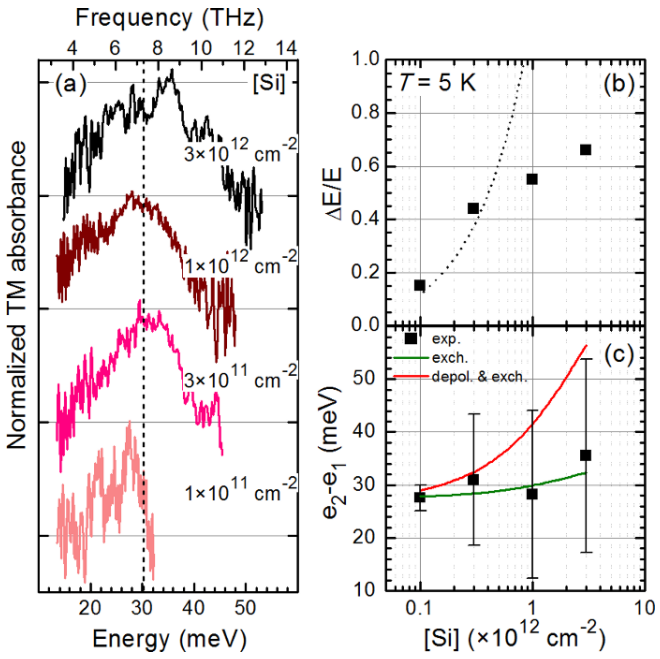

Figure 126 (a) Normalized absorbance of TM-polarized light for the samples under study measured at T = 5 K. Data are vertically shifted for clarity. The dashed line indicates the theoretical ISB transition energy. (b) Normalized linewidth of the absorbance as a function of the doping density in the MQWs. The dashed line indicates its theoretical trend, not taking into account the population of the first excited state. (c) ISB transition energy as a function of the doping density in the MQWs and theoretical evolution considering the exchange interaction (green) and both the exchange interaction and the depolarization shift (red). The error bars illustrate the absorption linewidth. (Reproduced from **[275]**)

The normalized linewidths (energy broadening divided by the peak energy, ΔE/E) of the absorbance spectra are plotted in Figure 126 (b), and are compared to calculations.

Based on the models in [126,288], we calculated the normalized linewidth at low doping density (1×10^{11} cm^{-2}) taking into account the scattering by interface roughness (dominant at this low doping density), longitudinal acoustic and optic phonons and alloy disorder. In our estimation, we set the mean height of roughness parameter to $\Delta = 0.2$ nm and adjusted the correlation length to $\lambda = 70$ nm, values that are consistent with AFM measurements. When increasing the Si concentration, the scattering by ionized impurities becomes dominant and sets a linear dependence of the linewidth on the doping density. From our experiment, increasing the doping concentration by one order of magnitude increases the normalized linewidth by a factor of 4.4.

The measured ISB transition energies extracted from the absorbance spectra are plotted in Figure 126 (c). The transition presents a blueshift that is assigned to many-body effects, namely exciton shift, exchange interaction and plasmon screening. From our calculations, the exciton shift β for the considered doping densities is of the order of 10^{-14}, *i.e.* negligible compared to 1. This is why the considered many-body effects are the exchange interaction and plasmon screening or depolarization (which formula were established in subsection 1.3.1 of Chapter 1).

Based on [122,145], the magnitude of the exchange interaction ΔE_{exch} (in red) was calculated as:

$$\Delta E_{exch} = -\frac{e\sqrt{2\pi n_s}}{4\pi\epsilon_R\epsilon_0}\, 0.18\sqrt{\frac{2n_s}{\pi}} \tag{96}$$

where e is the elementary charge, ϵ_0 is the electric permittivity, $\epsilon_R = 10$ is the dielectric constant in GaN [301], and n_s is the 2D density of charge.

The shift of the ISB energy induced by depolarization was calculated as $\Delta E_{dep} = E_{21}\left(\sqrt{1+\alpha}-1\right)$, where E_{21} is the transition energy (eventually corrected by the exchange interaction), and the depolarization shift is defined as:

$$\alpha = \frac{2e^2 n_s}{\epsilon_R\epsilon_0 E_{21}}\int_{-\infty}^{+\infty}\left[\int_{-\infty}^{z}\phi_2(z')\phi_1(z')\,dz'\right]^2 dz \tag{97}$$

where ϕ_j is the electron wavefunction for the j^{th} subband, and z is the growth direction.

The experimental results present a blueshift, as predicted by theory. However, the magnitude of the shift in the most doped samples (E3445m and E3447m) is smaller than expected. The deviation might be attributed to the population of the electron excited state, consistent with the saturation of the absorption. Our study completes the recent work of The University of Tokyo on *m*-GaN/AlGaN MQWs showing ISB transitions in the MIR [288]. They developed a model that both calculates the blueshift caused by many-body effects on the ISB transition energy, and quantifies the effect of scattering, mainly due to interface roughness, LO phonons, and ionized impurities, on the ISB absorption linewidth.

4.6.4. Conclusions

In summary, we have designed a series of nonpolar *m*-plane GaN/AlGaN MQWs for ISB absorption at 30 meV (7.3 THz), reproducing the design of the previously studied sample E3419m. To probe the effect of doping on the structural and optical properties of the nanostructures, the Si doping density in the wells was varied from 1×10^{11} cm^{-2} to 3×10^{12} cm^{-2}. All the structures display low-temperature ISB absorption in the THz range. Increasing the doping level leads to an enhancement and blueshift of the absorption peak energy, together with an increase of the linewidth. However, a saturation of the absorption is observed at 1×10^{12} cm^{-2}, and the magnitude of the blueshift and broadening increases less than theoretically predicted for the samples with higher doping levels. This is explained by the presence of free carriers in the excited electron level induced by the increase in n-doping, *i.e.* the increase of the Fermi level energy.

4.7. Si vs Ge-doping of *m*-plane GaN/AlGaN MQWs with ISB absorption in the Far-Infrared range

In the previous section, we discussed the effect of Si-doping density on the FIR ISB absorption energy and spectral broadening in *m*-plane GaN/AlGaN MQWs. In this section, we assess the effect of Ge-doping in *m*-plane GaN/AlGaN MQWs showing ISB absorption in the FIR, using the previously studied Si-doped structures as references.

4.7.1. Sample description

In this study, the *m*-plane 40-period GaN/AlGaN MQWs reproduce the previously studied Si-doped series (10 nm GaN / 18.5 nm $Al_{0.075}Ga_{0.925}N$). As before, at low doping levels, there should be only two electronic levels confined in the QWs separated by ~30 meV (7.3 THz). A 300 nm thick, n.i.d. GaN buffer layer was grown by plasma-assisted MBE prior to the heterostructures, and the MQW structures were capped with 50 nm of AlGaN using the same Al content as for the barriers. The GaN wells were homogeneously doped with germanium, at concentrations increasing from 5×10^{11} cm^{-2} to 5×10^{12} cm^{-2}. The list of samples is presented in Table 19.

Table 19 Structural and optical characteristics of the *m*-plane GaN/AlGaN MQWs: Ge doping concentration; FWHM of the ω-scan of the (3-300) x-ray reflection of the MQWs and of the GaN substrate measured with the *c* direction in the diffraction plane; and measured ISB transition energy.

Sample	Ge doping concentration ($\times 10^{12}$ cm^{-2})	ω-scan FWHM MQW (arcsec)	ω-scan FWHM GaN (arcsec)	Measured ISB transition energy (meV)
E3643m	5	48	40	24.1
E3541m	2	46	38	23.5
E3540m	0.5	52	42	25.1

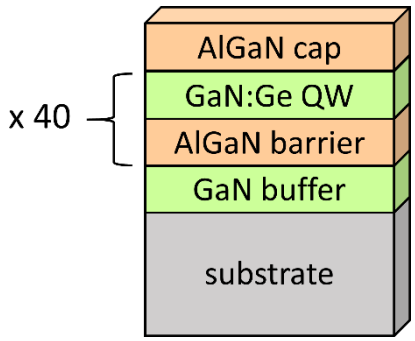

Figure 127 Sketch of the MQW structure.

4.7.2. Structural characterization

As a first evaluation of the structural quality of the samples, we recorded AFM images of their surfaces and obtained morphology and roughness similar to those observed on the Si-doped FIR structures, as illustrated by Figure 128 for sample E3540m.

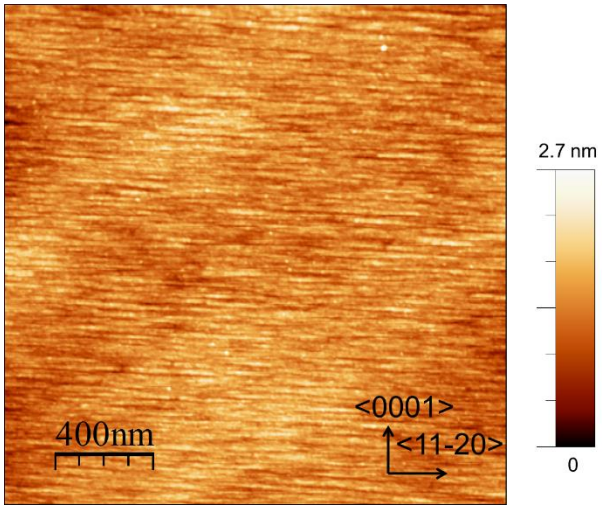

Figure 128 AFM image of sample E3540m showing smooth surface morphology (RMS = 0.28 nm), comparable to that observed on the Si-doped FIR structures.

As shown in Figure 129, we then verified the periodicity of the MQWs by HR-XRD, with the results in Table 19. The obtained period is less than 5% shifted away from the nominal value and the FWHM of the rocking curves reveal a very good mosaicity of the structures, comparable to the bulk GaN substrate.

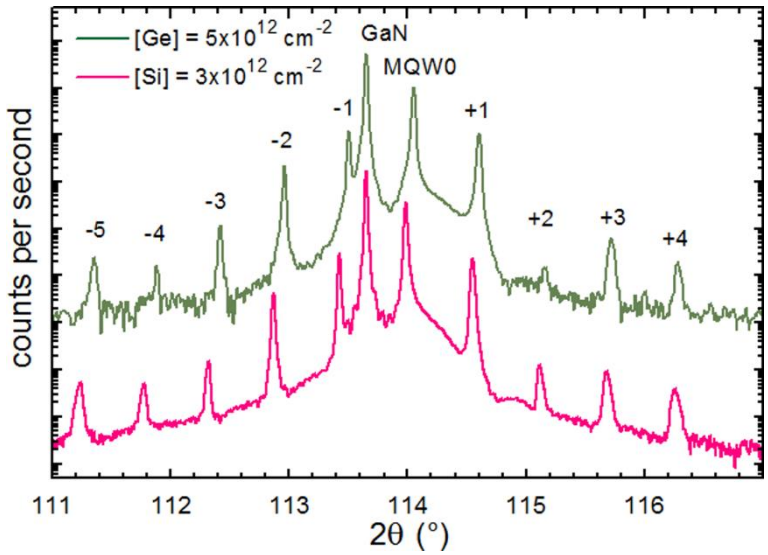

Figure 129 HR-XRD ω-2θ scans of the (3-300) reflection of samples E3643m (Ge-doped) and E3445m (Si-doped).

We analyzed sample E3541m by HR-TEM and HAADF-STEM. As expected, cross-section images of the stack viewed along the <11-20> and <0001> zone axis do not show any extended defects (neither dislocations nor stacking faults) generated during the epitaxial process over an in-plane length of ≈ 2 µm, as illustrated by Figure 130.

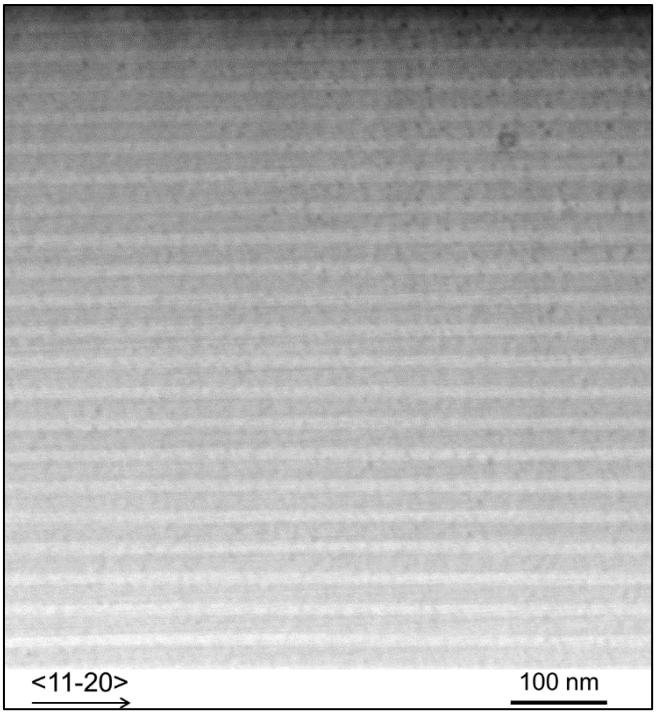

Figure 130 Cross-section HAADF-STEM image of sample E3541m viewed along <11-20>. Layers with dark and bright contrast correspond to the AlGaN barriers and GaN QWs, respectively.

4.7.3. Optical characterization

We assessed the ISB properties of the structures by FTIR, and compared the obtained data to the Si-doped MQWs. On Figure 131, we show the normalized TM absorbance spectra for the three Ge-doped samples, along with the normalized broadening of both the Si-doped and the Ge-doped series. For equivalent doping densities, the Ge-doped structures show ISB absorption peaks with smaller normalized broadening than for the Si-doped structures. When increasing the Ge doping density, we observe a slight widening of the ISB absorption peak and no shift of the ISB energy. However, for equivalent doping densities, the Ge-doped structures show ISB absorption peaks with slightly smaller normalized broadening than for the Si-doped structures.

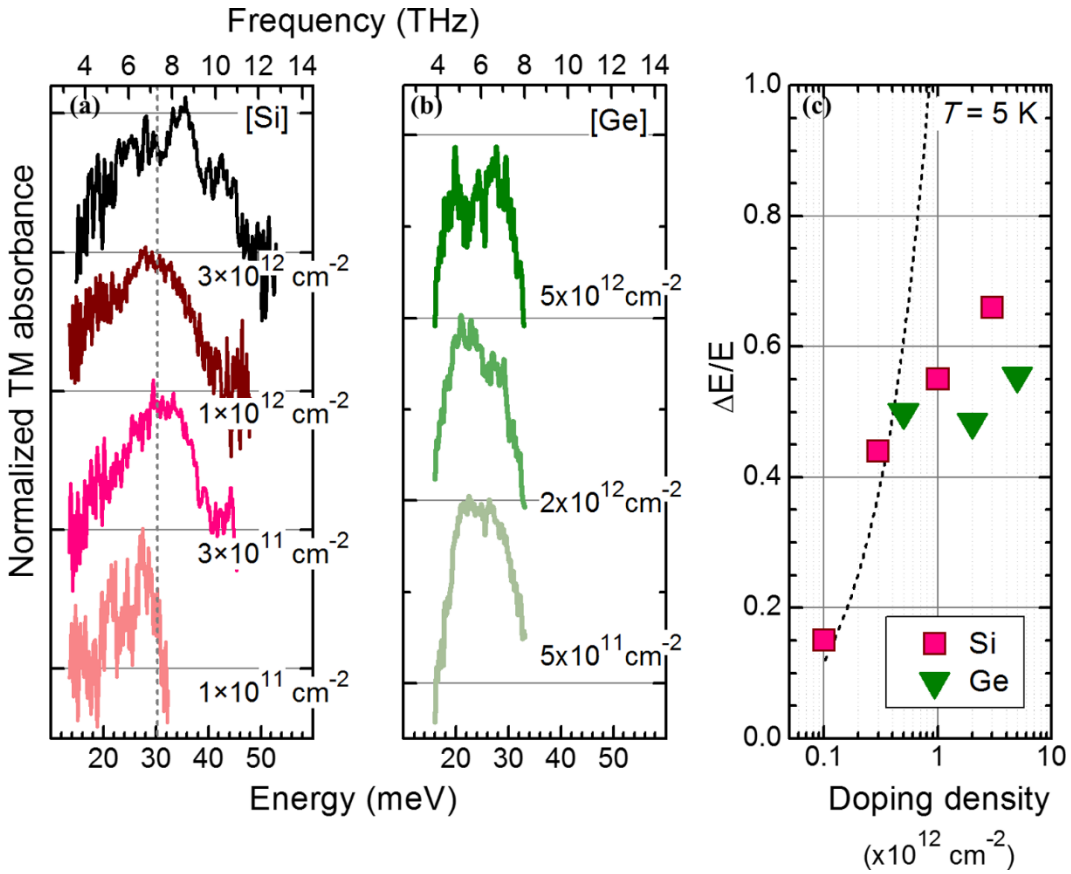

Figure 131 ISB absorption spectra in the FIR from (a) Si-doped (b) Ge-doped MQWs and (c) their normalized broadening in function of the doping density. (Modified from **[275]**)

For equivalent doping densities, the Ge-doped structures show ISB absorption peaks with smaller normalized broadening than for the Si-doped structures. When increasing the Ge doping density, we observe a slight widening of the ISB absorption peak and no shift of the ISB energy.

4.7.4. Conclusions

In summary, we have grown a series of Ge-doped nonpolar *m*-plane GaN/AlGaN MQWs for ISB absorption at 30 meV (7.3 THz), reproducing the design of the previously studied Si-doped series (10 nm GaN / 18.5 nm $Al_{0.075}Ga_{0.925}N$). To probe the effect of doping on the structural and optical properties of the nanostructures, the Ge doping density in the wells was varied from 5×10^{11} cm^{-2} to 5×10^{12} cm^{-2}. All the structures display low-temperature ISB absorption in the THz range. Structurally, the Ge-doped samples were very similar to those doped with Si in terms of surface roughness and x-ray rocking curve width. The structures did not show any extended defects (neither dislocations nor stacking faults) generated during the epitaxial process. Optically, for equivalent doping densities, the Ge-doped structures showed ISB absorption peaks with slightly smaller normalized broadening.

4.8. Conclusions on the nonpolar orientation study

In this chapter, we have evaluated the possibility to use nonpolar *a*- or *m*-plane GaN for infrared optoelectronics. This alternative to polar *c*-plane GaN was considered as an answer to the issues raised by the polarization-induced electric field in the polar structures.

We first considered the short-wavelength infrared range by studying GaN/AlN MQWs structures simultaneously grown on *c*-, *a*- and *m*-plane GaN. By varying the GaN QW widths, ISB absorption in the targeted range was obtained. Compared to nonpolar *a* plane samples, *m*-plane structures displayed better results in terms of mosaicity, surface roughness, PL linewidth and intensity, and ISB absorption. Furthermore, the *m*-plane GaN/AlN MQWs showed ISB absorption in the 1.5-2.9 µm range, covering the whole SWIR spectrum, with performance comparable to polar *c*-plane MQWs. Yet, the structural quality of the nonpolar structures was insufficient to consider any device processing.

We then extended the study to the mid-infrared range by studying *m*-oriented GaN/AlGaN MQWs with various QW widths and Al composition, designed to show ISB absorption in the targeted range. By introducing Ga in the AlN barriers, we reduced the average Al composition of the structure and thus the lattice mismatch. This lead to lower densities of cracks. However stacking faults were still present, and Al-rich clusters were observed in the AlGaN barriers. We demonstrated that the ISB absorption in these *m*-plane GaN/AlGaN MQWs could be tuned in the range of 4.0-5.8 µm, the longer wavelength being set by the second order of the GaN Reststrahlen band when using bulk substrates. However, the density of defects in these structures was still too high to compete with polar *c*-plane samples in this spectral range.

The possibility of using the nonpolar *m*-plane orientation of GaN was then considered for the FIR range. Indeed, ISB absorption in this range requires AlGaN barriers with much lower Al content, which implies a much lower lattice mismatch. We thus studied *m*-plane low-Al-composition GaN/AlGaN MQWs (Al composition in the AlGaN alloy below 10% and average Al concentration in the MQW below 6%), designed to show ISB absorption in the FIR. The structures displayed flat and regular layers in the two in-plane directions and a very good crystalline quality. No extended defects like stacking faults or dislocations were observed, and cracks propagating along the *a* direction were present only when the total MQW thickness exceeded 1.2 µm. Inhomogeneities of the Al composition in the barriers were observed along the growth axis *m.* Optically, the structures showed low-temperature ISB absorption in the 6.3 to 37.4 meV (1.5 to 9 THz) range. With this result, we provide an experimental demonstration of the possibility for GaN to cover a large part of the 7–10 THz band forbidden to GaAs-based technologies.

However, the demonstrated ISB absorption was spectrally broad due to the high Si doping density ($n_s = 3\times10^{12}$ cm^{-2}). To confirm the effect of doping on the structural and optical properties of the nanostructures, we reproduced one of the GaN/AlGaN MQWs designs with ISB absorption at 30 meV (10 nm GaN / 18.5 nm $Al_{0.075}Ga_{0.925}N$), and varied the Si doping density in the wells from 1×10^{11} cm^{-2} to 3×10^{12} cm^{-2}. The obtained structures displayed low-temperature ISB absorption in the THz range. Increasing the doping level lead to an enhancement and blueshift of the absorption peak energy, together with an increase of the linewidth. However, high levels of n-doping resulted in the presence of free carriers in the excited electron level, *i.e.* the increase of the Fermi level energy. This appeared as a saturation of the absorption at the doping density 1×10^{12} cm^{-2}, with the magnitude of the blueshift and broadening increasing less than theoretically predicted.

Finally, we assessed the possibility to use Ge as n-dopant instead of Si. We grew a series of Ge-doped nonpolar *m*-plane GaN/AlGaN MQWs for ISB absorption at 30 meV reproducing again the same design (10 nm GaN / 18.5 nm $Al_{0.075}Ga_{0.925}N$). The Ge doping density in the wells was varied from 5×10^{11} cm^{-2} to 5×10^{12} cm^{-2}. All the structures display low-temperature ISB absorption in the THz range. Structurally, the Ge-doped samples were very comparable to those doped with Si in terms of roughness and crystalline quality. No extended defects (neither dislocations nor stacking faults)

were generated during the epitaxial process. Optically, for equivalent doping densities, the Ge-doped structures showed ISB absorption peaks with slightly smaller normalized spectral broadening.

Conclusions and perspectives

Atoms are flying
Quantum wells are absorbing
And my dream comes true

The purpose of this work was to explore alternatives to Si-doped (0001)-oriented GaN/AlGaN MQWs for ISB absorption in the infrared range. On the one hand, we discussed the possibility to use Ge as an n-dopant. On the other hand, and this was our main issue, we assessed the optical and structural performance of GaN/AlGaN MQWs grown along the nonpolar orientations (1-100) and (11-20) (*m* and *a*-plane, respectively) of GaN to obtain square potential profiles with ISB absorption in the whole infrared domain.

Ge as an alternative dopant to Si

The growth process of GaN in presence of Ge was first studied. By verifying that the Ga kinetics and thus the Ga-bilayer formation was not disturbed by the Ge flux, we ensured that high quality growth surface could be obtained, even for Ge cell temperatures up to 1000°C. Then, we studied the structural, electrical and optical characteristics of Ge-doped GaN thin films, using n.i.d. thin films as references. For the carrier concentrations in the range of 7.8×10^{17} cm^{-3} to 6.7×10^{20} cm^{-3}, Ge incorporation showed no effect on the structural quality and mosaicity of the layers. By Hall Effect, we measured the resulting free carrier concentration and demonstrated that the incorporation of the dopant scales linearly with the Ge flux. Optically, the evolution of the band-to-band emission from the Ge-doped thin films as a function of the Ge concentration was in agreement with theoretical calculations taking into account the effects of high electron densities on the bandgap and on the band-to-band transition energies (BGR and the BME). These results show that Ge can be used as an alternative to Si as an n-type dopant for GaN grown by plasma-assisted MBE.

As a first example of the relevance of Ge doping, we studied its efficiency to screen the internal electric field in GaN/AlN NWs. Indeed, the internal electric field leads to the spatial separation of electron and holes, which results in the extension of the carrier lifetime. We observed a huge drop of the carrier lifetimes with increasing Ge-doping, which confirms the screening effect of the free carriers introduced by doping. On the other hand, carrier lifetimes were measured longer in undoped NWs than in undoped QWs with similar width, and the spectral shift associated to screening was much larger in NWs than in QWs. The long relaxation times measured in the NWs were explained as the result of the fact that, at low dopant concentrations, there is a radial electron-hole separation in the NWs. Increasing the dopant concentration resulted in a screening of the radial electric field, which lead to the realignment of the electron and hole wavefunctions, and hence to a large decrease of the radiative lifetime. Overall, these results point out that Ge-doping is an efficient dopant for GaN/AlN structures.

Coming to the heart of the topic, ISB transitions in GaN/AlGaN planar heterostructures, we then compared the structural and optical (band-to-band and ISB) performance of Ge- and Si-doped 2D GaN/AlGaN MQWs with ISB absorption in the short-wavelength and mid-infrared ranges. The GaN QWs were homogeneously doped with Si or Ge with different doping densities. Structurally, the use of Ge contributed to improve the mosaicity of the high lattice mismatched-GaN/AlN MQWs, but had no relevant effect on GaN/AlGaN MQWs. The band-to-band properties were not affected by the nature dopant. In terms of intersubband transitions, increasing the doping concentrations in both GaN/AlN MQWs and GaN/AlGaN MQWs induced an energy blueshift due to many-body effects

which was similar for both dopants. However, stronger spectral broadening of the ISB absorption is observed in the case of Si-doping.

Towards the THz range with nonpolar GaN

The main issue of this work was to explore the possibility of using nonpolar *a*- or *m*-plane GaN for infrared optoelectronics. This alternative to polar *c*-plane GaN is considered as a potential answer to the issues raised by the polarization-induced electric field in (0001)-oriented heterostructures, and a possible opening towards the development of THz GaN-based devices.

We first considered GaN/AlN MQWs with ISB absorption in the SWIR range, where the structures were simultaneously grown on *c*-, *a*- and *m*-plane GaN. Compared to nonpolar *a* plane samples, *m*-plane structures displayed better structural characteristics (mosaicity, surface roughness) as well as better optical performance (band-to-band emission linewidth and intensity, and ISB absorption). Furthermore, the *m*-plane GaN/AlN MQWs showed ISB absorption in the 1.5-2.9 µm range, covering the whole SWIR spectrum, with performance comparable to polar *c*-plane MQWs. These results allowed us to choose and move forward with the nonpolar *m*-plane orientation of GaN, eventhough the density of extended structural defects in the nonpolar structures resulting from the high lattice mismatch was too high to consider any further device processing.

By introducing Ga in the AlN barriers, we reduced the average Al composition of the structure and thus the lattice mismatch, and this way extended the study to *m*-GaN/AlGaN MQWs with ISB transition in the MIR range. Thanks to the reduced lattice mismatch, the density of cracks was reduced, but stacking faults were still present, and Al-rich clusters were observed in the AlGaN barriers. We demonstrated that the ISB absorption in these *m*-plane GaN/AlGaN MQWs could be tuned in the range of 4.0-5.8 µm, the longer wavelength being set by the second order of the GaN Reststrahlen band when using bulk substrates. Again, the density of defects in these structures was still too high to compete with polar *c*-plane samples in this spectral range, but these results showed how reducing the Al composition of the stack resulted in an improvement of the MQWs structural quality.

We then considered the possibility of using the nonpolar *m*-plane orientation of GaN to grow GaN/AlGaN MQWs with ISB absorption in the FIR range, where Al composition only as low as 10% in the alloy are required, allowing for an even much reduced lattice mismatch. As a result, the structures displayed flat and regular layers in the two in-plane directions and a very good crystalline quality. No extended defects like stacking faults or dislocations were observed, and cracks propagating along the *a* direction were present only when the total MQW thickness exceeded 1.2 µm. Inhomogeneities of the Al composition in the barriers were still observed along the growth axis *m* instead of the previously seen Al-rich clusters. Optically, the structures showed broadband ISB absorption in the 6.3 to 37.4 meV (1.5 to 9 THz) range at 5 K. With these results, we provided an experimental demonstration of the possibility for GaN ISB technologies to cover a large part of the 7–10 THz band forbidden to GaAs-based technologies.

The large spectral broadening of the THz ISB absorption was assigned to the high Si doping density ($n_s = 3\times10^{12}$ cm^{-2}), which we confirmed by studying the effect of Si-doping on the structural and optical properties of GaN/$Al_{0.075}Ga_{0.925}N$ MQWs designed for ISB absorption at 30 meV, where the Si doping density in the wells was varied from 1×10^{11} cm^{-2} to 3×10^{12} cm^{-2}. The structures displayed low-temperature ISB absorption in the THz range as expected, and we demonstrate that increasing the doping level lead to an enhancement and blueshift of the absorption peak energy, together with an increase of the linewidth. For high levels of n-doping, we observe the presence of

free carriers in the excited electron level, *i.e.* the increase of the Fermi level energy. This appeared as a saturation of the absorption at the doping density 1×10^{12} cm^{-2}, in agreement with the broadband ISB absorptions observed in the previous series of samples, with the magnitude of the blueshift and broadening increasing less than theoretically predicted.

Taking advantage of the conclusions we drew from the Ge-doping study, we assessed the possibility to use Ge as n-dopant instead of Si for the FIR *m*-plane GaN/$Al_{0.075}Ga_{0.925}N$ MQWs, in view of efficiently reaching high densities of doping. The Ge doping density in the wells was varied from 5×10^{11} cm^{-2} to 5×10^{12} cm^{-2}, and all the structures display low-temperature ISB absorption in the THz range. The structural quality of the Ge-doped samples was very similar to those doped with Si (roughness, mosaicity, and absence of any extended defects). Optically, for equivalent doping densities, the Ge-doped structures showed ISB absorption peaks with slightly smaller normalized spectral broadening.

Taking some perspective

From our results, we can say that Ge is indeed a possible alternative to Si to n-dope GaN. However, the improvement margin compared to Si-doping appears to be very slight when studying nonpolar *m*-plane GaN/AlGaN MQWs. To complete the study, we suggest to assess the effect of Ge-doping on *c*-plane GaN/AlGaN MQWs with ISB absorption in the FIR, using the 4-layer QW design from Beeler *et.al.* [173], which we did not have the time to do at the end of my thesis. Until further demonstration of their limitation is done, it is currently not possible to decide which one of the two dopants is the most favorable.

Concerning the alternative of nonpolar *m*-plane GaN to avoid any effect of the internal electric field, it appeared that *m*-plane structures could not compete with *c*-plane MQWs in the SWIR and MIR ranges due to the too high density of defects resulting from the high and anisotropic lattice mismatch. To be able to develop nonpolar devices in these ranges, further study and optimization of the homogeneity of nonpolar AlGaN ternary alloys in function of the growth conditions is required. However, the FIR heterostructures displayed outstanding structural quality and very good optical performance, allowing to obtain tunable THz ISB absorption in agreement with simulations and with a simple MQW design and growth process. Combined to the doping density adjustment we calibrated through our doping studies, these structures are very promising for further device processing, from QWIPs to QCLs. In view of realizing such devices, we suggest first to run electroluminescence experiments in the IR range, and to assess the possible resonant tunneling properties of THz heterostructures. Then, the demonstration of *m*-plane GaN/AlGaN THz devices could be considered starting by adapting the designs proposed for GaAs-based systems. Aside from the IR, these results and the comparative study of nonpolar orientations of GaN can also be of interest for further development of UV and green LEDs, where the presence of the internal electric field is also an issue [302]. Beside the scientific and technical challenges to be raised, remaining issues hampering future device development and large-scale commercialization may concern the actual high cost and very reduced size of the *m*-plane free-standing GaN substrates, which has already been improved during my PhD and can be improved even more, for example by using patterned substrates or facetted growth surfaces.

References

[1] Himwas C, Songmuang R, Le Si Dang, Bleuse J, Rapenne L, Sarigiannidou E and Monroy E 2012 Thermal stability of the deep ultraviolet emission from AlGaN/AlN Stranski-Krastanov quantum dots *Appl. Phys. Lett.* **101** 241914

[2] Ambacher O 1998 Growth and applications of Group III-nitrides *J. Phys. Appl. Phys.* **31** 2653–710

[3] Gogneau N, Jamond N, Chrétien P, Houzé F, Lefeuvre E and Tchernycheva M 2016 From single III-nitride nanowires to piezoelectric generators: New route for powering nomad electronics *Semicond. Sci. Technol.* **31** 103002

[4] Wu J 2009 When group-III nitrides go infrared: New properties and perspectives *J. Appl. Phys.* **106** 011101

[5] - Herschel Space Observatory *http://www.herschel.caltech.edu/*

[6] - Optic fiber telecom illustration *https://www.shutterstock.com/g/PeterPhoto123*

[7] - Night vision goggles Armasight PVS7 illustration *Google Image*

[8] Beeler M, Trichas E and Monroy E 2013 III-nitride semiconductors for intersubband optoelectronics: a review *Semicond. Sci. Technol.* **28** 074022

[9] Rogalski A. 2012 History of infrared detectors *Opto-Electron. Rev.* **20** 279

[10] Seebeck, T J 1822 Magnetische Polarisation der Metalle und Erze durch Temperatur−Differenz *Abh Dtsch. Akad Wiss Berl.* 265–373

[11] Byrnes J S and North Atlantic Treaty Organization 2009 *Unexploded ordnance detection and mitigation* (Dordrecht ; [London]: Springer in cooperation with NATO Public Diplomacy Division)

[12] Smith W 1873 Effect of Light on Selenium During the Passage of An Electric Current* *Nature* **7** 303–303

[13] Beeler M, Trichas E and Monroy E 2013 III-nitride semiconductors for intersubband optoelectronics: a review *Semicond. Sci. Technol.* **28** 074022

[14] Rogalski and Chrzanowski 2002 Infra red devices and techniques **10** 111–36

[15] - Bandgap vs lattice constant *Univ. Ulm - Inst. Für Optoelektron.*

[16] West L C and Eglash S J 1985 First observation of an extremely large-dipole infrared transition within the conduction band of a GaAs quantum well *Appl. Phys. Lett.* **46** 1156–8

[17] Levine B F, Choi K K, Bethea C G, Walker J and Malik R J 1987 New 10 μm infrared detector using intersubband absorption in resonant tunneling GaAlAs superlattices *Appl. Phys. Lett.* **50** 1092–4

[18] Levine B F 1993 Quantum-well infrared photodetectors *J. Appl. Phys.* **74** R1–R81

[19] Ma B S, Fan W J, Dang Y X, Cheah W K, Loke W K, Liu W, Li D S, Yoon S F, Zhang D H, Wang H and Tung C H 2007 GaInNAs double-barrier quantum well infrared photodetector with the photodetection at 1.24μm *Appl. Phys. Lett.* **91** 051102

[20] Gunapala S D, Bandara S V, Liu J K, Hill C J, Rafol S B, Mumolo J M, Trinh J T, Tidrow M Z and LeVan P D 2005 Development of mid-wavelength and long-wavelength megapixel portable QWIP imaging cameras *Infrared Phys. Technol.* **47** 67–75

[21] Walther C, Fischer M, Scalari G, Terazzi R, Hoyler N and Faist J 2007 Quantum cascade lasers operating from 1.2to1.6THz *Appl. Phys. Lett.* **91** 131122

[22] Yang Q, Manz C, Bronner W, Köhler K and Wagner J 2006 Room-temperature short-wavelength (λ∼3.7–3.9μm) GaInAs⁄AlAsSb quantum-cascade lasers *Appl. Phys. Lett.* **88** 121127

[23] Giorgetta F R, Baumann E, Graf M, Ajili L, Hoyler N, Giovannini M, Faist J, Hofstetter D, Krötz P and Sonnabend G 2007 16.5μm quantum cascade detector using miniband transport *Appl. Phys. Lett.* **90** 231111

[24] Adachi S 1994 GaAs and related materials *CERN Doc. Serv.*

[25] Baur J, Maier K, Kunzer M, Kaufmann U and Schneider J 1994 Determination of the GaN/AlN band offset via the (-/0) acceptor level of iron *Appl. Phys. Lett.* **65** 2211–3

[26] Wei S-H and Zunger A 1996 Valence band splittings and band offsets of AlN, GaN, and InN *Appl. Phys. Lett.* **69** 2719–21

[27] Dingle R, Sell D D, Stokowski S E and Ilegems M 1971 Absorption, Reflectance, and Luminescence of GaN Epitaxial Layers *Phys. Rev. B* **4** 1211–8

[28] Barker A S and Ilegems M 1973 Infrared Lattice Vibrations and Free-Electron Dispersion in GaN *Phys. Rev. B* **7** 743–50

[29] Birner S, Zibold T, Andlauer T, Kubis T, Sabathil M, Trellakis A and Vogl P 2007 nextnano: General Purpose 3-D Simulations *IEEE Trans. Electron Devices* **54** 2137–42

[30] R.A. Dragoset, A. Musgrove, C.W. Clark, W.C. Martin and K. Olsen Periodic Table : Atomic properties of the elements (2017)

[31] Gil B 2014 Basic Crystallography and Other Properties Linked with Symmetry *Physics of Wurtzite Nitrides and Oxides* (Springer International Publishing) pp 1–48

[32] Shannon R D and Prewitt C T 1969 Effective ionic radii in oxides and fluorides *Acta Crystallogr. B* **25** 925–46

[33] Vegard L 1921 Die Konstitution der Mischkristalle und die Raumfüllung der Atome *Z. Für Phys.* **5** 17–26

[34] Vurgaftman I and Meyer J R 2003 Band parameters for nitrogen-containing semiconductors *J. Appl. Phys.* **94** 3675–96

[35] Bernardini F, Fiorentini V and Vanderbilt D 1997 Spontaneous polarization and piezoelectric constants of III-V nitrides *Phys. Rev. B* **56** R10024–R10027

[36] Hellman E S 1998 The Polarity of GaN: a Critical Review *MRS Internet J. Nitride Semicond. Res.* **3** e11

[37] Keller S, Fichtenbaum N, Wu F, Lee G, DenBaars S P, Speck J S and Mishra U K 2006 Effect of the Nucleation Conditions on the Polarity of AlN and GaN Films Grown on C-face 6H-SiC *Jpn. J. Appl. Phys.* **45** L322–L325

[38] Sun C J, Kung P, Saxler A, Ohsato H, Bigan E, Razeghi M and Gaskill D K 1994 Thermal stability of GaN thin films grown on (0001) Al_2O_3, (01$\bar{1}$2) Al_2O_3 and (0001)$_{Si}$ 6H-SiC substrates *J. Appl. Phys.* **76** 236–41

[39] Kang S W, Shim H W, Lee D-Y, Han S-H, Kim D J, Kim J W, Oh B W, Kryliouk O and Anderson T J 2006 Effects on Optical Characteristics of GaN Polarity Controlled by Substrate *J. Semicond. Technol. Sci.* **6** 79

[40] Sun Q, Cho Y S, Lee I-H, Han J, Kong B H and Cho H K 2008 Nitrogen-polar GaN growth evolution on c-plane sapphire *Appl. Phys. Lett.* **93** 131912

[41] Faist J 2009 *Intersubband optoelectronics lecture notes* (ETH Zurich)

[42] Litimein F, Bouhafs B, Dridi Z and Ruterana P 2002 The electronic structure of wurtzite and zincblende AlN: an *ab initio* comparative study *New J. Phys.* **4** 64–64

[43] Chen G D, Smith M, Lin J Y, Jiang H X, Wei S, Asif Khan M and Sun C J 1996 Fundamental optical transitions in GaN *Appl. Phys. Lett.* **68** 2784–6

[44] Suzuki M, Uenoyama T and Yanase A 1995 First-principles calculations of effective-mass parameters of AlN and GaN *Phys. Rev. B* **52** 8132–9

[45] Bourne J and Jacobs R L 1972 The band structure of GaN *J. Phys. C Solid State Phys.* **5** 3462–8

[46] Bloom S, Harbeke G, Meier E and Ortenburger I B 1974 Band Structure and Reflectivity of GaN *Phys. Status Solidi B* **66** 161–8

[47] Williams B S 2007 Terahertz quantum-cascade lasers *Nat. Photonics* **1** 517–25

[48] Kobayashi A, Sankey O F, Volz S M and Dow J D 1983 Semiempirical tight-binding band structures of wurtzite semiconductors: AlN, CdS, CdSe, ZnS, and ZnO *Phys. Rev. B* **28** 935–45

[49] Jain S C, Willander M, Narayan J and Overstraeten R V 2000 III–nitrides: Growth, characterization, and properties *J. Appl. Phys.* **87** 965–1006

[50] Cláudio de Carvalho L, Schleife A, Fuchs F and Bechstedt F 2010 Valence-band splittings in cubic and hexagonal AlN, GaN, and InN *Appl. Phys. Lett.* **97** 232101

[51] Figge S, Kröncke H, Hommel D and Epelbaum B M 2009 Temperature dependence of the thermal expansion of AlN *Appl. Phys. Lett.* **94** -

[52] Roder C, Einfeldt S, Figge S and Hommel D 2005 Temperature dependence of the thermal expansion of GaN *Phys. Rev. B* **72** 085218

[53] Teisseyre H, Perlin P, Suski T, Grzegory I, Porowski S, Jun J, Pietraszko A and Moustakas T D 1994 Temperature dependence of the energy gap in GaN bulk single crystals and epitaxial layer *J. Appl. Phys.* **76** 2429–34

[54] Matsumoto T and Aoki M 1974 Temperature Dependence of Photoluminescence from GaN *Jpn. J. Appl. Phys.* **13** 1804–7

[55] Steude G, Hofmann D M, Meyer B K, Amano H and Akasaki I 1998 The Dependence of the Band Gap on Alloy Composition in Strained AlGaN on GaN *Phys. Status Solidi B* **205** R7–R8

[56] Lee S R, Wright A F, Crawford M H, Petersen G A, Han J and Biefeld R M 1999 The band-gap bowing of AlxGa1−xN alloys *Appl. Phys. Lett.* **74** 3344–6

[57] Levinshteĭn M E, Rumyantsev S L and Shur M 2001 *Properties of advanced semiconductor materials: GaN, AlN, InN, BN, SiC, SiGe* (New York: Wiley)

[58] Xu Y-N and Ching W Y 1993 Electronic, optical, and structural properties of some wurtzite crystals *Phys. Rev. B* **48** 4335–51

[59] Santic B 2003 On the hole effective mass and the free hole statistics in wurtzite GaN *Semicond. Sci. Technol.* **18** 219–24

[60] Ramos L E, Teles L K, Scolfaro L M R, Castineira J L P, Rosa A L and Leite J R 2001 Structural, electronic, and effective-mass properties of silicon and zinc-blende group-III nitride semiconductor compounds *Phys. Rev. B* **63**

[61] Bernardini F and Fiorentini V 2002 Nonlinear Behavior of Spontaneous and Piezoelectric Polarization in III-V Nitride Alloys *Phys. Status Solidi A* **190** 65–73

[62] Bougrioua Z, Laügt M, Vennéguès P, Cestier I, Gühne T, Frayssinet E, Gibart P and Leroux M 2007 Reduction of stacking faults in (11-20) and (11-22) GaN films by ELO techniques and benefit on GaN wells emission *Phys. Status Solidi A* **204** 282–9

[63] Arguello C A, Rousseau D L and Porto S P S 1969 First-Order Raman Effect in Wurtzite-Type Crystals *Phys. Rev.* **181** 1351–63

[64] Gorczyca I, Christensen N E, Peltzer y Blancá E L and Rodriguez C O 1995 Optical phonon modes in GaN and AlN *Phys. Rev. B* **51** 11936–9

[65] Lemos V, Argüello C A and Leite R C C 1972 Resonant Raman scattering of TO(A1), TO(E1) and E2 optical phonons in GaN *Solid State Commun.* **11** 1351–3

[66] Sanjurjo J A, López-Cruz E, Vogl P and Cardona M 1983 Dependence on volume of the phonon frequencies and the ir effective charges of several III-V semiconductors *Phys. Rev. B* **28** 4579–84

[67] Yang J, Brown G J, Dutta M and Stroscio M A 2005 Photon absorption in the Restrahlen band of thin films of GaN and AlN: Two phonon effects *J. Appl. Phys.* **98** 043517

[68] Ibáñez J, Hernández S, Alarcón-Lladó E, Cuscó R, Artús L, Novikov S V, Foxon C T and Calleja E 2008 Far-infrared transmission in GaN, AlN, and AlGaN thin films grown by molecular beam epitaxy *J. Appl. Phys.* **104** 033544

[69] Martin G, Strite S, Botchkarev A, Agarwal A, Rockett A, Morkoç H, Lambrecht W R L and Segall B 1994 Valence-band discontinuity between GaN and AlN measured by x-ray photoemission spectroscopy *Appl. Phys. Lett.* **65** 610–2

[70] Cociorva D, Aulbur W G and Wilkins J W 2002 Quasiparticle calculations of band offsets at AlN–GaN interfaces *Solid State Commun.* **124** 63–6

[71] Tchernycheva M, Nevou L, Doyennette L, Julien F, Warde E, Guillot F, Monroy E, Bellet-Amalric E, Remmele T and Albrecht M 2006 Systematic experimental and theoretical investigation of intersubband absorption in GaN⁄AlN quantum wells *Phys. Rev. B* **73** 125347

[72] Wright A F 1997 Elastic properties of zinc-blende and wurtzite AlN, GaN, and InN *J. Appl. Phys.* **82** 2833–9

[73] Polian A, Grimsditch M and Grzegory I 1996 Elastic constants of gallium nitride *J. Appl. Phys.* **79** 3343–4

[74] Ruterana P and Nouet G 2001 Atomic Structure of Extended Defects in Wurtzite GaN Epitaxial Layers *Phys. Status Solidi B* **227** 177–228

[75] Ponce F A 1997 Detects and interfaces in GaN epitaxy *MRS Bull.* **22** 51–7

[76] Moran B, Wu F, Romanov A E, Mishra U K, Denbaars S P and Speck J S 2004 Structural and morphological evolution of GaN grown by metalorganic chemical vapor deposition on SiC substrates using an AlN initial layer *J. Cryst. Growth* **273** 38–47

[77] Kehagias T, Delimitis A, Komninou P, Iliopoulos E, Dimakis E, Georgakilas A and Nouet G 2005 Misfit accommodation of compact and columnar InN epilayers grown on Ga-face GaN (0001) by molecular-beam epitaxy *Appl. Phys. Lett.* **86** 151905

[78] Hearne S J, Han J, Lee S R, Floro J A, Follstaedt D M, Chason E and Tsong I S T 2000 Brittle-ductile relaxation kinetics of strained AlGaN/GaN heterostructures *Appl. Phys. Lett.* **76** 1534–6

[79] Floro J A, Follstaedt D M, Provencio P, Hearne S J and Lee S R 2004 Misfit dislocation formation in the AlGaN⁄GaN heterointerface *J. Appl. Phys.* **96** 7087–94

[80] Liu R, Mei J, Srinivasan S, Ponce F A, Omiya H, Narukawa Y and Mukai T 2006 Generation of misfit dislocations by basal-plane slip in InGaN⁄GaN heterostructures *Appl. Phys. Lett.* **89** 201911

[81] Nakamura S, Pearton S and Fasol G 2000 *The Blue Laser Diode: the Complete Story* (Berlin, Heidelberg: Springer Berlin Heidelberg)

[82] Wu X H, Brown L M, Kapolnek D, Keller S, Keller B, DenBaars S P and Speck J S 1996 Defect structure of metal-organic chemical vapor deposition-grown epitaxial (0001) GaN/Al_2O_3 *J. Appl. Phys.* **80** 3228–37

[83] S.K. Mathis, A.E. Romanov, L.F. Chen, G.E. Beltz, W. Pompe and J.S. Speck 2001 Modeling of threading dislocation reduction in growing GaN layers *J. Cryst. Growth* **231** 371–90

[84] Ning X J, Chien F R, Pirouz P, Yang J W and Khan M A 1996 Growth defects in GaN films on sapphire: The probable origin of threading dislocations *J. Mater. Res.* **11** 580–92

[85] Northrup J E 1998 Theory of the (12-10) prismatic stacking fault in GaN *Appl. Phys. Lett.* **72** 2316–8

[86] Potin V, Ruterana P and Nouet G 2000 HREM study of stacking faults in GaN layers grown over sapphire substrate *J. Phys. Condens. Matter* **12** 10301–6

[87] Vermaut P, Nouet G and Ruterana P 1999 Observation of two atomic configurations for the $\{12\bar{1}0\}$ stacking fault in wurtzite (Ga, Al) nitrides *Appl. Phys. Lett.* **74** 694–6

[88] Northrup J E and Neugebauer J 1996 Theory of GaN (10-10) and (11-20) surfaces *Phys. Rev. B* **53** R10477–R10480

[89] Potin V, Nouet G and Ruterana P 1999 Evidence for multiple atomic structure for the {10$\bar{1}$0} inversion domain boundaries in GaN layers *Appl. Phys. Lett.* **74** 947–9

[90] Drum C M 1965 Intersecting faults on basal and prismatic planes in aluminium nitride *Philos. Mag.* **11** 313–34

[91] Blank H, Delavignette P, Gevers R and Amelinckx S 1964 Fault Structures in Wurtzite *Phys. Status Solidi B* **7** 747–64

[92] Ruterana P, Barbaray B, Béré A, Vermaut P, Hairie A, Paumier E, Nouet G, Salvador A, Botchkarev A and Morkoç H 1999 Formation mechanism and relative stability of the { 11-20 } stacking fault atomic configurations in wurtzite (Al,Ga,In) nitrides *Phys. Rev. B* **59** 15917–25

[93] Northrup J E, Neugebauer J and Romano L T 1996 Inversion Domain and Stacking Mismatch Boundaries in GaN *Phys. Rev. Lett.* **77** 103–6

[94] Kandaswamy P K, Bougerol C, Jalabert D, Ruterana P and Monroy E 2009 Strain relaxation in short-period polar GaN/AlN superlattices *J. Appl. Phys.* **106** 013526

[95] Kandaswamy P 2010 *Nanostructures Al(Ga)N/GaN pour l'optoélectronique intersousbande dans l'infrarouge proche et moyen* (PhD thesis)

[96] Bykhovski A D, Gelmont B L and Shur M S 1997 Elastic strain relaxation and piezoeffect in GaN-AlN, GaN-AlGaN and GaN-InGaN superlattices *J. Appl. Phys.* **81** 6332–8

[97] Xinjiao L, Zechuan X, Ziyou H, Huazhe C, Wuda S, Zhongcai C, Feng Z and Enguang W 1986 On the properties of AlN thin films grown by low temperature reactive r.f. sputtering *Thin Solid Films* **139** 261–74

[98] Ambacher O, Smart J, Shealy J R, Weimann N G, Chu K, Murphy M, Schaff W J, Eastman L F, Dimitrov R, Wittmer L, Stutzmann M, Rieger W and Hilsenbeck J 1999 Two-dimensional electron gases induced by spontaneous and piezoelectric polarization charges in N- and Ga-face AlGaN/GaN heterostructures *J. Appl. Phys.* **85** 3222–33

[99] Ambacher O, Foutz B, Smart J, Shealy J R, Weimann N G, Chu K, Murphy M, Sierakowski A J, Schaff W J, Eastman L F, Dimitrov R, Mitchell A and Stutzmann M 2000 Two dimensional electron gases induced by spontaneous and piezoelectric polarization in undoped and doped AlGaN/GaN heterostructures *J. Appl. Phys.* **87** 334–44

[100] Takeuchi T, Amano H and Akasaki I 2000 Theoretical Study of Orientation Dependence of Piezoelectric Effects in Wurtzite Strained GaInN/GaN Heterostructures and Quantum Wells *Jpn. J. Appl. Phys.* **39** 413–6

[101] Grandjean N, Damilano B, Dalmasso S, Leroux M, Laügt M and Massies J 1999 Built-in electric-field effects in wurtzite AlGaN/GaN quantum wells *J. Appl. Phys.* **86** 3714

[102] Im J S, Kollmer H, Off J, Sohmer A, Scholz F and Hangleiter A 1997 Effects of Piezoelectric Fields in GaInN/GaN and GaN/AlGaN Heterostructures and Quantum Wells *MRS Proc.* **482**

[103] Kamgar A, Kneschaurek P, Dorda G and Koch J 1974 Resonance Spectroscopy of Electronic Levels in a Surface Accumulation Layer *Phys. Rev. Lett.* **32** 1251–4

[104] Ando T, Fowler A B and Stern F 1982 Electronic properties of two-dimensional systems *Rev. Mod. Phys.* **54** 437–672

[105] Esaki L and Sakaki H 1977 New Photoconductor *IBM Tech. Discl. Bull.* **20** 2456–7

[106] Chiu L C, Smith J S, Margalit S, Yariv A and Cho A Y 1983 Application of internal photoemission from quantum-well and heterojunction superlattices to infrared photodetectors *Infrared Phys.* **23** 93–7

[107] Smith J S, Chiu L C, Margalit S, Yariv A and Cho A Y 1983 A new infrared detector using electron emission from multiple quantum wells *J. Vac. Sci. Technol. B Microelectron. Nanometer Struct.* **1** 376–8

[108] Coon D D and Karunasiri R P G 1984 New mode of IR detection using quantum wells *Appl. Phys. Lett.* **45** 649–51

[109] Coon D D, Karunasiri R P G and Liu H C 1986 Fast response quantum well photodetectors *J. Appl. Phys.* **60** 2636–8

[110] West L C and Eglash S J 1985 First observation of an extremely large-dipole infrared transition within the conduction band of a GaAs quantum well *Appl. Phys. Lett.* **46** 1156–8

[111] Levine B F, Malik R J, Walker J, Choi K K, Bethea C G, Kleinman D A and Vandenberg J M 1987 Strong 8.2 μm infrared intersubband absorption in doped GaAs/AlAs quantum well waveguides *Appl. Phys. Lett.* **50** 273–5

[112] Levine B F, Choi K K, Bethea C G, Walker J and Malik R J 1987 New 10 μm infrared detector using intersubband absorption in resonant tunneling GaAlAs superlattices *Appl. Phys. Lett.* **50** 1092–4

[113] Levine B F 1993 Quantum-well infrared photodetectors *J. Appl. Phys.* **74** R1–R81

[114] Faist J, Capasso F, Sivco D L, Sirtori C, Hutchinson A L and Cho A Y 1994 Quantum Cascade Laser *Science* **264** 553–6

[115] Waugh J L T and Dolling G 1963 Crystal Dynamics of Gallium Arsenide *Phys. Rev.* **132** 2410–2

[116] Binggeli N, Ferrara P and Baldereschi A 2001 Band-offset trends in nitride heterojunctions *Phys. Rev. B* **63** 245306

[117] Suzuki N and Iizuka N 1997 Feasibility Study on Ultrafast Nonlinear Optical Properties of 1.55-μm Intersubband Transition in AlGaN/GaN Quantum Wells *Jpn. J. Appl. Phys.* **36** L1006–L1008

[118] Hofstetter D, Baumann E, Giorgetta F R, Théron R, Wu H, Schaff W J, Dawlaty J, George P A, Eastman L F, Rana F, Kandaswamy P K, Guillot F and Monroy E 2010 Intersubband Transition-Based Processes and Devices in AlN/GaN-Based Heterostructures *Proc. IEEE* **98** 1234 –1248

[119] Machhadani H, Kandaswamy P, Sakr S, Vardi A, Wirtmüller A, Nevou L, Guillot F, Pozzovivo G, Tchernycheva M, Lupu A, Vivien L, Crozat P, Warde E, Bougerol C, Schacham S, Strasser G, Bahir G, Monroy E and Julien F H 2009 GaN/AlGaN intersubband optoelectronic devices *New J. Phys.* **11** 125023

[120] Hao M, Mahanty S, Qhalid Fareed R S, Tottori S, Nishino K and Sakai S 1999 Infrared properties of bulk GaN *Appl. Phys. Lett.* **74** 2788–90

[121] Welna M, Kudrawiec R, Motyka M, Kucharski R, Zając M, Rudziński M, Misiewicz J, Doradziński R and Dwiliński R 2012 Transparency of GaN substrates in the mid-infrared spectral range *Cryst. Res. Technol.* **47** 347–50

[122] Liu H C and Capasso F 2000 *Intersubband transitions in quantum wells: Physics and device applications* (San Diego, CA: Academic Press)

[123] Bastard G 1988 *Wave mechanics applied to semiconductor heterostructures* (Les Ulis Cedex, France; New York, N.Y.: Les Editions de Physique ; Halsted Press)

[124] Ando T 1985 Line Width of Inter-Subband Absorption in Inversion Layers: Scattering from Charged Ions *J. Phys. Soc. Jpn.* **54** 2671–5

[125] Ando T 1978 Broadening of Inter-Subband Transitions in Image-Potential-Induced Surface States outside Liquid Helium *J. Phys. Soc. Jpn.* **44** 765–73

[126] Unuma T, Yoshita M, Noda T, Sakaki H and Akiyama H 2003 Intersubband absorption linewidth in GaAs quantum wells due to scattering by interface roughness, phonons, alloy disorder, and impurities *J. Appl. Phys.* **93** 1586

[127] Unuma T, Takahashi T, Noda T, Yoshita M, Sakaki H, Baba M and Akiyama H 2001 Effects of interface roughness and phonon scattering on intersubband absorption linewidth in a GaAs quantum well *Appl. Phys. Lett.* **78** 3448–50

[128] Price P . 1981 Two-dimensional electron transport in semiconductor layers. I. Phonon scattering *Ann. Phys.* **133** 217–39

[129] Smet J H, Fonstad C G and Hu Q 1996 Intrawell and interwell intersubband transitions in multiple quantum wells for far-infrared sources *J. Appl. Phys.* **79** 9305–20

[130] Hyldgaard P and Wilkins J W 1996 Electron-electron scattering in far-infrared quantum cascade lasers *Phys. Rev. B* **53** 6889–92

[131] Ferreira R and Bastard G 1989 Evaluation of some scattering times for electrons in unbiased and biased single- and multiple-quantum-well structures *Phys. Rev. B* **40** 1074–86

[132] Sakaki H, Noda T, Hirakawa K, Tanaka M and Matsusue T 1987 Interface roughness scattering in GaAs/AlAs quantum wells *Appl. Phys. Lett.* **51** 1934–6

[133] Campman K L, Schmidt H, Imamoglu A and Gossard A C 1996 Interface roughness and alloy-disorder scattering contributions to intersubband transition linewidths *Appl. Phys. Lett.* **69** 2554–6

[134] Warburton R J, Weilhammer K, Kotthaus J P, Thomas M and Kroemer H 1998 Influence of Collective Effects on the Linewidth of Intersubband Resonance *Phys. Rev. Lett.* **80** 2185–8

[135] Kandaswamy P K, Machhadani H, Kotsar Y, Sakr S, Das A, Tchernycheva M, Rapenne L, Sarigiannidou E, Julien F H and Monroy E 2010 Effect of doping on the mid-infrared intersubband absorption in GaN/AlGaN superlattices grown on Si(111) templates *Appl. Phys. Lett.* **96** 141903

[136] Shtrichman I, Metzner C, Ehrenfreund E, Gershoni D, Maranowski K D and Gossard A C 2001 Depolarization shift of the intersubband resonance in a quantum well with an electron-hole plasma *Phys. Rev. B* **65**

[137] Bloss W L 1989 Effects of Hartree, exchange, and correlation energy on intersubband transitions *J. Appl. Phys.* **66** 3639–42

[138] Li J M, Han X X, Wu J J, Liu X L, Zhu Q S and Wang Z G 2005 Origin of the blueshift in the infrared absorbance of intersubband transitions in AlxGa1-x N/GaN multiple quantum wells *Phys. E Low-Dimens. Syst. Nanostructures* **25** 575–81

[139] Vinter B 1976 Many-body effects in n -type Si inversion layers. I. Effects in the lowest subband *Phys. Rev. B* **13** 4447–56

[140] Vinter B 1977 Many-body effects in n -type Si inversion layers. II. Excitations to higher subbands *Phys. Rev. B* **15** 3947–58

[141] Batke E, Weimann G and Schlapp W 1991 Quenching of collective phenomena in combined intersubband-cyclotron resonances in GaAs *Phys. Rev. B* **43** 6812–5

[142] Allen S J, Tsui D C and Vinter B 1976 On the absorption of infrared radiation by electrons in semiconductor inversion layers *Solid State Commun.* **20** 425–8

[143] Ando T 1977 Inter-subband optical transitions in a surface space-charge layer *Solid State Commun.* **21** 133–6

[144] Ando T 1977 Inter-subband optical absorption in space-charge layers on semiconductor surfaces *Z. Für Phys. B Condens. Matter Quanta* **26** 263–72

[145] Bandara K M S V, Coon D D, O B, Lin Y F and Francombe M H 1988 Exchange interactions in quantum well subbands *Appl. Phys. Lett.* **53** 1931

[146] Bandara K M S V, Coon D D, O B, Lin Y F and Francombe M H 1989 Erratum: Exchange interactions in quantum well subbands [Appl. Phys. Lett. 53, 1931 (1988)] *Appl. Phys. Lett.* **55** 206

[147] Beeler M and Monroy E 2015 III-nitride semiconductors: new infrared intersubband technologies *Gallium nitride (GaN): physics, devices, and technology* Devices, circuits, and systems ed F Medjdoub and K Iniewski (Boca Raton: CRC Press)

[148] Julien F H, Tchernycheva M, Nevou L, Doyennette L, Colombelli R, Warde E, Guillot F and Monroy E 2007 Nitride intersubband devices: prospects and recent developments *Phys. Status Solidi A* **204** 1987–95

[149] Razeghi M 2011 III-Nitride Optoelectronic Devices: From Ultraviolet Toward Terahertz *IEEE Photonics J.* **3** 263–7

[150] Gil B 2013 *III-Nitride Semiconductors and Their Modern Devices* (Oxford University Press)

[151] Tchernycheva M, Julien F H and Monroy E 2010 Review of nitride infrared intersubband devices *Proc. SPIE* **7602** 76021A

[152] C. B. Lim, A. Ajay, J. Lähnemann, D. A. Browne and E. Monroy 2017 Intersubband Optoelectronics using III-Nitride Semiconductors *HandBook of GaN Semiconductor Materials and Devices* ed W. Bi, H.-C. Kuo, P.-C. Ku and B. Shen (Taylor & Francis, UK)

[153] C. B. Lim, A. Ajay, J. Lähnemann, D. A. Browne and E. Monroy 2017 III-Nitride Nanostructures for Intersubband Optoelectronics *III-Nitride Materials, Devices and Nano-Structures* ed Z. C. Feng (World Scientific Europe, UK)

[154] Suzuki N and Iizuka N 1999 Effect of Polarization Field on Intersubband Transition in AlGaN/GaN Quantum Wells *Jpn. J. Appl. Phys.* **38** L363–L365

[155] Gmachl C, Ng H M and Cho A Y 2000 Intersubband absorption in GaN/AlGaN multiple quantum wells in the wavelength range of λ~1.75-4.2 μm *Appl. Phys. Lett.* **77** 334–6

[156] Gmachl C, Ng H M, George Chu S-N and Cho A Y 2000 Intersubband absorption at λ~1.55 μm in well- and modulation-doped GaN/AlGaN multiple quantum wells with superlattice barriers *Appl. Phys. Lett.* **77** 3722–4

[157] Iizuka N, Kaneko K and Suzuki N 2002 Near-infrared intersubband absorption in GaN/AlN quantum wells grown by molecular beam epitaxy *Appl. Phys. Lett.* **81** 1803–5

[158] Kishino K, Kikuchi A, Kanazawa H and Tachibana T 2002 Intersubband transition in (GaN)[sub m]/(AlN)[sub n] superlattices in the wavelength range from 1.08 to 1.61 μm *Appl. Phys. Lett.* **81** 1234–6

[159] Helman A, Tchernycheva M, Lusson A, Warde E, Julien F H, Moumanis K, Fishman G, Monroy E, Daudin B, Le Si Dang D, Bellet-Amalric E and Jalabert D 2003 Intersubband spectroscopy of doped and undoped GaN/AlN quantum wells grown by molecular-beam epitaxy *Appl. Phys. Lett.* **83** 5196–8

[160] Kandaswamy P K, Guillot F, Bellet-Amalric E, Monroy E, Nevou L, Tchernycheva M, Michon A, Julien F H, Baumann E, Giorgetta F R, Hofstetter D, Remmele T, Albrecht M, Birner S and Dang L S 2008 GaN/AlN short-period superlattices for intersubband optoelectronics: A systematic study of their epitaxial growth, design, and performance *J. Appl. Phys.* **104** 093501

[161] Bayram C, Péré-laperne N and Razeghi M 2009 Effects of well width and growth temperature on optical and structural characteristics of AlN/GaN superlattices grown by metal-organic chemical vapor deposition *Appl. Phys. Lett.* **95** 201906

[162] Andersson T G, Liu X Y, Aggerstam T, Holmström P, Lourdudoss S, Thylen L, Chen Y L, Hsieh C H and Lo I 2009 Macroscopic defects in GaN/AlN multiple quantum well structures grown by MBE on GaN templates *Microelectron. J.* **40** 360–2

[163] Liu X Y, Holmström P, Jänes P, Thylén L and Andersson T G 2007 Intersubband absorption at 1.5–3.5 μm in GaN/AlN multiple quantum wells grown by molecular beam epitaxy on sapphire *Phys. Status Solidi B* **244** 2892–905

[164] Berland K, Stattin M, Farivar R, Sultan D M S, Hyldgaard P, Larsson A, Wang S M and Andersson T G 2010 Temperature stability of intersubband transitions in AlN/GaN quantum wells *Appl. Phys. Lett.* **97** 043507

[165] Sherliker B, Halsall M, Kasalynas I, Seliuta D, Valusis G, Vengris M, Barkauskas M, Sirutkaitis V, Harrison P, Jovanovic V D, Indjin D, Ikonic Z, Parbrook P J, Wang T and Buckle P D 2007 Room temperature operation of AlGaN/GaN quantum well infrared photodetectors at a 3–4 μm wavelength range *Semicond. Sci. Technol.* **22** 1240–4

[166] Péré-Laperne N, Bayram C, Nguyen-The L, McClintock R and Razeghi M 2009 Tunability of intersubband absorption from 4.5 to 5.3 μm in a GaN/Al[sub 0.2]Ga[sub 0.8]N superlattices grown by metalorganic chemical vapor deposition *Appl. Phys. Lett.* **95** 131109

[167] Bayram C 2012 High-quality AlGaN/GaN superlattices for near- and mid-infrared intersubband transitions *J. Appl. Phys.* **111** 013514

[168] Huang C C, Xu F J, Yan X D, Song J, Xu Z Y, Cen L B, Wang Y, Pan J H, Wang X Q, Yang Z J, Shen B, Zhang B S, Chen X S and Lu W 2011 Intersubband transitions at atmospheric window in Al(x)Ga(1−x)N/GaN multiple quantum wells grown on GaN/sapphire templates adopting AlN/GaN superlattices interlayer *Appl. Phys. Lett.* **98** 132105

[169] Kandaswamy P K, Machhadani H, Bougerol C, Sakr S, Tchernycheva M, Julien F H and Monroy E 2009 Midinfrared intersubband absorption in GaN/AlGaN superlattices on Si(111) templates *Appl. Phys. Lett.* **95** 141911

[170] Machhadani H, Kotsar Y, Sakr S, Tchernycheva M, Colombelli R, Mangeney J, Bellet-Amalric E, Sarigiannidou E, Monroy E and Julien F H 2010 Terahertz intersubband absorption in GaN/AlGaN step quantum wells *Appl. Phys. Lett.* **97** 191101

[171] Beeler M, Bougerol C, Bellet-Amalric E and Monroy E 2014 Pseudo-square AlGaN/GaN quantum wells for terahertz absorption *Appl. Phys. Lett.* **105** 131106

[172] Beeler M, Bougerol C, Bellet-Amalaric E and Monroy E 2014 THz intersubband transitions in AlGaN/GaN multi-quantum-wells *Phys. Status Solidi A* **211** 761–4

[173] Beeler M, Bougerol C, Bellet-Amalric E and Monroy E 2013 Terahertz absorbing AlGaN/GaN multi-quantum-wells: Demonstration of a robust 4-layer design *Appl. Phys. Lett.* **103** 091108

[174] Iizuka N, Kaneko K and Suzuki N 2006 All-Optical Switch Utilizing Intersubband Transition in GaN Quantum Wells *IEEE J. Quantum Electron.* **42** 765–71

[175] Tchernycheva M, Nevou L, Doyennette L, Julien F H, Guillot F, Monroy E, Remmele T and Albrecht M 2006 Electron confinement in strongly coupled GaN⁄AlN quantum wells *Appl. Phys. Lett.* **88** 153113

[176] Kheirodin N, Nevou L, Machhadani H, Crozat P, Vivien L, Tchernycheva M, Lupu A, Julien F H, Pozzovivo G, Golka S, Strasser G, Guillot F and Monroy E 2008 Electrooptical Modulator at Telecommunication Wavelengths Based on GaN/AlN Coupled Quantum Wells *IEEE Photonics Technol. Lett.* **20** 724–6

[177] Hofstetter D, Schad S-S, Wu H, Schaff W J and Eastman L F 2003 GaN/AlN-based quantum-well infrared photodetector for 1.55 μm *Appl. Phys. Lett.* **83** 572–4

[178] Baumann E, Giorgetta F R, Hofstetter D, Lu H, Chen X, Schaff W J, Eastman L F, Golka S, Schrenk W and Strasser G 2005 Intersubband photoconductivity at 1.6 μm using a strain-compensated AlN⁄GaN superlattice *Appl. Phys. Lett.* **87** 191102

[179] Doyennette L, Nevou L, Tchernycheva M, Lupu A, Guillot F, Monroy E, Colombelli R and Julien F H 2005 GaN-based quantum dot infrared photodetector operating at 1.38 μm *Electron. Lett.* **41** 1077 – 1078

[180] Vardi A, Akopian N, Bahir G, Doyennette L, Tchernycheva M, Nevou L, Julien F H, Guillot F and Monroy E 2006 Room temperature demonstration of GaN/AlN quantum dot intraband infrared photodetector at fiber-optics communication wavelength *Appl. Phys. Lett.* **88** 143101

[181] Vardi A, Bahir G, Schacham S E, Kandaswamy P K and Monroy E 2009 Photocurrent spectroscopy of bound-to-bound intraband transitions in GaN/AlN quantum dots *Phys. Rev. B* **80** 155439

[182] Nevou L, Julien F H, Colombelli R, Guillot F and Monroy E 2006 Room-temperature intersubband emission of GaN/AlN quantum wells at λ=2.3 μm *Electron. Lett.* **42** 1308–9

[183] Nevou L, Tchernycheva M, Julien F H, Guillot F and Monroy E 2007 Short wavelength (λ=2.13 μm) intersubband luminescence from GaN⁄AlN quantum wells at room temperature *Appl. Phys. Lett.* **90** 121106

[184] Driscoll K, Liao Y, Bhattacharyya A, Zhou L, Smith D J, Moustakas T D and Paiella R 2009 Optically pumped intersubband emission of short-wave infrared radiation with GaN/AlN quantum wells *Appl. Phys. Lett.* **94** 081120

[185] Nevou L, Julien F H, Tchernycheva M, Guillot F, Monroy E and Sarigiannidou E 2008 Intraband emission at λ≈1.48 μm from GaN⁄AlN quantum dots at room temperature *Appl. Phys. Lett.* **92** 161105

[186] Vardi A, Bahir G, Guillot F, Bougerol C, Monroy E, Schacham S E, Tchernycheva M and Julien F H 2008 Near infrared quantum cascade detector in GaN/AlGaN/AlN heterostructures *Appl. Phys. Lett.* **92** 011112

[187] Vardi A, Kheirodin N, Nevou L, Machhadani H, Vivien L, Crozat P, Tchernycheva M, Colombelli R, Julien F H, Guillot F, Bougerol C, Monroy E, Schacham S and Bahir G 2008 High-speed operation of GaN/AlGaN quantum cascade detectors at λ ≈ 1.55 μm *Appl. Phys. Lett.* **93** 193509

[188] Romanov A E, Baker T J, Nakamura S, Speck J S and ERATO/JST UCSB Group 2006 Strain-induced polarization in wurtzite III-nitride semipolar layers *J. Appl. Phys.* **100** 023522

[189] Lahourcade L, Kandaswamy P K, Renard J, Ruterana P, Machhadani H, Tchernycheva M, Julien F H, Gayral B and Monroy E 2008 Interband and intersubband optical characterization of semipolar (11-22)-oriented GaN/AlN multiple-quantum-well structures *Appl. Phys. Lett.* **93** 111906

[190] Machhadani H, Beeler M, Sakr S, Warde E, Kotsar Y, Tchernycheva M, Chauvat M P, Ruterana P, Nataf G, De Mierry P, Monroy E and Julien F H 2013 Systematic study of near-infrared intersubband absorption of polar and semipolar GaN/AlN quantum wells *J. Appl. Phys.* **113** 143109

[191] Durmaz H, Nothern D, Brummer G, Moustakas T D and Paiella R 2016 Terahertz intersubband photodetectors based on semi-polar GaN/AlGaN heterostructures *Appl. Phys. Lett.* **108** 201102

[192] Lahourcade L, Bellet-Amalric E, Monroy E, Abouzaid M and Ruterana P 2007 Plasma-assisted molecular-beam epitaxy of AlN(11-22) on m sapphire *Appl. Phys. Lett.* **90** 131909

[193] Gmachl C and Ng H M 2003 Intersubband absorption at ~2.1 μm in A-plane GaN⁄AlN multiple quantum wells *Electron. Lett.* **39** 567–9

[194] Shao J, Zakharov D N, Edmunds C, Malis O and Manfra M J 2013 Homogeneous AlGaN/GaN superlattices grown on free-standing ($11\bar{0}0$) GaN substrates by plasma-assisted molecular beam epitaxy *Appl. Phys. Lett.* **103** 232103

[195] Shao J, Tang L, Edmunds C, Gardner G, Malis O and Manfra M 2013 Surface morphology evolution of m-plane (1-100) GaN during molecular beam epitaxy growth: Impact of Ga/N ratio, miscut direction, and growth temperature *J. Appl. Phys.* **114** 023508

[196] Armstrong A M, Kelchner K, Nakamura S, DenBaars S P and Speck J S 2013 Influence of growth temperature and temperature ramps on deep level defect incorporation in m-plane GaN *Appl. Phys. Lett.* **103** 232108

[197] Pesach A, Gross E, Huang C-Y, Lin Y-D, Vardi A, Schacham S E, Nakamura S and Bahir G 2013 Non-polar m-plane intersubband based InGaN/(Al)GaN quantum well infrared photodetectors *Appl. Phys. Lett.* **103** 022110

[198] Edmunds C, Shao J, Shirazi-HD M, Manfra M J and Malis O 2014 Terahertz intersubband absorption in non-polar m-plane AlGaN/GaN quantum wells *Appl. Phys. Lett.* **105** 021109

[199] Bayram C, Vashaei Z and Razeghi M 2010 Reliability in room-temperature negative differential resistance characteristics of low-aluminum content AlGaN/GaN double-barrier resonant tunneling diodes *Appl. Phys. Lett.* **97** 181109

[200] Park S-H 2000 Crystal Orientation Effects on Electronic Properties of Wurtzite GaN/AlGaN Quantum Wells with Spontaneous and Piezoelectric Polarization *Jpn. J. Appl. Phys.* **39** 3478–82

[201] Rinke P, Winkelnkemper M, Qteish A, Bimberg D, Neugebauer J and Scheffler M 2008 Consistent set of band parameters for the group-III nitrides AlN, GaN, and InN *Phys. Rev. B* **77** 075202

[202] Potin V, Vermaut P, Ruterana P and Nouet G 1998 Extended defects in wurtzite nitride semiconductors *J. Electron. Mater.* **27** 266–75

[203] Liliental-Weber Z, Kisielowski C, Ruvimov S, Chen Y, Washburn J, Grzegory I, Bockowski M, Jun J and Porowski S 1996 Structural characterization of bulk GaN crystals grown under high hydrostatic pressure *J. Electron. Mater.* **25** 1545–50

[204] Kotsar Y 2012 *Puits quantiques GaN/Al(Ga)N pour l'opto´electronique inter-sous-bande dans l'infrarouge proche, moyen et lointain* (PhD thesis)

[205] Kandaswamy P K 2010 *Al(Ga)N/GaN nanostructures for intersubband optoelectronics in the near- and mid-infrared* (PhD thesis)

[206] Villain J and Pimpinelli A 1999 *Physique de la croissance cristalline* (Eyrolles , Centre d'études nucléaires de Saclay)

[207] Barabási A-L and Stanley H E 1995 *Fractal concepts in surface growth* (New York, NY, USA: Press Syndicate of the University of Cambridge)

[208] Politi P, Grenet G, Marty A, Ponchet A and Villain J 2000 Instabilities in crystal growth by atomic or molecular beams *Phys. Rep.* **324** 271–404

[209] Almond M J, Jenkins C E, Rice D A and Hagen K 1992 Organometallic precursors to the formation of GaN by MOCVD: structural characterisation of Me3Ga · NH3 by gas-phase electron diffraction *J. Organomet. Chem.* **439** 251–61

[210] Etzkorn E V and Clarke D R 2001 Cracking of GaN films *J. Appl. Phys.* **89** 1025–34

[211] Kapolnek D, Wu X H, Heying B, Keller S, Keller B P, Mishra U K, DenBaars S P and Speck J S 1995 Structural evolution in epitaxial metalorganic chemical vapor deposition grown GaN films on sapphire *Appl. Phys. Lett.* **67** 1541–3

[212] Martinez-Criado G, Kuball M, Benyoucef M, Sarua A, Frayssinet E, Beaumont B, Gibart P, Miskys C R and Stutzmann M 2003 Free-standing GaN grown on epitaxial lateral overgrown GaN substrates *J. Cryst. Growth* **255** 277–81

[213] Molnar R J, Götz W, Romano L T and Johnson N M 1997 Growth of gallium nitride by hydride vapor-phase epitaxy *J. Cryst. Growth* **178** 147–56

[214] Richter E, Hennig C, Weyers M, Habel F, Tsay J-D, Liu W-Y, Brückner P, Scholz F, Makarov Y, Segal A and Kaeppeler J 2005 Reactor and growth process optimization for growth of thick GaN layers on sapphire substrates by HVPE *J. Cryst. Growth* **277** 6–12

[215] K. Kelly M, P. Vaudo R, M. Phanse V, Görgens L, Ambacher O and Stutzmann M 1999 Large Free-Standing GaN Substrates by Hydride Vapor Phase Epitaxy and Laser-Induced Liftoff *Jpn. J. Appl. Phys.* **38** L217

[216] Motoki K, Okahisa T, Matsumoto N, Matsushima M, Kimura H, Kasai H, Takemoto K, Uematsu K, Hirano T, Nakayama M, Nakahata S, Ueno M, Hara D, Kumagai Y, Koukitu A and Seki H 2001 Preparation of Large Freestanding GaN Substrates by Hydride Vapor Phase Epitaxy Using GaAs as a Starting Substrate *Jpn. J. Appl. Phys.* **40** L140

[217] Xu X, Vaudo R ., Loria C, Salant A, Brandes G . and Chaudhuri J 2002 Growth and characterization of low defect GaN by hydride vapor phase epitaxy *J. Cryst. Growth* **246** 223–9

[218] Held R, Crawford D E, Johnston A M, Dabiran A M and Cohen P I 1997 In situ control of gan growth by molecular beam epitaxy *J. Electron. Mater.* **26** 272–80

[219] Shon J W, Ohta J, Ueno K, Kobayashi A and Fujioka H 2014 Fabrication of full-color InGaN-based light-emitting diodes on amorphous substrates by pulsed sputtering *Sci. Rep.* **4**

[220] Cho A Y and Arthur J R 1975 Molecular beam epitaxy *Prog. Solid State Chem.* **10** 157–91

[221] Speck J S and Chichibu S F 2011 Nonpolar and Semipolar Group III Nitride-Based Materials *MRS Bull.* **34** 304–12

[222] Adelmann C, Brault J, Mula G, Daudin B, Lymperakis L and Neugebauer J 2003 Gallium adsorption on (0001) GaN surfaces *Phys. Rev. B* **67** 165419

[223] Mula G, Adelmann C, Moehl S, Oullier J and Daudin B 2001 Surfactant effect of gallium during molecular-beam epitaxy of GaN on AlN (0001) *Phys. Rev. B* **64** 195406

[224] Neugebauer J, Zywietz T, Scheffler M, Northrup J, Chen H and Feenstra R 2003 Adatom Kinetics On and Below the Surface: The Existence of a New Diffusion Channel *Phys. Rev. Lett.* **90** 056101

[225] Lieberman M A and Lichtenberg A J 1994 *Principles of Plasma Discharges and Materials Processing (Chap. 9)* (Wiley, New York)

[226] Myoung J M, Gluschenkov O, Kim K and Kim S 1999 Growth kinetics of GaN and effects of flux ratio on the properties of GaN films grown by plasma-assisted molecular beam epitaxy *J. Vac. Sci. Technol. Vac. Surf. Films* **17** 3019–28

[227] Bellet-Amalric E, Adelmann C, Sarigiannidou E, Rouvière J L, Feuillet G, Monroy E and Daudin B 2004 Plastic strain relaxation of nitride heterostructures *J. Appl. Phys.* **95** 1127–33

[228] Northrup J, Neugebauer J, Feenstra R and Smith A 2000 Structure of GaN(0001) : The laterally contracted Ga bilayer model *Phys. Rev. B* **61** 9932–5

[229] Adelmann H C 2002 *Growth and strain relaxation mechanisms of group III nitride heterostructures* (PhD thesis)

[230] Iliopoulos E and Moustakas T D 2002 Growth kinetics of AlGaN films by plasma-assisted molecular-beam epitaxy *Appl. Phys. Lett.* **81** 295–7

[231] Monroy E, Daudin B, Bellet-Amalric E, Gogneau N, Jalabert D, Enjalbert F, Brault J, Barjon J and Dang L S 2003 Surfactant effect of In for AlGaN growth by plasma-assisted molecular beam epitaxy *J. Appl. Phys.* **93** 1550–6

[232] Lahourcade L, Renard J, Gayral B, Monroy E, Chauvat M P and Ruterana P 2008 Ga kinetics in plasma-assisted molecular-beam epitaxy of GaN(11-22): Effect on the structural and optical properties *J. Appl. Phys.* **103** 093514

[233] Horcas I, Fernández R, Gómez-Rodríguez J M, Colchero J, Gómez-Herrero J and Baro A M 2007 WSXM: A software for scanning probe microscopy and a tool for nanotechnology *Rev. Sci. Instrum.* **78** 013705

[234] Ajay A, Schörmann J, Jiménez-Rodriguez M, Lim C B, Walther F, Rohnke M, Mouton I, Amichi L, Bougerol C, Den Hertog M I, Eickhoff M and Monroy E 2016 Ge doping of GaN beyond the Mott transition *J. Phys. Appl. Phys.* **49** 445301

[235] Beeler M, Lim C B, Hille P, Bleuse J, Schörmann J, de la Mata M, Arbiol J, Eickhoff M and Monroy E 2015 Long-lived excitons in GaN/AlN nanowire heterostructures *Phys. Rev. B* **91** 205440

[236] Romano L T, Van de Walle C G, Ager J W, Götz W and Kern R S 2000 Effect of Si doping on strain, cracking, and microstructure in GaN thin films grown by metalorganic chemical vapor deposition *J. Appl. Phys.* **87** 7745

[237] Fritze S, Dadgar A, Witte H, Bügler M, Rohrbeck A, Bläsing J, Hoffmann A and Krost A 2012 High Si and Ge n-type doping of GaN doping - Limits and impact on stress *Appl. Phys. Lett.* **100** 122104

[238] Nenstiel C, Bügler M, Callsen G, Nippert F, Kure T, Fritze S, Dadgar A, Witte H, Bläsing J, Krost A and Hoffmann A 2015 Germanium - the superior dopant in n-type GaN *Phys. Status Solidi RRL - Rapid Res. Lett.* **9** 716–21

[239] Dadgar A, Fritze S, Schulz O, Hennig J, Bläsing J, Witte H, Diez A, Heinle U, Kunze M, Daumiller I, Haberland K and Krost A 2013 Anisotropic bow and plastic deformation of GaN on silicon *J. Cryst. Growth* **370** 278–81

[240] Fang Z, Robin E, Rozas-Jiménez E, Cros A, Donatini F, Mollard N, Pernot J and Daudin B 2015 Si Donor Incorporation in GaN Nanowires *Nano Lett.* **15** 6794–801

[241] Richter T, Meijers H L R, Calarco R and Marso M 2008 Doping Concentration of GaN Nanowires Determined by Opto-Electrical Measurements *Nano Lett.* **8** 3056–9

[242] Wang H and Chen A-B 2000 Calculation of shallow donor levels in GaN *J. Appl. Phys.* **87** 7859

[243] Bogusławski P and Bernholc J 1997 Doping properties of C, Si, and Ge impurities in GaN and AlN *Phys. Rev. B* **56** 9496–505

[244] Oshima Y, Yoshida T, Watanabe K and Mishima T 2010 Properties of Ge-doped, high-quality bulk GaN crystals fabricated by hydride vapor phase epitaxy *J. Cryst. Growth* **312** 3569–73

[245] Hofmann P, Krupinski M, Habel F, Leibiger G, Weinert B, Eichler S and Mikolajick T 2016 Novel approach for n-type doping of HVPE gallium nitride with germanium *J. Cryst. Growth* **450** 61–5

[246] Nakamura S, Mukai T and Senoh M 1992 Si- and Ge-Doped GaN Films Grown with GaN Buffer Layers *Jpn. J. Appl. Phys.* **31** 2883–8

[247] Zhang X, Kung P, Saxler A, Walker D, Wang T C and Razeghi M 1995 Growth of AlxGa1−xN:Ge on sapphire and silicon substrates *Appl. Phys. Lett.* **67** 1745

[248] Dadgar A, Bläsing J, Diez A and Krost A 2011 Crack-Free, Highly Conducting GaN Layers on Si Substrates by Ge Doping *Appl. Phys. Express* **4** 011001

[249] Kirste R, Hoffmann M P, Sachet E, Bobea M, Bryan Z, Bryan I, Nenstiel C, Hoffmann A, Maria J-P, Collazo R and Sitar Z 2013 Ge doped GaN with controllable high carrier concentration for plasmonic applications *Appl. Phys. Lett.* **103** 242107

[250] Hageman P R, Schaff W J, Janinski J and Liliental-Weber Z 2004 n-type doping of wurtzite GaN with germanium grown with plasma-assisted molecular beam epitaxy *J. Cryst. Growth* **267** 123–8

[251] Gunning B P, Clinton E A, Merola J J, Doolittle W A and Bresnahan R C 2015 Control of ion content and nitrogen species using a mixed chemistry plasma for GaN grown at extremely high growth rates >9 μm/h by plasma-assisted molecular beam epitaxy *J. Appl. Phys.* **118** 155302

[252] Schäfer M, Günther M, Länger C, Müßener J, Feneberg M, Uredat P, Elm M T, Hille P, Schörmann J, Teubert J, Henning T, Klar P J and Eickhoff M 2015 Electrical transport properties of Ge-doped GaN nanowires *Nanotechnology* **26** 135704

[253] Schörmann J, Hille P, Schäfer M, Müßener J, Becker P, Klar P J, Kleine-Boymann M, Rohnke M, de la Mata M, Arbiol J, Hofmann D M, Teubert J and Eickhoff M 2013 Germanium doping of self-assembled GaN nanowires grown by plasma-assisted molecular beam epitaxy *J. Appl. Phys.* **114** 103505

[254] Lahourcade L, Pernot J, Wirthmüller A, Chauvat M P, Ruterana P, Laufer A, Eickhoff M and Monroy E 2009 Mg doping and its effect on the semipolar GaN(1122) growth kinetics *Appl. Phys. Lett.* **95** 171908

[255] Monroy E, Andreev T, Holliger P, Bellet-Amalric E, Shibata T, Tanaka M and Daudin B 2004 Modification of GaN(0001) growth kinetics by Mg doping *Appl. Phys. Lett.* **84** 2554

[256] Northrup J E 2005 Effect of magnesium on the structure and growth of GaN(0001) *Appl. Phys. Lett.* **86** 122108

[257] Zhang Y, Evans J R G and Yang S 2011 Corrected Values for Boiling Points and Enthalpies of Vaporization of Elements in Handbooks *J. Chem. Eng. Data* **56** 328–37

[258] Berggren K-F and Sernelius B E 1981 Band-gap narrowing in heavily doped many-valley semiconductors *Phys. Rev. B* **24** 1971–86

[259] Moss T S 1954 Theory of the Spectral Distribution of Recombination Radiation from InSb *Proc. Phys. Soc. B* **67** 775

[260] Arnaudov B, Paskova T, Goldys E M, Evtimova S and Monemar B 2001 Modeling of the free-electron recombination band in emission spectra of highly conducting n-GaN *Phys. Rev. B* **64** 045213

[261] Schuster F, Winnerl A, Weiszer S, Hetzl M, Garrido J A and Stutzmann M 2015 Doped GaN nanowires on diamond: Structural properties and charge carrier distribution *J. Appl. Phys.* **117** 044307

[262] Beeler M, Hille P, Schörmann J, Teubert J, de la Mata M, Arbiol J, Eickhoff M and Monroy E 2014 Intraband Absorption in Self-Assembled Ge-Doped GaN/AlN Nanowire Heterostructures *Nano Lett.* **14** 1665–73

[263] Hille P, Müßener J, Becker P, de la Mata M, Rosemann N, Magén C, Arbiol J, Teubert J, Chatterjee S, Schörmann J and Eickhoff M 2014 Screening of the quantum-confined Stark effect in AlN/GaN nanowire superlattices by germanium doping *Appl. Phys. Lett.* **104** 102104

[264] Sénès M, Smith K L, Smeeton T M, Hooper S E and Heffernan J 2007 Strong carrier confinement in In x Ga 1 − x N ⁄ Ga N quantum dots grown by molecular beam epitaxy *Phys. Rev. B* **75**

[265] Guillot F, Bellet-Amalric E, Monroy E, Tchernycheva M, Nevou L, Doyennette L, Julien F H, Dang L S, Remmele T, Albrecht M, Shibata T and Tanaka M 2006 Si-doped GaN⁄AlN quantum dot superlattices for optoelectronics at telecommunication wavelengths *J. Appl. Phys.* **100** 044326

[266] Gačević Ž, Das A, Teubert J, Kotsar Y, Kandaswamy P K, Kehagias T, Koukoula T, Komninou P and Monroy E 2011 Internal quantum efficiency of III-nitride quantum dot superlattices grown by plasma-assisted molecular-beam epitaxy *J. Appl. Phys.* **109** 103501

[267] Lefebvre P, Kalliakos S, Bretagnon T, Valvin P, Taliercio T, Gil B, Grandjean N and Massies J 2004 Observation and modeling of the time-dependent descreening of internal electric field in a wurtzite G a N / A l 0.15 Ga 0.85 N quantum well after high photoexcitation *Phys. Rev. B* **69**

[268] Furtmayr F, Teubert J, Becker P, Conesa-Boj S, Morante J R, Chernikov A, Schäfer S, Chatterjee S, Arbiol J and Eickhoff M 2011 Carrier confinement in GaN/AlxGa1−xN nanowire heterostructures (0<x≤1) *Phys. Rev. B* **84** 205303

[269] Renard J, Kandaswamy P K, Monroy E and Gayral B 2009 Suppression of nonradiative processes in long-lived polar GaN/AlN quantum dots *Appl. Phys. Lett.* **95** 131903

[270] Bertelli M, Löptien P, Wenderoth M, Rizzi A, Ulbrich R, Righi M, Ferretti A, Martin-Samos L, Bertoni C and Catellani A 2009 Atomic and electronic structure of the nonpolar GaN(1-100) surface *Phys. Rev. B* **80** 115324

[271] Rigutti L, Teubert J, Jacopin G, Fortuna F, Tchernycheva M, De Luna Bugallo A, Julien F H, Furtmayr F, Stutzmann M and Eickhoff M 2010 Origin of energy dispersion in Al(x)Ga(1−x)N/GaN nanowire quantum disks with low Al content *Phys. Rev. B* **82** 235308

[272] Rivera C, Jahn U, Flissikowski T, Pau J, Muñoz E and Grahn H T 2007 Strain-confinement mechanism in mesoscopic quantum disks based on piezoelectric materials *Phys. Rev. B* **75** 045316

[273] Lim C B, Beeler M, Ajay A, Lähnemann J, Bellet-Amalric E, Bougerol C and Monroy E 2015 Intersubband transitions in nonpolar GaN/Al(Ga)N heterostructures in the short and mid-wavelength infrared regions *J Appl Phys* **118** 014309

[274] Lim C B, Ajay A, Bougerol C, Haas B, Schörmann J, Beeler M, Lähnemann J, Eickhoff M and Monroy E 2015 Nonpolar *m* -plane GaN/AlGaN heterostructures with intersubband transitions in the 5–10 THz band *Nanotechnology* **26** 435201

[275] Lim C B, Ajay A, Bougerol C, Lähnemann J, Donatini F, Schörmann J, Bellet-Amalric E, Browne D A, Jiménez-Rodríguez M and Monroy E 2016 Effect of doping on the far-infrared intersubband transitions in nonpolar *m* -plane GaN/AlGaN heterostructures *Nanotechnology* **27** 145201

[276] Kandaswamy P K, Guillot F, Bellet-Amalric E, Monroy E, Nevou L, Tchernycheva M, Michon A, Julien F H, Baumann E, Giorgetta F R, Hofstetter D, Remmele T, Albrecht M, Birner S and Dang L S 2008 GaN/AlN short-period superlattices for intersubband optoelectronics: A systematic study of their epitaxial growth, design, and performance *J. Appl. Phys.* **104** 093501

[277] Heying B, Averbeck R, Chen L F, Haus E, Riechert H and Speck J S 2000 Control of GaN surface morphologies using plasma-assisted molecular beam epitaxy *J. Appl. Phys.* **88** 1855–60

[278] Lim C B, Beeler M, Ajay A, Lähnemann J, Bellet-Amalric E, Bougerol C, Schörmann J, Eickhoff M and Monroy E 2016 Short-wavelength, mid- and far-infrared intersubband absorption in nonpolar GaN/Al(Ga)N heterostructures *Jpn. J. Appl. Phys.* **55** 05FG05

[279] Einfeldt S, Kirchner V, Heinke H, Dießelberg M, Figge S, Vogeler K and Hommel D 2000 Strain relaxation in AlGaN under tensile plane stress *J. Appl. Phys.* **88** 7029

[280] Einfeldt S, Heinke H, Kirchner V and Hommel D 2001 Strain relaxation in AlGaN/GaN superlattices grown on GaN *J. Appl. Phys.* **89** 2160–7

[281] Vennegues P, Founta S, Mariette H and Daudin B 2010 Influence of Stacking Sequences and Lattice Parameter Differences on the Microstructure of Nonpolar AlN Films Grown on (11-20) 6H-SiC by Plasma-Assisted Molecular Beam Epitaxy *Jpn. J. Appl. Phys.* **49** 040201

[282] Vennéguès P and Bougrioua Z 2006 Epitaxial orientation of III-nitrides grown on R-plane sapphire by metal-organic-vapor-phase epitaxy *Appl. Phys. Lett.* **89** 111915

[283] Chiang C H, Chen K M, Wu Y H, Yeh Y S, Lee W I, Chen J F, Lin K L, Hsiao Y L, Huang W C and Chang E Y 2011 Nonpolar a-plane GaN grown on r-plane sapphire using multilayer AlN buffer by metalorganic chemical vapor deposition *Appl. Surf. Sci.* **257** 2415–8

[284] Okamoto K, Tanaka T, Kubota M and Ohta H 2007 Pure Blue Laser Diodes Based on Nonpolar *m* -Plane Gallium Nitride with InGaN Waveguiding Layers *Jpn. J. Appl. Phys.* **46** L820–L822

[285] Young E C, Romanov A E, Gallinat C S, Hirai A, Beltz G E and Speck J S 2010 Anisotropy of tensile stresses and cracking in nonbasal plane AlxGa1−xN/GaN heterostructures *Appl. Phys. Lett.* **96** 041913

[286] Brault J, Bellet-Amalric E, Tanaka S, Enjalbert F, Le Si Dang D, Sarigiannidou E, Rouviere J-L, Feuillet G and Daudin B 2003 Characteristics of AlN growth on vicinal SiC(0001) substrates by molecular beam epitaxy *Phys. Status Solidi B* **240** 314–7

[287] Lim C B, Ajay A, Bougerol C, Bellet-Amalric E, Schörmann J, Beeler M and Monroy E 2016 Effect of Al incorporation in nonpolar *m* -plane GaN/AlGaN multi-quantum-wells using

plasma-assisted molecular-beam epitaxy: Al incorporation in nonpolar *m* -plane GaN/AlGaN multi-QWs *Phys. Status Solidi A*

[288] Kotani T, Arita M and Arakawa Y 2015 Doping dependent blue shift and linewidth broadening of intersubband absorption in non-polar m-plane AlGaN/GaN multiple quantum wells *Appl. Phys. Lett.* **107** 112107

[289] Sawicka M, Chèze C, Turski H, Smalc-Koziorowska J, Kryśko M, Kret S, Remmele T, Albrecht M, Cywiński G, Grzegory I and Skierbiszewski C 2013 Growth mechanisms in semipolar and nonpolar m-plane AlGaN/GaN structures grown by PAMBE under N-rich conditions *J. Cryst. Growth* **377** 184–91

[290] Leroux M, Grandjean N, Beaumont B, Nataf G, Semond F, Massies J and Gibart P 1999 Temperature Dependence of Photoluminescence Intensities of Undoped and Doped GaN *Phys. Status Solidi B* **216** 605–8

[291] Kim J-H, Kwon B-J, Cho Y-H, Huault T, Leroux M and Brault J 2010 Carrier transfer and recombination dynamics of a long-lived and visible range emission from multi-stacked GaN/AlGaN quantum dots *Appl. Phys. Lett.* **97** 061905

[292] Simon J, Pelekanos N T, Adelmann C, Martinez-Guerrero E, André R, Daudin B, Dang L S and Mariette H 2003 Direct comparison of recombination dynamics in cubic and hexagonal GaN/AlN quantum dots *Phys. Rev. B* **68** 035312

[293] Simon J, Martinez-Guerrero E, Adelmann C, Mula G, Daudin B, Feuillet G, Mariette H and Pelekanos N T 2001 Time-Resolved Photoluminescence Studies of Cubic and Hexagonal GaN Quantum Dots *Phys. Status Solidi B* **224** 13–6

[294] Harris J C, Someya T, Kako S, Hoshino K and Arakawa Y 2000 Time-resolved photoluminescence of GaN/Al0.5Ga0.5N quantum wells *Appl. Phys. Lett.* **77** 1005

[295] Friel I, Thomidis C, Fedyunin Y and Moustakas T D 2004 Investigation of excitons in AlGaN/GaN multiple quantum wells by lateral photocurrent and photoluminescence spectroscopies *J. Appl. Phys.* **95** 3495–502

[296] Kotani T, Arita M and Arakawa Y 2014 Observation of mid-infrared intersubband absorption in non-polar m-plane AlGaN/GaN multiple quantum wells *Appl. Phys. Lett.* **105** 261108

[297] Kotani T, Arita M, Hoshino K and Arakawa Y 2016 Temperature dependence of mid-infrared intersubband absorption in AlGaN/GaN multiple quantum wells *Appl. Phys. Lett.* **108** 052102

[298] Hofstetter D, Di Francesco J, Kandaswamy P K and Monroy E 2011 Intersubband spectroscopy probing higher order interminiband transitions in AlN-GaN-based superlattices *Appl. Phys. Lett.* **98** 071104

[299] Reshchikov M A and Morkoç H 2005 Luminescence properties of defects in GaN *J. Appl. Phys.* **97** 061301

[300] Cho Y-H, Gainer G H, Lam J B, Song J J, Yang W and Jhe W 2000 Dynamics of anomalous optical transitions in Al x Ga 1 − x N alloys *Phys. Rev. B* **61** 7203–6

[301] Chin V W L, Tansley T L and Osotchan T 1994 Electron mobilities in gallium, indium, and aluminum nitrides *J. Appl. Phys.* **75** 7365

[302] Kim K-C, Schmidt M C, Sato H, Wu F, Fellows N, Saito M, Fujito K, Speck J S, Nakamura S and DenBaars S P 2007 Improved electroluminescence on nonpolar m -plane InGaN/GaN quantum wells LEDs *Phys. Status Solidi RRL – Rapid Res. Lett.* **1** 125–7

Publications and conference contributions

Book chapters

[1] **Intersubband Optoelectronics using III-Nitride Semiconductors**
C. B. Lim, A. Ajay, J. Lähnemann, D. A. Browne, and E. Monroy
In *"HandBook of GaN Semiconductor Materials and Devices"*, edited by W. Bi, H.-C. Kuo, P.-C. Ku, and B. Shen (Taylor & Francis, UK, to appear in 2017).

[2] **III-Nitride Nanostructures for Intersubband Optoelectronics**
C. B. Lim, A. Ajay, J. Lähnemann, D. A. Browne, and E. Monroy
In *"III-Nitride Materials, Devices and Nano-Structures"*, edited by Z. C. Feng (World Scientific Europe, UK, ISBN: 978-1-78634-318-5, June 2017).

Publications in international journals

2017

[1] **Intersubband Absorption in Si- and Ge-Doped GaN/AlN Heterostructures in Self-Assembled Nanowire and 2D layers**
A. Ajay, C.B. Lim, D.A. Browne, J. Polaczynski, E. Bellet-Amalric, M. Den Hertog, and E. Monroy
Phys. Status Solidi B, 1600734. doi:10.1002/pssb.201600734 (2017)

[2] **Short-wave infrared (λ=3 μm) intersubband polaritons in the GaN/AlN system**
T. Laurent, J-M. Manceau, E. Monroy, C.B Lim, S. Rennesson, F. Semond, F.H. Julien and R. Colombelli
Appl. Phys. Lett. **110**, 131102 (2017)

2016

[3] **Effect of Al incorporation in nonpolar m-plane GaN/AlGaN multi-quantum-wells using plasma-assisted molecular-beam epitaxy**
C.B. Lim, A. Ajay, C. Bougerol, E. Bellet-Amalric, J. Schörmann, M. Beeler and E. Monroy
Phys. Status Solidi A. doi:10.1002/pssa.201600849 (2016)

[4] **Ge doping of GaN beyond the Mott transition**
A. Ajay, J. Schörmann, M. Jimenez-Rodriguez, C. B. Lim, F. Walther, M. Rohnke, I. Mouton, L. Amichi, C. Bougerol, M. I. Den Hertog, M. Eickhoff, et E. Monroy
J. Phys. D: Appl. Phys. ***49*** 445301 (2016)

[5] **Effect of doping on the far-infrared intersubband transitions in nonpolar *m*-plane GaN/AlGaN heterostructures**
C.B. Lim, A. Ajay, C. Bougerol, J. Lähnemann, F. Donatini, J. Schörmann, E. Bellet-Amalric, D.A. Browne, M. Jiménez-Rodriguez, and E. Monroy
Nanotechnology **27**, 145201 (2016)

[6] **Short-wavelength, mid- and far-infrared intersubband absorption in nonpolar GaN/Al(Ga)N heterostructures**
C. B. Lim, M. Beeler, A. Ajay, J. Lähnemann, E. Bellet-Amalric, C. Bougerol, J. Schörmann, M. Eickhoff, and E. Monroy
Jpn. J. Appl. Phys. **55** 05FG05 (2016)

2015

[7] **Nonpolar *m*-plane GaN/AlGaN heterostructures with intersubband transitions in the 5 to 10 THz band**
C. B. Lim, A. Ajay, C. Bougerol, J. Schörmann, M. Beeler, J. Lähnemann, M. Eickhoff, and E. Monroy
Nanotechnology **26**, 435201 (2015)

[8] **Intersubband transitions in nonpolar GaN/Al(Ga)N heterostructures in the short- and mid-wavelength infrared regions**
C. B. Lim, M. Beeler, A. Ajay, J. Lähnemann, E. Bellet-Amalric, C. Bougerol, and E. Monroy
J. Appl. Phys. **118**, 014309 (2015)

[9] **Long-lived excitons in GaN/AlN nanowire heterostructures**
M. Beeler, C. B. Lim, P. Hille, J. Bleuse, J. Schörmann, M. de la Mata, J. Arbiol, M. Eickhoff, and E. Monroy
Phys. Rev. B **91**, 205440 (2015)

Contributions to international conferences

[1] (Invited) **Molecular-beam epitaxy of polar/semipolar/nonpolar GaN/AlGaN heterostructures for intersubband devices**
C. B. Lim, A. Ajay, D. A. Browne C. Bougerol, E. Bellet-Amalric and E. Monroy
19th European Workshop on Molecular Beam Epitaxy (EuroMBE19), Korobitsyno, St. Petersburg, Russia. March 2017.

[2] (Oral) **Doping of nonpolar m-plane GaN/AlGaN multi-quantum-wells with intersubband transitions in the THz range: Effect of Si and Ge doping**
C. B. Lim, A. Ajay, C. Bougerol, J. Schörmann, D. A. Browne, and E. Monroy
Int. Workshop on Nitride Semiconductors (IWN 2016), Orlando, USA. Oct. 2016.

[3] (Poster) **Effect of Si and Ge doping in GaN/AlGaN multi-quantum-wells with intersubband transitions**

C. B. Lim, A. Ajay, and E. Monroy
Int. Workshop on Nitride Semiconductors (IWN 2016), Orlando, USA. Oct. 2016.

[4] (Oral) **Effect of Al incorporation in nonpolar m-plane GaN/AlGaN multi-quantum-wells using plasma-assisted molecular-beam epitaxy**
C. B. Lim, A. Ajay, M. Beeler, C. Bougerol, E. Bellet-Amalric, J. Schörmann, and E. Monroy
E-MRS Fall Meeting 2016, Warsaw, Poland. Sept. 2016.

[5] (Invited) **Nonpolar m-plane GaN epitaxy using plasma-assisted MBE for infrared optoelectronics**
C. B. Lim, A. Ajay, C. Bougerol, E. Bellet-Amalric, J. Schörmann, D. A. Browne, and E. Monroy
EMN Meeting on Epitaxy, Budapest, Hungary. Sept. 2016.

[6] (Poster) **Infrared intersubband absorption in nonpolar GaN/Al(Ga)N multi-quantum wells**
C. B. Lim, M. Beeler, A. Ajay, J. Lähnemann, E. Bellet-Amalric, C. Bougerol, J. Schörmann, and E. Monroy
Dautreppe seminar 2015, Grenoble, France. Dec. 2015.

[7] (Invited) **Short-wavelength, mid- and far-infrared intersubband absorption in nonpolar GaN/Al(Ga)N heterostructures**
C. B. Lim, M. Beeler, A. Ajay, J. Lähnemann, E. Bellet-Amalric, C. Bougerol, J. Schörmann, and E. Monroy
6th Int. Symp. on Growth of III-Nitrides (ISGN-6), Hamamatsu, Japan. Nov. 2015.
Award to the best young scientist

[8] (Oral) **Short-wavelength, mid- and far-infrared absorption in nonpolar GaN/Al(Ga)N heterostructures**
C. B. Lim, M. Beeler, A. Ajay, J. Lähnemann, E. Bellet-Amalric, C. Bougerol, and E. Monroy
11th Int. Conf. on Nitride Semiconductors (ICNS-11), Beijing, China. Sept. 2015.

[9] (Oral) **Nonpolar GaN/Al(Ga)N superlattices for intersubband optoelectronics**
C. B. Lim, M. Beeler, E. Bellet-Amalric, C. Bougerol, and E. Monroy
10th Int. Symp. on Semiconductor Light Emitting Devices (ISSLED-10), Kaohsiung, Taiwan. Dec. 2014.